CERN-THESIS-2024-206
//2024

JET RADIUS DEPENDENCE OF DIJET MOMENTUM BALANCE AND SUPPRESSION IN PB+PB COLLISIONS AT 5.02 TEV WITH THE ATLAS DETECTOR

BY

ANABEL CRISTINA ROMERO HERNANDEZ

DISSERTATION

Submitted in partial fulfillment of the requirements
for the degree of Doctor of Philosophy in Physics
in the Graduate College of the
University of Illinois Urbana-Champaign, 2024

Urbana, Illinois

Doctoral Committee:

Associate Professor Jacquelyn Noronha-Hostler, Chair
Professor Anne Sickles, Director of Research
Professor Douglas Beck
Assistant Professor Elizabeth Goldschmidt

Abstract

The quark gluon plasma (QGP) is a high energy, high density state of matter that existed less than a second after the big bang. The QGP is made of elementary particles called partons that interact through the strong force, one of the fundamental forces of nature. The QGP can be created in ultra-relativistic heavy ion collisions in order to study the strong force. This is done by colliding accelerated beams of heavy nuclei and measuring the products of the collisions with a particle detector. In particle collisions, partons can scatter off each other with a large momentum transfer, and when they come out of the collisions, they create collimated sprays of particles that are called jets. In heavy ion collisions, these hard scattered partons make their way through the QGP, interacting with it and losing energy, a phenomenon known as jet quenching. Jets created in heavy ion collisions are modified with respect to jets created in vacuum due to the strong interactions with the QGP. When partons are hard scattered, pairs of jets called dijets are emitted in opposite directions with the same energy. When dijets are created in heavy ion collisions, they lose energy when they interact with the QGP. Traveling different path lengths within the QGP can cause the dijets to become imbalanced in momentum due to the associated energy loss. Thus, dijet measurements of jet quenching are a powerful tool for studying the QGP and the strong force.

This thesis describes a measurement of the jet radius dependence of the momentum balance between leading back-to-back dijets in Pb+Pb and *pp* collisions at a per-nucleon-pair center of mass energy $\sqrt{s_{\mathrm{NN}}}$ =5.02 TeV. The data was collected by the ATLAS detector at the LHC, with a total integrated luminosity of 1.72 nb^{-1} of Pb+Pb collisions collected in 2018, and 255 pb^{-1} of *pp* collisions collected in 2017. Jets were reconstructed using the anti-k_t algorithm with jet radius parameters $R = 0.2, 0.3, 0.4, 0.5$ and 0.6. The dijet momentum balance distributions are constructed for leading jets with transverse momentum p_{T} from 100 to 562 GeV for $R = 0.2, 0.3$ and 0.4 jets, and from 158 to 562 GeV for $R = 0.5$ and 0.6 jets. The absolutely normalized dijet momentum balance distributions are constructed to compare measurements of the dijet yields in Pb+Pb collisions directly to the dijet cross sections in *pp* collisions. For all jet radii considered here, there is a suppression of more balanced dijets in Pb+Pb collisions compared to *pp* collisions, while for more imbalanced dijets there is an enhancement. There is a jet radius dependence to the dijet yields, being stronger for

more imbalanced dijets than for more balanced dijets. Additionally, jet pair nuclear modification factors are measured. The subleading jet yields are found to be more suppressed than leading jet yields in dijets. A jet radius dependence of the pair nuclear modification factors is observed, with the suppression decreasing with increasing jet radius. These measurements provide new constraints on jet quenching scenarios in the quark-gluon plasma.

To my dearest babies: Emilio, Eduardo, Sasha, and Mario.

Acknowledgments

This work wouldn't have been possible without the support of many people: family, friends, and colleagues.

I'd like to thank my advisor, Anne Sickles, for guiding my research work, which allowed me to grow greatly as a professional. I'd also like to thank her for having my back in difficult moments and helping me get through the hardest parts of this journey.

I'd like to thank the people in my research group for being great friends and colleagues. They made grad school and work more bearable, and also taught me a lot. I thank the postdocs whom I worked with: Yongsun Kim, Tim Rinn, Sebastian Tapia, and Anthony Hodges. I especially thank Tim and Sebastian for teaching me the most and being patient and supportive of my learning. I thank the older grad students in my group: Akshat Puri, Mike Phipps, Virginia Bailey, and Xiaoning Wang, with whom I worked for many years, and we learned from each other. Xiaoning, in particular, has a special place in my heart because she's such a lovely person. I thank the younger grad students in my group: Apurva Narde, Grace Garmire, Justin Bennett, Mina Savic, and (future grad student) Abraham Holtermann; though we worked together for a shorter time, it was still great seeing the new generation and passing the torch.

I'd like to thank my ATLAS collaborators for providing valuable feedback to my analysis and helping improve the scientific quality of my work. In particular, I thank the heavy ion group conveners and jet subconveners, Martin Rybar, Aaron Angerami, Qipeng Hu, Riccardo Longo, Dhanush Hangal, Chris McGinn, and my editorial board, Dennis Perepelitsa, Zvi Citron, and David Miller.

I'd like to thank my lovely grad school friends: Chandana Gopal, Luis de Jesus, Shraddha Agrawal, Xiaoning Wang, Mayisha Nakib, Katie Bolan, Blake Erickson, Varsha Subramanyan, and many others, for fun hang outs and emotional support. I'd also like to thank the friends I met through the Women and Gender Minorities in Physics group: Preetha Sarkar, Karmela Padavic-Callaghan, Rita Garrido Menacho, Devyn Shafer, Brianne Gutmann, and many others, for making the department feel more welcoming towards minorities, and contributing greatly to the diversity, equity, and inclusion efforts in academia.

I'd like to thank my friends from undergrad. I'm so grateful we've been able to keep in touch despite the distance and all the things that have made our lives complicated. In particular I thank Eduardo Hernandez,

who is a wonderful person and my closest friend.

I'd like to thank my family for their love and support: my grandmother, Argelis Rivero –who sadly passed away in 2022 but who was always very proud of me–; my great aunts, Maria Eugenia and Mariela Rivero; my aunts, Morella and Maureen Hernandez; my uncle, Alfredo Hernandez; my cousins, Jahan and Daniel Khan, Diego and Matias Hernandez, Santiago and Nicolas Cardona; my siblings, Andrea and Hector David Romero; and my parents, Carolina Hernandez and Hector Romero, for supporting my education throughout the years.

Finally, I'd like to thank my partner, Ivan Tulli, for his infinite love and support.

Contents

Chapter 1

Introduction

1.1 Quantum Chromodynamics

The Standard Model (SM) of particle physics is a quantum field theory that models matter and three of the four fundamental forces of nature [1, 2]. Matter in the SM is described by fundamental fermionic particles quarks and leptons, while interactions are mediated by bosonic force carriers. The SM particles are shown in Figure 1.1. In terms of interactions, the SM describes the electromagnetic force, the weak force, and the strong force, with gravity being left out. The SM is an instance of a gauge theory with gauge group $SU(3) \times SU(2) \times U(1)$.

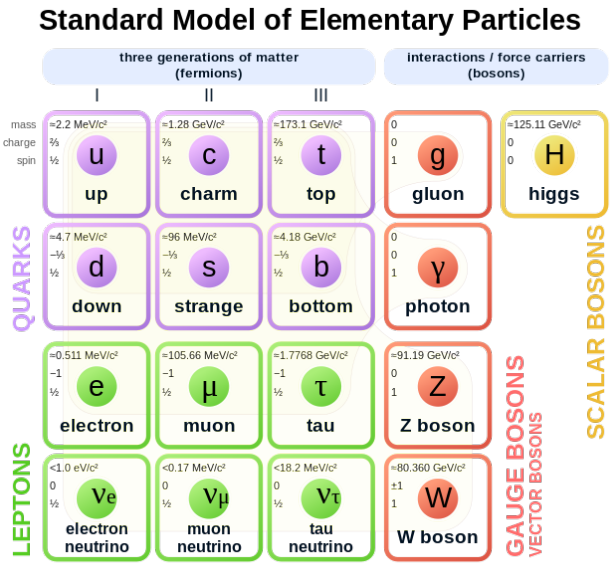

Figure 1.1: Fundamental particles of the Standard Model. Figure taken from [3].

Among the building blocks of the SM is Quantum Chromodynamics (QCD). QCD is a gauge theory with gauge group SU(3) that models the strong interaction between quarks and gluons, where gluons are the force carriers, and quarks are matter. Quarks and gluons are collectively called partons and carry color charge that enables the strong interactions. Color charge can be of types red, blue, and green, along with the

corresponding anti-charges.

The QCD Lagrangian has the form

$$\mathcal{L}_{\text{QCD}} = -\frac{1}{4} G^a_{\mu\nu} G^{\mu\nu}_a + \sum_{I=1}^{6} \left(\mathrm{i} \overline{\Psi}_{iI} \not{D}_{ij} \Psi_{jI} - m_I \overline{\Psi}_I \Psi_I \right) . \tag{1.1}$$

The first term is the usual Yang-Mills term, with $G^a_{\mu\nu}$ being the gluon field strength. Here, $\mu, \nu = 0, 1, 2, 3$ are Minkowski spacetime indices and $a = 1, ..., 8$ corresponds to the eight types of gluons. $G^a_{\mu\nu}$ is given in terms of the gauge field $A^a_\mu(x)$ representing the gluons by an expression of the form

$$G^a_{\mu\nu} = \partial_\mu A^a_\nu - \partial_\nu A^a_\mu + g f^a_{bc} A^b_\mu A^b_\nu, \tag{1.2}$$

where f^a_{bc} are the so-called structure constants of $SU(3)$ and g is the coupling constant (subject to renormalization).

The second term in the action corresponds to the usual Dirac Lagrangian coupled to the gauge field A^a_μ, where the fields $\Psi_{jI}(x)$ are spinors representing the quarks, $j = 1, 2, 3$ being the color index, and $I = 1, ..., 6$ being the flavor index. The Dirac operator $\not{D}$ involves the Dirac γ^μ matrices and the gauge covariant derivative, while m_I is the quark mass of the corresponding flavor of quark (also subject to renormalization).

1.1.1 Asymptotic freedom and color confinement

A notable feature of QCD is that gluons can interact among themselves. This self-interaction has the consequence that the coupling of QCD is small at small distances and large at large distances. This in turn leads to two other characteristic features of QCD, which go by the name of asymptotic freedom and color confinement.

The QCD coupling constant α_s as a function of momentum transfer Q is shown in Figure 1.2 [2], where Q gives the energy scale of the strong interaction. The QCD coupling constant is obtained using perturbation theory to make predictions for experimental observables. Various experiments and models are used to extract the value of α_s, including measurements of jets, τ, and quarkonia, along with up to next-to-next-to-next-to leading order (N^3LO) calculations. The coupling constant α_s is observed to decrease with increasing Q, meaning that strong interactions are stronger at low energies and weaker at high energies, asymptotically approaching zero at very high energies. This implies that at high energies, partons can move "freely", a phenomenon known as asymptotic freedom.

On the other hand, at low energies, partons can only exist in bound states that are color neutral, a phenomenon known as color confinement. Since there are three types of color charges and anti-charges, the

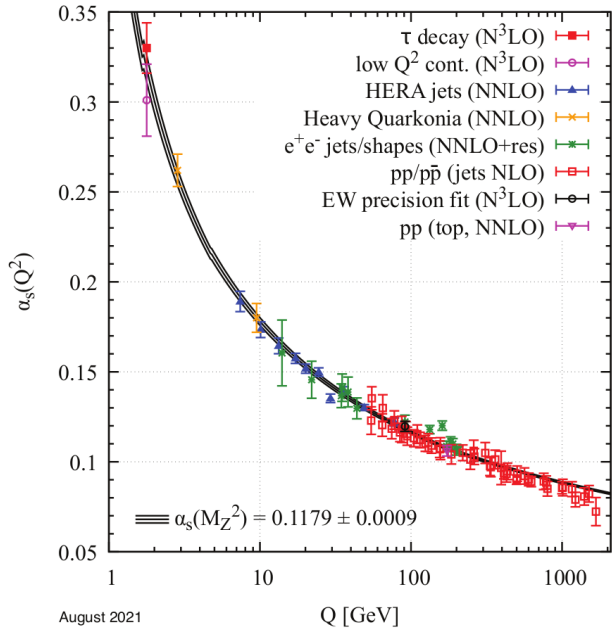

Figure 1.2: QCD coupling constant α_s as a function of momentum transfer Q. Figure taken from [2].

bound states of partons can be of two types: baryons, which have three quarks (each one with a different color), and mesons, which have two quarks (each one with a color and an anti-color). Baryons and mesons are collectively called hadrons, and the process in which hadrons are formed is called hadronization.

Figure 1.3 shows a phase diagram of QCD matter as a function of temperature and baryon density. Hadrons exist in the low temperature, low baryon density region of the phase space. At higher temperatures and densities, partons are deconfined, and a state of matter called a quark gluon plasma is formed [4].

1.2 Quark Gluon Plasma

About 10 μs seconds after the Big Bang, the only thing that existed was a hot, dense state of matter composed of quarks and gluons [4]. Under normal conditions, partons are found only in a confined state within hadrons [1]. In the conditions of the early universe though, partons gained asymptotic freedom, and reminiscent of particles in a plasma, this state of matter was called the quark gluon plasma (QGP). Interestingly, experiments have shown that the QGP behaves like a liquid with very low specific viscosity and shows a flow behaviour that is consistent with an ideal fluid [4].

Nowadays, the QGP can be created using particle accelerators, such as the Relativistic Heavy Ion Collider or the Large Hadron Collider [5]. A diagram of how the QGP is produced using particle colliders is shown in Figure 1.4. Two opposing beams of heavy nuclei that have been accelerated close to the speed of light

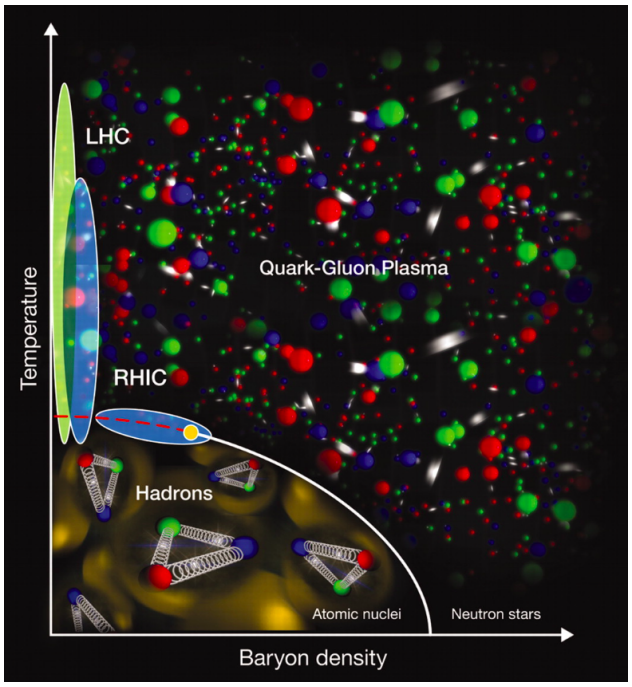

Figure 1.3: Phase diagram of QCD matter as a function of temperature and baryon density. Figure taken from [4].

are collided. The QGP is produced during the collision, existing in a liquid form for approximately $10^{-22}s$. Then the QGP expands, its particles cool down and hadronize, and interactions end in a freeze out [6].

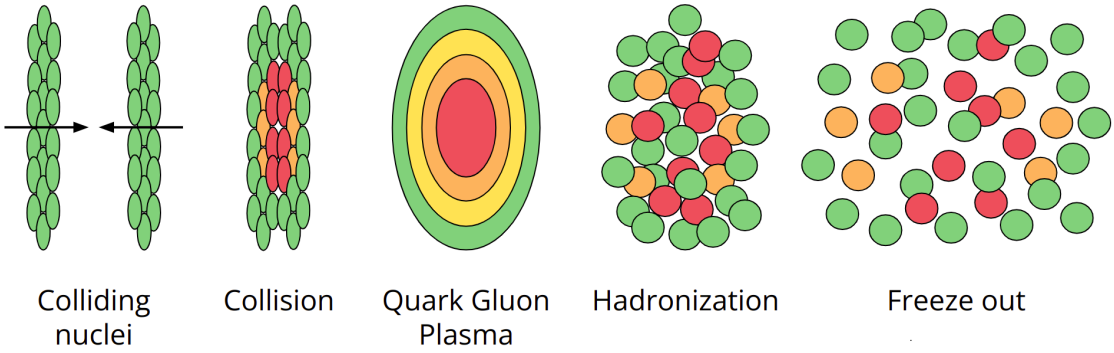

Figure 1.4: Diagram of the QGP formation and evolution in ultrarelativistic heavy ion collisions.

During these ultrarelativistic heavy ion collisions, partons undergo mostly low momentum scatterings that contribute to the formation of the QGP [7]. However, a few scatterings can involve a large momentum transfer and are called hard scatterings. These hard scatterings happen before the QGP is formed, so the hard scattered partons interact with the other particles in the QGP as it evolves.

1.2.1 Collision geometry

The QGP formation and evolution depends on the collision geometry. Ideally, the collision geometry would be characterized by the impact parameter of the colliding nuclei. However, the impact parameter cannot be directly measured in experiments, so the geometry is instead characterized by the collision centrality.

The collision centrality is defined through the Glauber model [8]. In Monte Carlo simulations of the Glauber model, nuclei are modeled with a nucleon density given by a Fermi-Dirac distribution, and the number N_{part} of nucleons participating in the collision is counted for a given impact parameter. Nucleons are counted as collision participants if the distance between them is smaller than $\sqrt{\sigma_{\text{inel}}^{\text{NN}}}$, where $\sigma_{\text{inel}}^{\text{NN}}$ is the inelastic scattering cross section of the nucleons measured from experiments. In other words, the nucleons are considered participants if they are closer than their probability of interaction in units of length. An illustration of a Glauber collision is shown in Figure 1.5, where the nucleons are drawn as circles with radius $\sqrt{\sigma_{\text{inel}}^{\text{NN}}/\pi}/2$ and the participating nucleons are shown in darker colors. The plane perpendicular to the collision line is called the transverse plane[1] and it is where the impact parameter lies.

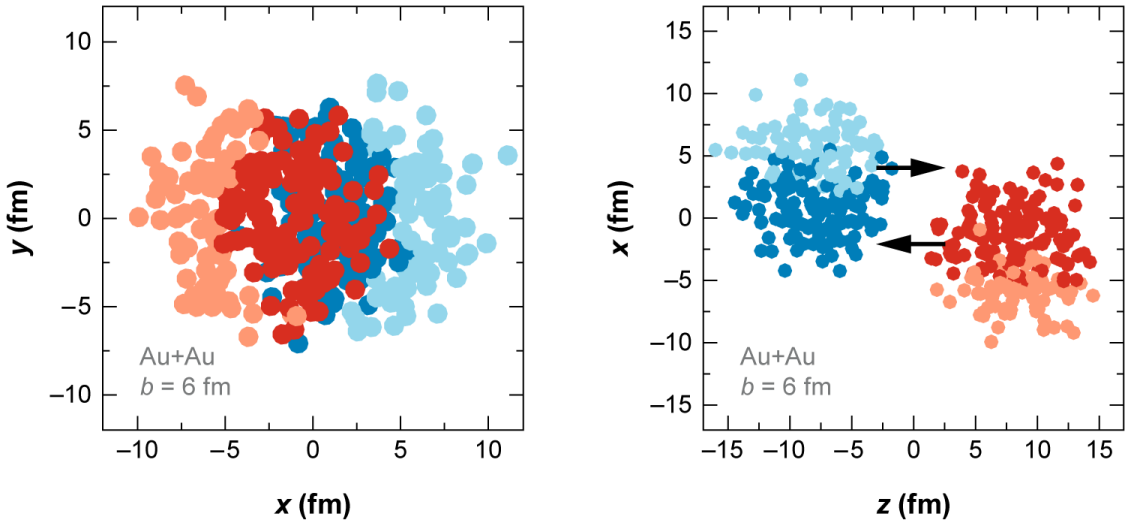

Figure 1.5: Illustration of a Glauber collision viewed (left) from the transverse (x-y) plane and (right) from the collision line (z axis). The nucleons are drawn as circles. Darker circles represent participating nucleons. Figure taken from [8]

The Glauber model assumes a monotonic relationship between N_{part} and the number of particles emitted in the collision. The cross section per unit of the number of charged particles N_{ch} is called the charged particle multiplicity, and an illustration of this distribution in Glauber collisions is shown in Figure 1.6. In the Glauber model, the collision centrality is defined as the percentiles of the charged particle multiplicity distribution. The impact parameter is varied in the Glauber simulations and an average $\langle N_{\text{part}} \rangle$ is obtained

[1] It is worth mentioning that quantities measured in the transverse plane are usually denoted with a $_T$ subscript.

per centrality. A smaller impact parameter correlates with a larger number of participants, which in turn yields a larger number of emitted particles. The Glauber model has been tested in experiments, as will be seen in Section 2.1 with the measurements of the nuclear modification factor.

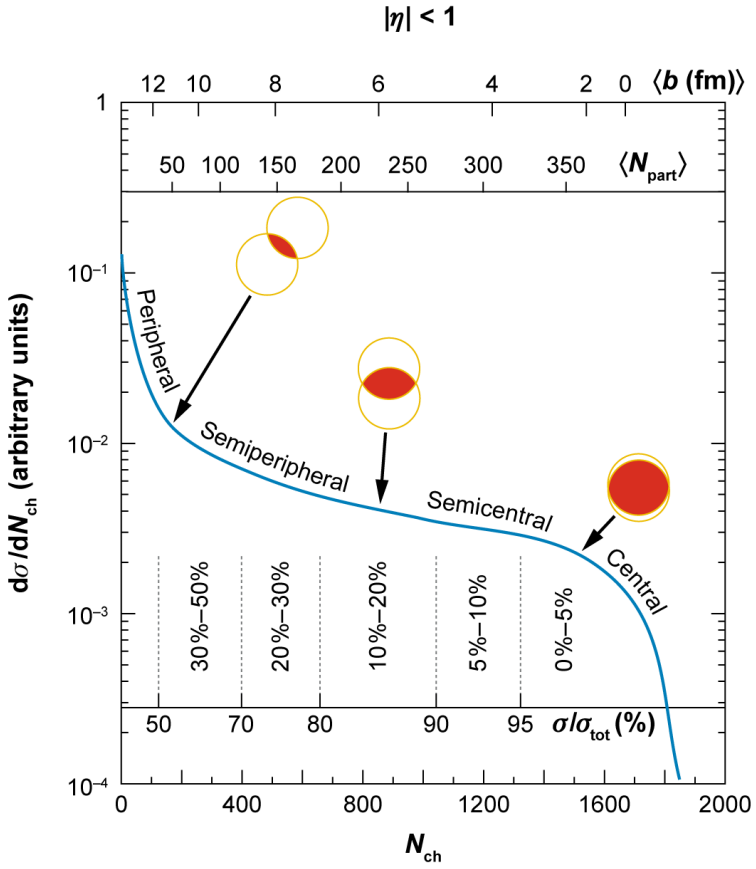

Figure 1.6: Illustration of the charged particle multiplicity distribution in Glauber collisions. Figure taken from [8]

In this sense, the collision centrality corresponds to the amount of overlap between the cross sections of the colliding nuclei. If the colliding nuclei overlap fully, it is called a central collision, and if they overlap little, it is called a peripheral collision. Central collisions are expected to produce more particles and deposit more energy in particle detectors than peripheral collisions.

In experiments, centrality can be defined in terms of other quantities, like the energy measured by the particle detectors, instead of the particle multiplicity. In the ATLAS experiment, centrality is defined as the percentiles of the distribution of collisions as a function of the total energy measured in the forward calorimeters, as shown in Figure 1.7. In this case, 0-10% corresponds to the 10% most energetic, most central collisions, while 40–100% corresponds to the 60% lowest energy, peripheral collisions.

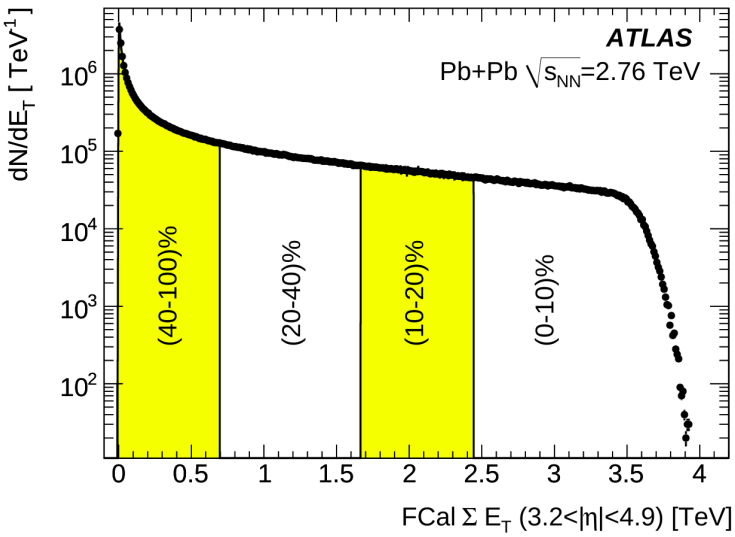

Figure 1.7: Number of collisions as a function of total energy measured in the ATLAS forward calorimeters. The percentiles correspond to the centrality intervals. Figure taken from [9].

1.2.2 Flow in the QGP

Interactions among partons in the QGP create a collective behavior called flow [10]. The main idea is that the initial geometry of the colliding nuclei creates pressure gradients inside the QGP that cause particles to be emitted anisotropically [11].

The azimuthal distribution of emitted particles can be described by a Fourier series with terms of n^{th} order given by $\frac{dN}{d\phi} \propto 1 + \sum_{n=1}^{\infty} 2v_n cos(n\phi_n)$, where N is the number of particles, v_n is the magnitude of the n^{th} order modulation, and ϕ_n is the angle between the particle and the n^{th} event plane [12].

Figure 1.8 shows a diagram illustrating flow with an elliptic geometry [5]. In this diagram, the red and blue spheres represent the colliding nuclei in their initial state, while the yellow-red ellipse represent the volume of the QGP that is formed during the interactions. Then the QGP expands with a pressure gradient given by the elliptic geometry and particles are emitted with a modulation.

Flow has been measured in large systems such as Pb+Pb (lead collisions) and Au+Au (gold collisions). At a low per-nucleon-pair center of mass energy of $\sqrt{s_{\rm NN}} = 130$ GeV, the STAR experiment first measured elliptic flow in Au+Au collisions [13]. Figure 1.9 shows the v_2 coefficient measured by STAR as a function of centrality and charged particle transverse momentum. It is observed that v_2 is larger towards mid-central collisions and for larger charged particle transverse momentum. The non-zero v_2 is expected from the elliptical initial geometry of the Au+Au system.

Flow has been measured at larger energies as well. For example, the ALICE experiment has measured the v_n coefficients up to the fifth order for Pb+Pb collisions at $\sqrt{s_{\rm NN}}$= 2.76 and 5.02 TeV [14, 15]. These can be

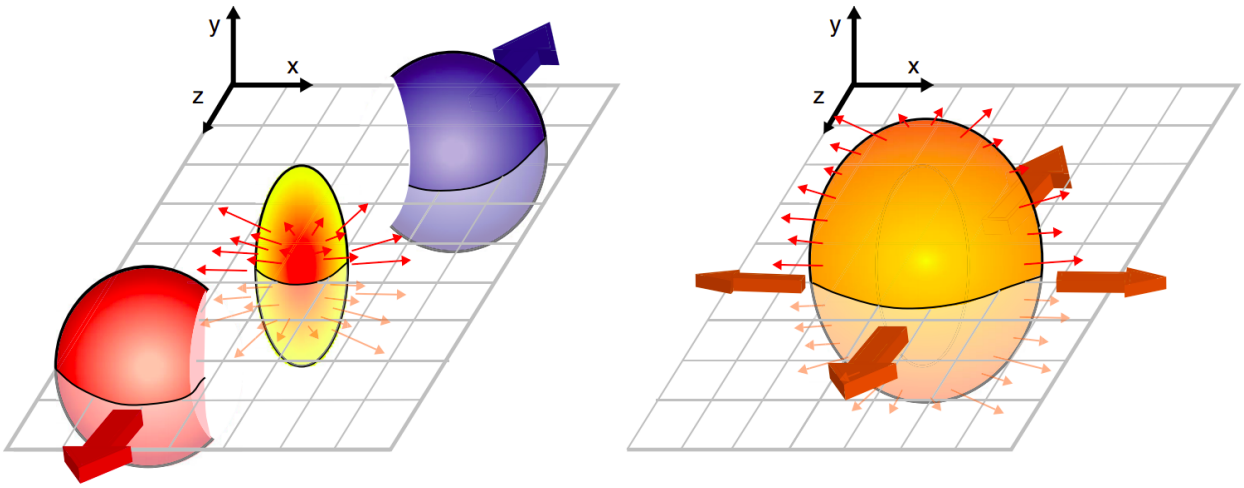

Figure 1.8: Diagram of an elliptic collision geometry that gives rise to flow in the QGP. (left) The red and blue spheres represent the colliding nuclei, while the yellow-red ellipse represent the volume of the QGP created. (right) The QGP expands with a pressure gradient given by the elliptic geometry. Figure taken from [5].

seen as a function of centrality in Figure 1.10 and as a function of charged particle transverse momentum in Figure 1.11. In this case, non-zero v_3, v_4, and v_5 are observed in addition to v_2, and correspond, respectively, to more triangular, quadrilateral, and pentagonal geometries of the colliding nuclei that arise from fluctuations in the initial position of the nucleons.

Flow can also be measured in smaller systems [16]. Figure 1.12 shows the v_2 and v_3 coefficients measured by the PHENIX experiment for three systems: proton-gold (p+Au), deuteron-gold (d+Au), and helium-3-gold (^{3}He+Au). The hydrodynamic evolution of this systems as obtained from the SONIC model [17] is also shown. It is observed that the ^{3}He+Au system has a more triangular geometry and the d+Au system has a more elliptical geometry. This leads to the ^{3}He+Au system having a larger v_3 than the other two systems, while both the d+Au and ^{3}He+Au systems have a larger v_2 than the p+Au system. In general, the v_2 coefficient correlates with an elliptic initial geometry, v_3 correlates with a triangular initial geometry, and so on [16, 18].

Flow in the QGP can be understood in terms of viscous hydrodynamics [7, 19] and flow measurements can be used to constrain the properties of the QGP. Elliptic flow has been used to obtain the specific viscosity of the QGP [20]. The basic procedure for obtaining the QGP specific viscosity is by implementing theory models in simulations and comparing them to data. The theory models estimate the initial properties of the QGP and then tune them to data such as the v_n coefficients. The QGP system evolves from some initial state to a final state following equations of state that include viscous terms. In Ref. [20], fourteen model parameters are used to estimate the specific viscosity η/s as a function of temperature using Bayesian methods. These parameters include: initial energy density of the QGP, initial transverse densities of the

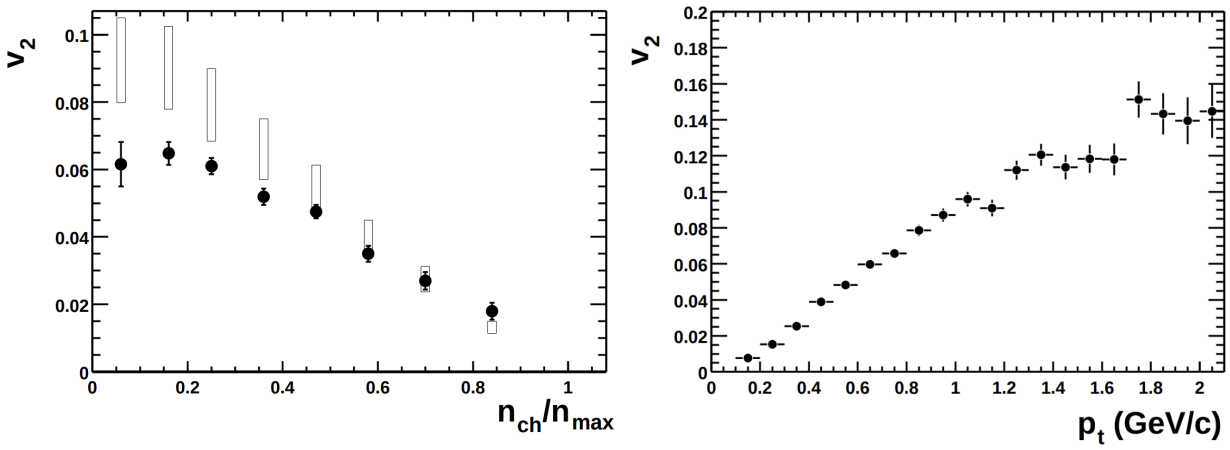

Figure 1.9: v_2 coefficient as a function of centrality (left) and charged particle transverse momentum (right), measured by the STAR experiment in Au+Au collisions at a per-nucleon-pair center of mass energy $\sqrt{s_{\mathrm{NN}}} = 130$ GeV. Figure taken from [13].

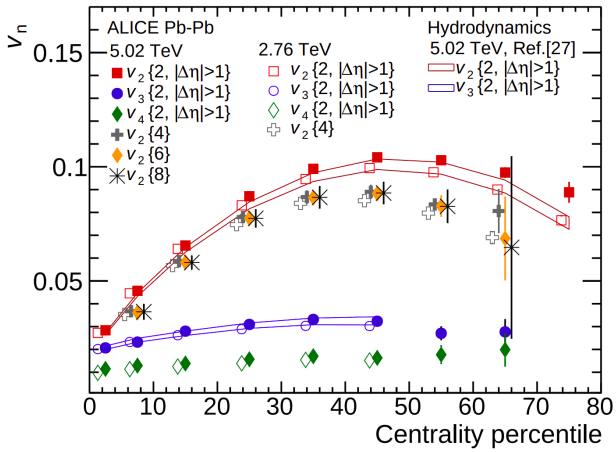

Figure 1.10: v_n coefficients as a function of centrality, measured by the ALICE experiment for Pb+Pb collisions at a per-nucleon-pair center of mass energy $\sqrt{s_{\mathrm{NN}}} = 2.76$ and 5.02 TeV. Figure taken from [15].

colliding nuclei, effective size of the nucleons, dimensionless parameters, among others. The specific viscosity of the QGP has been found to be very small and close to the theoretical limit of $\hbar/4\pi k_B$ [21], which makes the QGP the most perfect fluid known.

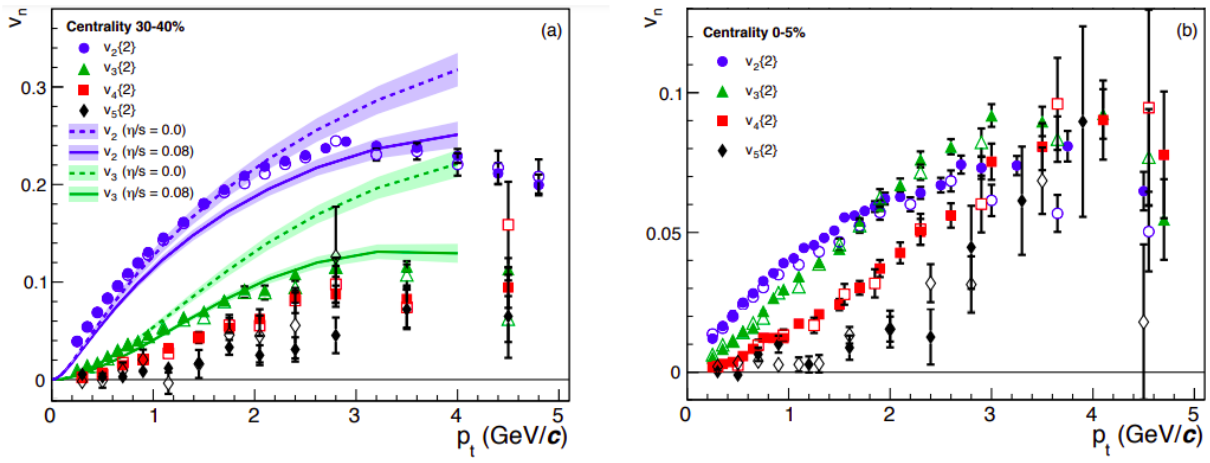

Figure 1.11: v_n coefficients as a function of charged particle transverse momentum for mid-central (left) and central Pb+Pb collisions (right), measured by the ALICE experiment at a per-nucleon-pair center of mass energy $\sqrt{s_{\rm NN}} = 5.02$ TeV. Figure taken from [14].

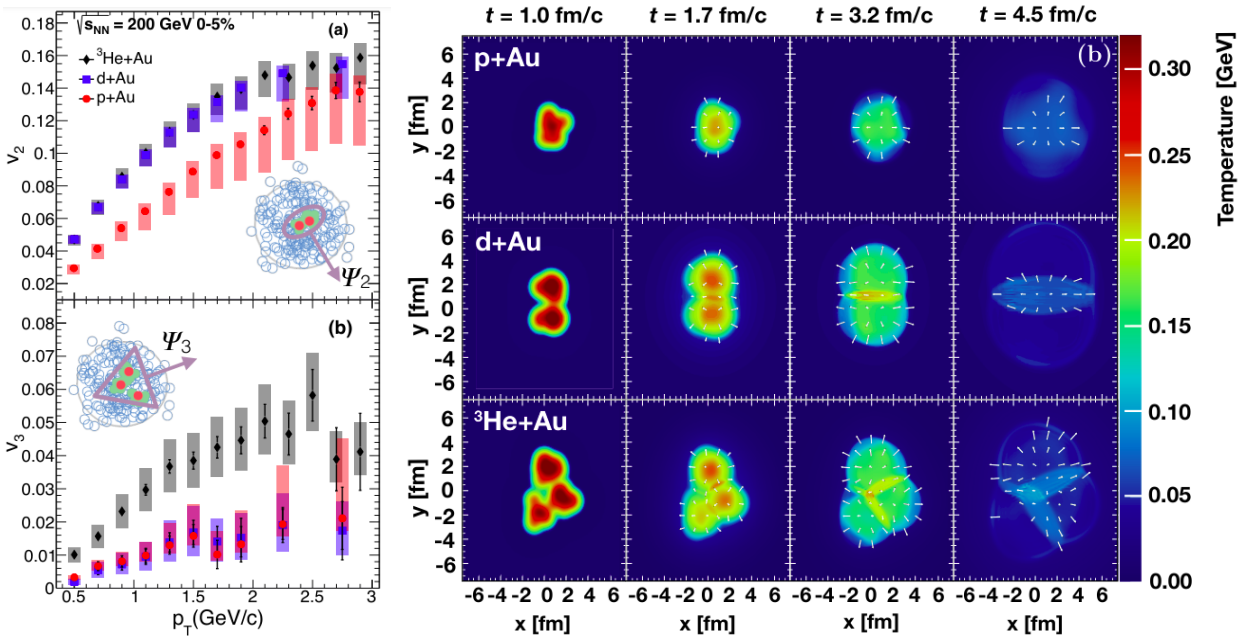

Figure 1.12: (left) v_n coefficients as a function of momentum measured by the PHENIX experiment for three systems: proton-gold (p+Au), deuteron-gold (d+Au), and helium-3-gold (^{3}He+Au). (right) Hydrodynamic evolution of the systems in the transverse $x-y$ plane, showing the system temperature (color scale), obtained from the SONIC model. Systems have a per-nucleon-pair center of mass energy $\sqrt{s_{NN}} = 200$ GeV. Figures taken from [16].

1.3 Jets

Due to color confinement, separating the quarks inside a hadron requires an amount of energy that increases with the distance between the quarks. When the energy between the quarks is large enough, a new quark–antiquark pair is created. This hadronization process is illustrated in Figure 1.13. When partons are hard scattered, they undergo various hadronizations until no more energy is available, resulting in a collimated spray of particles called a jet. By measuring jets, the kinematics of the initial hard scattered partons can be reconstructed. Jets are emitted in pairs, called dijets, that travel in opposite directions with the same momentum magnitude.

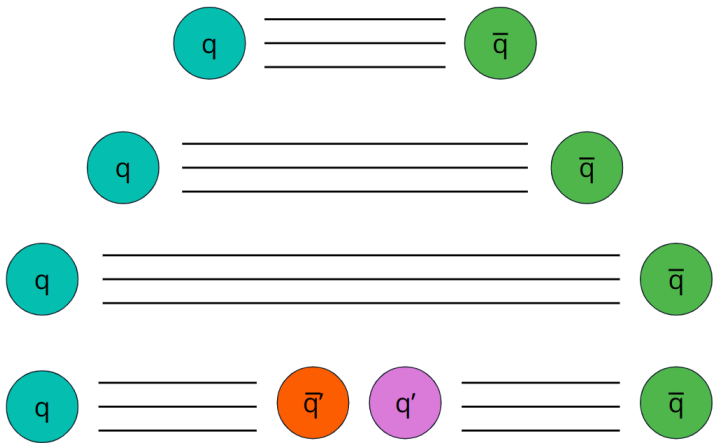

Figure 1.13: Illustration of quarks being separated until a new quark-antiquark pair is created.

Jet experiments consist of a particle accelerator that collides two beams of nuclei, and a particle detector around the beam line, centered at the collision point. The z-axis is typically defined along the beam line and the perpendicular plane is called the transverse plane. Cylindrical coordinates (r, ϕ) are used in the transverse plane, with ϕ being the azimuthal angle around the z-axis. The pseudorapidity is defined as $\eta = -\ln\tan(\theta/2)$ in terms of the polar angle θ, and is preferred over θ because of Lorentz invariant properties.

Jets of energy E and momentum p have energy and momentum in the transverse plane given by $E_{\mathrm{T}} = E\sin\theta$ and $p_{\mathrm{T}} = p\sin\theta$, respectively. Jet measurements focus on these transverse quantities because the total momentum of hard scattered partons in the transverse plane is known to be zero due to the initial momentum being fully along the beam direction. The rapidity is defined as $y = 0.5\ln[(E + p_z)/(E - p_z)]$ where p_z is the z-component of the momentum along the beam direction. At sufficiently high energy, when the jet mass is small compared to the jet momentum, y and η are approximately the same.

1.3.1 Jet definition

The formal definition of jets involves computational algorithms that cluster detector signals within some parameters. The preferred clustering algorithm is the anti-k_t algorithm [22]. This algorithm uses an iterative procedure that takes a list of "objects" and groups them within a jet radius R. The objects can be particles, tracks, calorimeter segments, etc., as long as they have momentum p_{T} and position given by coordinates (ϕ, η). The jet radius R is an input parameter of the algorithm, selected by the user.

The procedure for clustering anti-k_t jets of radius R is the following. First, a list of "objects" is considered. For every pair of objects, distances $d_{ij} = \min(p_{T,i}^{-2}, p_{T,j}^{-2})\frac{\Delta_{ij}^2}{R^2}$ and $d_{iB} = p_{T,i}^{-2}$ are calculated, where $\Delta_{ij}^2 = (\eta_i - \eta_j)^2 + (\phi_i - \phi_j)^2$ is the distance between objects i and j, and (ϕ_i, η_i) and $p_{T,i}$ are the position and momentum of object i, respectively. Then comes an iterative process that compares the distances d_{ij} and d_{iB} to find the smallest distance. If $d_{ij} < d_{iB}$, the pair of objects is combined into a single object, i.e., their four-momenta are added and their positions are averaged by their energy. If $d_{ij} > d_{iB}$, the object is considered a jet and taken out of the list. The process is repeated until all objects are taken out of the list. The anti-k_t algorithm gives preference to clustering objects that are higher in energy and are spatially close.

1.3.2 Jets in vacuum

Jets in proton (pp) collisions are well described by QCD. Jet cross sections are obtained from next to leading order (NLO) calculations in perturbative QCD and corrected for non-perturbative effects. The non-perturbative effects include contributions from the parton distribution functions (PDFs), the formation of hadrons, and the background from the collisions [23–27]. PDFs describe the distribution of quark momenta within nucleons [1].

The cross section for hadron production from jets in pp collisions (the process $pp \to hX$) can be obtained to leading order from perturbative QCD as [28]:

$$d\sigma_{pp\to hX} \approx \sum_{abjd} \int dx_a \int dx_b \int dz_j f_{a/p}(x_a, \mu_f) \otimes f_{b/p}(x_b, \mu_f) \otimes d\sigma_{ab\to jd}(\mu_f, \mu_F, \mu_R) \otimes D_{j\to h}(z_j, \mu_F) \quad (1.3)$$

Here, x_a and x_b are the initial fractions of momentum carried by partons a and b, each one in a colliding proton, with respect to the proton momentum. Similarly, z_j is the fraction of momentum carried by the hadron in the final state, with respect to the total jet momentum. The PDFs of the interacting partons a and b are given by $f_{a/p}(x_a, \mu_f)$ and $f_{b/p}(x_b, \mu_f)$, respectively, where μ_f is the factorization scale. The cross section for the hard scattering of the partons is given by $d\sigma_{ab\to jd}(\mu_f, \mu_F, \mu_R)$, where μ_F is the fragmentation

scale and μ_R is the renormalization scale. The scales are usually given by the scale of the hadron transverse momentum p_{T} or the momentum transfer Q. Finally, $D_{j\to h}(z_j, \mu_F)$ is the fragmentation function (FF) from parton j to hadron h. The hard scattering cross section can be calculated from perturbative QCD, while PDFs and FFs are obtained experimentally.

The CMS experiment has measured the jet cross sections in pp collisions with a center of mass energy of $\sqrt{s} = 2.76$, 7, 8, and 13 TeV, and has found that they agree with theory predictions within uncertainties [26, 27]. Similarly, ATLAS has measured the jet cross sections for $\sqrt{s} = 7$, 8, and 13 TeV, which agree with theory as well [23–25]. Figure 1.14 shows the jet cross sections measured by CMS and ATLAS.

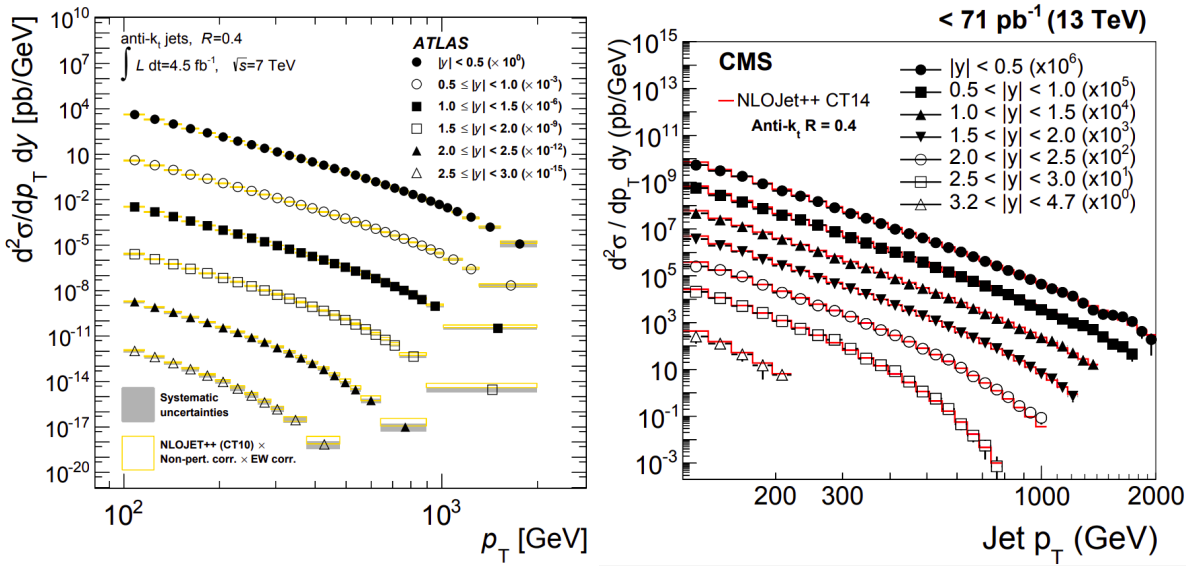

Figure 1.14: Distributions of $R = 0.4$ jets per unit of transverse momentum p_T and rapidity y as a function of p_T. (left) Jet distribution measured by ATLAS in proton collisions at a center of mass energy $\sqrt{s} = 7$ TeV. The data (black points) is compared to theory (yellow points) [23]. (right) Jet distribution measured by CMS in pp collisions at a center of mass energy $\sqrt{s} = 13$ TeV. The data (black points) is compared to theory (red points) [26].

1.3.3 Jets in medium

In heavy ion collisions (such as Pb+Pb), jets come from hard scattered partons that traversed the QGP. Jets can lose energy due to strong interactions with the medium, a phenomenon that is known as jet quenching.

The cross section for hadron production is thus modified with respect to pp collisions. First, the PDFs of nuclei are different than for single protons, which modifies the initial state. Second, partons traversing the QGP experience energy loss in the form of collisions and radiation, as seen in the diagrams in Figure 1.15. In

this case, the hadron production cross section for colliding nuclei A and B is given by [28]:

$$d\sigma_{AB\to hX} \approx \sum_{abjj'd} \int dx_a \int dx_b \int dz_j f'_{a/A}(x_a,\mu_f) \otimes f'_{b/B}(x_b,\mu_f) \otimes d\sigma_{ab\to jd}(\mu_f,\mu_F,\mu_R) \\ \otimes P_{j\to j'} \otimes D_{j'\to h}(z'_j,\mu_F) \tag{1.4}$$

where the PDFs are now for nuclei and an additional interaction term $P_{j\to j'}$ is included to account for the parton energy loss.

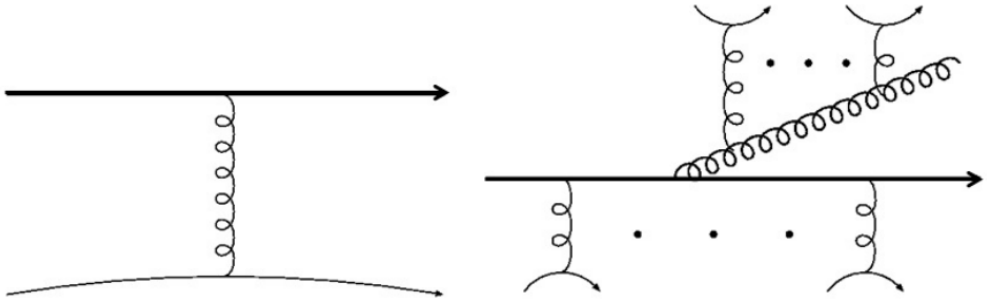

Figure 1.15: Diagrams for parton energy loss in the form of collisions (left) and radiation (right). Figure taken from [28].

Jet energy loss can be studied in a variety of ways, such as the measurements of the nuclear modification factor, the jet v_n, the fragmentation functions, and the dijet momentum balance, which are described in detail in Chapter 2. Jet quenching and hydrodynamic flow are the most important signatures of the QGP and confirm its existence.

This thesis focuses on studying jet energy loss by measuring dijets created in heavy ion collisions. Each jet in a dijet from a heavy ion collision follows a different path within the QGP, and interactions with the medium can cause each jet to lose a different amount of energy [29]. Figure 1.16 shows an illustration of dijets in vacuum (proton collisions) and in medium (heavy ion collisions). The most energetic jet in the dijet is called the leading jet, and the second most energetic, the subleading jet. Jet energy loss can be studied by comparing the momenta of the leading and subleading jets in vacuum and in medium [9, 30–32].

1.4 Overview of this thesis

In order to understand the properties of the QGP at short distances, high transverse momentum (p_{T}) probes such as jets are used [33]. Jets traversing the QGP experience jet quenching, characterized by a reduction in the overall jet energy compared to expectations from collisions in vacuum. This phenomenon is understood to arise from radiative and collisional energy loss reducing the jet p_{T} by moving energy associated with the

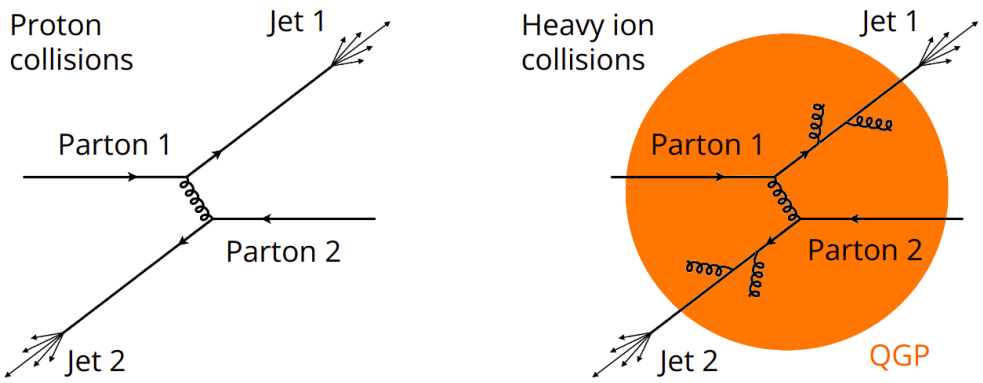

Figure 1.16: Illustration of dijets in a proton collision (left) and a heavy ion collision (right).

initial parton to wider angles, with some of it ending up outside the jet cone [34].

Jet quenching is typically quantified by the overall rate of jets in a given centrality interval in Pb+Pb collisions and at a given p_{T} compared to expectations from pp collisions, commonly known as the nuclear modification factor:

$$R_{\mathrm{AA}} = \frac{1}{N_{\mathrm{evt}}^{\mathrm{AA}}} \frac{\mathrm{d}N_{\mathrm{jet}}^{\mathrm{AA}}}{\mathrm{d}p_{\mathrm{T}}} \Bigg/ \left(\langle T_{\mathrm{AA}} \rangle \frac{\mathrm{d}\sigma_{\mathrm{jet}}^{pp}}{\mathrm{d}p_{\mathrm{T}}} \right), \tag{1.5}$$

where $N_{\mathrm{evt}}^{\mathrm{AA}}$ is the total number of minimum-bias Pb+Pb events and $\langle T_{\mathrm{AA}} \rangle$ is the mean nuclear thickness function [35] for the centrality interval. This normalization accounts for the geometric enhancement in hard scattering rates in Pb+Pb collisions with respect to pp collisions. The jet yield in Pb+Pb collisions is $N_{\mathrm{jet}}^{\mathrm{AA}}$, and the jet cross section in pp collisions is $\sigma_{\mathrm{jet}}^{pp}$, both measured as a function of the jet transverse momentum p_{T}. The nuclear modification factor is described in detail in Section 2.1.

Measurements of the azimuthal anisotropy of jets [36] have shown that the geometry of the overlapping nuclei affects the relative rates of jets measured in Pb+Pb collisions. Jet anisotropies are discussed in detail in Section 2.2. Additionally, jets are also expected to experience jet-by-jet fluctuations in the energy-loss process [37].

Jets are largely produced in pairs in $2 \rightarrow 2$ partonic scattering processes. The QCD evolution of the partons after the scattering gives rise to dijets. The two jets are expected to experience asymmetric energy loss due to traversing unequal path lengths in the QGP [29], driven by the geometry of the overlapping nuclei and the relative orientation of the jet trajectories through the QGP. In heavy-ion collisions, dijets provide a complementary probe to single jets for studying jet quenching. In general, the measurement of the p_{T} balance of dijets provides a way to constrain the relative importance of fluctuations and geometry in jet quenching.

In order to compare the transverse momenta of the two jets comprising a dijet, the dijet momentum

balance is measured:

$$x_{\mathrm{J}} = p_{\mathrm{T},2}/p_{\mathrm{T},1} \tag{1.6}$$

The dijet is constructed using the two highest p_{T} jets in a collision, with $p_{\mathrm{T},1}$ being the transverse momentum of the highest-p_{T} jet, the leading jet, and $p_{\mathrm{T},2}$ being the transverse momentum of the second-highest-p_{T} jet, the subleading jet.

In pp collisions, the showering process in vacuum, as well as higher-order scattering processes, can lead to imbalanced dijet transverse momenta. However, the most probable situation is that the jets are nearly balanced in p_{T} [38, 39]. Previous dijet measurements in Pb+Pb collisions have shown that jets are more likely to be more imbalanced in Pb+Pb collisions than in pp collisions [38–41]. Reference [39] addressed the absolute rate at which $R = 0.4$ dijets are produced in Pb+Pb collisions, assessing whether leading dijets are suppressed at levels similar to those for inclusive jets [42]. This dijet momentum balance measurement is discussed in detail in Section 2.4.

This thesis corresponds to the work in Reference [43] and extends the dijet momentum balance studies of Reference [39] by varying the jet radius parameter of dijets in Pb+Pb and pp collisions at a per-nucleon-pair center of mass energy $\sqrt{s_{\mathrm{NN}}} = 5.02$ TeV. Measurements of the jet radius dependence of the dijet balance are particularly interesting because they are sensitive to the location of the lost energy from jet quenching than is available with single jet measurements.

These measurements use 1.72 nb^{-1} of Pb+Pb collisions, collected in 2018, and 255 pb^{-1} of pp data, collected in 2017, with the ATLAS detector [44] at the LHC. Jets are reconstructed using the anti-k_t algorithm [22] with radius parameters $R = 0.2, 0.3, 0.4, 0.5$ and 0.6. The analysis is conducted independently for each of the jet radius values. In each case, leading dijets are constructed from the two highest-p_{T} jets in the event and are required to have the two jets nearly back-to-back in azimuth with $\Delta\phi = |\phi_1 - \phi_2| \geq 7\pi/8$ and $|y| < 2.1$. The measurement is performed for p_{T} values from 100 to 562 GeV for $R = 0.2, 0.3$ and 0.4 and from 158 to 562 GeV for $R = 0.5$ and 0.6. Subleading jets are reported for $x_{\mathrm{J}} > 0.32$ for each leading jet p_{T} selection. Collisions in which the two highest-p_{T} jets do not meet the selection criteria are discarded.

The primary observable for this measurement is the two-dimensional yield of dijets:

$$\frac{\mathrm{d}^2 N_{\mathrm{pair}}}{\mathrm{d}p_{\mathrm{T},1}\mathrm{d}p_{\mathrm{T},2}} \tag{1.7}$$

where N_{pair} is the number of dijets passing the selection criteria. Projections of these two-dimensional distributions can be used to construct x_{J} distributions as a function of $p_{\mathrm{T},1}$ and $p_{\mathrm{T},2}$.

This thesis presents results of the absolutely normalized x_{J} distributions in Pb+Pb collisions:

$$\frac{1}{\langle T_{\mathrm{AA}}\rangle N_{\mathrm{evt}}^{\mathrm{AA}}}\frac{\mathrm{d}N_{\mathrm{pair}}^{\mathrm{AA}}}{\mathrm{d}x_{\mathrm{J}}} \tag{1.8}$$

and the equivalent in pp collisions with integrated luminosity L_{pp}:

$$\frac{1}{L_{pp}}\frac{\mathrm{d}N_{\mathrm{pair}}^{pp}}{\mathrm{d}x_{\mathrm{J}}} \tag{1.9}$$

Similarly, the dijet-yield-normalized x_{J} distributions are defined as:

$$\frac{1}{N_{\mathrm{pair}}}\frac{\mathrm{d}N_{\mathrm{pair}}}{\mathrm{d}x_{\mathrm{J}}} \tag{1.10}$$

which have a normalization that was used in previous dijet measurements [38–41].

The absolutely normalized x_{J} distributions allow a direct comparison between the dijet rates measured in Pb+Pb and pp collisions. This comparison is quantified by the ratio:

$$J_{\mathrm{AA}} = \frac{1}{\langle T_{\mathrm{AA}}\rangle N_{\mathrm{evt}}^{\mathrm{AA}}}\frac{\mathrm{d}N_{\mathrm{pair}}^{\mathrm{AA}}}{\mathrm{d}x_{\mathrm{J}}} \Bigg/ \left(\frac{1}{L_{pp}}\frac{\mathrm{d}N_{\mathrm{pair}}^{pp}}{\mathrm{d}x_{\mathrm{J}}}\right). \tag{1.11}$$

Finally, the absolutely normalized x_{J} distributions can be integrated over the measurement range of $0.32 < x_{\mathrm{J}} < 1.0$ (and the corresponding ranges in $p_{\mathrm{T},1}$ and $p_{\mathrm{T},2}$) to construct the absolutely normalized dijet yields in Pb+Pb collisions:

$$\frac{1}{\langle T_{\mathrm{AA}}\rangle N_{\mathrm{evt}}^{\mathrm{AA}}}\int_{0.32\times p_{\mathrm{T},1}}^{p_{\mathrm{T},1}}\frac{\mathrm{d}^2N_{\mathrm{pair}}^{\mathrm{AA}}}{\mathrm{d}p_{\mathrm{T},1}\mathrm{d}p_{\mathrm{T},2}}\mathrm{d}p_{\mathrm{T},2} \tag{1.12}$$

and the dijet cross sections in pp collisions:

$$\frac{1}{L_{pp}}\int_{0.32\times p_{\mathrm{T},1}}^{p_{\mathrm{T},1}}\frac{\mathrm{d}^2N_{\mathrm{pair}}^{pp}}{\mathrm{d}p_{\mathrm{T},1}\mathrm{d}p_{\mathrm{T},2}}\mathrm{d}p_{\mathrm{T},2}. \tag{1.13}$$

Analogously to the nuclear modification factor, the pair nuclear modification factors for dijets as a function of the leading and subleading jet p_{T} respectively, can be defined as:

$$R_{\mathrm{AA}}^{\mathrm{pair}}(p_{\mathrm{T},1}) = \frac{\frac{1}{\langle T_{\mathrm{AA}}\rangle N_{\mathrm{evt}}^{\mathrm{AA}}}\int_{0.32\times p_{\mathrm{T},1}}^{p_{\mathrm{T},1}}\frac{\mathrm{d}^2N_{\mathrm{pair}}^{\mathrm{AA}}}{\mathrm{d}p_{\mathrm{T},1}\mathrm{d}p_{\mathrm{T},2}}\mathrm{d}p_{\mathrm{T},2}}{\frac{1}{L_{pp}}\int_{0.32\times p_{\mathrm{T},1}}^{p_{\mathrm{T},1}}\frac{\mathrm{d}^2N_{\mathrm{pair}}^{pp}}{\mathrm{d}p_{\mathrm{T},1}\mathrm{d}p_{\mathrm{T},2}}\mathrm{d}p_{\mathrm{T},2}} \tag{1.14}$$

and

$$R_{\mathrm{AA}}^{\mathrm{pair}}(p_{\mathrm{T},2}) = \frac{\frac{1}{\langle T_{\mathrm{AA}}\rangle N_{\mathrm{evt}}^{\mathrm{AA}}} \int_{p_{\mathrm{T},2}}^{p_{\mathrm{T},2}/0.32} \frac{\mathrm{d}^2 N_{\mathrm{pair}}^{\mathrm{AA}}}{\mathrm{d}p_{\mathrm{T},1}\mathrm{d}p_{\mathrm{T},2}} \mathrm{d}p_{\mathrm{T},1}}{\frac{1}{L_{pp}} \int_{p_{\mathrm{T},2}}^{p_{\mathrm{T},2}/0.32} \frac{\mathrm{d}^2 N_{\mathrm{pair}}^{pp}}{\mathrm{d}p_{\mathrm{T},1}\mathrm{d}p_{\mathrm{T},2}} \mathrm{d}p_{\mathrm{T},1}}. \tag{1.15}$$

By integrating over $p_{\mathrm{T},2}$ ($p_{\mathrm{T},1}$), one can access information from $R_{\mathrm{AA}}^{\mathrm{pair}}(p_{\mathrm{T},1})$ ($R_{\mathrm{AA}}^{\mathrm{pair}}(p_{\mathrm{T},2})$) about the differential rate of dijet production in leading (subleading) jet p_{T} bins. Comparison of these two quantities at a fixed jet p_{T} provides information about the suppression of leading and subleading jets.

This thesis provides a measurement of dijets in Pb+Pb and pp collisions focusing on the x_{J}, J_{AA}, and $R_{\mathrm{AA}}^{\mathrm{pair}}$ distributions for various jet radii. Together, they provide a comprehensive study of jet energy loss of dijets in a QGP.

Chapter 2

Measurements of jet quenching

2.1 Nuclear modification factor

The nuclear modification factor [45–47] is an observable that quantifies jet quenching by comparing the number of jets in collisions where there is a QGP (for example, Pb+Pb collisions) with collisions in vacuum (pp collisions). The nuclear modification factor R_{AA} is defined as the ratio of the jet yield in Pb+Pb collisions to the jet cross section in pp collisions:

$$R_{\mathrm{AA}} = \frac{\frac{1}{N_{\mathrm{evt}}} \frac{d^2 N_{\mathrm{jet}}}{dp_T dy}\Big|_{\mathrm{cent}}}{\langle T_{\mathrm{AA}} \rangle \frac{d^2 \sigma_{\mathrm{jet}}}{dp_T dy}\Big|_{\mathrm{pp}}} \tag{2.1}$$

Here, the jet yields are obtained as a function of jet transverse momentum p_{T} and rapidity y. The Pb+Pb jet yield is obtained for different collision centralities and is normalized by the number of events N_{evt} and the mean nuclear thickness function $\langle T_{\mathrm{AA}} \rangle$, which is the average number of nucleon-nucleon collisions divided by the total inelastic nucleon-nucleon cross section, as obtained for a given centrality from Monte Carlo simulations of the Glauber model [8]. Heavy ion collisions are expected to have a larger number of per-collision hard scatterings compared to proton collisions (because Pb has ~ 200 times more nucleons than p), so $\langle T_{\mathrm{AA}} \rangle$ is introduced as a normalization factor to compensate for this effect, as well as to account for the units in the jet cross section.

Figure 2.1 shows the nuclear modification factor as a function of jet transverse momentum for various collision centralities [45], measured by the ATLAS experiment. These R_{AA} measurements show that jet quenching increases with collision centrality, with approximately half of the jets being suppressed in the most central collisions. Additionally, jet quenching decreases (increasing R_{AA}) with the jet transverse momentum. The CMS and ALICE experiments have also measured the R_{AA}, and their results are in agreement with ATLAS, as can be seen on Figure 2.2 [47].

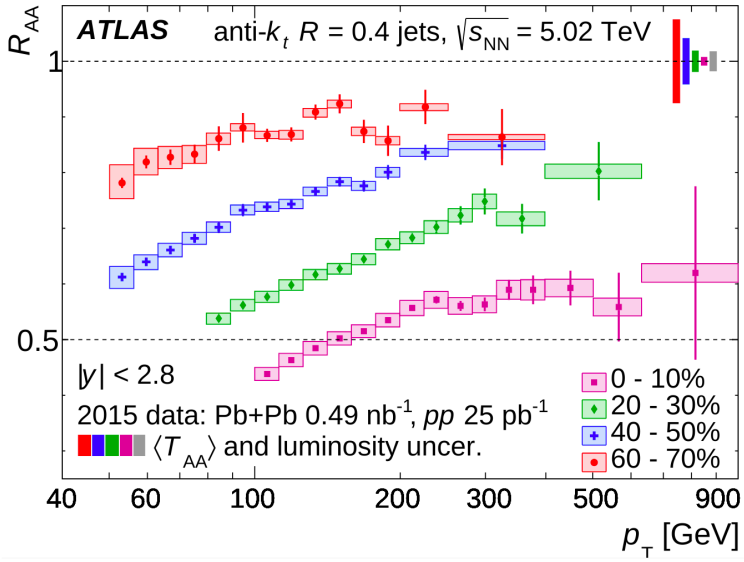

Figure 2.1: The nuclear modification factor R_{AA} as a function of jet transverse momentum p_T, for various collision centralities and for per-nucleon-pair center of mass energy $\sqrt{s_{NN}} = 5.02$ TeV, measured by ATLAS. Figure taken from [45].

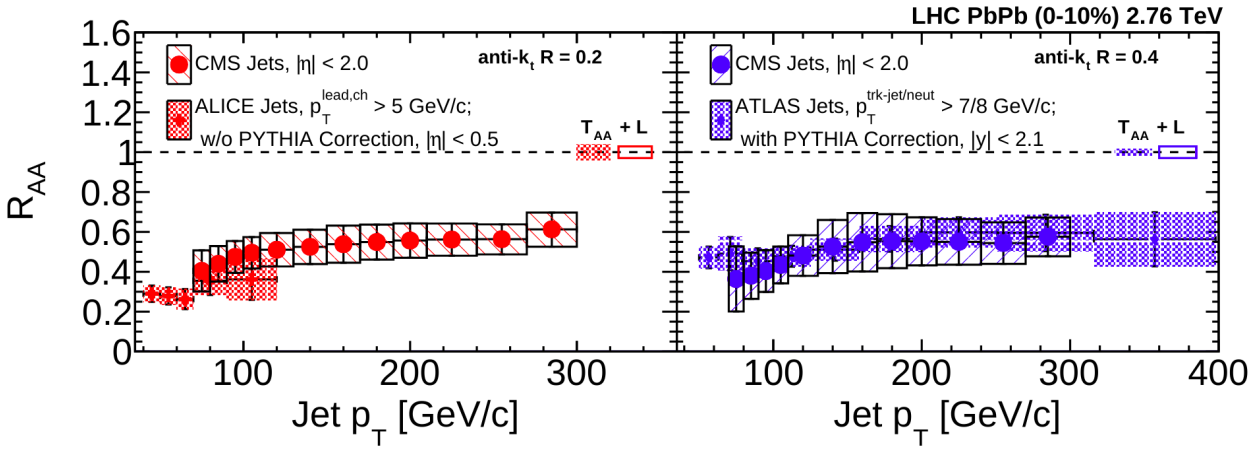

Figure 2.2: Comparison of the nuclear modification factor R_{AA} measured by the CMS, ALICE, and ATLAS experiments. The R_{AA} is shown as a function of jet transverse momentum p_T for central collisions and for per-nucleon-pair center of mass energy $\sqrt{s_{NN}} = 2.76$ TeV. Figure taken from [47].

The nuclear modification factor can be measured for various types of probes in order to study various types of interactions. For example, jets initiated by different partons are expected to interact differently with the QGP due to the difference in their masses and flavors. That is the case of the b-jet R_{AA} [48, 49], where the R_{AA} of jets initiated by a b quark is measured. Figure 2.3 shows the b-jet R_{AA} as a function of N_{part} (and centrality) in Pb+Pb and pp collisions, and the ratio of the b-jet R_{AA} to the inclusive jet R_{AA} in 0–20% central Pb+Pb and pp collisions. The b-jet R_{AA} is observed to be larger than the inclusive R_{AA} where no parton selections are made.

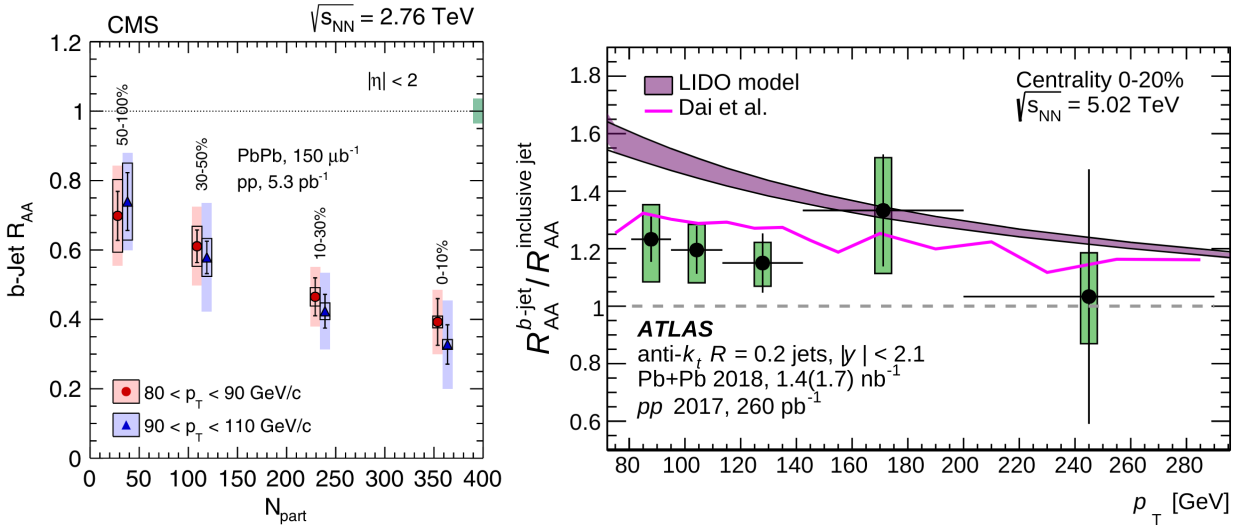

Figure 2.3: (left) b-jet R_{AA} as a function of N_{part} (and centrality) in Pb+Pb and pp collisions with per-nucleon-pair center of mass energy $\sqrt{s_{NN}} = 2.76$ TeV. (right) Ratio of the b-jet R_{AA} to the inclusive jet R_{AA} in 0–20% central Pb+Pb and pp collisions with per-nucleon-pair center of mass energy $\sqrt{s_{NN}} = 5.02$ TeV. Figure taken from [48, 49].

Another example is the $R_{\mathrm{AA}}^{\mathrm{pair}}$ of dijets [39]. Figure 2.4 shows the R_{AA} of leading and subleading jets as a function of jet transverse momentum for 0–10% central Pb+Pb and pp. This figure shows that subleading jets are more suppressed than leading jets in Pb+Pb collisions compared to pp collisions.

Even uncolored probes can be used to measured the R_{AA}, as is the case of photons [50] and Z bosons [51]. Since photons and Z bosons do not carry color charge, they are not expected to interact with the QGP. Thus, their yields in Pb+Pb collisions are expected to be the same in pp collisions, giving $R_{\mathrm{AA}} \approx 1$. This is seen in Figure 2.5, which shows the R_{AA} of photons as a function of photon transverse energy and the R_{AA} of Z bosons as a function of $\langle N_{\mathrm{part}} \rangle$ (which correlates with centrality). In both cases, these uncolored probes allow for a test of the Glauber model [8] and the quantities obtained from it, such as $\langle T_{\mathrm{AA}} \rangle$ or $\langle N_{\mathrm{part}} \rangle$.

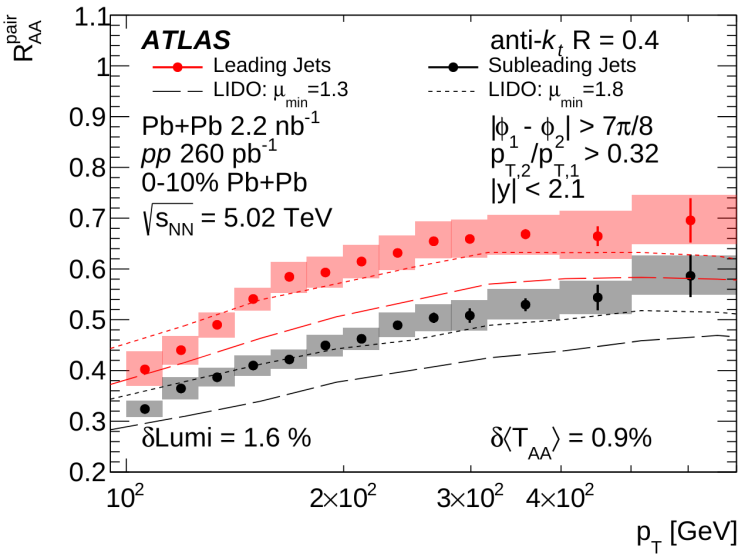

Figure 2.4: R_{AA} of leading and subleading jets as a function of jet transverse momentum p_T, for 0–10% central Pb+Pb and pp collisions at per-nucleon-pair center of mass energy $\sqrt{s_{NN}} = 5.02$ TeV. Figure taken from [39].

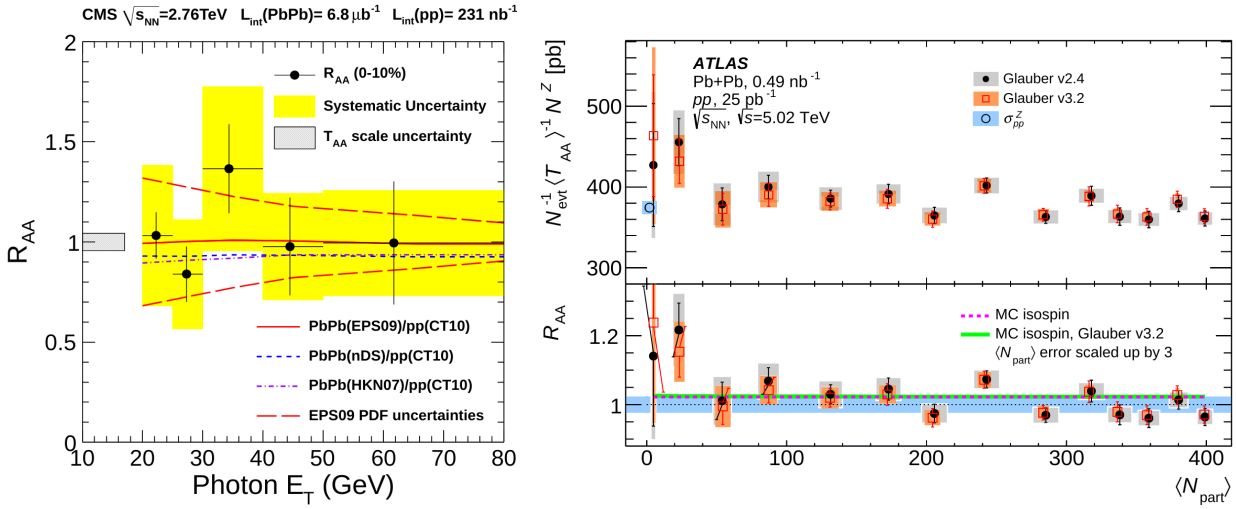

Figure 2.5: (left) Photon R_{AA} as a function of photon transverse energy E_{T}, for 0–10% central Pb+Pb and pp collisions at per-nucleon-pair center of mass energy $\sqrt{s_{NN}} = 2.76$ TeV. (right) Z boson R_{AA} as a function of $\langle N_{\mathrm{part}} \rangle$, for Pb+Pb and pp collisions with per-nucleon-pair center of mass energy $\sqrt{s_{NN}} = 5.02$ TeV. Figure taken from [50, 51].

2.2 Jet v_n

In a heavy ion collision with an initial elliptic geometry, jets are emitted with an azimuthal anisotropy [52]. Jets that follow a path close to the major semi-axis of the ellipse are expected to be more suppressed than those that travel through the minor semi-axis. This difference in jet suppression is due to the path length dependence of in medium parton energy loss, which causes jets to lose more energy and be more quenched when travelling a longer distance within the QGP. This causes an azimuthal modulation of jets that can be described by a Fourier series $\frac{dN_{jet}}{d\Delta\phi_n} \propto 1 + 2v_n cos(n\Delta\phi_n)$, where N_{jet} is the number of jets, v_n is the magnitude of the n^{th} order modulation, and $\Delta\phi_n$ is the angle between the jet and the n^{th} event plane [12].

The angular distribution of jets with respect to the second, third, and fourth order event planes can be seen in Figure 2.6 for jets in 10–20% central Pb+Pb collisions. It can be seen that the modulation has the biggest contribution from the elliptic (second order) term, followed by the triangular (third order) and quadrilateral (fourth order) terms. Similarly, Figure 2.7 shows the jet v_2, v_3, and v_4 coefficients as a function of centrality. The measurements show a non-zero v_2 and v_3 coefficients, while v_4 is consistent with zero within uncertainties.

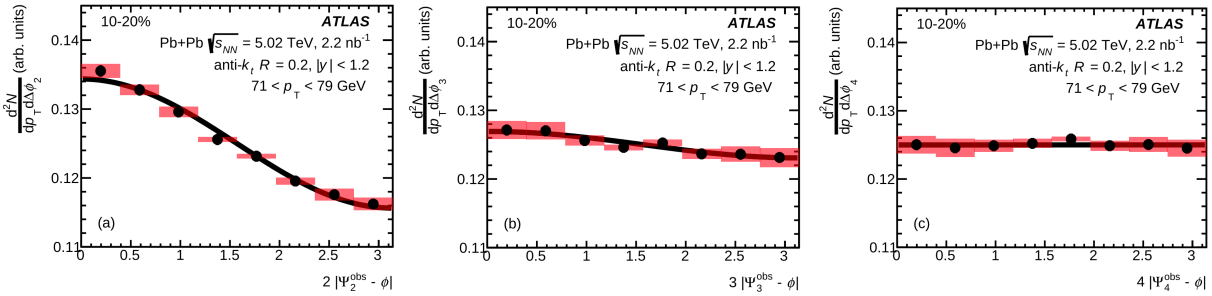

Figure 2.6: Angular distribution of jets with respect to the second (left), third (middle), and fourth (right) order event planes for jets with $71 < p_T < 79$ GeV in 10-–20% central Pb+Pb collisions. Figure taken from [52].

Pb+Pb collisions have an initial collision geometry given by the amount of overlap between the cross sections of the colliding nuclei, which depends on the centrality. For mid-central collisions, this overlap region has an approximately elliptic shape, so a non-zero v_2 is expected to arise from this initial state geometry, while any non-zero v_3 and v_4 have to come from fluctuations of the position of the nucleons in the initial state.

Given that jet energy loss can be explained in terms of a path length dependence, the v_2 in mid-central collisions is expected to show a stronger p_T dependence than for peripheral or central collisions. In peripheral collisions there is little energy loss because less QGP is created. In central collisions the initial geometry is circular, which does not introduce a strong path length dependence, so jet energy loss is also expected

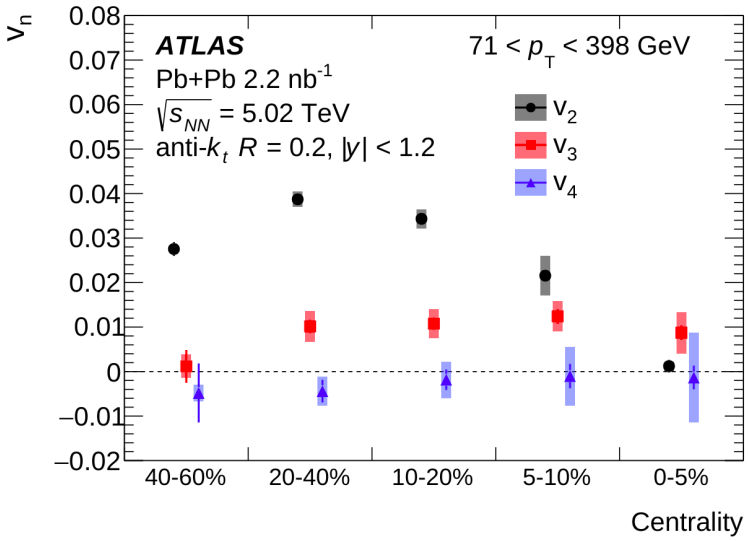

Figure 2.7: Jet v_2, v_3, and v_4 coefficients as a function of centrality. Figure taken from [52].

to be small in this case. This can be seen in Figure 2.8, which shows the jet v_2 coefficient as a function of centrality for different momentum ranges.

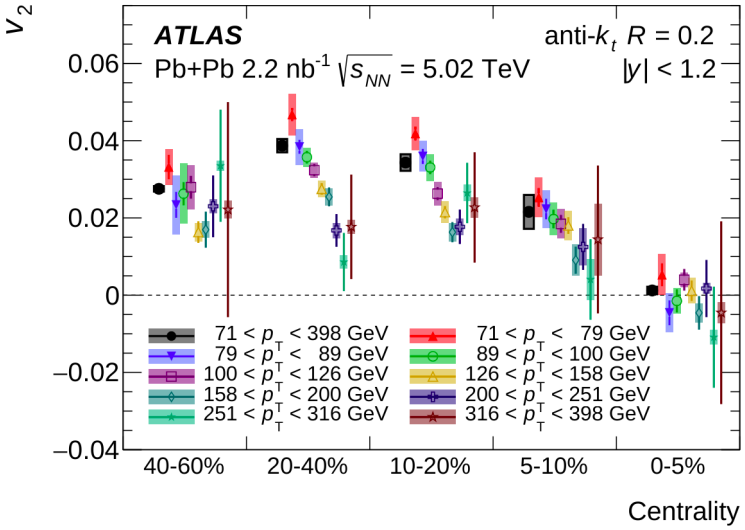

Figure 2.8: Jet v_2 coefficient as a function of centrality for different momentum ranges. Figure taken from [52].

2.3 Fragmentation functions

Interactions with the QGP can modify not only jets as a whole, as evidenced by the R_{AA} and jet v_n measurements, but also the jet substructure. These modifications of the jet substructure can be quantified

through measurements of fragmentation functions [53]. Consider the fragmentation functions:

$$D(p_T) = \frac{1}{N_{\text{jet}}} \frac{dn_{\text{ch}}}{dp_T} \tag{2.2}$$

$$D(z) = \frac{1}{N_{\text{jet}}} \frac{dn_{\text{ch}}}{dz} \tag{2.3}$$

where n_{ch} is the number of charged particles inside a jet, N_{jet} is the number of jets, p_T is the transverse momentum of a charged particle, and $z = \frac{p_T}{p_T^{\text{jet}}} cos\Delta R$, with p_T^{jet} being the jet transverse momentum, and $\Delta R = \sqrt{\Delta\eta^2 + \Delta\phi^2}$ being the distance between each charged particle and the jet axis. Note that z is the fraction of the jet transverse momentum carried by a charged particle inside a jet, projected to the jet axis.

Additionally, differences between Pb+Pb and pp collisions can be quantified by the ratios:

$$R_{D(z)} = \frac{D(z)|_{\text{PbPb}}}{D(z)|_{\text{pp}}} \tag{2.4}$$

$$R_{D(p_T)} = \frac{D(p_T)|_{\text{PbPb}}}{D(p_T)|_{\text{pp}}} \tag{2.5}$$

These fragmentation functions have been measured by ATLAS [53]. Figure 2.9 shows the $D(p_T)$ and $D(z)$ fragmentation functions as a function of p_T and z, respectively, for Pb+Pb collisions of various centralities and pp collisions. In terms of $D(p_T)$, it is observed for both Pb+Pb and pp collisions that the number of charged particles inside a jet decreases as a function of the charged particle momentum. Similarly, $D(z)$ also shows that the number of charged particles inside a jet decrease as a function of the fraction of jet momentum they contribute in the direction of the jet. In other words, there are more low momentum particles inside a jet than there are high momentum particles.

To quantify the differences between the fragmentation functions in Pb+Pb and pp collisions, the $R_{D(p_T)}$ and $R_{D(z)}$ ratios are shown in Figure 2.10. This figure shows that the momentum carried by the particles inside a jet gets redistributed when the jet traverses the QGP. There is an enhancement of particles at low z and p_T, a depletion at mid p_T and z, and an enhancement at high z and p_T. The enhancement at low z and p_T and the depletion at mid p_T and z can be interpreted as the medium causing the particles inside the jet to fragment into more particles of lower momenta. Additionally, Pb+Pb collisions produce more jets initiated by quarks than by gluons compared to pp collisions, and quark jets tend to lose less energy than gluon jets, which explains the enhancement at high p_T and z [54].

An additional fragmentation function can be defined that takes into account not only the particles within

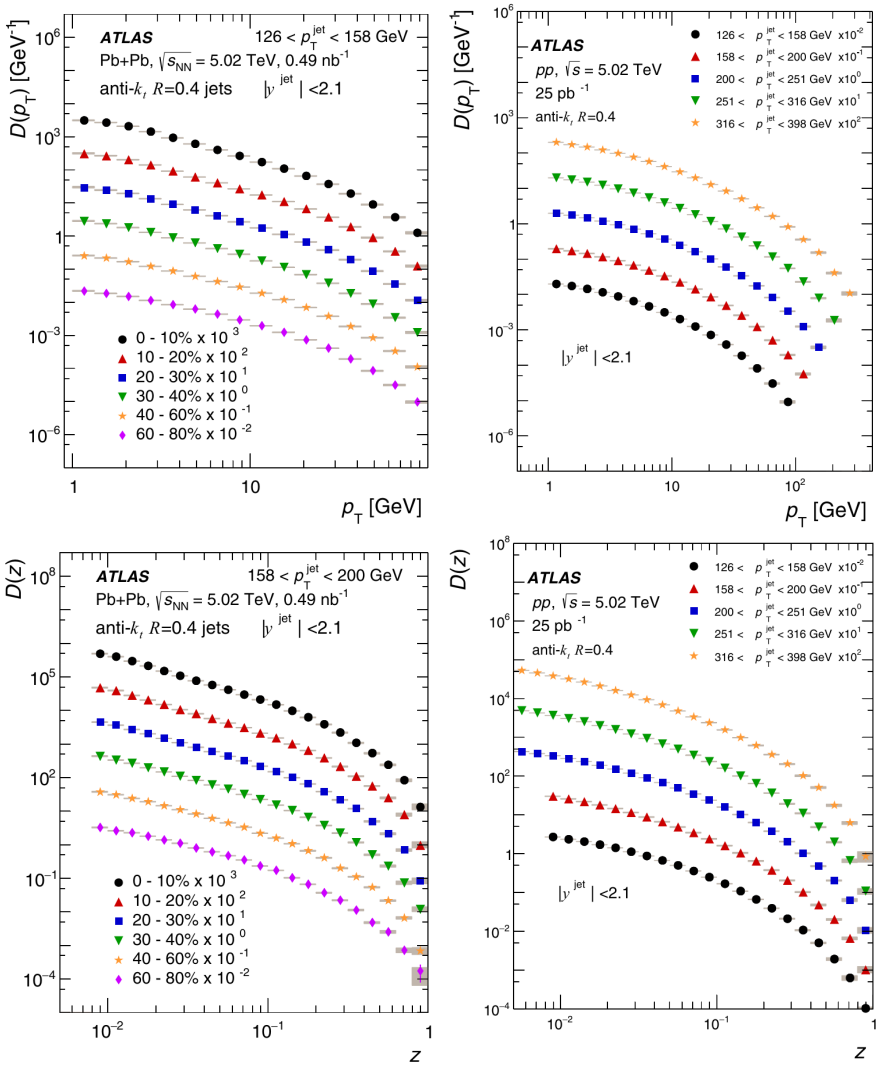

Figure 2.9: The $D(p_T)$ fragmentation function (top) as a function of charged particle momentum p_T and the $D(z)$ fragmentation function (bottom) as a function of z. Distributions are shown for Pb+Pb collisions of various centralities (left) and pp collisions (right). Figure taken from [53].

a jet but also the particles around it. The $D(p_T, r)$ fragmentation functions extends $D(p_T)$ from 1D to 2D by considering the distribution of charged particles in an area $2\pi r dr$ at distance r of the jet axis, as seen in Figure 2.11. The $D(p_T, r)$ fragmentation function and its corresponding ratio $R_{D(p_T,r)}$ of Pb+Pb to pp are defined as:

$$D(p_T, r) = \frac{1}{N_{\text{jet}}} \frac{1}{2\pi r dr} \frac{dn_{\text{ch}}(p_T, r)}{dp_T} \tag{2.6}$$

$$R_{D(p_T,r)} = \frac{D(p_T, r)|_{\text{PbPb}}}{D(p_T, r)|_{\text{pp}}} \tag{2.7}$$

where N_{jet} is the number of jets, n_{ch} is the number of charged particles, r is the distance of a charged particle

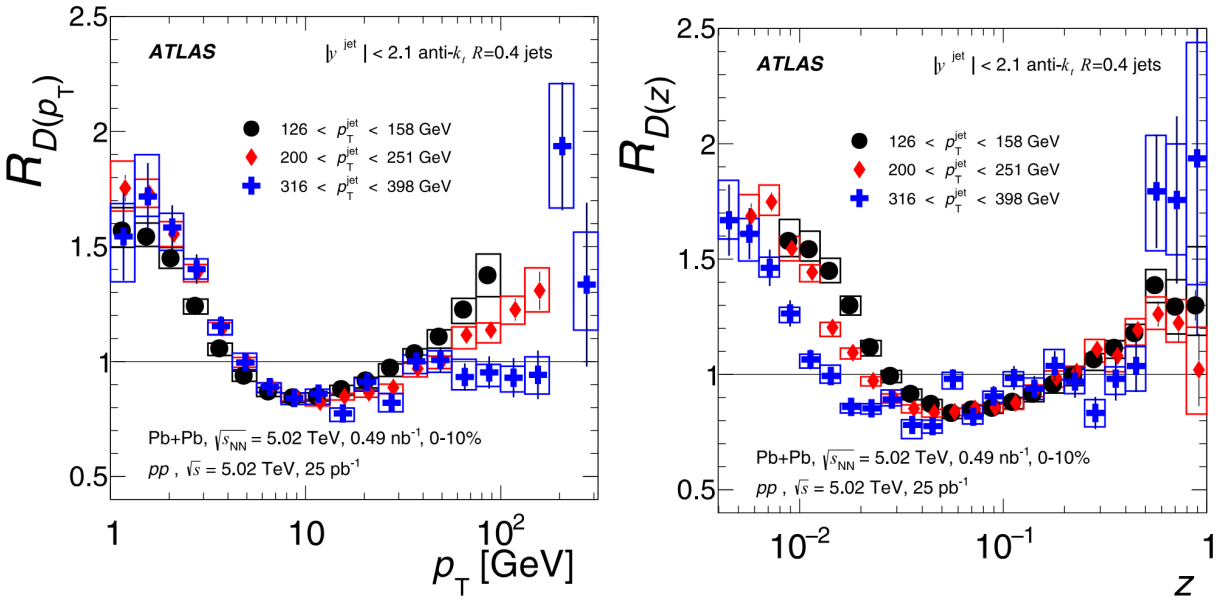

Figure 2.10: $R_{D(p_T)}$ ratio (left) of fragmentation functions as a function of charged particle momentum p_T and $R_{D(z)}$ ratio (right) of fragmentation functions as a function of z, for pp collisions and 0–10% central Pb+Pb collisions and three jet momentum $p_{\mathrm{T}}^{\mathrm{jet}}$ selections. Figure taken from [53].

to the jet axis, and p_{T} is the transverse momentum of a charged particle.

The $D(p_T, r)$ fragmentation function and the corresponding $R_{D(p_T,r)}$ ratio are shown in Figure 2.12 [56]. The $D(p_T, r)$ fragmentation function shows that charged particles with higher momentum are contained within a smaller radius, while charged particles with lower momentum are emitted at larger radii with respect to the jet axis. $R_{D(p_T,r)}$ shows that in Pb+Pb collisions there is a depletion of particles with $p_T > 4$ GeV and an enhancement of particles with lower momentum, with respect to pp collisions.

Overall, the fragmentation functions indicate that interactions with the medium cause jets to fragment into particles of lower momenta that are emitted at larger angles. While most particles are contained within a jet radius $R = 0.4$, the particles outside of the jet can account for the jet energy loss.

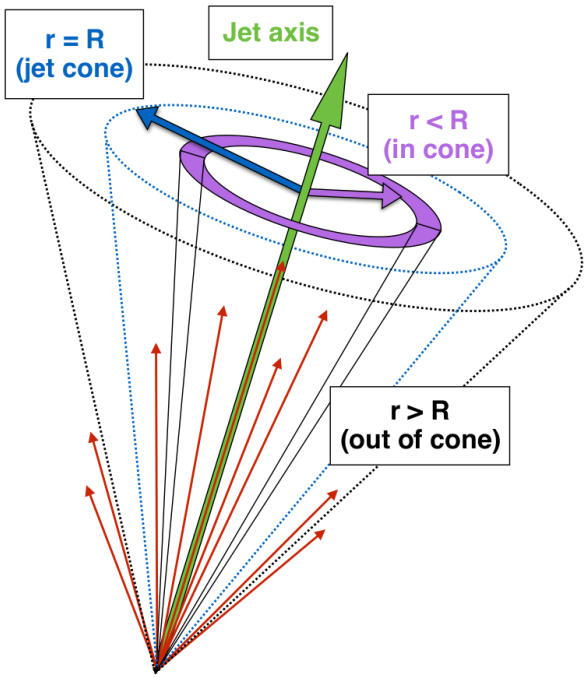

Figure 2.11: Diagram of jet and particles at distance r from the jet axis. Figure taken from [55].

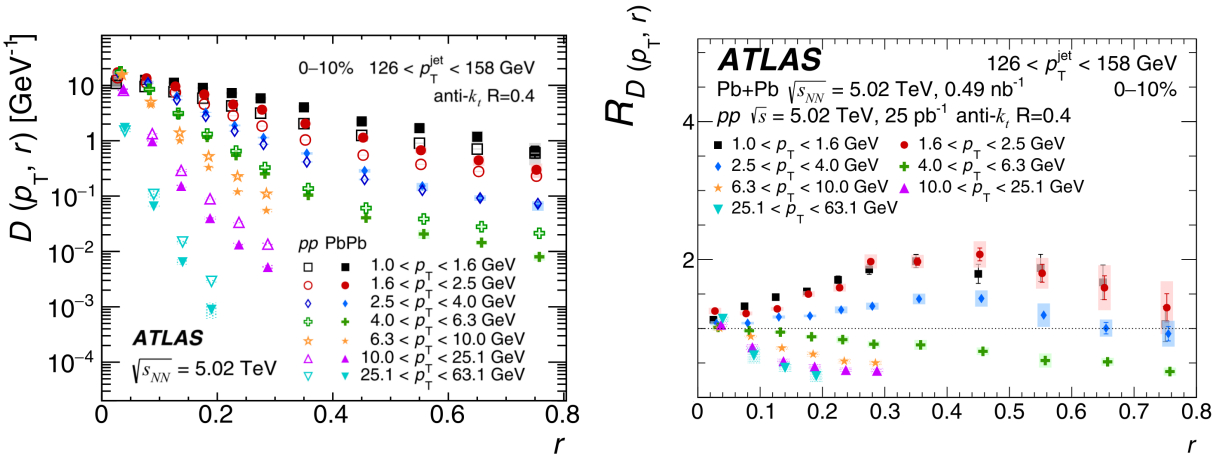

Figure 2.12: The $D(p_T, r)$ fragmentation function (left) and the corresponding $R_{D(p_T,r)}$ ratio (right) as a function of the particle distance r to the jet axis, for 0–10% central collisions. Figure taken from [56].

2.4 Dijet momentum balance

Dijets are pairs of jets created with the same momentum magnitude but in opposite directions. The dijet momentum balance is defined as:

$$x_J = \frac{p_{T,2}}{p_{T,1}} \tag{2.8}$$

where $p_{T,1}$ and $p_{T,2}$ are the transverse momenta of the two jets in the dijet, with $p_{T,1} > p_{T,2}$. The jet with the highest transverse momentum ($p_{T,1}$) is called the leading jet, while the second highest ($p_{T,2}$) is called the subleading jet. Thus, x_{J} compares the momenta of the jets in a dijet. Large x_{J} values correspond to more balanced or symmetric dijets, whereas low x_{J} values correspond to imbalanced or asymmetric dijets.

As was seen previously with the jet v_n, the jet energy loss is dependent on the path length. Since each of the jets in a dijet can traverse a different distance within the QGP, the dijet momentum balance is an observable sensitive to the jet energy loss.

The absolutely normalized x_{J} distribution in Pb+Pb collisions is defined as:

$$\frac{1}{\langle T_{\mathrm{AA}} \rangle N_{\mathrm{evt}}} \frac{\mathrm{d}N_{\mathrm{pair}}}{\mathrm{d}x_{\mathrm{J}}} \tag{2.9}$$

where N_{evt} is the total number of events, $\langle T_{\mathrm{AA}} \rangle$ is the mean nuclear thickness function, and N_{pair} is the number of dijets. The analogous x_{J} distribution in pp collisions with integrated luminosity L_{pp} is:

$$\frac{1}{L_{pp}} \frac{\mathrm{d}N_{\mathrm{pair}}}{\mathrm{d}x_{\mathrm{J}}} \tag{2.10}$$

Figure 2.13 shows the absolutely normalized x_{J} distributions in pp and Pb+Pb collisions of various centralities [39]. For pp collisions, the x_{J} distribution is peaked at $x_{\mathrm{J}} \approx 1$, which means the dijets are balanced in momentum when produced in vacuum. However, for Pb+Pb collisions, the dijet yields are suppressed for higher x_{J} values ($x_{\mathrm{J}} > 0.5$) and enhanced at lower x_{J} values ($x_{\mathrm{J}} < 0.5$), compared to pp collisions. Furthermore, these differences between Pb+Pb and pp collisions are dependent on centrality, with the differences being larger for more central collisions. The x_{J} distributions in Pb+Pb collisions show that dijets are modified in the presence of a QGP, with balanced dijets being suppressed and imbalanced dijets being enhanced.

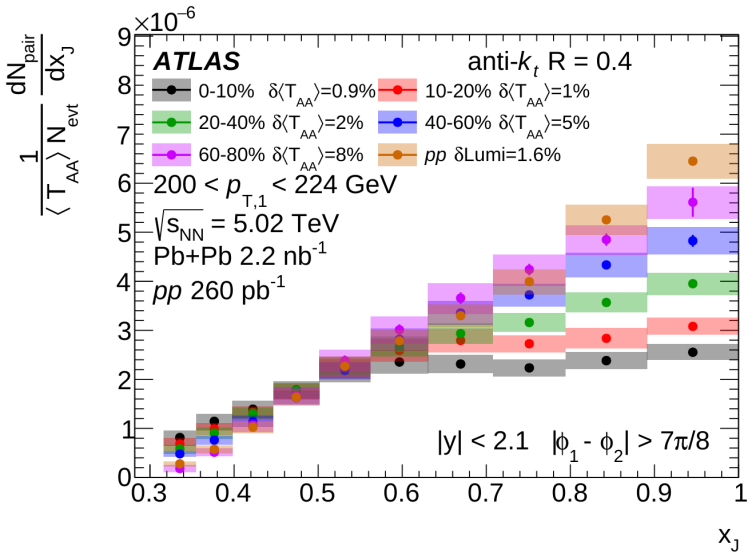

Figure 2.13: Absolutely normalized x_J distributions in pp and Pb+Pb collisions of various centralities. Figure taken from [39].

2.5 Jet radius dependent measurements

It has been observed that jets have a modified fragmentation and are quenched in the presence of a QGP compared to vacuum; the QGP causes jets to widen and lose energy. In this context, measurements in which jets are reconstructed with various radius parameters are sensitive to the jet energy loss and distribution. Measurements of the suppression of jets of different radii are of great interest to understand where the lost energy is with respect to the jet axis, how the energy is distributed among the jet particles, and to measure the possible response of the QGP to the presence of the jet [57, 58].

A few measurements have looked at the jet radius dependence of jet quenching. ATLAS measured the central to peripheral ratio of jet yields R_{CP} at low momentum ($p_{\mathrm{T}} < 100$ GeV) for jet radii $R = 0.2$, 0.3, 0.4, and 0.5 [59]. Figure 2.14 shows the double ratio of R_{CP} for jet radius R with respect to $R = 0.2$ as a function of jet transverse momentum in 0–10% central Pb+Pb collisions. A decrease in jet quenching (an increased jet yield) with increasing jet radius was observed, with a moderate dependence on the jet radius.

In contrast, recent measurements from ALICE [61] in a similar momentum region suggest that jet quenching increases for larger radii jets at fixed p_{T}. Figure 2.15 shows the double ratio of R_{AA} for $R = 0.4$ and 0.6 jets with respect to $R = 0.2$ as a function of charged particle transverse momentum in 0–10% central Pb+Pb collisions. No significant jet radius dependence was observed for $R = 0.4$ jets, while a decrease in the R_{AA} was observed for $R = 0.6$ jets, both with respect to $R = 0.2$ jets.

At higher momentum ($p_{\mathrm{T}} > 400$ GeV in central Pb+Pb collisions), CMS measured the R_{AA} for jet radii $R = 0.3$, 0.4, 0.6, 0.8, and 1.0 [62]. Figure 2.16 shows the double ratio of R_{AA} for jet radius R with respect

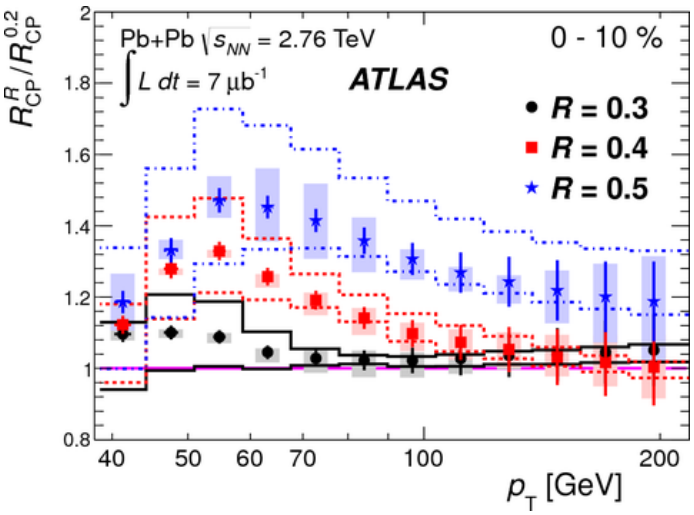

Figure 2.14: Double ratio of R_{CP} for jet radius R with respect to $R = 0.2$ as a function of jet transverse momentum in 0–10% central Pb+Pb collisions at $\sqrt{s_{\mathrm{NN}}}$= 5.02 TeV. Figure taken from [60].

to $R = 0.2$ as a function of jet radius in Pb+Pb collisions of various centralities. In this case no significant dependence of the jet R_{AA} on the jet radius was observed.

With respect to these previous measurements, the results in this thesis represent an advancement in the understanding of the jet radius dependence of jet quenching due to the improved precision and broad jet transverse momentum range. The results are described in detail in Section 4.4.

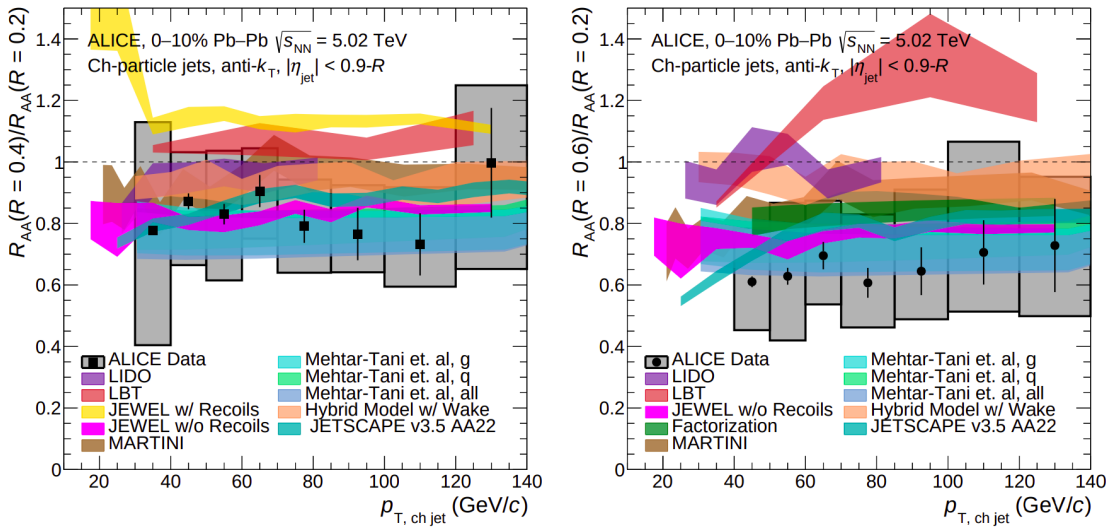

Figure 2.15: Double ratio of R_{AA} for $R = 0.4$ (left) and $R = 0.6$ (right) jets with respect to $R = 0.2$ as a function of charged particle transverse momentum in 0–10% central Pb+Pb collisions at $\sqrt{s_{\mathrm{NN}}}$= 5.02 TeV. Figure taken from [61].

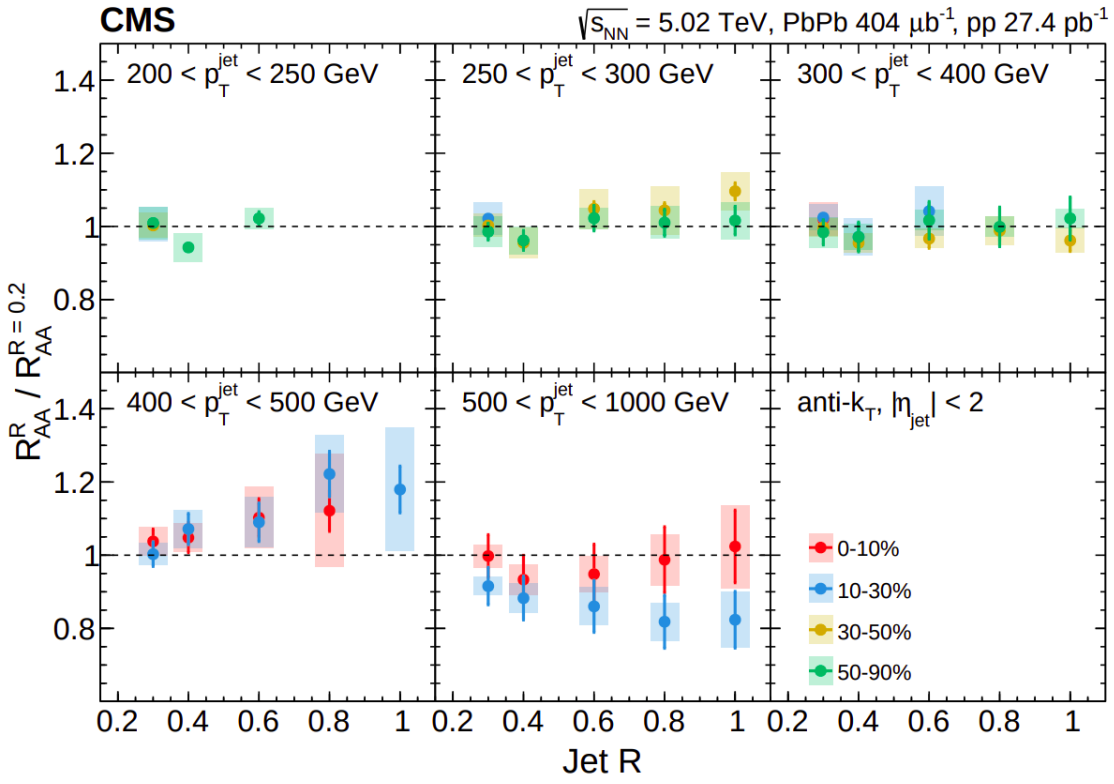

Figure 2.16: Double ratio of R_{AA} for jet radius R with respect to $R = 0.2$ as a function of jet radius in Pb+Pb collisions of various centralities at $\sqrt{s_{\mathrm{NN}}}$= 5.02 TeV. Figure taken from [62].

Chapter 3

The LHC and ATLAS

3.1 The Large Hadron Collider at CERN

The Large Hadron Collider (LHC) is a circular particle accelerator built by the European Organization for Nuclear Research (CERN) [63–65] that collides particle beams. The LHC has a circumference of $\sim$27 km and is buried between 50 and 175 m under France and Switzerland. The LHC is the largest accelerator in the CERN accelerator complex, as seen in Figure 3.1. Various particle experiments make use of the CERN accelerator complex, with ATLAS being one of the main detectors at the LHC.

The LHC ring has two vacuum beam pipes, each corresponding to one of the particle beams that travel in opposite directions. The LHC is made up of segments alternating these components:

- **Radio frequency (RF) cavities**: Used to accelerate the beams. There are 16 RF cavities, 8 for each beam direction. Each RF cavity provides the beam with a voltage of 2 MV (an accelerating field of 5 MV/m) at a frequency of 400 MHz. The cavities are kept at a temperature of 4.5 K.
- **Dipole magnets**: Used to bend the beams. There are 1232 dipole magnets along the LHC ring, providing a magnetic field of up to 7.7 T. These magnets are cooled at a temperature of 1.9 K using liquid Helium.
- **Quadrupole magnets**: Used to focus the beams. There are 392 quadrupole magnets along the LHC ring.
- **Injection and extraction systems**: Used to deliver the beams from the pre-accelerators.

The LHC can collide a variety of beams, such as protons, called pp collisions, or lead, which are called Pb+Pb collisions [67, 68]. The proton beams are delivered in bunches with a peak luminosity of 10^{34} $cm^{-2}s^{-1}$ particles that collide every 25 ns with a center of mass energy $\sqrt{s}$ of up to 14 TeV. The lead beams are delivered in bunches with a peak luminosity of 10^{27} $cm^{-2}s^{-1}$ particles that collide every 75 or 100 ns with a per-nucleon-pair center of mass energy $\sqrt{s_{\mathrm{NN}}}$ of up to 5.5 TeV. Each collision is called an event.

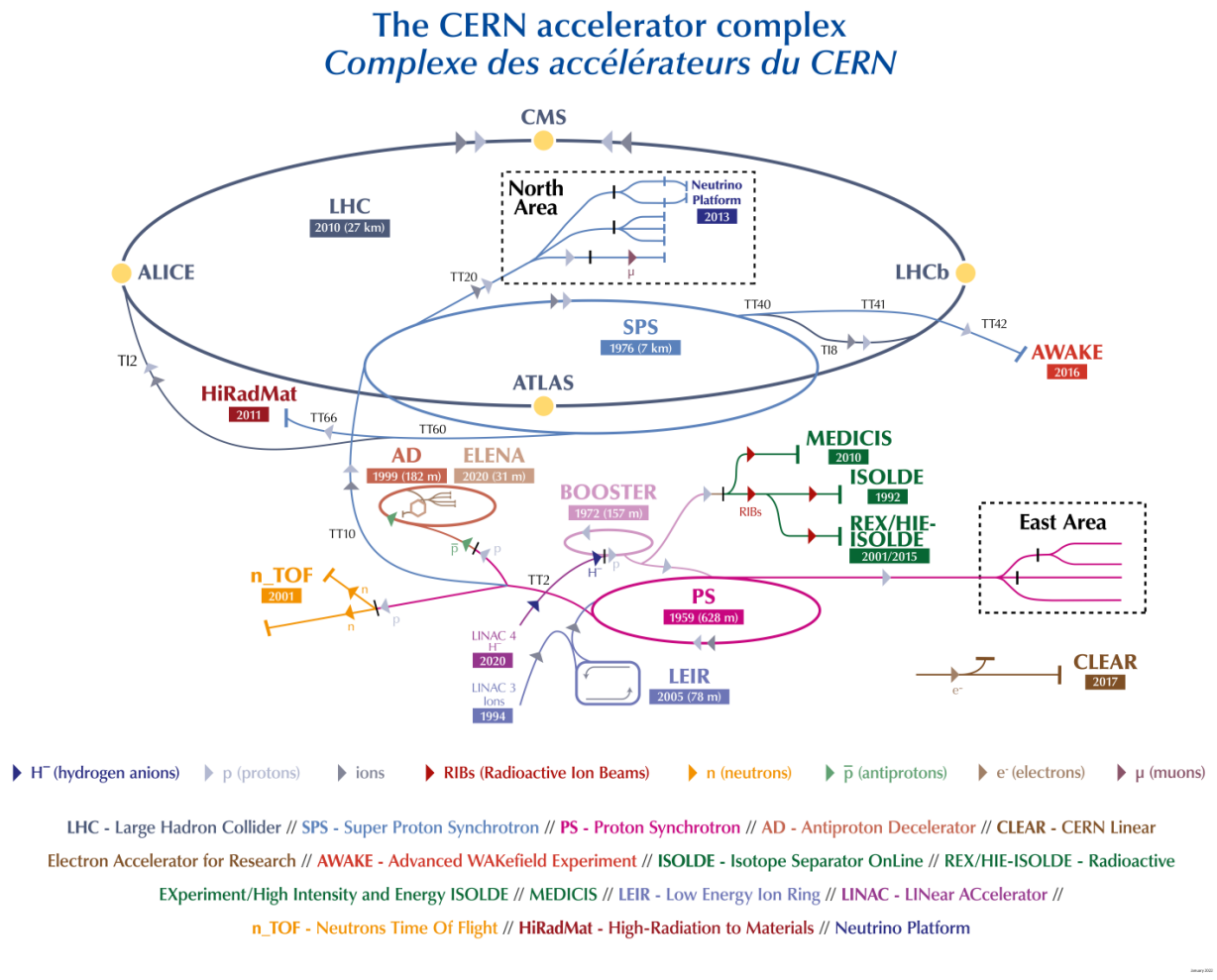

Figure 3.1: Schematic view of the CERN accelerator complex. Figure taken from [66].

3.2 The ATLAS detector at the LHC

ATLAS is one of the main experiments at the LHC [67]. The ATLAS detector consists of several layers of subdetectors made of different technologies. The subdetectors are arranged in an overall cylindrical geometry around the beam line, with a 2π azimuthal coverage. The central part of the detector is called the barrel (concentric with the beam line) while the two ends of the detector are called the end caps (perpendicular to the beam line). Figure 3.2 shows a diagram of the ATLAS detector [69].

3.2.1 Coordinate system

The ATLAS coordinate system is centered at the point where the beams collide. The z axis corresponds to the beam line, the y axis points towards earth's surface, and x points towards the center of the LHC ring.

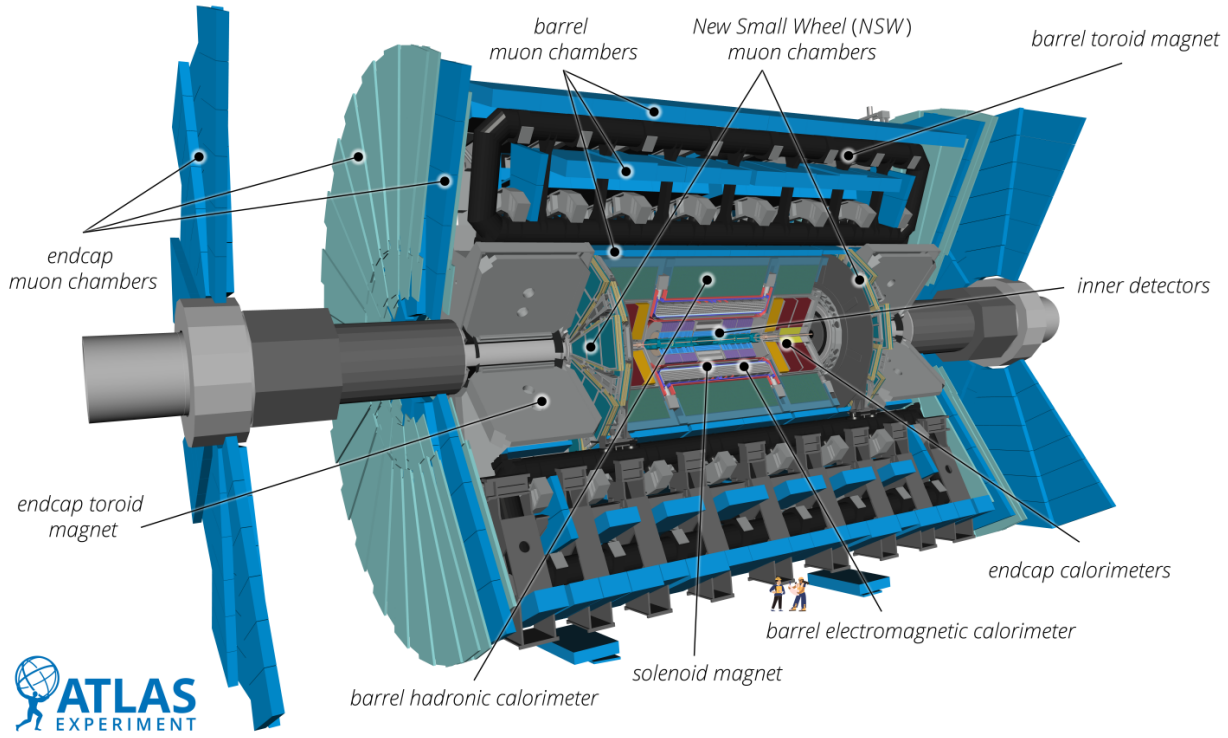

Figure 3.2: Schematic view of the ATLAS detector. Figure taken from [69].

Spherical coordinates (r, ϕ, θ) are defined in this coordinate system. The pseudo-rapidity is defined in terms of the polar angle θ as $\eta = -\ln(\tan(\theta/2))$ and is used due to Lorentz invariant properties. The angular distance between two objects i and j is calculated as: $\Delta R_{ij} = \sqrt{(\eta_i - \eta_j)^2 + (\phi_i - \phi_j)^2}$.

The measured energy E and momentum p are projected to the transverse $x - y$ plane and are referred to as transverse energy and transverse momentum, often denoted as E_T and p_T, respectively. The rapidity is defined as $y = \frac{1}{2}\ln(\frac{E+p_z}{E-p_z})$ in terms of the energy E and momentum p_z along the beam line.

3.2.2 Inner detector and superconducting solenoid

The inner detector (ID) [70–72] is used to accurately measure the position of charged particles coming from the collisions, called tracks. The ID consists of three detectors: the pixel detector, the Semi-Conductor Tracker (SCT), and the Transition Radiation Tracker (TRT). They are made of a semiconductor or gaseous material that the incoming charged particles ionize as they go through it. The material is kept at a high voltage so that the ionization is collected to form a signal. The ID covers a pseudorapidity region of $|\eta| < 2.5$ and is surrounded by a superconducting solenoid that provides a 2 T magnetic field used to bend the particles. Figure 3.3 shows an schematic view of the ID.

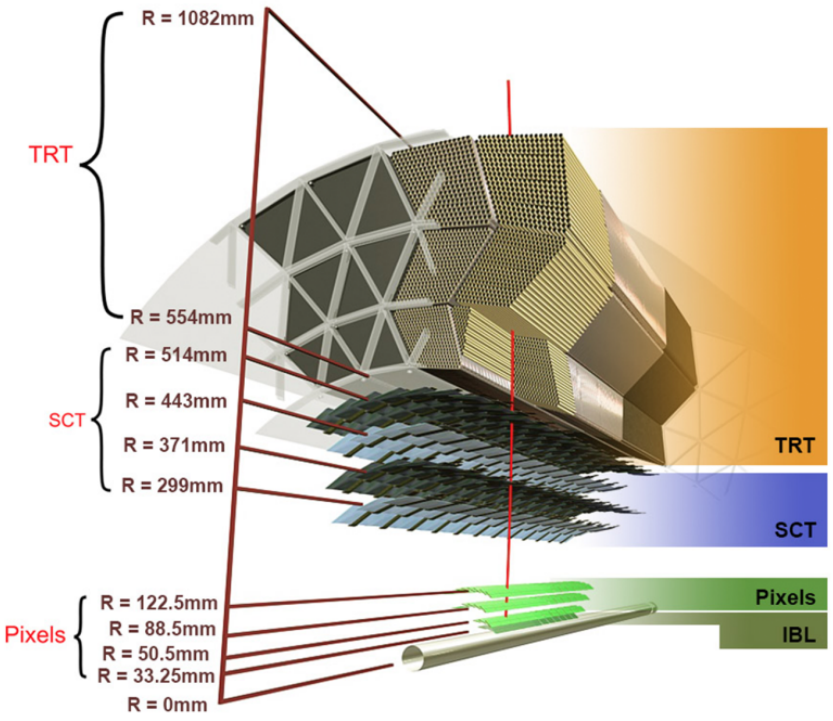

Figure 3.3: Schematic view of the Inner Detector. Figure taken from [73].

Pixel detector Consists of a barrel made of four layers of silicon pixel sensors, two end caps made of three disks of silicon pixel sensors, and an insertable B layer (IBL) [74, 75]. The pixel sensors have a size of $50 \times 400\ \mu m^2$ in $R - \phi \times z$. The IBL is made of carbon fiber staves containing pixels with a size of $50\ \mu m \times 50\ \mu m$. The pixels provide an intrinsic accuracy of $10\ \mu m$ in $R - \phi$ and $115\ \mu m$ in z in the barrel, and $10\ \mu m$ in $R - \phi$ and $115\ \mu m$ in R in the end caps. There are over 92 million pixels/readout channels in total, covering an approximate area of $1.9\ m^2$ around the collision point. The pixel detector provides four measurements per track.

Semi Conductor Tracker Consists of layers of silicon strips with a small angle of 40 $m$rad, both for the barrel and end caps. In the barrel, the strips have a pitch of $80\ \mu m$, with two $6\ cm$ long rectangular sensors that are daisy-chained, parallel to the beam line. In the end caps, the radial strips have a mean pitch of $80\ \mu m$, with trapezoidal sensors. The SCT provides an intrinsic accuracy of $17\ \mu m$ in $R - \phi$ and $580\ \mu m$ in z in the barrel, and $17\ \mu m$ in $R - \phi$ and $580\ \mu m$ in R in the disks. There are approximately $60\ m^2$ of silicon distributed in the full SCT, with about 6 million readout channels. The SCT provides eight measurements per track.

Transition Radiation Tracker Consists of gaseous straw tubes of 4 mm in diameter with a gold plated tungsten wire at the center. In the barrel, the straws are 144 cm long and parallel to the beam line. In the end cap, the straws are 37 cm long, arranged radially in wheels. The TRT provides an intrinsic accuracy of 130 μm. There are approximately 350 thousand readout channels in the 12 m^3 volume of the TRT.

3.2.3 Calorimeter system

Used to measure the energy of particles coming from the collisions within a pseudorapidity of $|\eta| < 4.9$ [76]. The system consists mainly of hadronic, electromagnetic, and forward calorimeters. The calorimeters are made from an "active" material that the incoming particles ionize, creating a signal, and a dense "absorber" material in which the particles lose most of their energy but no signal is created. Figure 3.4 shows an schematic view of the calorimeter system.

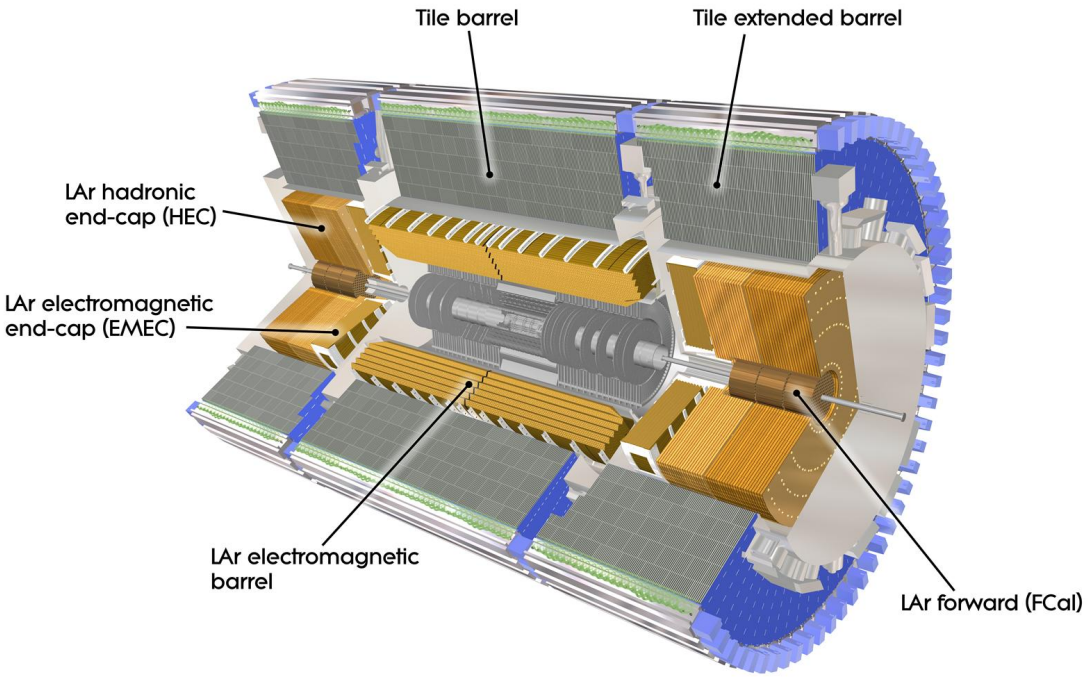

Figure 3.4: Schematic view of the calorimeter system. Figure taken from [77].

Electromagnetic calorimeter Used to measure the energy of electrons, positron, and photons [78]. Consists of alternating layers of liquid argon (LAr) as the active material and dense metals (lead, tungsten, and copper) as the absorber material. The barrel is located at $|\eta| < 1.5$ while the end caps are at $1.4 < |\eta| < 3.2$.

Hadronic calorimeter Used to measure the energy of hadrons [79]. The barrel of the hadronic calorimeter consists of alternating layers of scintillating tiles as the active material and steel as the absorber material. The scintillators produce photons when particles travel through them and excite its molecules. This light is collected to form a signal. There are approximately 420 thousand scintillating tiles/readout channels. The barrel is within $|\eta| < 1.7$. On the other hand, the end caps of the hadronic calorimeter consist of alternating layers of liquid argon as the active material and copper as the absorber material. The hadronic end caps are at $1.5 < |\eta| < 3.2$.

Forward calorimeter The forward calorimeter (FCal) consists of alternating layers of liquid argon as the active material, and copper and tunsgsten as the absorber materials. The FCal is located at $3.2 < |\eta| < 4.9$.

Minimum-bias detector Used to detect when a collision occurs. Consists of scintillators that detect charged particles over a region of $2.1 < |\eta| < 3.9$. It uses two hodoscopes of 12 counters located at $z = \pm 3.6$ m along the beam line, from the center of the ATLAS detector.

Zero degree calorimeter Used to measure neutrons that do not interact during the collisions. Consists of alternating layers of quartz rods and tungsten plates. The zero degree calorimeters are located at $z = \pm 140$ m along the beam line, from the center of the ATLAS detector. They cover the region $|\eta| > 8.3$.

3.2.4 Muon spectrometer and toroid magnet

The muon spectrometer is used to measure the energy and position of muons [80, 81]. It consists of muon chambers of various types and toroid magnets, covering $|\eta| < 2.7$ [82].

Muon tracks are measured by a combination of chambers: Monitored Drift Tubes (MDT), Resistive Plate Chambers (RPC), Thin Gap Chambers (TGC), small Thin Gap Chambers (sTGC), and micromegas detectors (MM) [83]. There are three cylindrical layers of chambers in the barrel region around the beam line, and three planar layers of chambers in the end caps. The MDTs are aluminum tubes 3 cm in diameter, with a wire at the center, filled with a gas mixture. The RPCs consist of two plastic electrode plates separated by 2 mm, filled with a gas mixture. The TGCs are multi-wire proportional chambers (a grid of wires sandwiched between two electrode plates filled with gas) with a gas gap of 2.8 mm and a wire pitch of 1.8 mm, filled with a gas mixture. The sTGCs are multi-wire proportional chambers with a gas gap of 1.4 mm and a wire pitch of 1.8 mm, filled with a gas mixture. The MMs are a metal mesh sandwiched between two planar electrodes separated by a few mm. All the chambers are kept at a high voltage to collect the charges ionized by the passage of the muons through the chambers.

The magnets produce a field integral between 1.5 and 7.5 Tm, depending on the η range. In $|\eta| < 1.4$, a large barrel toroid provides the magnetic field. In $1.6 < |\eta| < 2.7$, two smaller end cap magnets provide the magnetic field. In the $1.4 < |\eta| < 1.6$ transition region, the magnetic field is provided by both the barrel and end cap magnets.

3.2.5 Trigger system

The trigger system has two levels [84], level 1 (L1) and the high level trigger (HLT). The L1 trigger is implemented in the electronics and looks for physics objects (jets, electrons, photons, etc) at a basic hardware level. The HLT is implemented in the software [85] and looks for physics objects with algorithms. The L1 trigger reduces the event rate from 40 MHz bunch crossings to 100 kHz in pp collisions and to 75 kHz in Pb+Pb collisions. Then, the HLT further reduces the rate to approximately 1.2 kHz events, which are recorded.

The L1 trigger applies a sliding window algorithm to look for jet candidates with a total energy above 30 GeV. These jet candidates then go to the HLT where jets are fully reconstructed and the background is subtracted.

Various jet triggers are used. The jet triggers require the leading $R = 0.4$ in the event to have a p_{T} above some threshold. Each jet trigger is used in the p_{T} range in which it is fully efficient. The highest p_{T} jet trigger samples the full luminosity, while the other jet triggers sample a preset fraction of the total events.

In addition to the jet triggers, three minimum-bias triggers are used, each one corresponding to one of the following conditions: total E_{T} in the calorimeter less than 50 GeV at L1 and at least one track reconstructed at HLT; total E_{T} in the calorimeter between 50 and 600 GeV at L1; total E_{T} greater than 600 GeV at L1. More details about the triggering used in ATLAS heavy-ion collisions can be found in Reference [86].

3.3 ATLAS heavy ion jet reconstruction

3.3.1 Jet reconstruction and background subtraction

A dedicated procedure is used in ATLAS to subtract the background and reconstruct and calibrate jets [36, 42]. The anti-k_t algorithm [22], implemented in the FastJet software package [87], is used to reconstruct jets with radius R. Calorimeter towers are used as input for the anti-k_t algorithm for both pp and Pb+Pb collisions. Towers are defined by collecting calorimeter signals corresponding to solid angles of $\Delta\phi \times \Delta\eta = 0.1 \times 0.1$.

Background present in particle collisions is called the underlying event (UE) and corresponds to detector measurements that do not come from hard scatterings of partons. In heavy ion collisions, the UE consists

of the decay products of the QGP, and can contribute considerably to jet energy measurements, as seen in Figure 3.5, which shows the average transverse energy subtracted from $R = 0.4$ jets in Pb+Pb collisions.

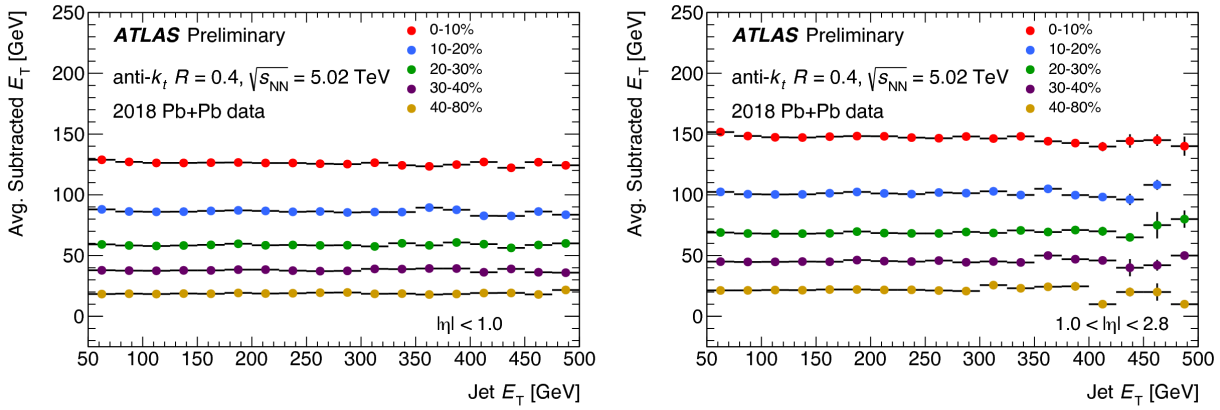

Figure 3.5: Average transverse energy E_T subtracted from $R = 0.4$ jets in Pb+Pb collisions at $\sqrt{s_{\mathrm{NN}}} = 5.02$ TeV, for $|\eta| < 1.0$ (left) and $1.0 < |\eta| < 2.8$ (right) and various collision centralities [88].

In Pb+Pb collisions, an iterative procedure is used to subtract the UE in an event-by-event manner [89]. The procedure is shown schematically in Figure 3.6. In the first iteration, the average transverse energy density $\frac{dE_{\mathrm{T}}}{d\eta}$ is estimated in slices of $\Delta\eta = 0.1$ from the calorimeter tower energies. "Seeds" corresponding to real jets are excluded from the background estimation, as well as regions that are within $\Delta R < 0.4$ of a seed. Two kinds of seeds are considered, $R = 0.2$ jets and $R = 0.4$ trackjets. Trackjets are jets clustered from tracks (instead of calorimeter towers) with $p_{\mathrm{T}}^{\mathrm{track}} > 4$ GeV, and are required to have $p_{\mathrm{T}}^{\mathrm{trackjet}} > 7$ GeV. Each $R = 0.2$ jet seed must have at least one tower with energy $E_{\mathrm{T}}^{\mathrm{tower}} > 3$ GeV, and a ratio of the maximum tower energy to the mean tower energy $E_{\mathrm{max}}^{\mathrm{tower}}/\langle E^{\mathrm{tower}}\rangle > 4$. The average UE transverse energy density is estimated as $\rho(\eta,\phi) \propto \frac{dE_T}{d\eta}(1 + 2v_n \cos(n\phi_n))$, where the v_n terms correct for hydrodynamic flow [90] up to the fourth order modulation. This average background is then subtracted from the towers and the jet kinematics are recalculated. In the second iteration, there are additional requirements of $p_{\mathrm{T}}^{\mathrm{jet}} > 25$ GeV for the $R = 0.2$ jet seeds and $p_{\mathrm{T}}^{\mathrm{trackjet}} > 7$ GeV for the trackjets. In pp collisions, the same background subtraction procedure is used but without the flow modulation.

3.3.2 Jet calibration

The jet calibration has various contributions. First, Monte Carlo (MC) simulations are used to obtain correction factors dependent on R, η, and p_{T}. These factors are applied to the measured jet energy to correct for the detector response [91, 92]. Then, *in situ* studies of jets opposing photons or jets [93] are used to obtain another correction, which is applied to account for differences between data and MC. Finally, a

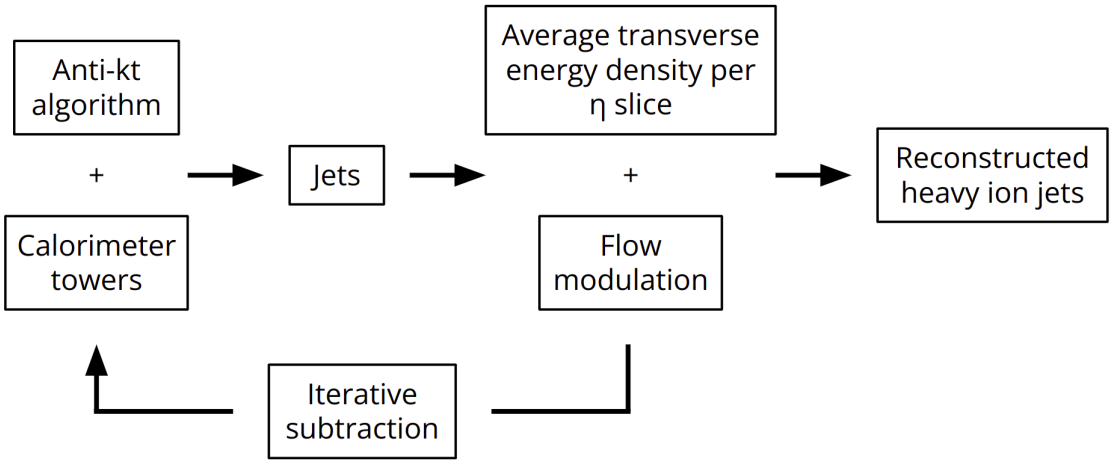

Figure 3.6: Schematic diagram of the UE subtraction and jet reconstruction.

"cross-calibration" is applied, which calibrates the heavy ion jets with respect to the jets in pp collisions at a center of mass energy of 13 TeV. This allows for the use of uncertainties obtained for the latter jets [92].

3.3.3 Fake jets

The UE subtraction removes an average background level but it does not remove the fluctuations around that level. Some of the remaining UE fluctuations can sometimes pass the criteria of the anti-k_t algorithm and be tagged as jets. These are called fake jets and they are UE fluctuations that are reconstructed as jets.

The UE fluctuations were studied to develop a criteria for fake jet rejection in Pb+Pb collisions at a per-nucleon-pair center of mass energy of $\sqrt{s_{\mathrm{NN}}} = 5.02$ TeV. These studies focused on obtaining the mean $\langle E_{\mathrm{T}} \rangle$ and standard deviation $\sigma(E_{\mathrm{T}})$ of the transverse energy E_{T} of the fluctuations as a function of centrality and jet size. $\langle E_{\mathrm{T}} \rangle$ and $\sigma(E_{\mathrm{T}})$ were obtained for windows of $n \times n$ towers defined by a grid in the $\eta - \phi$ space. The mean of the fluctuations was defined as $\langle E_{\mathrm{T}} \rangle = \frac{1}{N} \sum_{i=0}^{N} E_{\mathrm{T}}^{i}$, where E_{T}^{i} is the transverse energy of the i^{th} window and N is the total number of windows. Similarly, the standard deviation of the fluctuations was defined as $\sigma(E_{\mathrm{T}}) = \sqrt{\langle E_{\mathrm{T}}^2 \rangle - \langle E_{\mathrm{T}} \rangle^2}$.

Figure 3.7 shows an example grid where each square represents a window of 7×7 towers, an area equivalent to the size of an $R = 0.4$ jet. This figure also shows the standard deviation and mean of the transverse energy E_{T} of the UE fluctuations, as a function of the total energy in the forward calorimeters, which correlates with centrality. The mean $\langle E_{\mathrm{T}} \rangle$ of the fluctuations is close to zero due to the UE subtraction removing the average UE. The standard deviation $\sigma(E_{\mathrm{T}})$ of the fluctuations increases with centrality due the UE being larger for collisions in which more QGP is created.

Figure 3.8 shows the average $\sigma(E_{\mathrm{T}})$ of the UE fluctuations as a function of jet area in units of towers, for

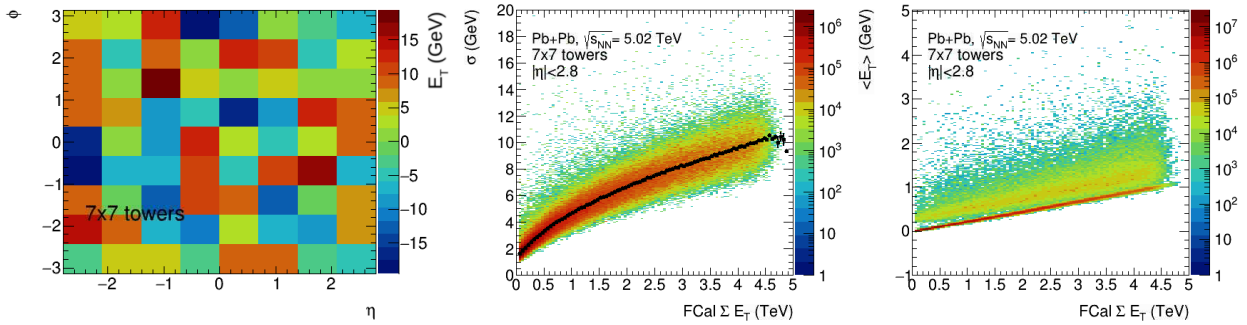

Figure 3.7: (left) Transverse energy E_{T} of groups of 7×7 towers (equivalent to the area of an $R = 0.4$ jet) as a function of η and ϕ, for one event in 0–10% central Pb+Pb collisions. Standard deviation $\sigma(E_{\mathrm{T}})$ (middle) and mean $\langle E_{\mathrm{T}} \rangle$ (right) of the transverse energy of UE fluctuations as a function of the total energy in the forward calorimeters, for groups of 7×7 towers.

various Pb+Pb collision centralities. It is observed that the UE fluctuations increase with the jet area. The relationship between the fluctuations and the jet area was characterized by a fit $\sigma = \sigma_{1\mathrm{x}1} A^k$, where σ is the average standard deviation of E_{T}, A is the jet area, $\sigma_{1\mathrm{x}1}$ is a reference (σ for an area of 1×1 towers), and k is a constant that depends on the centrality.

The studies on fake jet rejection focused on tagging $R = 0.4$ jets as "real" or "fake" based on their matching to tracks or smaller $R = 0.2$ jets. These criteria for fake jet rejection are based on the fact that real jets are expected to have associated tracks that pass some minimum energy cuts, and have a hard core that is represented by a smaller jet. Figure 3.9 shows the fake jet rate for $R = 0.4$ jets as a function of jet transverse momentum for Pb+Pb collisions of various centralities. The fake jet rate is lower for more peripheral collisions because the fluctuations are smaller.

The area scaling in Figure 3.8 along with the fake jet rate of $R = 0.4$ jets in Figure 3.9 can be used to obtain the fake jet rates for other jet radii. For $R = 0.4$ jets, the fake jet rate drops below 5% for $p_{\mathrm{T}} > 100$ GeV in central collisions. From the area scaling, this fake jet rate drop occurs approximately at 130 GeV for $R = 0.5$ jets and at 160 GeV for $R = 0.6$ jets.

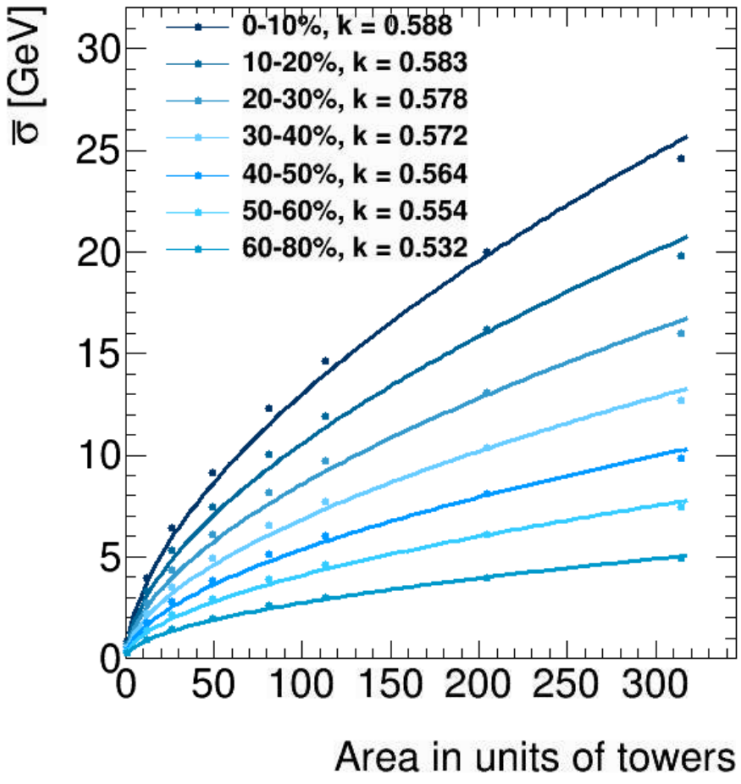

Figure 3.8: Average $\sigma(E_{\mathrm{T}})$ of the UE fluctuations as a function of jet area in units of towers, for various Pb+Pb collision centralities.

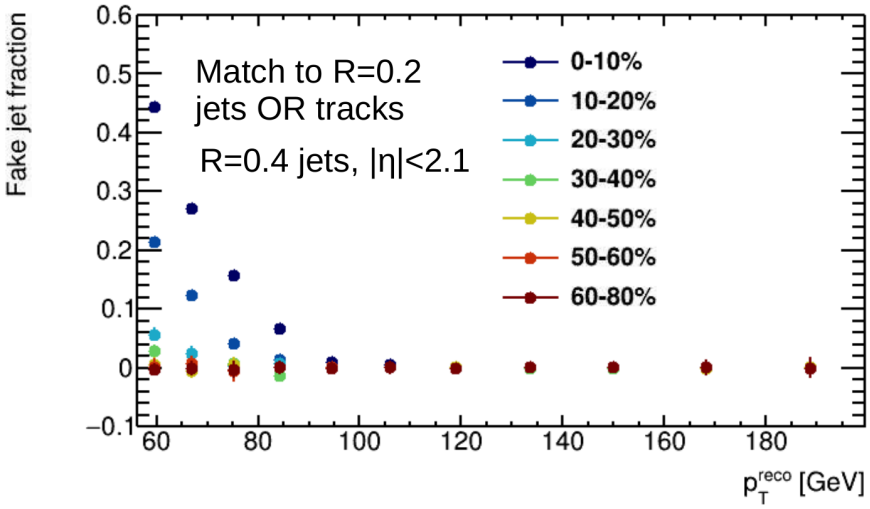

Figure 3.9: Fake jet rate of $R = 0.4$ jets in Pb+Pb collisions of various centralities as a function of jet transverse momentum.

3.3.4 Jet performance

To evaluate the performance of the jet reconstruction, MC simulations of jets are compared to the reconstructed jets that would be experimentally measured. The MC simulations consist of simulated dijets from *pp* collisions obtained from the event generator PYTHIA 8 [94] along with the simulated detector response obtained from GEANT4 [95, 96]. The *pp* dijets are embedded in UE data from Pb+Pb collisions by adding the simulated and real signals at the detector level and digitizing them. These overlaid events are then reconstructed following the same procedure as in data.

In the MC simulations, "true" jets are clustered from stable particles with a proper lifetime of 30 *ps* or greater, but excluding neutrinos and muons, which are not measured in the calorimeter. True jets are matched within $0.75R$ to the nearest "reconstructed" jet. Reconstructed jets are defined at the detector level and include effects from the detector response.

The jet performance is characterized by the jet reconstruction efficiency, the jet energy scale (JES), and jet energy resolution (JER). The jet reconstruction efficiency is defined as the ratio of the number of true jets that match a reconstructed jet to the total number of true jets. The JES and JER are defined as the mean and standard deviation of the $p_{\mathrm{T}}^{\mathrm{reco}}/p_{\mathrm{T}}^{\mathrm{truth}}$ distribution, respectively, where $p_{\mathrm{T}}^{\mathrm{reco}}$ is the reconstructed jet transverse momentum and $p_{\mathrm{T}}^{\mathrm{truth}}$ is the true jet transverse momentum.

The jet reconstruction efficiency can be seen as a function of $p_{\mathrm{T}}^{\mathrm{truth}}$ in Figure 3.10 for various jet radii. The jet reconstruction efficiency drops at low momentum because low momentum measurements cannot be distinguished from background measurements, causing some jets to not to be reconstructed.

The JES and JER can be seen as a function of $p_{\mathrm{T}}^{\mathrm{truth}}$ in Figure 3.10 for various jet radii. The deviation of the JES from unity for high-p_{T} $R = 0.2$ and $R = 0.3$ jets is due to the different cuts used in the determination of the jet calibration compared to this analysis. The broadening of the JER with centrality is due to the UE fluctuations, which are larger in more central collisions and cause the jet p_{T} to smear. Additionally, a larger jet radius allows for a larger contribution of the UE fluctuations, causing the larger R jets to have a larger JER.

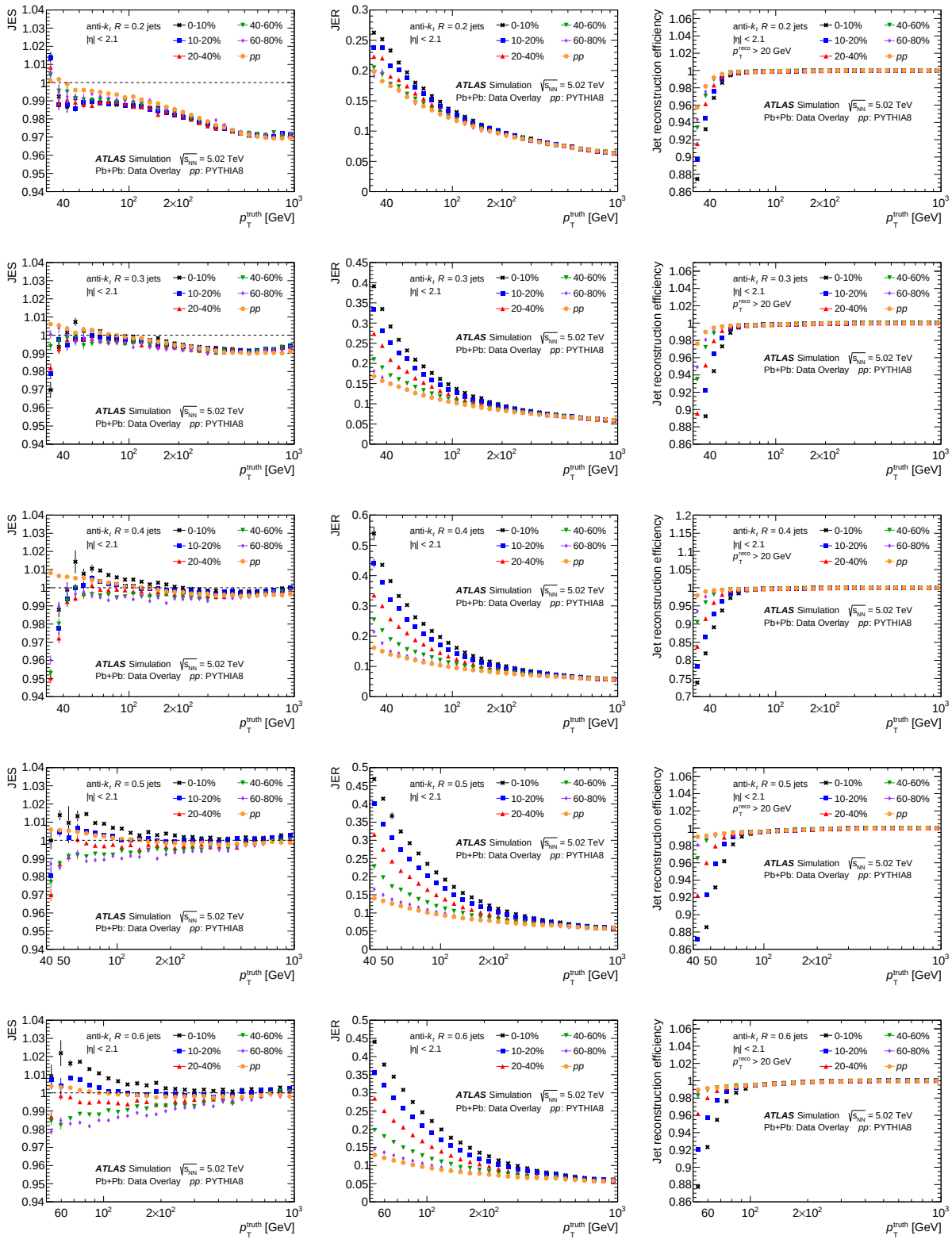

Figure 3.10: The JES (left), JER (middle), and jet reconstruction efficiency as a function of $p_{\mathrm{T}}^{\mathrm{truth}}$, for $R = 0.2, 0.3, 0.4, 0.5$ and 0.6 (top to bottom) in pp and Pb+Pb collisions of various centralities.

Chapter 4

Jet radius dependence of dijet momentum balance

4.1 Data and Monte Carlo selections

This analysis used *pp* and Pb+Pb data collected by the ATLAS detector at a per-nucleon-pair center of mass energy of $\sqrt{s_{\mathrm{NN}}} = 5.02$ TeV. The *pp* data was collected in 2017 with a total integrated luminosity of 255 pb^{-1}. The Pb+Pb data was collected in 2018 with a total integrated luminosity of 1.72 nb^{-1}.

4.1.1 Collision centrality

The overlap area of the two colliding nuclei in Pb+Pb collisions is characterized by the collision centrality. In ATLAS, the collision centrality is defined in percentiles of the total energy in the forward calorimeters, denoted as $\Sigma E_{\mathrm{T}}^{\mathrm{FCal}}$ [97], in minimum-bias collisions. Five centrality intervals are considered: 0–10% (largest $\Sigma E_{\mathrm{T}}^{\mathrm{FCal}}$, most central collisions), 10–20%, 20–40%, 40–60%, and 60–80% (smallest $\Sigma E_{\mathrm{T}}^{\mathrm{FCal}}$, peripheral collisions). The procedure uses the TGlauberMC v3.2 package [98], as described in Section 1.2.1, to obtain the mean nuclear thickness function $\langle T_{\mathrm{AA}} \rangle$ [35] and its uncertainty [99] for each centrality interval. The $\langle T_{\mathrm{AA}} \rangle$ values and their uncertainties are listed in Table 4.1 for each centrality interval.

Centrality selection	$\langle T_{\mathrm{AA}} \rangle \pm \delta\langle T_{\mathrm{AA}} \rangle$ $[mb^{-1}]$
0–10%	23.35 ± 0.20
10–20%	14.33 ± 0.17
20–40%	6.79 ± 0.16
40–60%	1.96 ± 0.09
60–80%	0.39 ± 0.03

Table 4.1: The $\langle T_{\mathrm{AA}} \rangle$ values and its uncertainties for the centrality intervals used in this analysis.

4.1.2 Data selection

Events with multiple collisions, called pileup, were suppressed by using the anti-correlation, expected from the nuclear geometry, between $\Sigma E_{\mathrm{T}}^{\mathrm{FCal}}$ and the energy in both ZDCs, which is proportional to the number

of observed spectator neutrons. Pileup constitutes a small fraction, less than 0.5%, of the Pb+Pb events. Pileup was not rejected in *pp* collisions.

Various minimum-bias and jet triggers [84, 100] were used to select events. The triggers considered in this analysis for the Pb+Pb collisions are listed in Table 4.2 along with the leading jet p_{T} ranges, luminosity sampled by the trigger, and average prescale that were used. Similarly, the triggers used in *pp* collisions are listed in Table 4.3.

Trigger	$p_{\mathrm{T}}^{\mathrm{jet}}$ range [GeV] $R = 0.2, 0.3, 0.4$	$p_{\mathrm{T}}^{\mathrm{jet}}$ range [GeV] $R = 0.5, 0.6$	Luminosity	Average prescale
HLT_noalg_pc_L1TE50_VTE600.0ETA49		79 - 121	1.72 nb^{-1}	32.75
HLT_noalg_cc_L1TE600.0ETA49		79 - 121	1.72 nb^{-1}	78.62
HLT_mb_sptrk_L1ZDC_A_C_VTE50		79 - 121	1.72 nb^{-1}	33.23
HLT_j50_ion_L1J12	79 - 84	121 - 141	98.6 $\mathrm{mb}^{-}1$	17.42
HLT_j60_ion_L1J15	84 - 112	141 - 165	274.6 $\mathrm{mb}^{-}1$	6.26
HLT_j85_ion_L1J30	112 - 124	165 - +	1.72 nb^{-1}	1.00
HLT_j100_ion_L1J30	124+		1.72 nb^{-1}	1.00

Table 4.2: List of triggers, leading jet p_{T} ranges, luminosity sampled by the trigger, and average prescale, used for the Pb+Pb data.

Trigger	$p_{\mathrm{T}}^{\mathrm{jet}}$ range [GeV] $R = 0.2, 0.3, 0.4$	$p_{\mathrm{T}}^{\mathrm{jet}}$ range [GeV] $R = 0.5, 0.6$	Luminosity	Average prescale
HLT_j50_L1J15	79 - 84	77 - 92	282 nb^{-1}	71.84
HLT_j60_L1J20	84 - 112	92 - 130	9 pb^{-1}	28.53
HLT_j85_L1J20	112 - 124	130 - 137	132.2 pb^{-1}	1.94
HLT_j100_L1J20	124+	137+	257 pb^{-1}	1.00

Table 4.3: List of triggers, leading jet p_{T} ranges, luminosity sampled by the trigger, and average prescale, used for the *pp* data.

The minimum-bias triggers correspond to one of the following conditions: total E_{T} in the calorimeter less than 50 GeV at L1 with at least one track reconstructed at HLT; total E_{T} in the calorimeter between 50 and 600 GeV at L1; total E_{T} in the calorimeter greater than 600 GeV at L1. More details about the triggering used in ATLAS heavy-ion collisions can be found in Reference [86].

The jet triggers require the leading $R = 0.4$ in the event to have a p_{T} above some threshold. Each jet trigger is used in the p_{T} range in which it is fully efficient. The highest p_{T} jet trigger samples the full luminosity, while the other jet triggers sample a preset fraction of the total events, called the prescale.

The efficiency of the jet triggers was obtained for the $R = 0.6$ jets to ensure that the triggers were used in the p_{T} range in which they are fully efficient. The trigger efficiencies for $R = 0.6$ jets in Pb+Pb collisions of various centralities are shown in Figure 4.1. Similarly, the trigger efficiencies for $R = 0.6$ jets in *pp* collisions are shown in Figure 4.2.

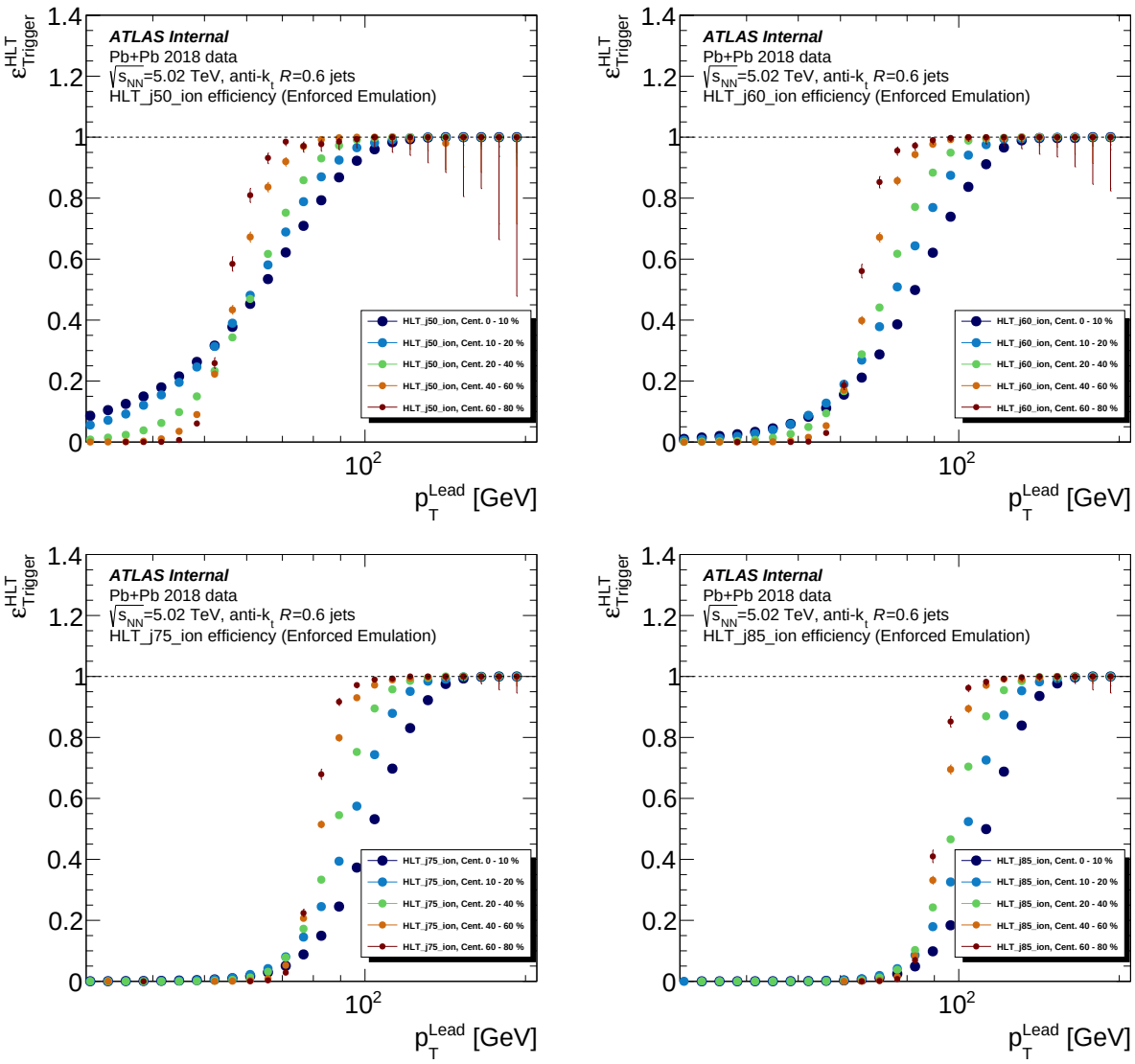

Figure 4.1: Trigger efficiencies for $R = 0.6$ jets in Pb+Pb collisions of various centralities.

4.1.3 Monte Carlo samples

Three Monte Carlo (MC) samples were used to assess the detector performance, to correct for detector effects, and for uncertainty studies.

The first is a *pp* MC sample. This sample simulated the ATLAS detector conditions in 2017 and contained 3.2×10^7 PYTHIA 8 [94] *pp* jet events generated at a center of mass energy $\sqrt{s} = 5.02$ TeV. For PYTHIA 8, the A14 tune [101] and the NNPDF23LO parton distribution functions (PDFs) [102] were used. The detector conditions were simulated using GEANT4 [95, 96].

The second is a Pb+Pb MC sample referred to as the "overlay". This sample simulated the ATLAS detector conditions in 2018, contained 3.2×10^7 *pp* PYTHIA 8 jet events, and was overlaid with minimum-bias

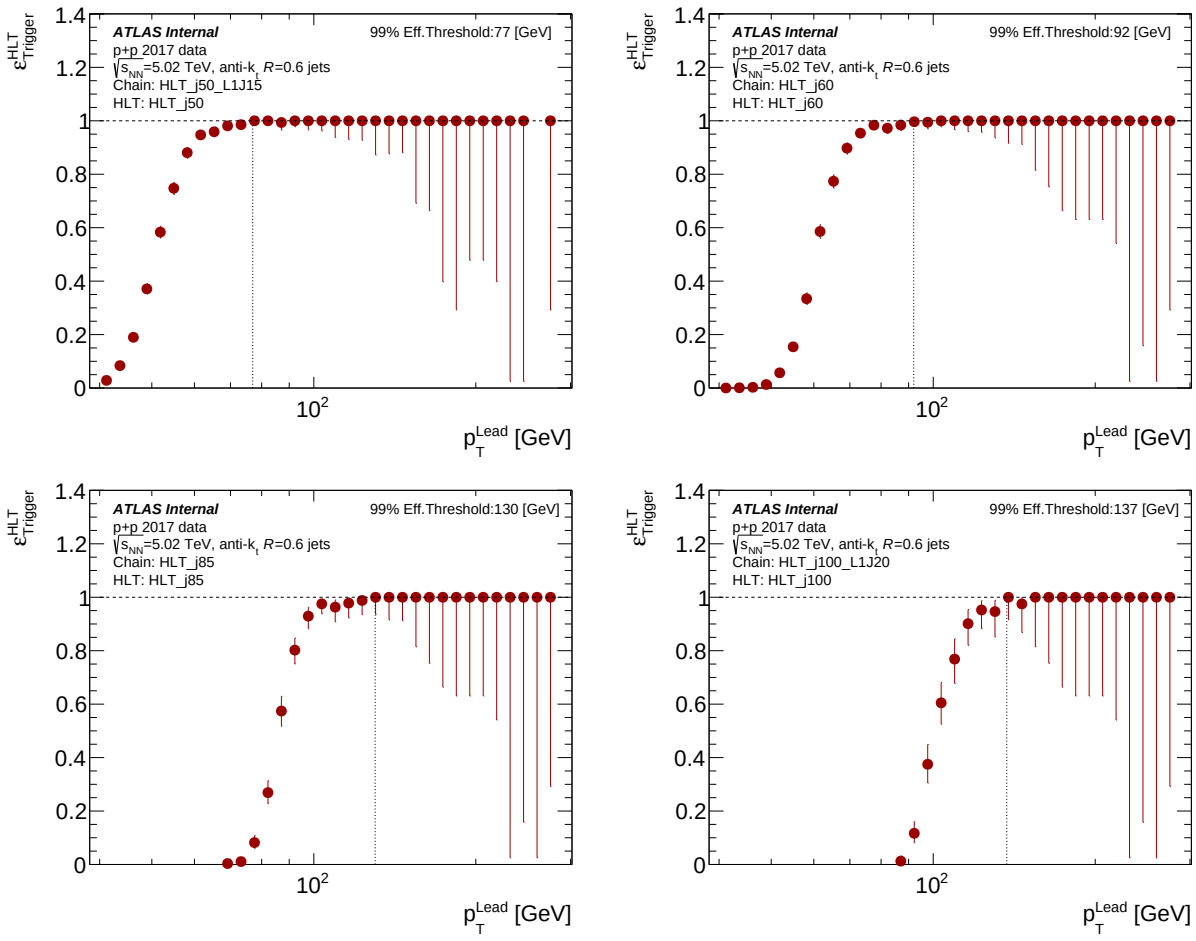

Figure 4.2: Trigger efficiencies for $R = 0.6$ jets in pp collisions.

Pb+Pb data to include the UE. It used the same PYTHIA 8 tune and PDFs as the pp MC sample, and the detector conditions were also simulated with GEANT4. The minimum-bias Pb+Pb data and the PYTHIA 8 jet simulations were combined by adding the signals at the detector level and digitizing them. These overlaid events were then reconstructed following the same procedure as in data. This Pb+Pb MC sample was reweighted to have the same centrality distribution as measured in data.

The pp and Pb+Pb MC samples were used for the jet performance described in Section 3.3.4 and the unfolding described in Section 4.2.3.

The third is a pp HERWIG7 [103, 104] sample using the UEEE5 tune [105] and the CTEQ6L1 PDFs [106]. This sample was used for flavor uncertainty studies as well as comparisons with pp data. The detector response in this sample was simulated using GEANT4 [95, 96].

4.2 Analysis

4.2.1 Jet selection and measured $(p_{\mathrm{T},1}^{\mathrm{reco}}, p_{\mathrm{T},2}^{\mathrm{reco}})$ distributions

In each event, the highest-$p_{\mathrm{T}}^{\mathrm{reco}}$ jet were reconstructed as the leading jet and the second highest as the subleading jet. Both jets were required to have $|y| < 2.1$ and to be back-to-back with $|\phi_1 - \phi_2| > 7\pi/8$. Reconstructed leading jets were required to have $p_{\mathrm{T},1}^{\mathrm{reco}} > 79$ GeV, based on the minimum p_{T} for which the triggers are fully efficient for the various jet radii. Reconstructed subleading jets were required to have $p_{\mathrm{T},2}^{\mathrm{reco}} > 32$ GeV for $R = 0.2, 0.3$ and 0.4 jets, $p_{\mathrm{T},2}^{\mathrm{reco}} > 41$ GeV for $R = 0.5$ jets, and $p_{\mathrm{T},2}^{\mathrm{reco}} > 51$ GeV for $R = 0.6$ jets. The minimum $p_{\mathrm{T},2}^{\mathrm{reco}}$ was based on 0.32 of the minimum p_{T} for which the rate of jets created by UE fluctuations becomes negligible, based on the studies described in Section 3.3.3. Dijets meeting these criteria represent approximately 62% of inclusive $R = 0.2$ jets with $100 < p_{\mathrm{T}} < 562$ GeV, and approximately 72% of inclusive $R = 0.6$ jets with $158 < p_{\mathrm{T}} < 562$ GeV. Events in which the leading dijets do not meet these criteria were discarded.

The two-dimensional $(p_{\mathrm{T},1}^{\mathrm{reco}}, p_{\mathrm{T},2}^{\mathrm{reco}})$ distributions were measured with dijets that pass these criteria. The $(p_{\mathrm{T},1}^{\mathrm{reco}}, p_{\mathrm{T},2}^{\mathrm{reco}})$ distributions were constructed symmetrically across $p_{\mathrm{T},1}^{\mathrm{reco}} = p_{\mathrm{T},2}^{\mathrm{reco}}$ to account for the possibility of swapping the leading and subleading jets due to the JER. The measured $(p_{\mathrm{T},1}^{\mathrm{reco}}, p_{\mathrm{T},2}^{\mathrm{reco}})$ distributions for the various jet radii are shown in Figures 4.3-4.7 for Pb+Pb collisions of various centralities and pp collisions.

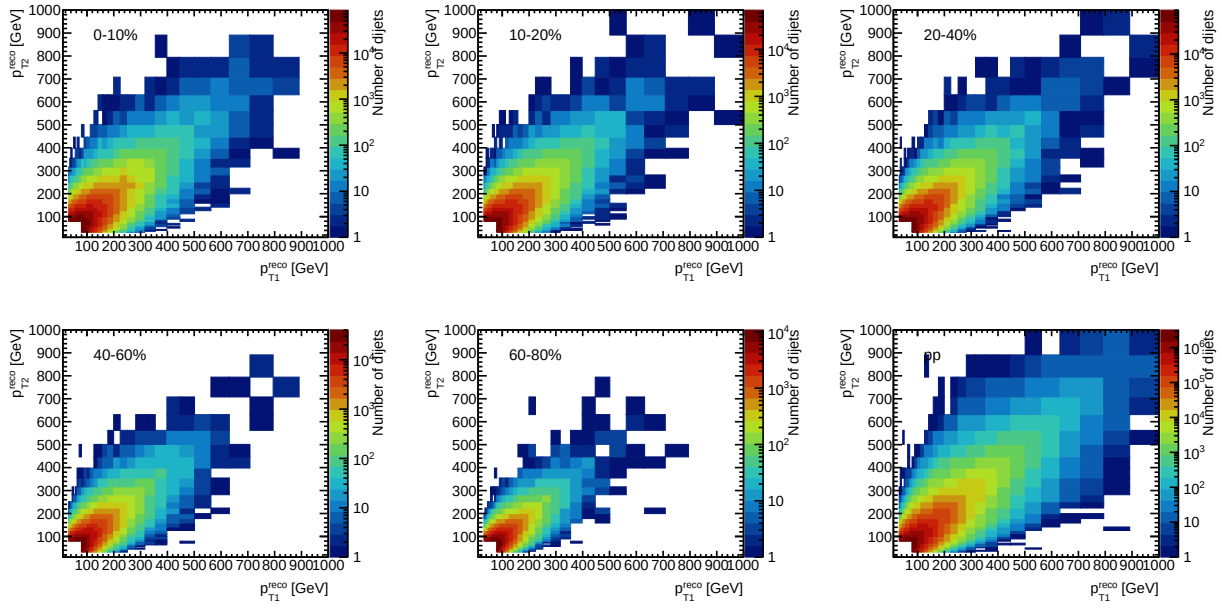

Figure 4.3: Measured $(p_{\mathrm{T},1}^{\mathrm{reco}}, p_{\mathrm{T},2}^{\mathrm{reco}})$ distributions for $R = 0.2$ jets in Pb+Pb collisions of various centralities and pp collisions.

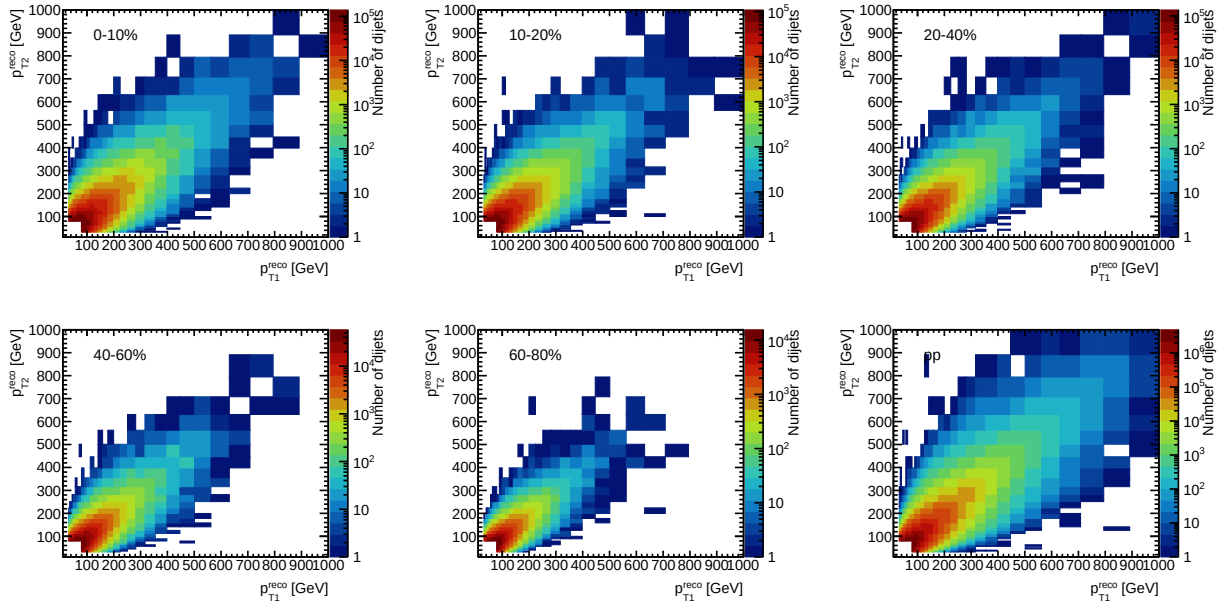

Figure 4.4: Measured $(p_{\mathrm{T},1}^{\mathrm{reco}}, p_{\mathrm{T},2}^{\mathrm{reco}})$ distributions for $R = 0.3$ jets in Pb+Pb collisions of various centralities and pp collisions.

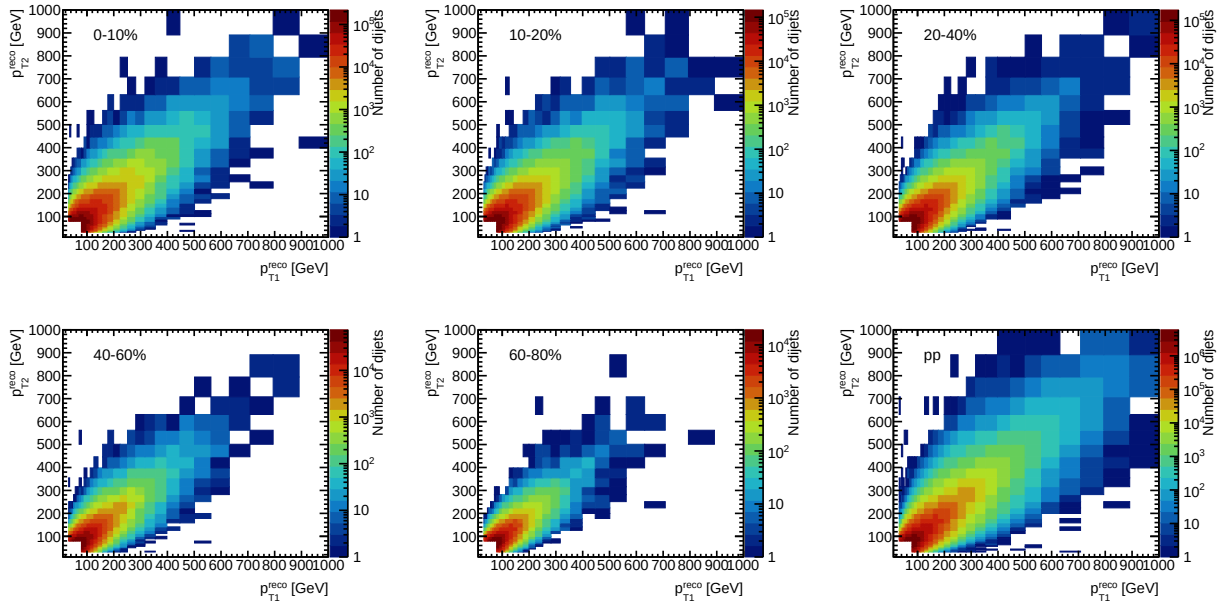

Figure 4.5: Measured $(p_{\mathrm{T},1}^{\mathrm{reco}}, p_{\mathrm{T},2}^{\mathrm{reco}})$ distributions for $R = 0.4$ jets in Pb+Pb collisions of various centralities and pp collisions.

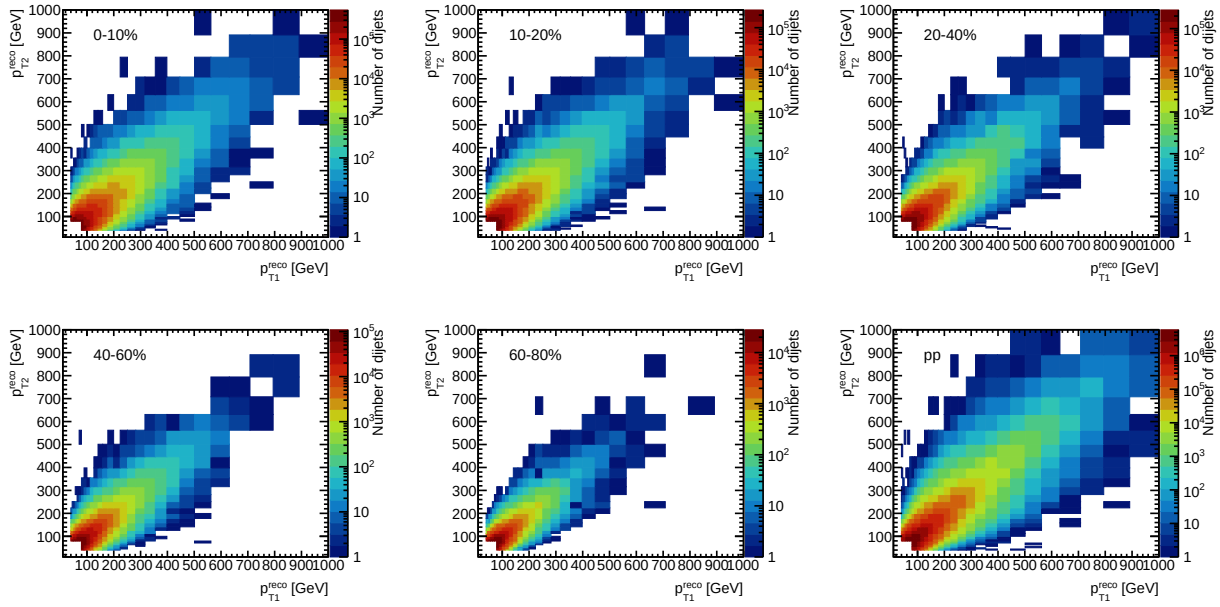

Figure 4.6: Measured $(p_{\mathrm{T},1}^{\mathrm{reco}}, p_{\mathrm{T},2}^{\mathrm{reco}})$ distributions for $R = 0.5$ jets in Pb+Pb collisions of various centralities and pp collisions.

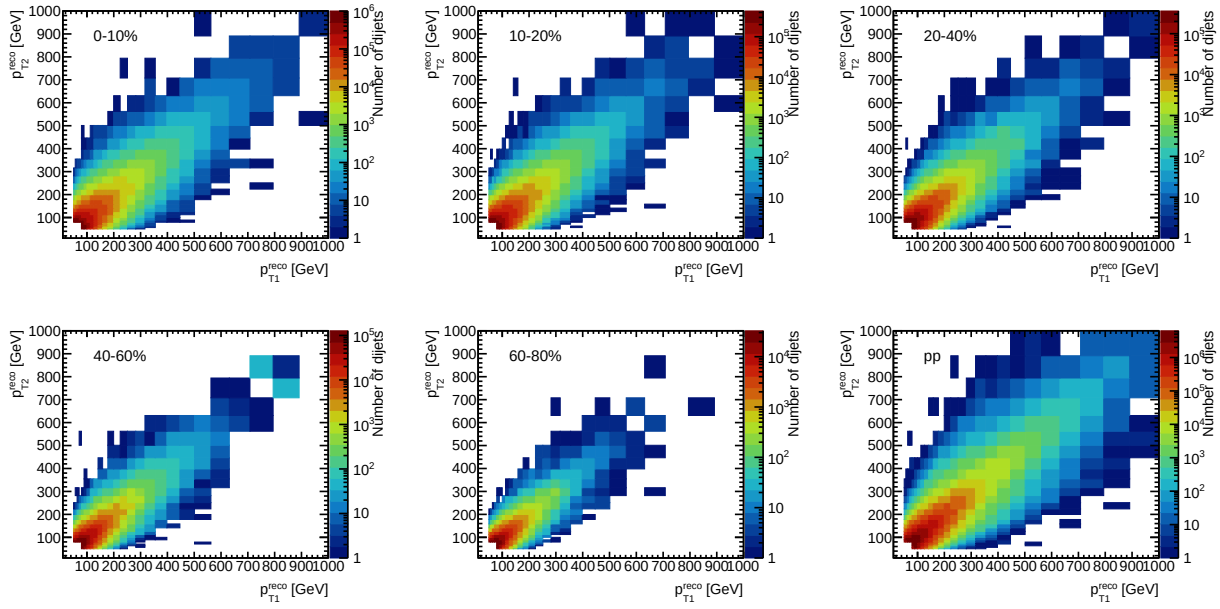

Figure 4.7: Measured $(p_{\mathrm{T},1}^{\mathrm{reco}}, p_{\mathrm{T},2}^{\mathrm{reco}})$ distributions for $R = 0.6$ jets in Pb+Pb collisions of various centralities and pp collisions.

4.2.2 Combinatoric dijet subtraction and efficiency correction

The measured $(p_{\mathrm{T},1}^{\mathrm{reco}}, p_{\mathrm{T},2}^{\mathrm{reco}})$ distributions have a contribution from both the real dijets and a background of pairs of uncorrelated jets, called combinatoric dijets, that arise from UE fluctuations. To correct for the effects of the combinatoric dijets, a subtraction and an efficiency correction were applied.

In order to remove the combinatoric dijets, a $|\phi_1 - \phi_2|$ sideband method was used. The contribution from combinatoric dijets is largely independent of $|\phi_1 - \phi_2|$ because the UE subtraction accounts for the azimuthal anisotropy due to hydrodynamic flow up to the fourth order modulation. The combinatoric dijet yield was obtained for each $(p_{\mathrm{T},1}^{\mathrm{reco}}, p_{\mathrm{T},2}^{\mathrm{reco}})$ bin for dijets with $1 < |\phi_1 - \phi_2| < 1.4$. This $1 < |\phi_1 - \phi_2| < 1.4$ region was chosen because it is away from the $|\phi_1 - \phi_2| > 7\pi/8$ signal band dominated by real dijets, and because it is away from the $|\phi_1 - \phi_2| < 0.5$ region where jet splittings occur. This can be seen in Figures 4.8-4.12, which show the $|\phi_1 - \phi_2|$ distributions for the various jet radii. The combinatoric dijet yield was then scaled to the size of the signal band, with a factor of $(\pi/8)/0.4$, and it was subtracted from the measured $(p_{\mathrm{T},1}^{\mathrm{reco}}, p_{\mathrm{T},2}^{\mathrm{reco}})$ distribution bin-by-bin.

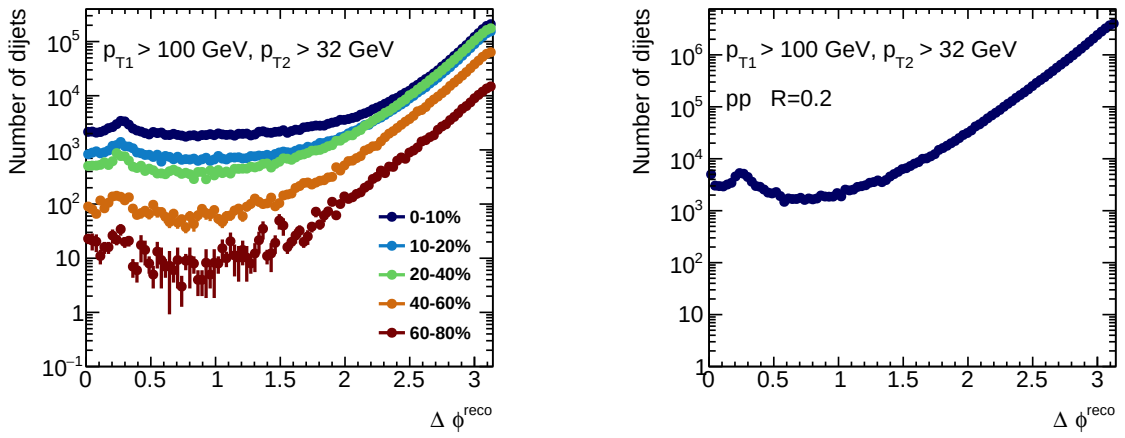

Figure 4.8: $|\phi_1 - \phi_2|$ distribution for $R = 0.2$ jets with $p_{\mathrm{T},1} > 100$ GeV, in Pb+Pb collisions of various centralities (left) and pp collisions (right).

The effect of combinatoric dijets is the strongest in the 0–10% central Pb+Pb data at low $p_{\mathrm{T},1}^{\mathrm{reco}}$. In the most central collisions, before the subtraction, combinatoric dijets constitute 2% of the $R = 0.2$ dijets with $p_{\mathrm{T},1}^{\mathrm{reco}} > 100$ GeV and $p_{\mathrm{T},2}^{\mathrm{reco}} > 32$ GeV, and 1% of the $R = 0.6$ dijets with $p_{\mathrm{T},1}^{\mathrm{reco}} > 158$ GeV and $p_{\mathrm{T},2}^{\mathrm{reco}} > 51$ GeV. The combinatoric dijet rate decreases with increasing $p_{\mathrm{T},1}^{\mathrm{reco}}$ and towards more peripheral events.

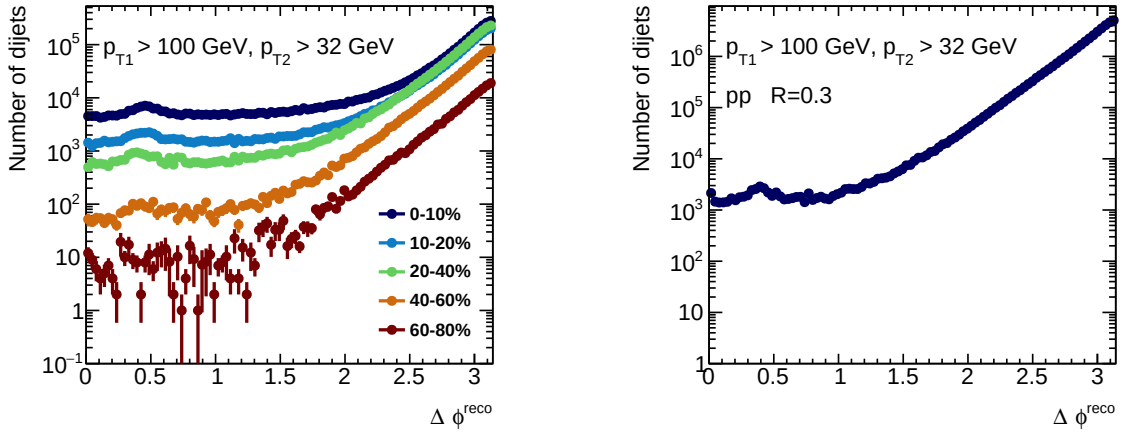

Figure 4.9: $|\phi_1 - \phi_2|$ distribution for $R = 0.3$ jets with $p_{T,1} > 100$ GeV, in Pb+Pb collisions of various centralities (left) and pp collisions (right).

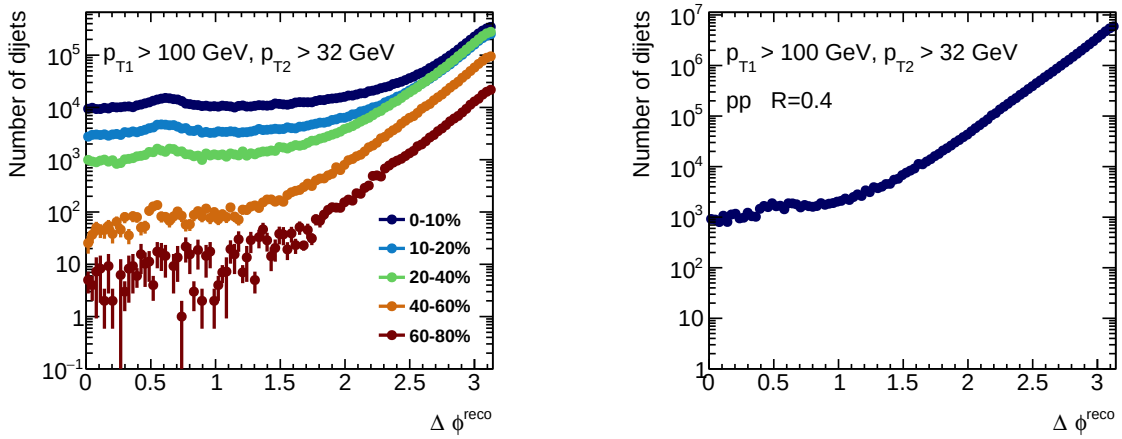

Figure 4.10: $|\phi_1 - \phi_2|$ distribution for $R = 0.4$ jets with $p_{T,1} > 100$ GeV, in Pb+Pb collisions of various centralities (left) and pp collisions (right).

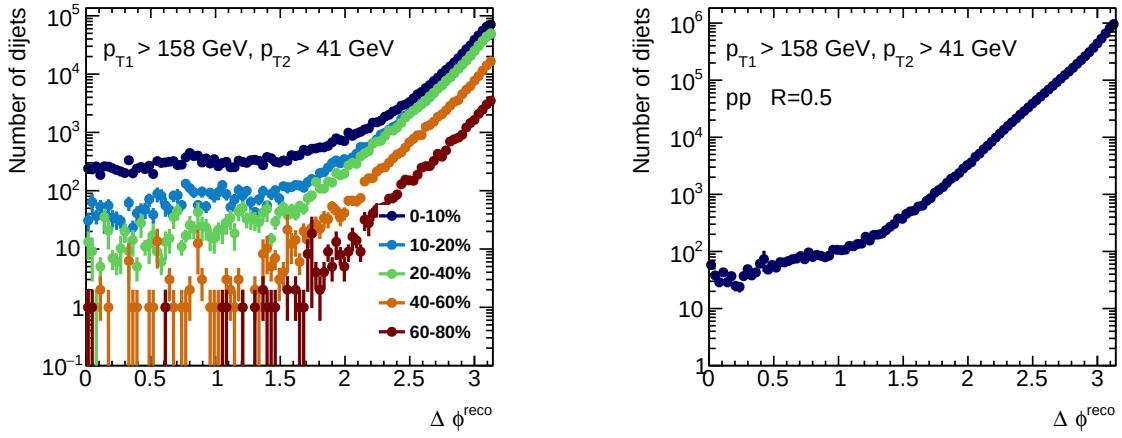

Figure 4.11: $|\phi_1 - \phi_2|$ distribution for $R = 0.5$ jets with $p_{T,1} > 100$ GeV, in Pb+Pb collisions of various centralities (left) and pp collisions (right).

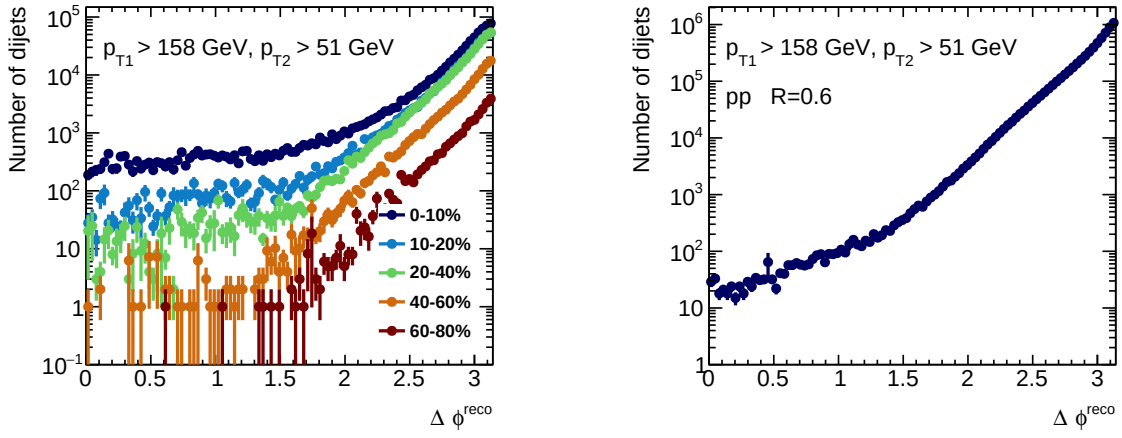

Figure 4.12: $|\phi_1 - \phi_2|$ distribution for $R = 0.6$ jets with $p_{T,1} > 100$ GeV, in Pb+Pb collisions of various centralities (left) and pp collisions (right).

In order to verify the combinatoric dijet subtraction, a cross check was done using the overlay sample. The check was to look at reconstructed combinatoric dijets for $R = 0.6$ jets, where the leading jet is matched to a true jet with truth $p_{\mathrm{T},1} > 79$ GeV and reconstructed $p_{\mathrm{T},1} > 158$ GeV, and the subleading jet is a reconstructed jet with $p_{\mathrm{T},2} > 51$ GeV which does not match a true jet. This allowed for the creation of a sample of the dominant contribution to the combinatoric jets that is subtracted in data, without any true dijets being included. As shown in Figure 4.13 for the two most central Pb+Pb collisions, a flat $|\phi_1 - \phi_2|$ distribution is observed between 1.0 and π for combinatoric jets, with only minor modulation observed in the most central collisions.

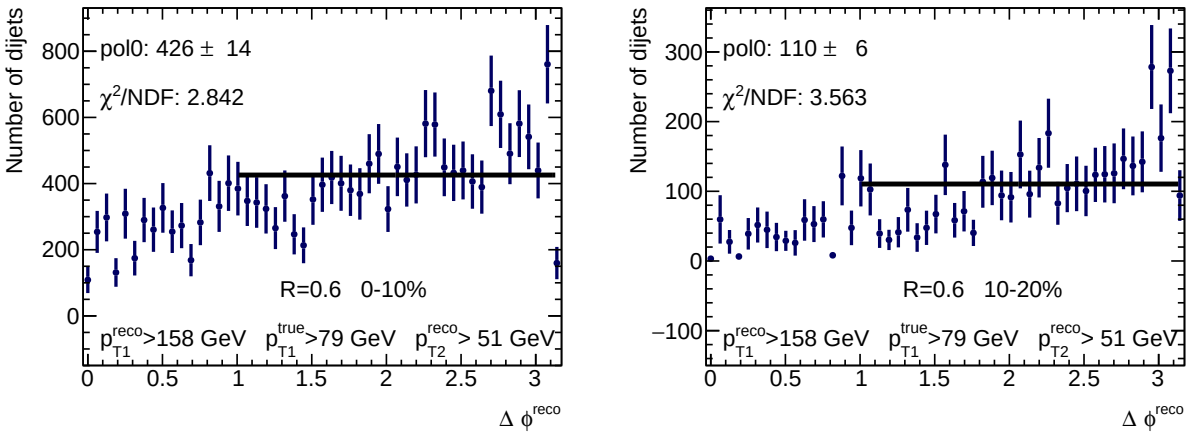

Figure 4.13: $|\phi_1 - \phi_2|$ distributions for $R = 0.6$ combinatoric dijets in the overlay for the two most central Pb+Pb collisions.

Another check was to apply the combinatoric subtraction in the overlay following the same procedure as in data. This study focused on $R = 0.6$ dijets in 0-10% central Pb+Pb collisions, with $158 < p_{\mathrm{T},1} < 178$ GeV where the combinatoric contribution is largest. The leading jet is a truth matched jet with truth $p_{\mathrm{T},1} > 70$ GeV and reconstructed $p_{\mathrm{T},1} > 79$ GeV, and the subleading jet is a reconstructed jet with $p_{\mathrm{T},2} > 51$ GeV for which no matching to truth is required. The result of this study is seen in Figure 4.14 where the x_{J} distributions are shown. In this figure, the "measured" sample corresponds to the two most energetic reconstructed jets in the event with $|\phi_1 - \phi_2| > 7\pi/8$ and $|\eta| < 2.1$, the "Subtracted" sample is the measured distribution with the combinatoric subtraction applied, and the "real" are the truth matched dijets. Closure is observed within the statistical uncertainties, with the subtracted x_{J} distribution matching the real x_{J} distribution.

When an uncorrelated third jet replaces a jet in a real dijet, the real dijet is lost and a combinatoric dijet is gained. Thus, in addition to the combinatoric background subtraction, an efficiency correction was applied to bring back the real dijet that was replaced by a combinatoric dijet.

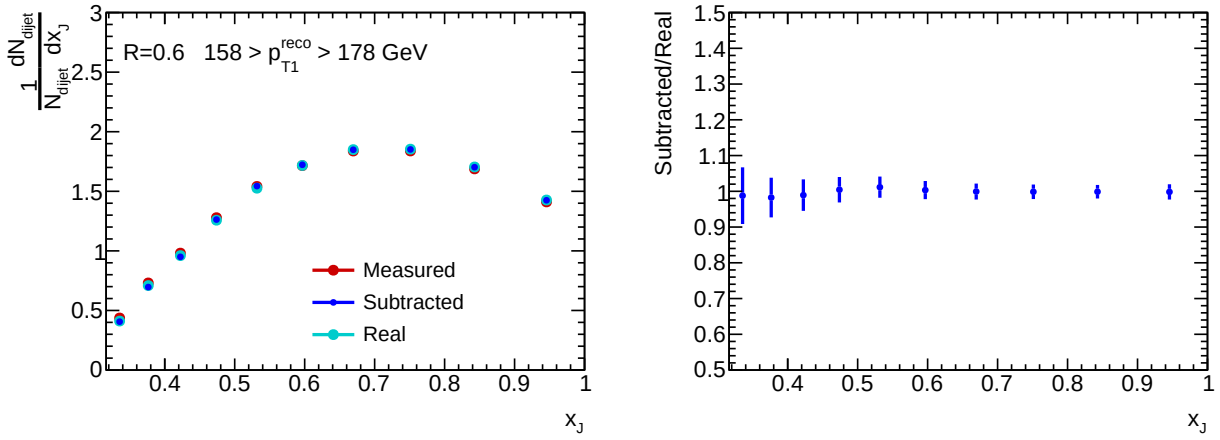

Figure 4.14: x_J distributions (left) for back-to-back $R = 0.6$ dijets in the 0-10% Pb+Pb overlay before and after applying the combinatoric subtraction, compared to the real distribution. The ratio (right) of the combinatoric subtracted x_J distribution to the real x_J distribution is also shown.

The yield $\frac{dn}{dp_{\mathrm{T}}}$ of reconstructed inclusive jets was measured in minimum-bias data, with the events being reweighted to match the FCal distribution of the triggered data used in the dijet measurement. The efficiency correction ϵ was derived from the jet yield using Poisson probabilities as:

$$\epsilon = e^{-\int_{p_{\mathrm{T}}}^{\infty} \frac{(\pi/8)}{2\pi} \frac{dn}{dp_{\mathrm{T}}} dp_{\mathrm{T}}} \tag{4.1}$$

Figures 4.15-4.18 show the minimum-bias jet p_{T} distribution and the corresponding efficiency obtained from Equation 4.1 as a functions of jet p_{T}, for the various jet radii and Pb+Pb centrality selections. The effect is most significant in the most central events and decreases rapidly with centrality. The inefficiency is larger for larger jet radius. The inverse of the shown efficiency was applied as an efficiency correction to the measured subleading jet distribution before unfolding.

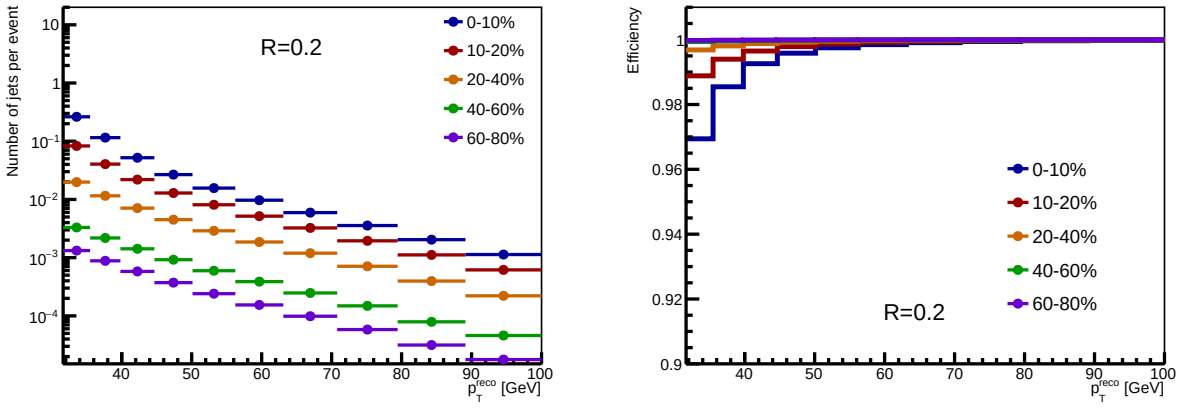

Figure 4.15: Minimum-bias jet p_{T} distributions (left) and efficiency correction (right) as a functions of jet p_{T}, for $R = 0.2$ jets in Pb+Pb collisions of various centralities.

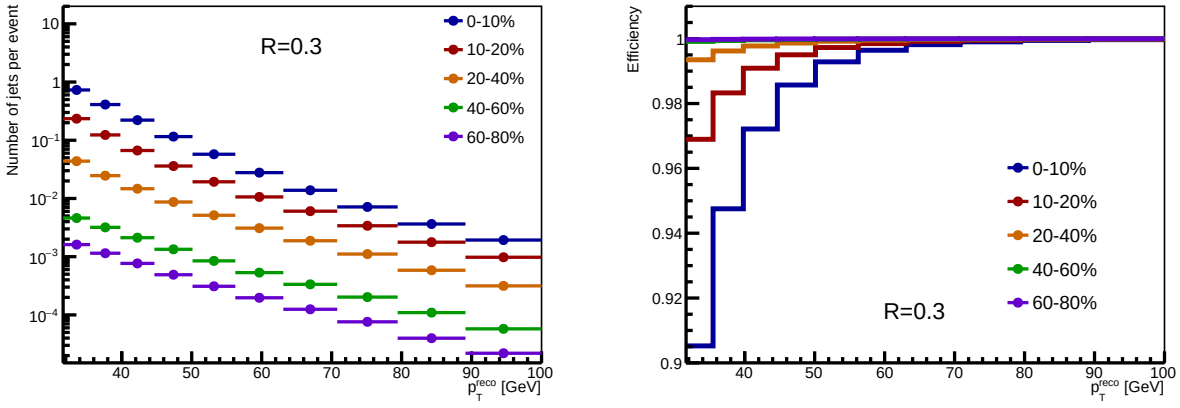

Figure 4.16: Minimum-bias jet p_{T} distributions (left) and efficiency correction (right) as a functions of jet p_{T}, for $R = 0.3$ jets in Pb+Pb collisions of various centralities.

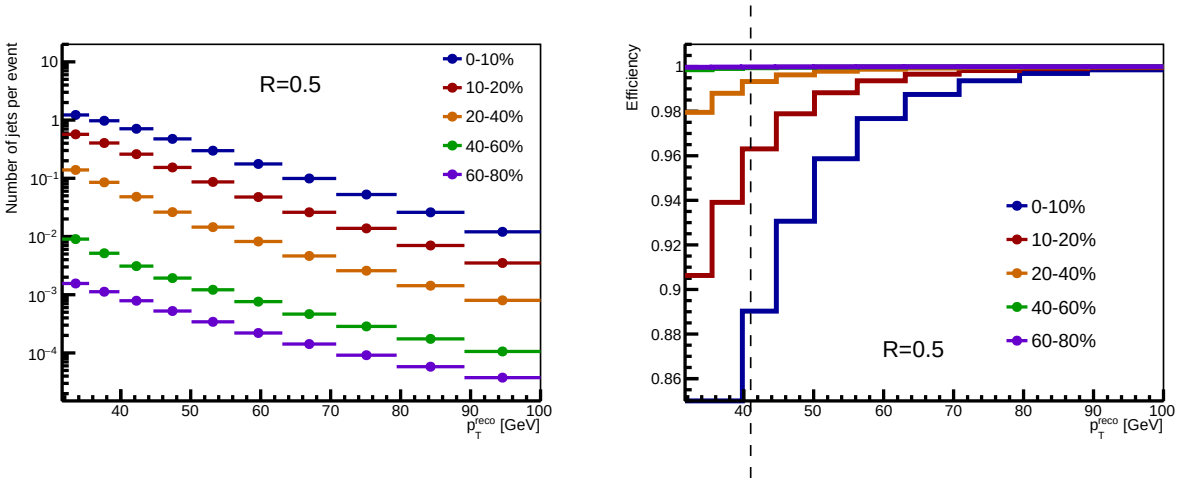

Figure 4.17: Minimum-bias jet p_{T} distributions (left) and efficiency correction (right) as a functions of jet p_{T}, for $R = 0.5$ jets in Pb+Pb collisions of various centralities. The vertical line represents the minimum p_{T} used for these jets

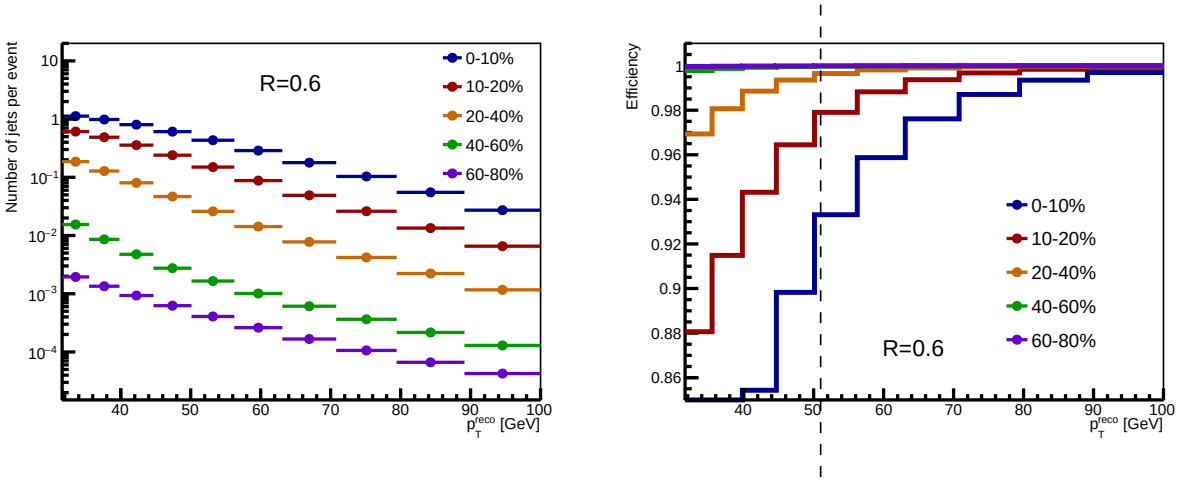

Figure 4.18: Minimum-bias jet p_{T} distributions (left) and efficiency correction (right) as a functions of jet p_{T}, for $R = 0.6$ jets in Pb+Pb collisions of various centralities. The vertical line represents the minimum p_{T} used for these jets.

4.2.3 Unfolding

The measured $(p_{\mathrm{T},1}^{\mathrm{reco}}, p_{\mathrm{T},2}^{\mathrm{reco}})$ distributions were unfolded in order to correct for the effects of the JES and JER: bin migration of both the leading and the subleading jet p_{T}, and possible swapping of the leading and subleading jet. The unfolding used the iterative Bayesian procedure [107] implemented in the RooUnfold [108] software package. The unfolding was two-dimensional, in leading and subleading jet p_{T}.

Response matrices were constructed using the overlay sample, with the response matrices containing the relationship between truth-level dijets $(p_{\mathrm{T},1}^{\mathrm{truth}}, p_{\mathrm{T},2}^{\mathrm{truth}})$ and reconstructed dijets $(p_{\mathrm{T},1}^{\mathrm{reco}}, p_{\mathrm{T},2}^{\mathrm{reco}})$. The response matrices were populated symmetrically in $p_{\mathrm{T},1}$ and $p_{\mathrm{T},2}$, similar to the $(p_{\mathrm{T},1}^{\mathrm{reco}}, p_{\mathrm{T},2}^{\mathrm{reco}})$ distributions in data. Separate response matrices were generated for pp collisions as well as for each centrality selection in Pb+Pb collisions, and for each R value used in this analysis.

Reconstructed dijets were required to pass the same p_{T}, y, and $|\phi_1 - \phi_2|$ criteria as in data. Both jets were required to have $|y| < 2.1$ and to be back-to-back with $|\phi_1 - \phi_2| > 7\pi/8$. Reconstructed leading jets were required to have $p_{\mathrm{T},1}^{\mathrm{reco}} > 79$ GeV, based on the minimum p_{T} for which the triggers are fully efficient for the various jet radii. Reconstructed subleading jets were required to have $p_{\mathrm{T},2}^{\mathrm{reco}} > 32$ GeV for $R = 0.2, 0.3$ and 0.4 jets, $p_{\mathrm{T},2}^{\mathrm{reco}} > 41$ GeV for $R = 0.5$ jets, and $p_{\mathrm{T},2}^{\mathrm{reco}} > 51$ GeV for $R = 0.6$ jets. Reconstructed jets were matched to true jets with $\Delta R < 0.75R$.

True dijets were required to have $|\phi_1^{\mathrm{truth}} - \phi_2^{\mathrm{truth}}| > 7\pi/8$, with each jet being within $|y_{\mathrm{truth}}| < 2.1$. In order to account for migration from lower jet $p_{\mathrm{T}}^{\mathrm{reco}}$, the response matrices were populated with true jets down to a $p_{\mathrm{T},1}^{\mathrm{truth}}$ of 20 GeV and a $p_{\mathrm{T},2}^{\mathrm{truth}}$ of 10 GeV. True dijets that did not match a reconstructed dijet passing the selection criteria were accounted for by using an efficiency correction in the unfolding (different from the combinatoric dijet efficiency described in the previous section).

Reweighting The unfolding requires an assumption of an initial distribution, called the prior, which is similar to the measured distribution. The prior weights were given by the data to MC ratios of the $(p_{\mathrm{T},1}^{\mathrm{reco}}, p_{\mathrm{T},2}^{\mathrm{reco}})$ distributions. The response matrices were reweighted along the $p_{\mathrm{T},1}^{\mathrm{truth}}$ and $p_{\mathrm{T},2}^{\mathrm{truth}}$ axes by these prior weights. Figures 4.19–4.23 show the prior weights for the various jet radii and centralities in Pb+Pb collisions.

Statistical uncertainties The statistical uncertainties in the unfolded results were calculated by using the bootstrapping method outlined in Reference [109]. In this method, replicas of the data and MC were produced using weights given by a Poisson distribution with mean 1, and the statistical uncertainties were obtained from the standard deviation of the replicas. Applying this bootstrapping method is particularly important for the treatment of correlations among the jets in the same event. An example of such correlations is some small R jets being reconstructed as a single large R jet. The Poisson weights were assigned based on

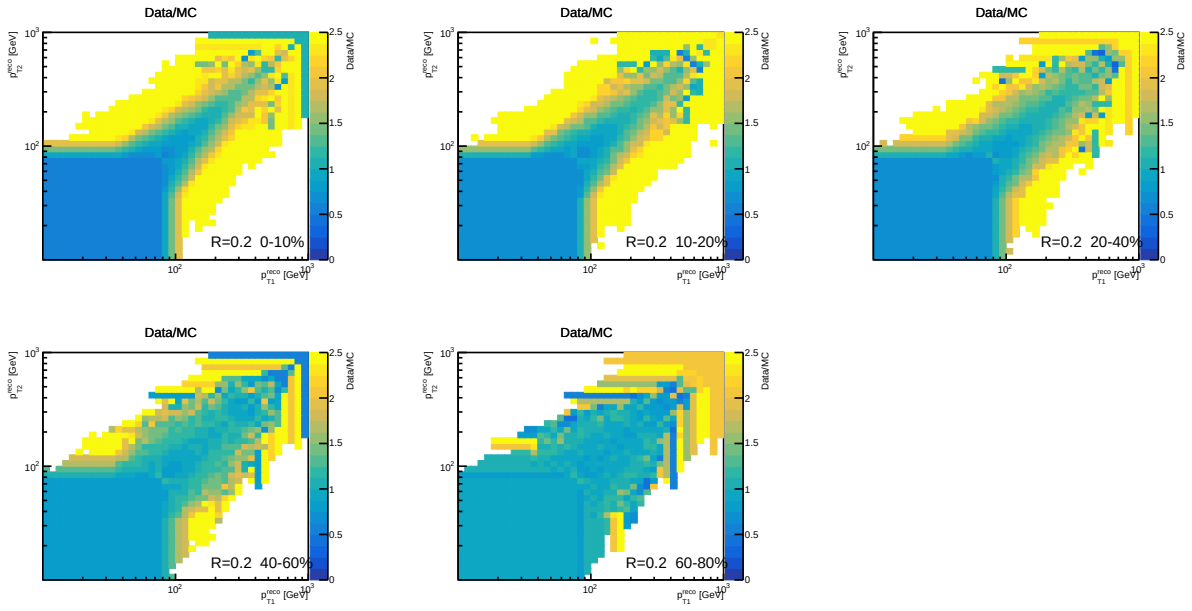

Figure 4.19: Data/MC weights for $R = 0.2$ jets in Pb+Pb collisions of various centralities.

the event number. Jets in the same event were given the same weight and are treated as correlated, whereas jets in different events were given different weights and treated as uncorrelated. For this analysis, 100 replicas of the data $(p_{\mathrm{T},1}^{\mathrm{reco}}, p_{\mathrm{T},2}^{\mathrm{reco}})$ distributions and 100 replicas of the response matrices were considered. The nominal data was unfolded with each of the response matrix replicas to obtain the statistical uncertainties of the MC. Similarly, each replica of the data was unfolded with the nominal response matrix to obtain the statistical uncertainties of the data. The total statistical uncertainties were obtained by adding the standard deviations of the data and MC replicas in quadrature.

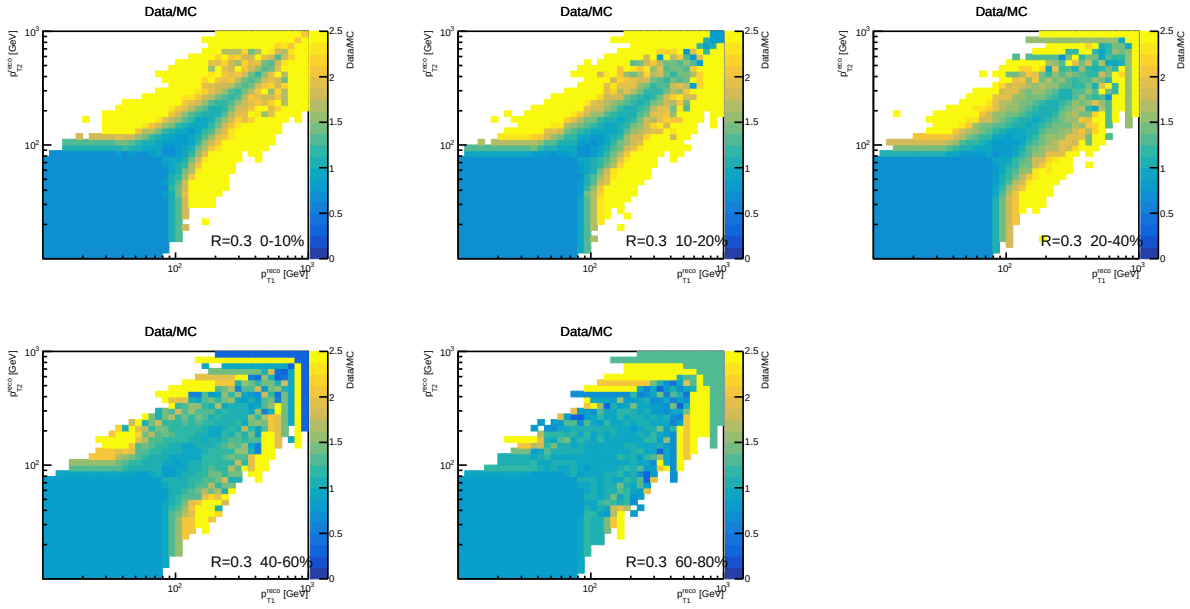

Figure 4.20: Data/MC weights for $R = 0.3$ jets in Pb+Pb collisions of various centralities.

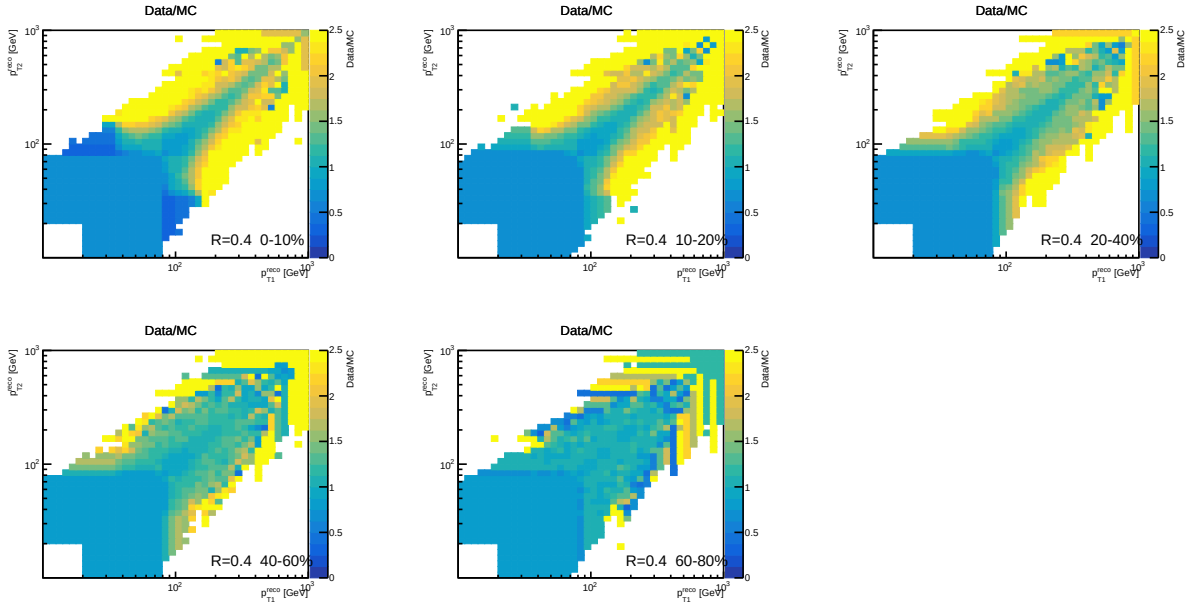

Figure 4.21: Data/MC weights for $R = 0.4$ jets in Pb+Pb collisions of various centralities.

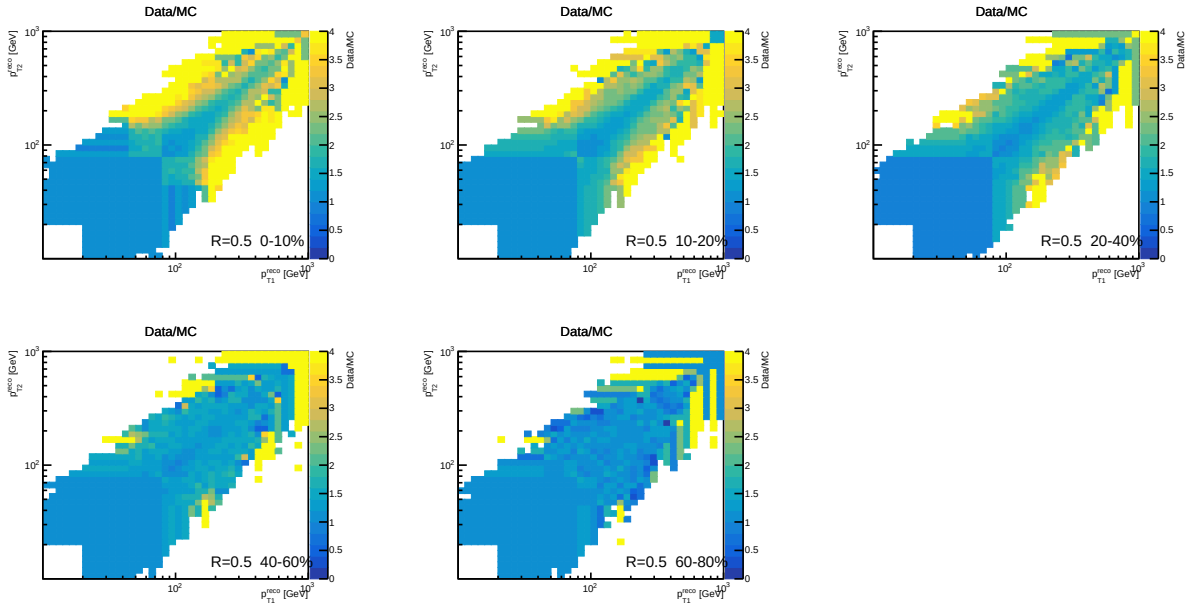

Figure 4.22: Data/MC weights for $R = 0.5$ jets in Pb+Pb collisions of various centralities.

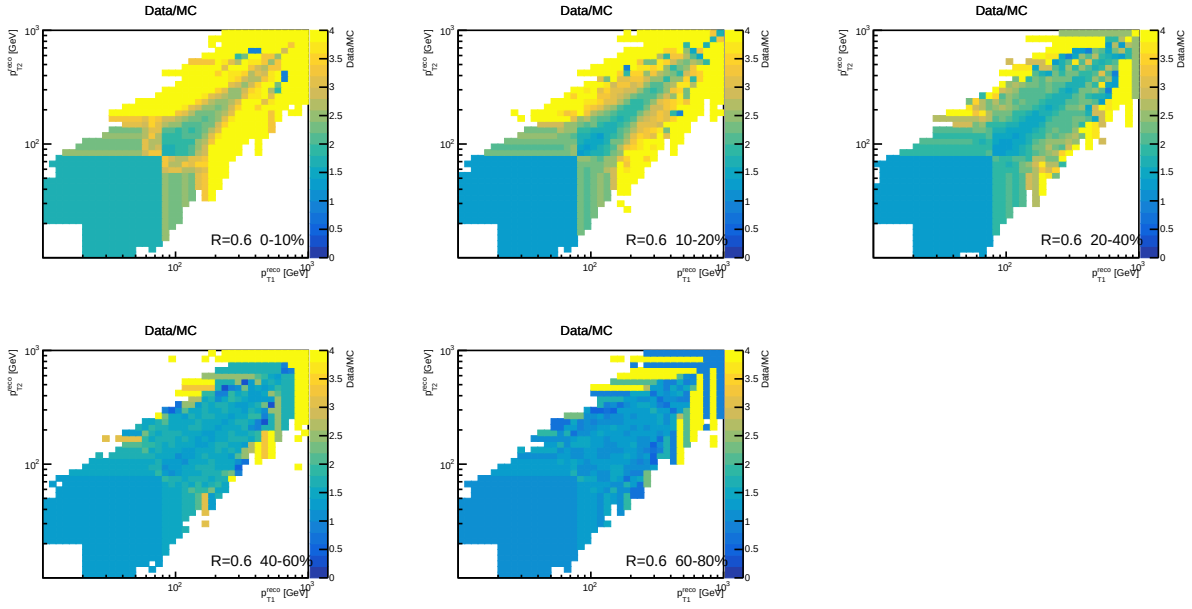

Figure 4.23: Data/MC weights for $R = 0.6$ jets in Pb+Pb collisions of various centralities.

Tuning the number of iterations The unfolding depends on the number of iterations used. The optimal number of iterations was obtained by balancing the statistical uncertainties and the unfolding convergence. The number of iterations was tuned separately for *pp* collisions and each centrality selection in Pb+Pb.

The statistical uncertainty σ_{stat} was obtained from the bootstrapping method. The unfolding convergence σ_{conv} was calculated as the absolute difference between iteration n and iteration $n-1$ of the unfolded x_{J} distribution. These two contributions were added in quadrature over all x_{J} and $p_{\text{T},1}$ bins, with the total σ_{total} being given by:

$$\sigma_{\text{total}} = \sqrt{\sigma_{\text{conv}}^2 + \sigma_{\text{stat}}^2} \tag{4.2}$$

Figures 4.24-4.27 show σ_{total} as a function of the number of iterations for the various jet radii in *pp* collisions and in Pb+Pb collisions of various centralities. The optimal number of iterations was obtained from minimizing σ_{total} as a function of the number of iterations. The values used in this analysis are shown in Table 4.4.

Centrality bin	0–10%	10–20%	20–40%	40–60%	60–80%	pp
Number of iterations for $R = 0.2$	3	3	3	2	2	3
Number of iterations for $R = 0.3$	4	3	3	2	2	3
Number of iterations for $R = 0.4$	6	4	4	4	4	4
Number of iterations for $R = 0.5$	6	6	4	2	2	5
Number of iterations for $R = 0.6$	7	6	6	2	2	7

Table 4.4: Optimal number of iterations used for the various jet radii in Pb+Pb collisions of various centralities and in *pp* collisions.

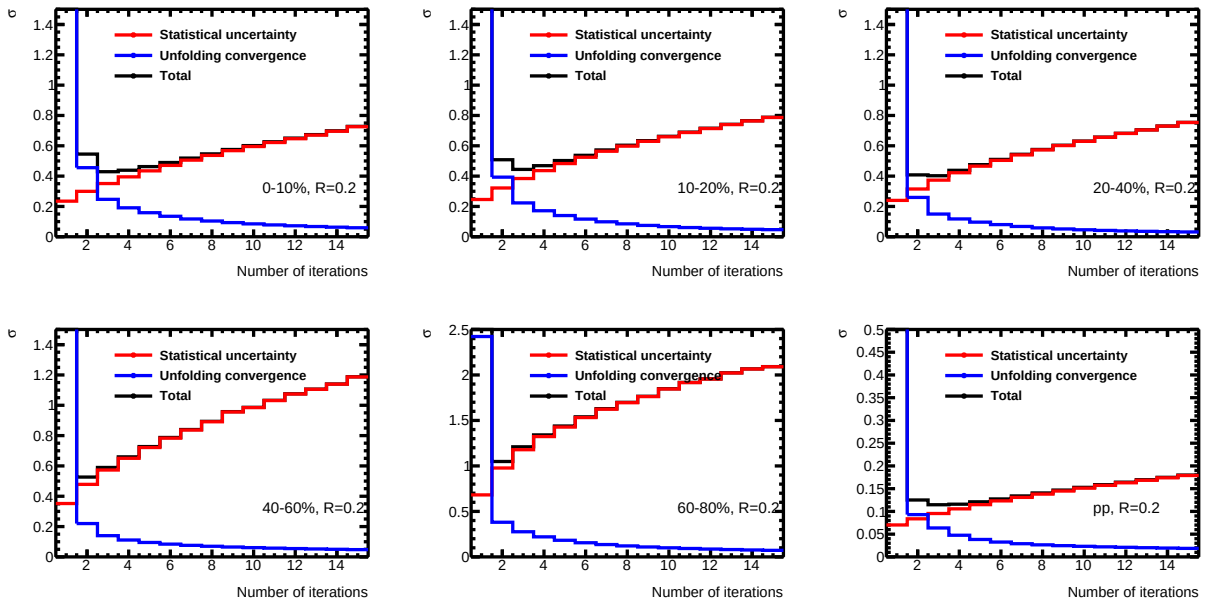

Figure 4.24: σ_{total} as a function of the number of iterations for $R = 0.2$ jets in pp collisions and in Pb+Pb collisions of various centralities.

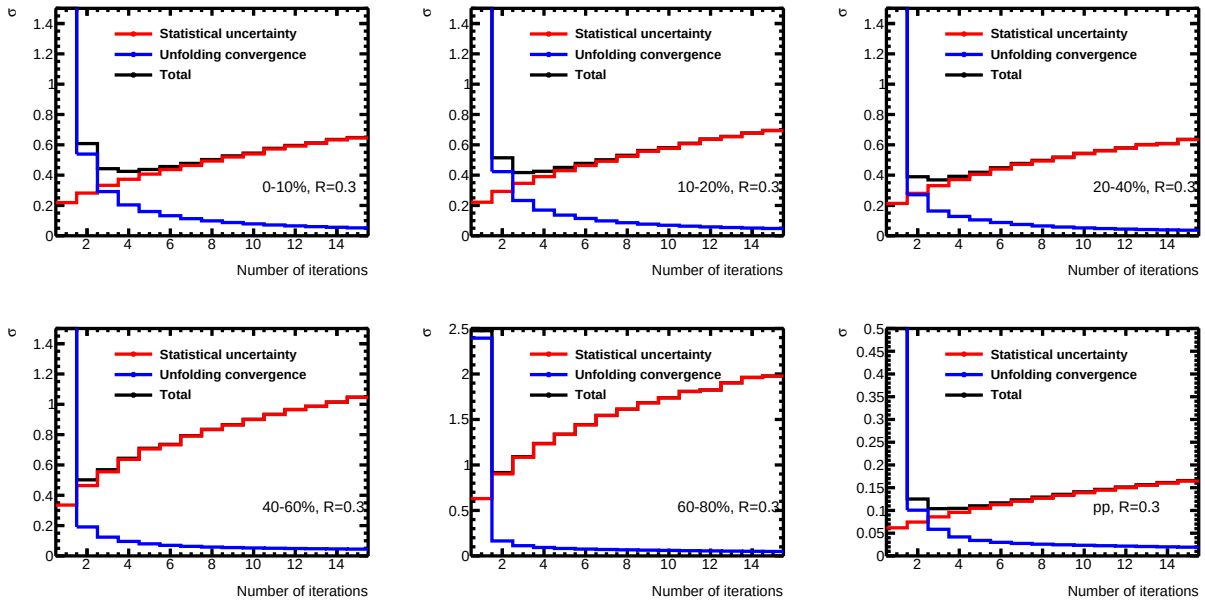

Figure 4.25: σ_{total} as a function of the number of iterations for $R = 0.3$ jets in pp collisions and in Pb+Pb collisions of various centralities.

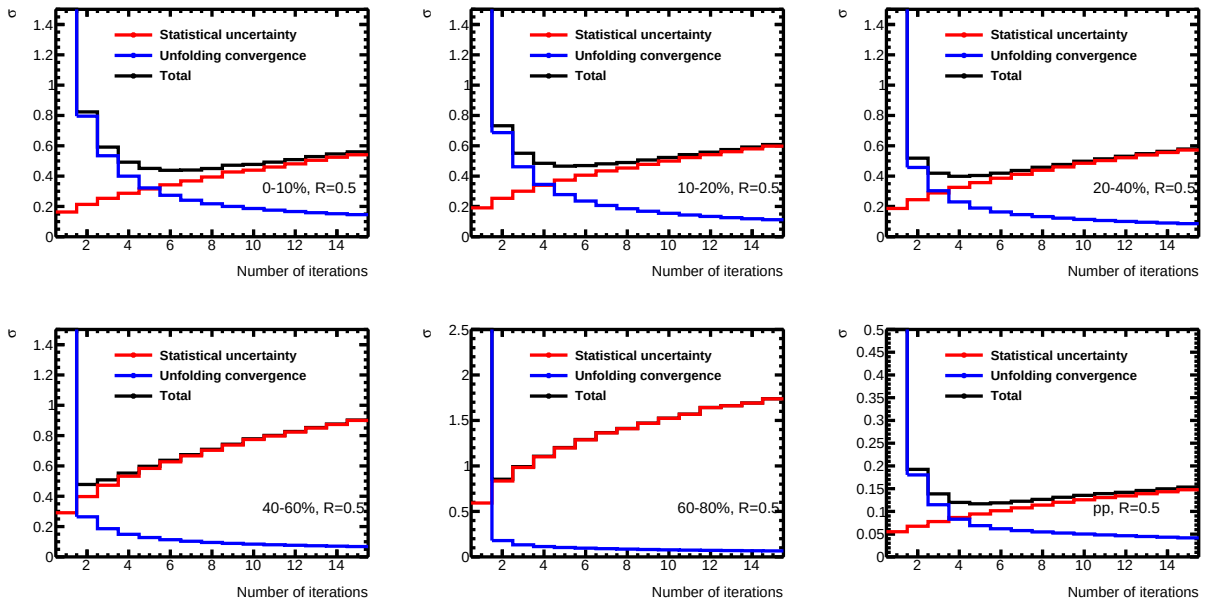

Figure 4.26: σ_{total} as a function of the number of iterations for $R = 0.5$ jets in pp collisions and in Pb+Pb collisions of various centralities.

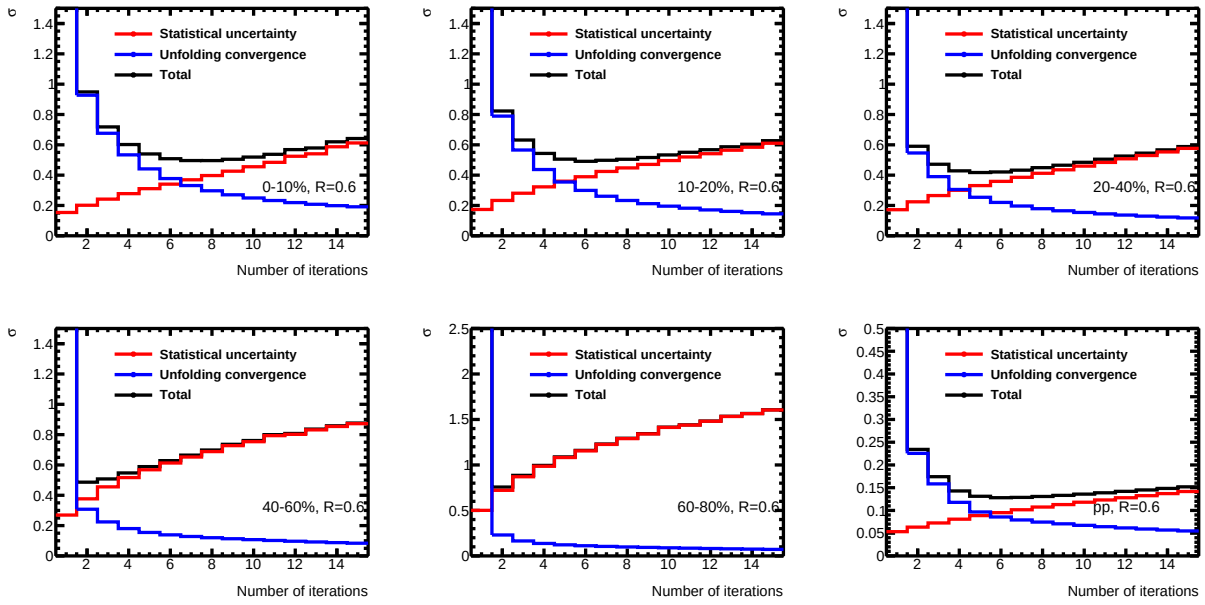

Figure 4.27: σ_{total} as a function of the number of iterations for $R = 0.6$ jets in pp collisions and in Pb+Pb collisions of various centralities.

The number of iterations is generally larger for the larger jets due to the worse JER. However, it is worth noticing that it also depends on the underlying distribution, which has a different shape for the various jet radii, and thus a different number of iterations is required to converge to the different shapes. This can be seen in Figure 4.28 for *pp* collisions, where the JER is similar for the various jet radii, but the shape and optimal number of iterations is different. An analogous plot for 0–10% central Pb+Pb collisions is shown in Figure 4.29.

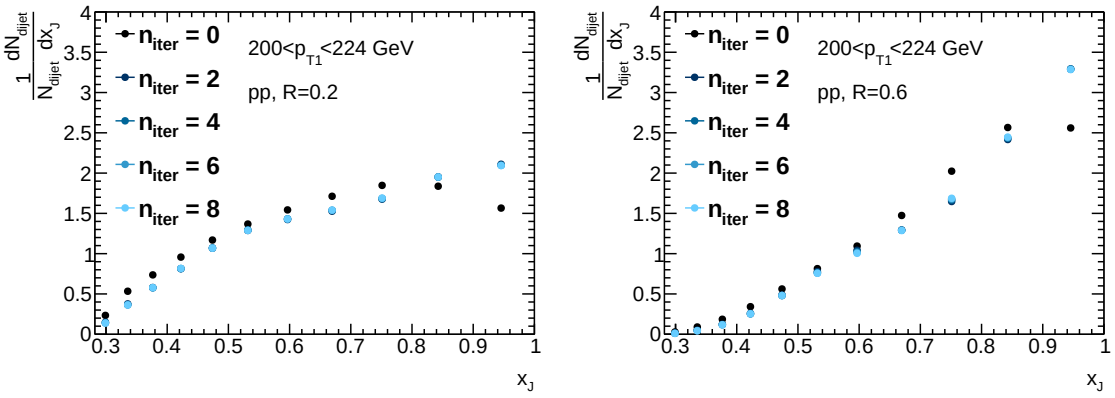

Figure 4.28: Self normalized x_J distributions in *pp* collisions, before unfolding and unfolded with different number of iterations, for the $R = 0.2$ (left) and $R = 0.6$ (right) jets.

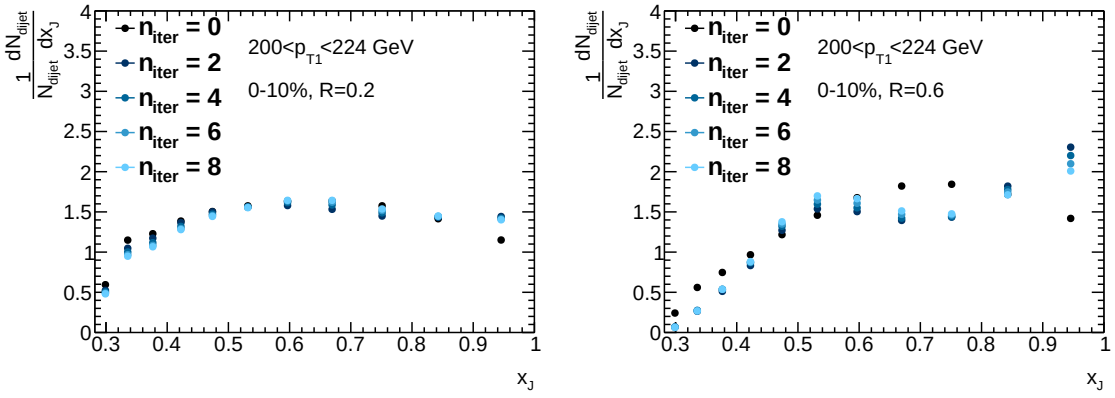

Figure 4.29: Self normalized x_J distributions in 0–10% Pb+Pb collisions, before unfolding and unfolded with different number of iterations, for the $R = 0.2$ (left) and $R = 0.6$ (right) jets.

Closure Self-closure and half-closure tests were done in order to verify that the unfolding can undo the JES and JER effects and extract the true underlying distributions.

In the self-closure test, the same MC sample was used to generate the response matrix and to produce

fake data to unfold. In this case, it was observed that the ratio of the unfolded result to the underlying true distribution was identically one, for all centralities in Pb+Pb collisions and in pp collisions. The results of the self-closure test are shown in Figure 4.30 for $R = 0.6$ jets for selected $p_{\mathrm{T},1}$ bins in 0–10% Pb+Pb collisions, where perfect closure is observed. Similar results are obtained for other $p_{\mathrm{T},1}$ bins, centrality bins, and jet radii.

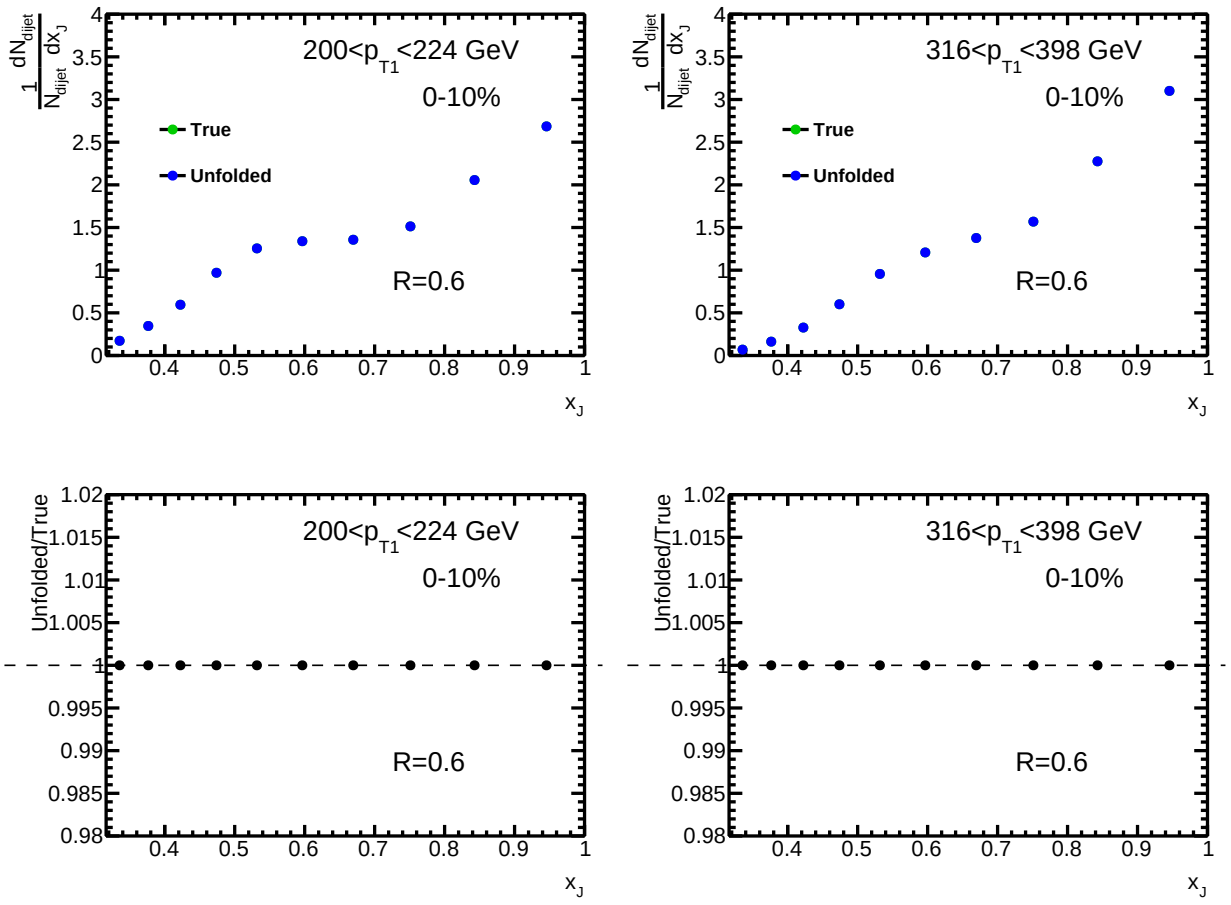

Figure 4.30: Self-closure test results. Unfolded and true self-normalized x_{J} distributions (top) for $R = 0.6$ jets in 0–10% Pb+Pb collisions, and the corresponding ratios of unfolded to true (bottom), for selected $p_{\mathrm{T},1}$ bins.

In the half-closure test, one half of the MC sample was used to generate the response matrix, and the other half of the MC was used as fake data to unfold. Unlike the self-closure test, the two samples are statistically independent. The results of the half-closure test are shown in Figure 4.31 for $R = 0.6$ jets for selected $p_{\mathrm{T},1}$ bins in 0–10% Pb+Pb collisions.

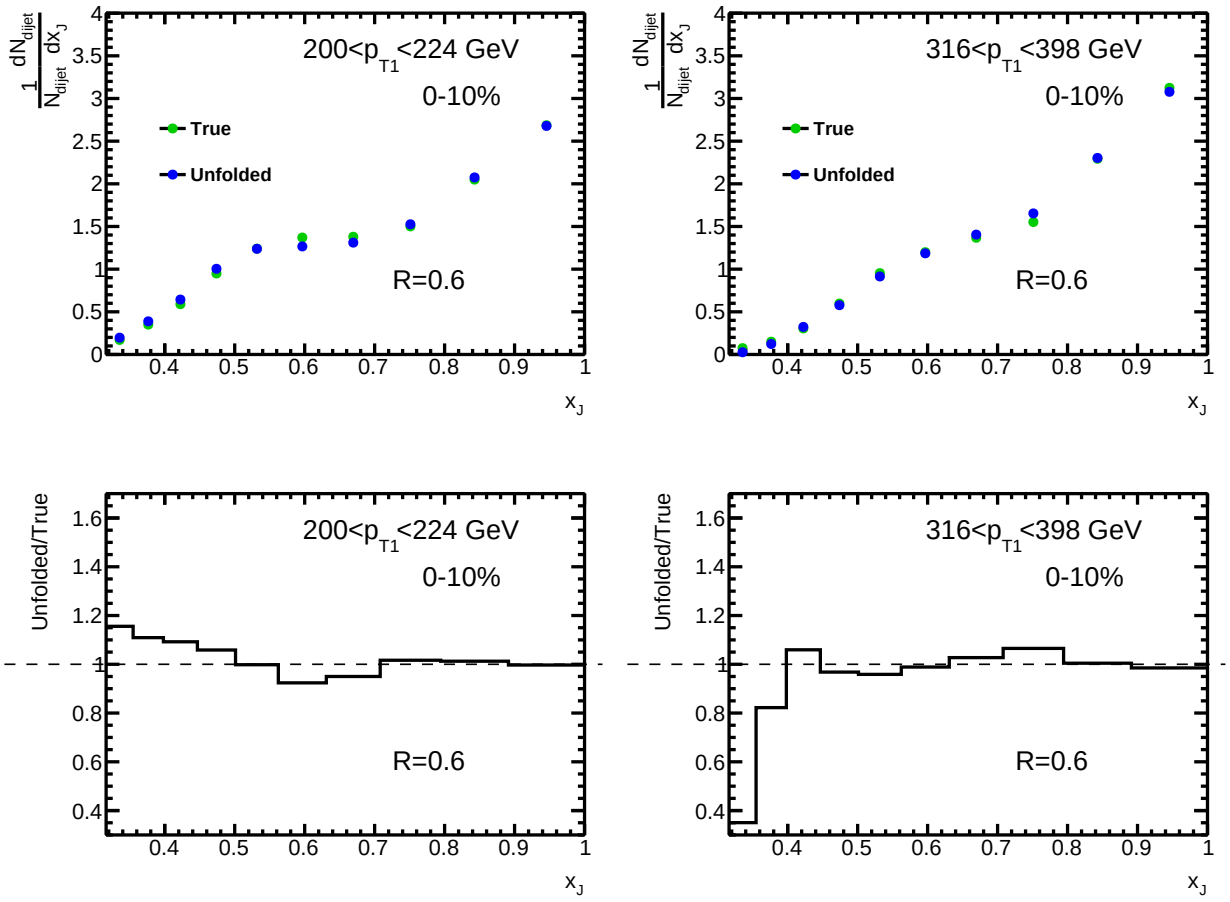

Figure 4.31: Half-closure test results. Unfolded and true self-normalized x_{J} distributions (top) for $R = 0.6$ jets in 0–10% Pb+Pb collisions, and the corresponding ratios of unfolded to true (bottom), for selected $p_{\mathrm{T},1}$ bins.

4.2.4 Extraction of observables

The $(p_{\mathrm{T},1}, p_{\mathrm{T},2})$ distributions are projected into bins of x_{J} in a scheme [38, 39, 110] that is shown in Figure 4.32. First, when the $(p_{\mathrm{T},1}, p_{\mathrm{T},2})$ distributions are constructed, they are symmetrized across the $p_{\mathrm{T},1} = p_{\mathrm{T},2}$ diagonal. The symmetric $(p_{\mathrm{T},1}, p_{\mathrm{T},2})$ distributions are then unfolded and unsymmetrized. Then, the counts in each $(p_{\mathrm{T},1}, p_{\mathrm{T},2})$ bin are divided by two, with each half corresponding to consecutive x_{J} bins. Finally, the counts per x_{J} bin are added up and used to build the x_{J} histogram, while applying the appropriate normalization. The statistical errors are propagated accordingly.

To obtain $R_{\mathrm{AA}}^{\mathrm{pair}}$, the unfolded and unsymmetrized $(p_{\mathrm{T},1}, p_{\mathrm{T},2})$ distributions are integrated over $p_{\mathrm{T},2}$ to obtain $R_{\mathrm{AA}}^{\mathrm{pair}}(p_{\mathrm{T},1})$, and over $p_{\mathrm{T},1}$ to obtain $R_{\mathrm{AA}}^{\mathrm{pair}}(p_{\mathrm{T},2})$. Additionally, the normalization of $R_{\mathrm{AA}}^{\mathrm{pair}}$ uses the values of listed in Table 4.1.

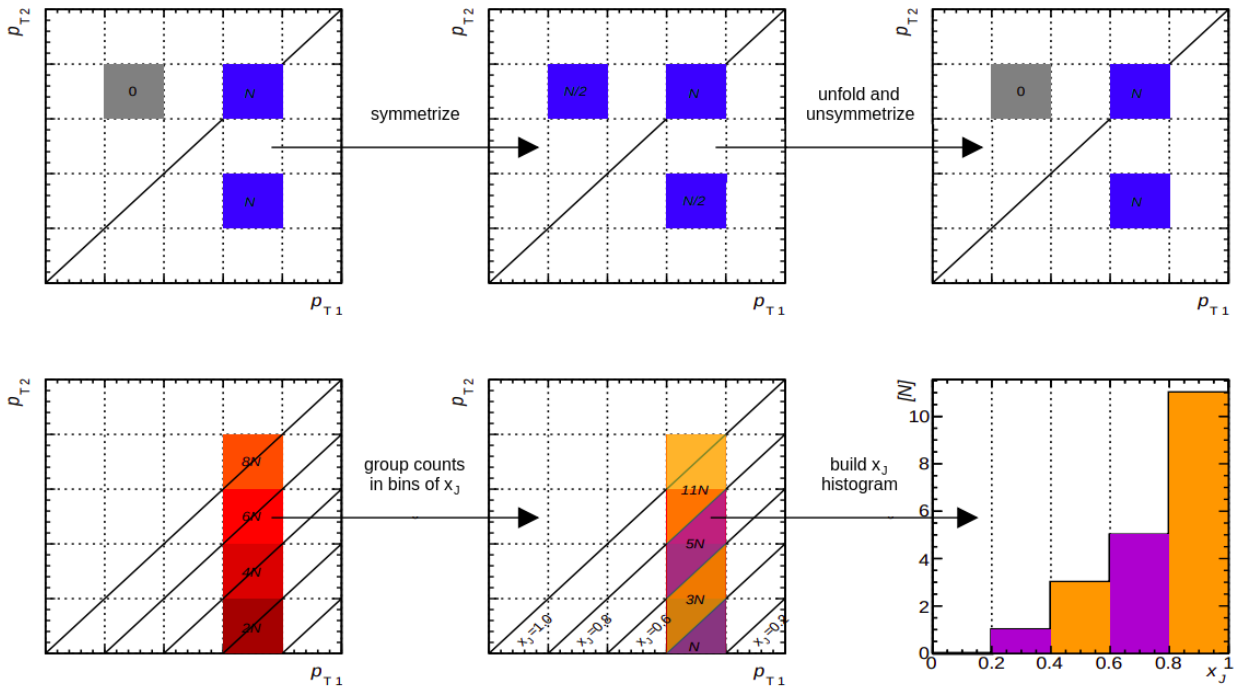

Figure 4.32: Diagram of the x_J projection scheme.

Centrality	$N_{\text{evt}}^{\text{AA}}$ (L_{pp})	$\langle T_{\text{AA}} \rangle$ $[mb^{-1}]$	$\delta\langle T_{\text{AA}} \rangle / \langle T_{\text{AA}} \rangle$ ($\delta L_{pp}/L_{pp}$)
0–10%	16.41 $\times 10^8$	23.35	0.87 %
10–20%	16.41 $\times 10^8$	14.33	1.0 %
20–40%	32.82 $\times 10^8$	6.79	2.4 %
40–60%	32.82 $\times 10^8$	1.96	4.8 %
60–80%	32.82 $\times 10^8$	0.394	8.2 %
pp	256.8 pb^{-1}	N/A	1.0 %

Table 4.5: Number of events in Pb+Pb collisions and luminosity in pp collisions, $\langle T_{\text{AA}} \rangle$ in Pb+Pb collisions and the corresponding uncertainties.

4.3 Systematic uncertainties

Systematic uncertainties in this measurement arise from these sources: the JES and JER; the unfolding, which has contributions from the choice of prior weight and the subleading jet p_{T} cut used; the combinatoric dijets, which has contributions from both the subtraction and the efficiency correction; and the global normalization. Each component is described in detail in the following sections.

4.3.1 Jet uncertainties

JES uncertainty The JES uncertainty has five components. The first component pertains to the calorimeter response in pp collisions at a center of mass energy $\sqrt{s} = 13$ TeV, where a centrality-independent component is obtained from *in situ* studies [111]. The second component corresponds to the difference in energy scale

between the jet reconstruction in this analysis and in 13 TeV pp collisions. This uses the cross-calibration procedure described in Reference [92], which is centrality-independent.

The third component pertains to the MC description of the relative abundances of jets initiated by quarks or gluons, as well as the corresponding detector responses. These centrality-independent flavor uncertainties were previously studied for $R = 0.2$ and $R = 0.4$ jets [39], so this analysis only focused on obtaining them for the remaining jet radii. PYTHIA 8 and HERWIG7 MC samples were used to obtain these uncertainties.

The flavor uncertainties consist of a flavor fraction uncertainty σ_R^{flavor} and a flavor response uncertainty σ_f^{flavor} given by:

$$\sigma_f^{\text{flavor}} = |(f_g^{\text{PYTHIA}} - f_g^{\text{HERWIG}})(R_g^{\text{PYTHIA}} - R_q^{\text{PYTHIA}})/\langle R^{\text{PYTHIA}}\rangle| \tag{4.3}$$

$$\sigma_R^{\text{flavor}} = |f_g^{\text{PYTHIA}}(R_g^{\text{PYTHIA}} - R_g^{\text{HERWIG}})| \tag{4.4}$$

where f_q and f_g are the fractions of quark and gluon jets in the MC samples, and R_g and R_q are the gluon and quark jet responses, respectively.

The flavor fractions and JES from PYTHIA 8 and HERWIG7 are shown in Figures 4.33–4.35 for $R = 0.3$, $R = 0.5$ and $R = 0.6$ jets. Gluon jets dominate at lower momentum, while quark jets are prevalent at high momentum. The detector response is generally better for gluon jets than for quark jets.

The flavor uncertainties are shown in Figure 4.36. The depletion at low p_{T} in the $R = 0.5$ and $R = 0.6$ flavor uncertainties comes from the uncertainty switching sign and crossing zero before taking the absolute value.

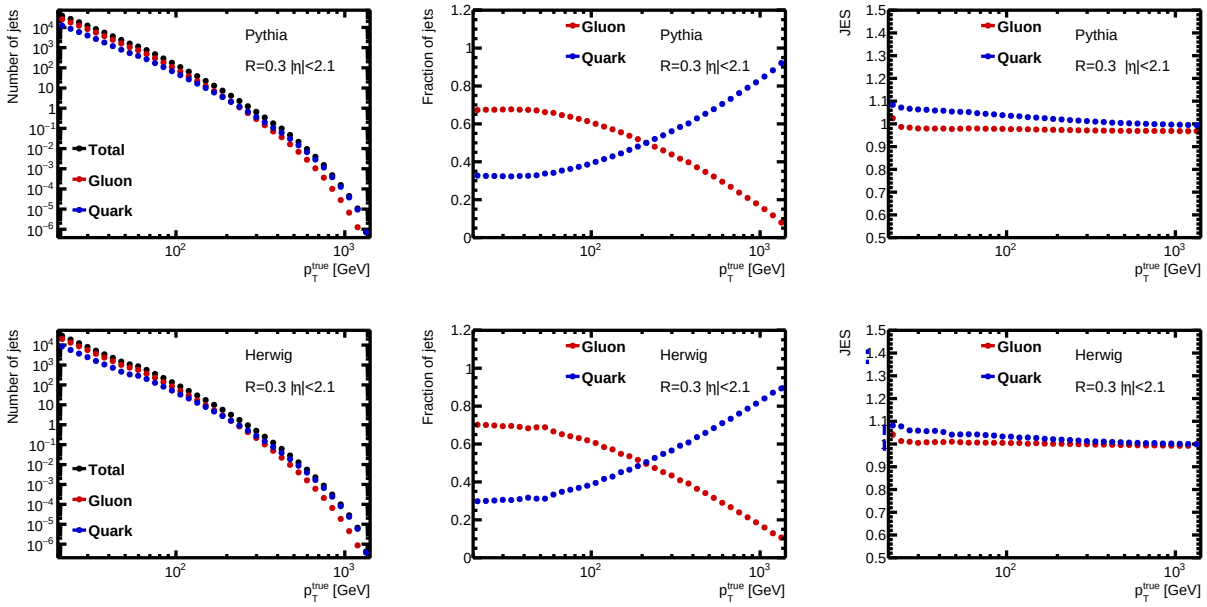

Figure 4.33: Flavor fractions and responses for $R = 0.3$ jets. (left) Number of quark (blue), gluon (red) and inclusive (black) jets as a function of p_T^{jet}. (middle) Fraction of quark (blue) and gluon (red) jets as a function of p_T^{jet}. (right) JES of quark (blue) and gluon (red) jets as a function of p_T^{jet}. The top row plots are from PYTHIA 8 and the bottom row plots are from HERWIG7.

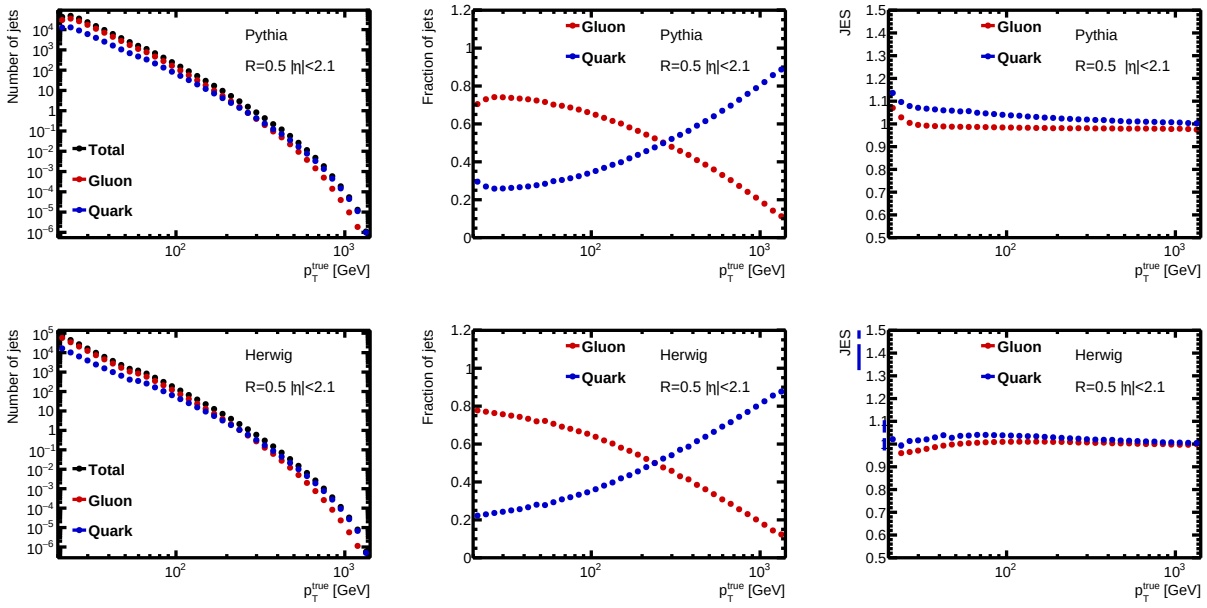

Figure 4.34: Flavor fractions and responses for $R = 0.5$ jets. (left) Number of quark (blue), gluon (red) and inclusive (black) jets as a function of p_T^{jet}. (middle) Fraction of quark (blue) and gluon (red) jets as a function of p_T^{jet}. (right) JES of quark (blue) and gluon (red) jets as a function of p_T^{jet}. The top row plots are from PYTHIA 8 and the bottom row plots are from HERWIG7.

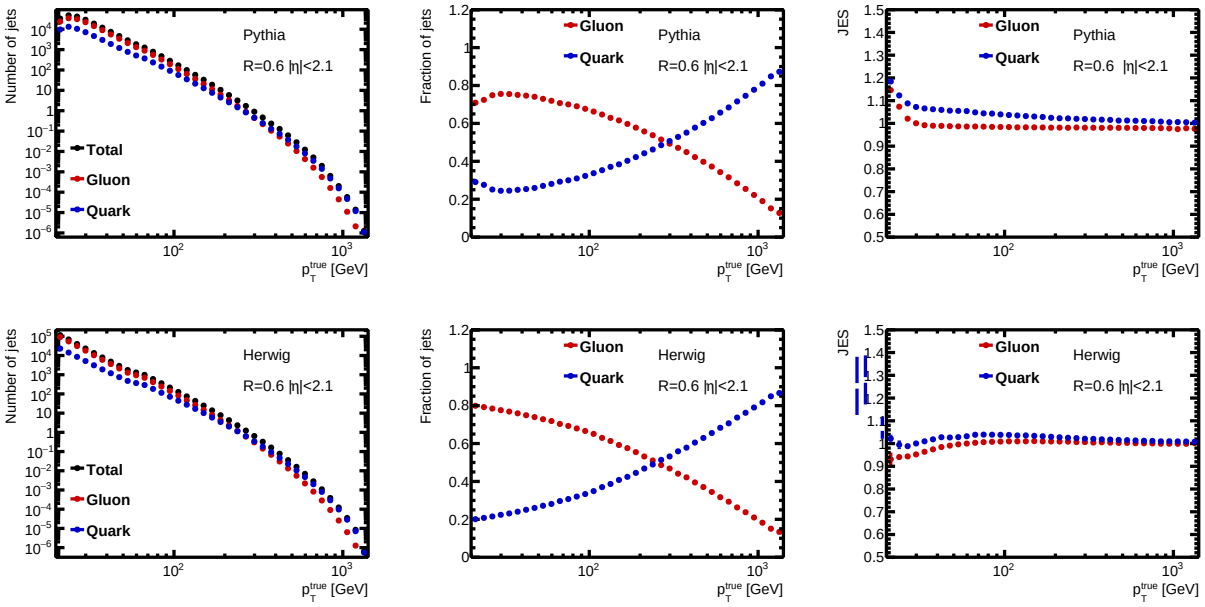

Figure 4.35: Flavor fractions and responses for $R = 0.6$ jets. (left) Number of quark (blue), gluon (red) and inclusive (black) jets as a function of $p_{\mathrm{T}}^{\mathrm{jet}}$. (middle) Fraction of quark (blue) and gluon (red) jets as a function of $p_{\mathrm{T}}^{\mathrm{jet}}$. (right) JES of quark (blue) and gluon (red) jets as a function of $p_{\mathrm{T}}^{\mathrm{jet}}$. The top row plots are from Pythia 8 and the bottom row plots are from Herwig7.

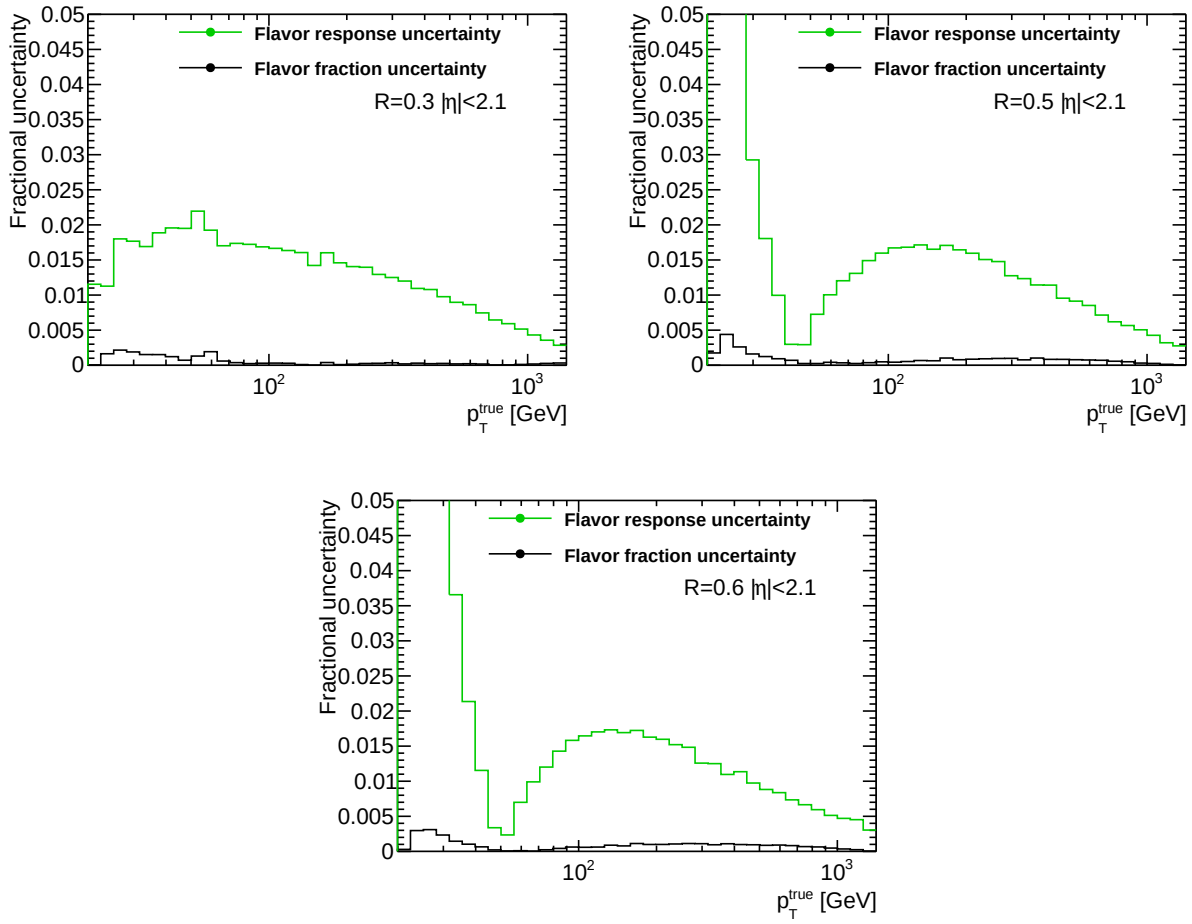

Figure 4.36: Flavor uncertainties for $R = 0.3$ (top left), $R = 0.5$ (top right), and $R = 0.6$ (bottom) jets. The flavor response uncertainty (green) and the flavor fraction uncertainties (black) are shown as a function of jet p_{T}.

The fourth component corresponds to the differences between data and MC. The differences come from the parton shower modifications due to jet quenching [112], which are not present in the MC and cause the detector response to be slightly different in data. This uncertainty is first evaluated by comparing the transverse momentum $p_{\mathrm{T}}^{\mathrm{jet}}$ of $R = 0.4$ jets, which is measured in the calorimeter, with the total momentum $p_{\mathrm{T}}^{\mathrm{track}}$ of charged particles inside the jet, which are measured as tracks in the inner detector. This is quantified by r_{trk} [92], which is defined as:

$$r_{\mathrm{trk}} = \frac{\sum p_{\mathrm{T}}^{\mathrm{track}}}{p_{\mathrm{T}}^{\mathrm{jet}}} \tag{4.5}$$

where tracks are required to have $p_{\mathrm{T}}^{\mathrm{track}} > 4$ GeV in order to exclude particles from the UE. Differences between the $r_{\mathrm{trk}}^{\mathrm{data}}$ in data and the $r_{\mathrm{trk}}^{\mathrm{MC}}$ in MC are then quantified by R_{trk}, which is defined as:

$$R_{\mathrm{trk}} = \frac{r_{\mathrm{trk}}^{\mathrm{data}}}{r_{\mathrm{trk}}^{\mathrm{MC}}} \tag{4.6}$$

This uncertainty is centrality-dependent but does not depend on $p_{\mathrm{T}}^{\mathrm{jet}}$ or η. The centrality-dependent component of this uncertainty is at most 1.25% in the most central collisions. The centrality-independent component adds an additional 0.5% uncertainty and accounts for differences between the 2018 peripheral Pb+Pb data and the 2017 pp data.

Finally, the fifth component corresponds to the jet radius dependence of the JES. A centrality-independent contribution is assessed by comparing the ratio of p_{T} for matched $R = 0.2$, $R = 0.3$, $R = 0.5$, and $R = 0.6$ jets with $R = 0.4$ jets measured in data and the MC sample. For $R = 0.5$ and 0.6 jets, an additional centrality-dependent contribution accounts for differences with respect to the uncertainties derived for $R = 0.4$ jets. The response matrices were recomputed using the MC sample with a JES that was modified as a function of p_{T} and η by one standard deviation.

JER uncertainty The uncertainty due to the JER was evaluated by repeating the unfolding procedure with modified response matrices, where an additional contribution is added to the resolution of the reconstructed p_{T} in the MC sample using a Gaussian smearing procedure. The smearing factor was evaluated using an *in situ* technique in 13 TeV pp data that involves studies of dijet p_{T} balance [113]. Further, an uncertainty was included to account for differences between the tower-based jet reconstruction and the jet reconstruction used in analyses of 13 TeV pp data, as well as differences in calibration procedures. Similarly to the JES, an additional uncertainty was assigned to the JER to account for differences between the $R = 0.4$ jets and the other jet radii. The modifications to the response were propagated through the unfolding and the resulting uncertainty was symmetrized.

4.3.2 Unfolding uncertainties

Prior sensitivity As described in Section 4.2.3, the response matrices were reweighted prior to unfolding by weights that are nominally given by the data/MC ratios of the $(p_{\mathrm{T},1}^{\mathrm{reco}}, p_{\mathrm{T},2}^{\mathrm{reco}})$ distributions. To assess the uncertainty associated to the choice of prior weights, an alternative set of weights was used, which are given by functions dependent on p_{T}, centrality, and jet radius. The deviation from the nominal result was symmetrized and taken as an uncertainty.

For 0–10% and 10–20% central Pb+Pb events, the alternative prior weights are given by:

$$w(p_{T,1}, p_{T,2}, \mathrm{cent}, \mathrm{R}) = \frac{0.4^2 + \mathrm{C_0(cent)}\left(\frac{\mathrm{p_{T,1}}}{100}\right)^3}{\left(\frac{\mathrm{p_{T,2}}}{\mathrm{p_{T,1}}} - \mathrm{C_1(R)}\right)^2 + \mathrm{C_0(cent)}\left(\frac{\mathrm{p_{T,1}}}{100}\right)^3} \times \left(\frac{1 - \frac{\mathrm{p_{T,2}}}{\mathrm{p_{T,1}}}}{1 + \mathrm{e}^{-(\mathrm{p_{T,1}}-120)/10}} + 0.1 + \frac{\mathrm{p_{T,2}}}{\mathrm{p_{T,1}}}\right) \tag{4.7}$$

For 20–80% central Pb+Pb events, the alternative prior weights are given by:

$$w(p_{T,1}, p_{T,2}, \mathrm{cent}, \mathrm{R}) = \frac{0.4^2 + \mathrm{C_0(cent)}\left(\frac{\mathrm{p_{T,1}}}{100}\right)^3}{\left(\frac{\mathrm{p_{T,2}}}{\mathrm{p_{T,1}}} - \mathrm{C_1(R)}\right)^2 + \mathrm{C_0(cent)}\left(\frac{\mathrm{p_{T,1}}}{100}\right)^3} \tag{4.8}$$

In pp collisions, the alternative prior weights are given by:

$$w(p_{T,1}, p_{T,2}, \mathrm{cent}, \mathrm{R}) = \frac{0.5^2 + \mathrm{C_0(cent)}\left(\frac{\mathrm{p_{T,1}}}{100}\right)^5}{\left(\frac{\mathrm{p_{T,2}}}{\mathrm{p_{T,1}}} - 0.5\right)^2 + \mathrm{C_0(cent)}\left(\frac{\mathrm{p_{T,1}}}{100}\right)^5} \tag{4.9}$$

The C_0 values for each centrality are shown in Table 4.6 and account for the centrality dependence to the modification. Note that even though Equations 4.7–4.9 and the C_0 values were applied in the same way for the various jet radii, this alternative weighting was actually different for each radii because the MC samples used to construct the response matrices were different. The C_1 values for each jet radius are shown in Table 4.7.

Centrality bin	C_0 values
0–10%	0.01
10–20%	0.01
20–40%	0.06
40–60%	0.1
60–80%	0.5
pp	0.5

Table 4.6: C_0 values used in Equations 4.7-4.9 to generate the alternative prior weights, for various Pb+Pb centrality bins and pp collisions.

The effect of the prior weights on the x_{J} distributions in the MC sample is shown in Figure 4.37 for $R = 0.2$ jets and in Figure 4.38 for $R = 0.6$ jets, both for 0–10% Pb+Pb collisions. The functions were chosen

R	C_1 values
0.2	0.25
0.3	0.25
0.4	0.5
0.5	0.3
0.6	0.3

Table 4.7: C_1 values used in Equations 4.7-4.9 to generate the alternative prior weights, for the various jet radii.

so that the nominal and alternative weights would give variations that enclose the raw data, as seen in these figures.

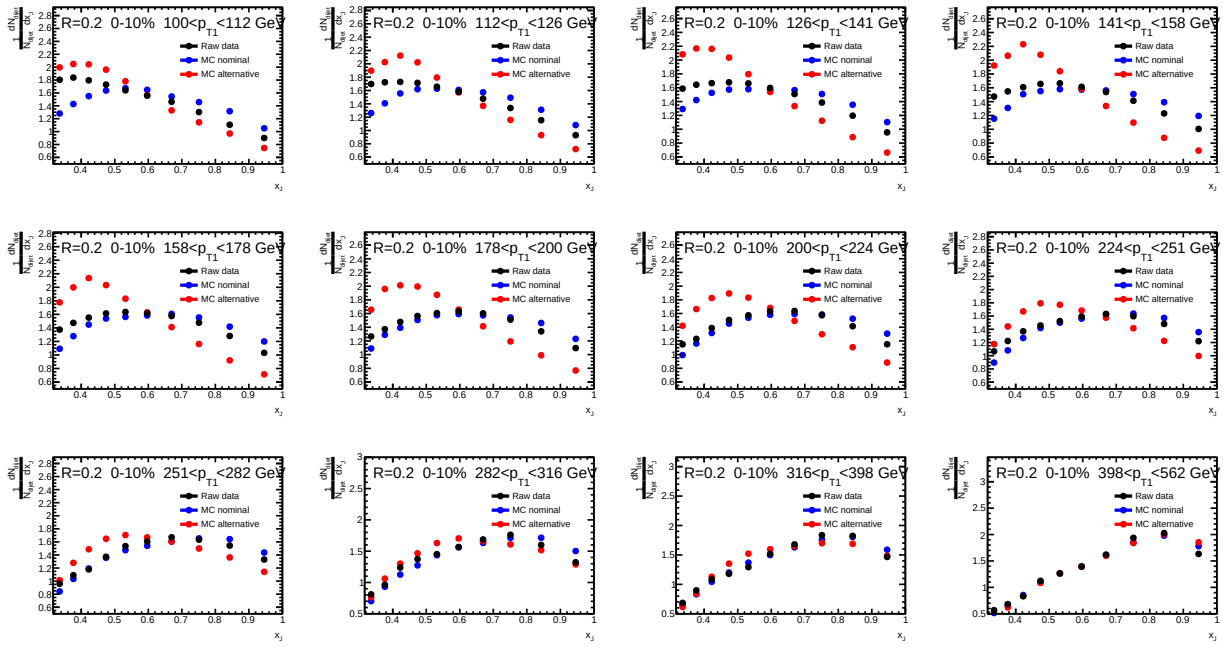

Figure 4.37: x_{J} distributions in MC using the nominal and alternative prior weights, for $R = 0.2$ jets in 0–10% Pb+Pb collisions and for various $p_{\mathrm{T},1}$ bins. For comparison, the x_{J} distributions in data before unfolding are also shown.

Jet selection The unfolding is sensitive to the minimum subleading jet $p_{\mathrm{T},2}^{\mathrm{reco}}$ used in the analysis. This is because at low momentum there can be contributions from the UE in the form of worse JER or fake jets, which can affect the unfolding. Nominally, the analysis was performed requiring subleading jets with $p_{\mathrm{T},2}^{\mathrm{reco}} > 32$ GeV for $R = 0.2, 0.3$ and 0.4 jets, $p_{\mathrm{T},2}^{\mathrm{reco}} > 41$ GeV for $R = 0.5$ jets, and $p_{\mathrm{T},2}^{\mathrm{reco}} > 51$ GeV for $R = 0.6$ jets. To assess the associated uncertainty, the analysis was repeated raising this transverse momentum threshold to $p_{\mathrm{T},2}^{\mathrm{reco}} > 39$ GeV for $R = 0.2, 0.3$ and 0.4 jets, $p_{\mathrm{T},2}^{\mathrm{reco}} > 51$ GeV for $R = 0.5$ jets, and $p_{\mathrm{T},2}^{\mathrm{reco}} > 63$ GeV for $R = 0.6$ jets. The deviation from the nominal result was symmetrized and taken as an uncertainty.

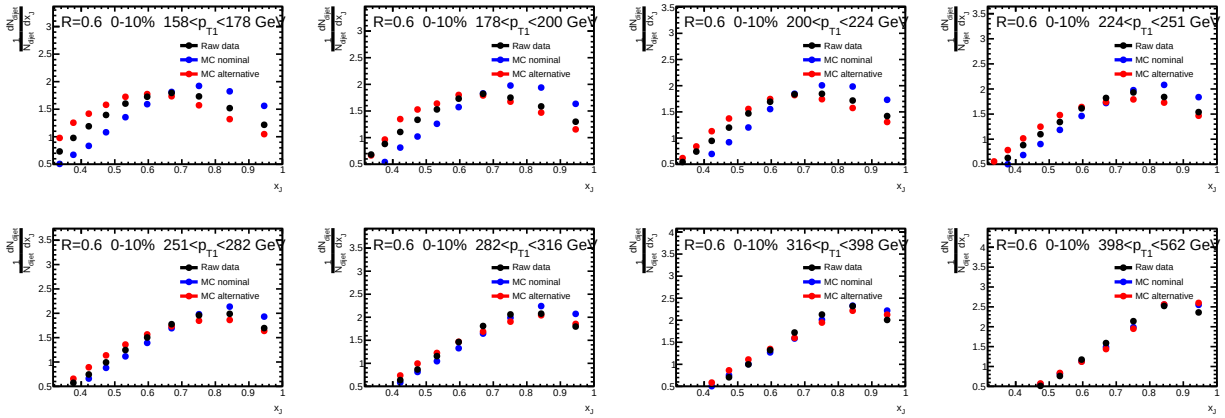

Figure 4.38: x_{J} distributions in MC using the nominal and alternative prior weights, for $R = 0.6$ jets in 0–10% Pb+Pb collisions and for various $p_{\mathrm{T},1}$ bins. For comparison, the x_{J} distributions in data before unfolding are also shown.

4.3.3 Combinatoric dijet uncertainties

The uncertainty related to the combinatoric dijets was evaluated for both the subtraction and the efficiency correction. Variations of the analysis were made for these two contributions separately as described below. The deviation from the nominal result was taken as the uncertainty contribution. Both of these contributions were found to be negligible compared to the other sources of systematic uncertainties.

Subtraction As discussed in Section 4.2.2, a nominal sideband of $1 < |\phi_1 - \phi_2| < 1.4$ was used to estimate the combinatoric dijet contribution in data and perform the combinatoric dijet subtraction. To evaluate the associated uncertainty, the analysis was repeated using an alternative sideband of $1.1 < |\phi_1 - \phi_2| < 1.5$.

Efficiency correction As discussed in Section 4.2.2, an efficiency correction was applied to correct for subleading jets that are superseded by a third uncorrelated jet. The associated uncertainty was evaluated by repeating the analysis without applying the efficiency correction.

4.3.4 Global uncertainties

The global uncertainties refer to the determination of the mean nuclear thickness function $\langle T_{\mathrm{AA}} \rangle$, and the pp luminosity. These uncertainties apply only to the absolutely normalized x_{J} distributions, the J_{AA} distributions, and the $R_{\mathrm{AA}}^{\mathrm{pair}}(p_{\mathrm{T},1})$ and $R_{\mathrm{AA}}^{\mathrm{pair}}(p_{\mathrm{T},2})$ distributions. They are independent of the jet transverse momentum. The $\langle T_{\mathrm{AA}} \rangle$ uncertainties are shown in Table 4.1, while the luminosity uncertainty in pp collisions is $\delta L_{\mathrm{pp}} = 1\%$ [114].

4.3.5 Total uncertainty

The systematic uncertainties of the absolutely-normalized x_{J} distributions for central Pb+Pb and pp collisions can be seen in Figure 4.39 for $R = 0.2$ jets and in Figure 4.40 for $R = 0.6$ jets. In central Pb+Pb collisions for $R = 0.2$ jets, the total uncertainties are driven by the JES and JER uncertainties; for $R = 0.6$ jets in these collisions, the total systematic uncertainties are largely driven by the unfolding's sensitivity to the choice of prior. In pp collisions, the total uncertainties are largely driven by the JES and JER uncertainties for both the $R = 0.2$ and $R = 0.6$ jets. The fractional uncertainties are largest at low x_{J} in both collision systems; however, the yield in these x_{J} regions is small. Similar trends were obtained for the systematic uncertainties of $R = 0.3$, $R = 0.4$, and $R = 0.5$ jets, with similar values of the fractional uncertainties.

The systematic uncertainty contributions are similarly propagated to the calculation of $R_{\mathrm{AA}}^{\mathrm{pair}}$ and J_{AA}. For these quantities that involve ratios, the correlation between the systematic uncertainties was considered. The ratios allow the cancellation of systematic uncertainties and improve the precision of the measurements. Various types of ratios were obtained in this analysis. Type 1 corresponds to the ratios of Pb+Pb to pp collisions: $R_{\mathrm{AA}}^{\mathrm{pair}}$, J_{AA}. Type 2 corresponds to the ratios of subleading to leading $R_{\mathrm{AA}}^{\mathrm{pair}}$: $R_{\mathrm{AA}}^{\mathrm{pair}}(p_{\mathrm{T},2})/R_{\mathrm{AA}}^{\mathrm{pair}}(p_{\mathrm{T},1})$. Type 3 corresponds to the ratios of R to $R = 0.2$: $R_{\mathrm{AA}}^{\mathrm{pair}}(R)/R_{\mathrm{AA}}^{\mathrm{pair}}(0.2)$, $J_{\mathrm{AA}}(R)/J_{\mathrm{AA}}(0.2)$. Table 4.8 shows how the correlations were treated, depending on the type of ratio.

Uncertainty	Type 1 quantities	Type 2 quantities	Type 3 quantities
Centrality-independent $R = 0.4$ JES	Correlated	Correlated	Correlated
Centrality-dependent $R = 0.4$ JES	Uncorrelated	Correlated	Correlated
Baseline $R = 0.4$ JER	Correlated	Correlated	Correlated
R-dependent JES and JER (centrality-independent)	Correlated	Correlated	Uncorrelated
R-dependent JES and JER (centrality-dependent)	Uncorrelated	Correlated	Uncorrelated
Prior sensitivity	Uncorrelated	Correlated	Uncorrelated
Combinatoric dijet subtraction	Uncorrelated	Correlated	Uncorrelated
Combinatoric dijet efficiency correction	Uncorrelated	Correlated	Uncorrelated
Jet selection	Uncorrelated	Correlated	Uncorrelated
Global uncertainties	Uncorrelated	Correlated	Correlated

Table 4.8: Correlations between the systematic uncertainty components for the three types of ratios considered in this analysis.

The resulting uncertainties in $R_{\mathrm{AA}}^{\mathrm{pair}}(p_{\mathrm{T},1})$ and $R_{\mathrm{AA}}^{\mathrm{pair}}(p_{\mathrm{T},2})$ are shown for 0–10% central Pb+Pb collisions in Figure 4.41 for $R = 0.2$ and $R = 0.6$ jets. In this case, the uncertainties are dominated by the JES and JER. Similar trends were obtained for the systematic uncertainties of $R = 0.3$, $R = 0.4$, and $R = 0.5$ jets, with similar values of the fractional uncertainties.

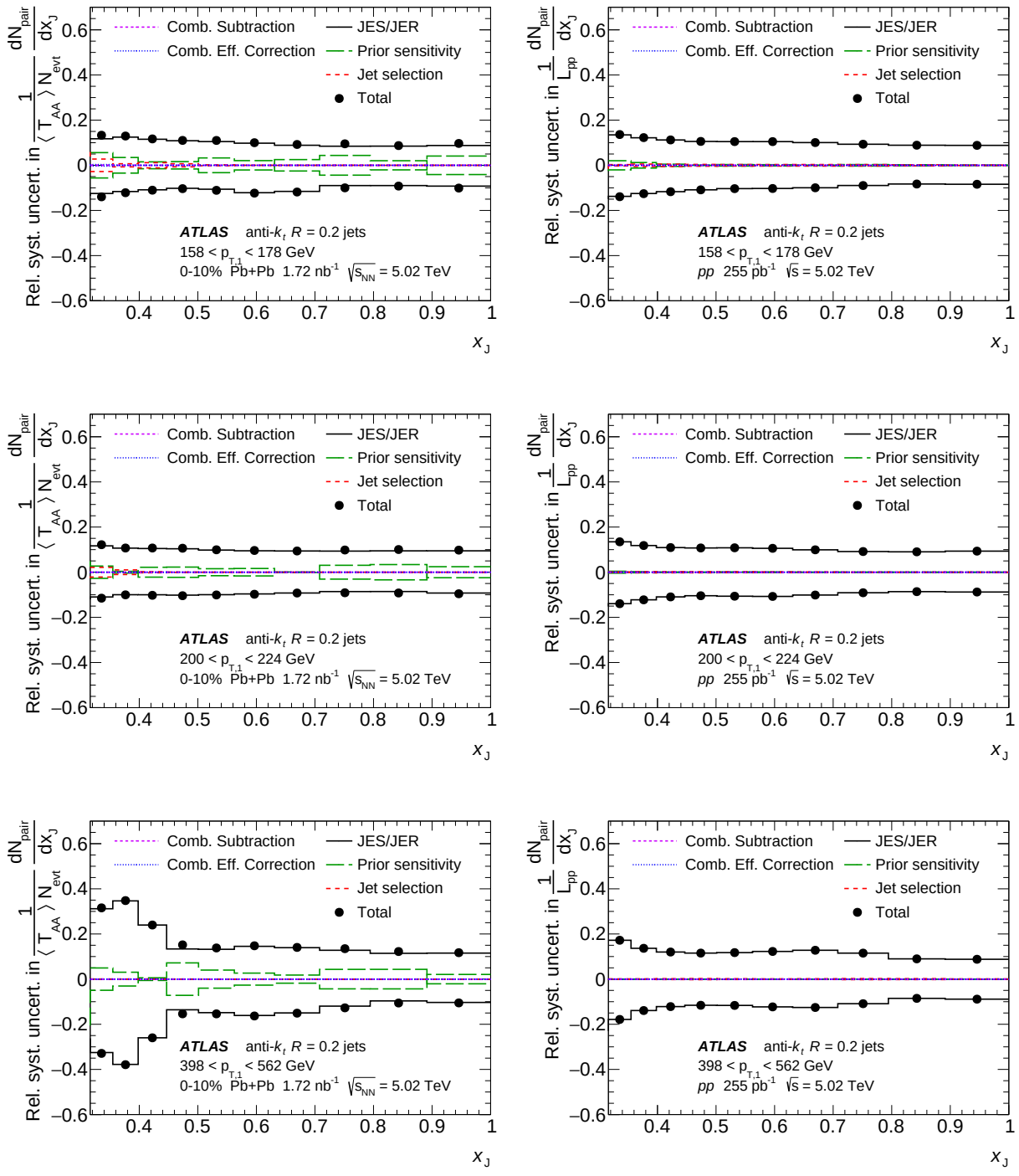

Figure 4.39: Systematic uncertainties of the absolutely normalized x_J distributions in 0–10% central Pb+Pb collisions (left) and pp collisions (right) for $R = 0.2$ jets. Leading jets with $158 < p_{T,1} < 178$ GeV (top), $200 < p_{T,1} < 224$ GeV (middle), $398 < p_{T,1} < 562$ GeV (bottom) are shown. Jets are selected with $|y| < 2.1$ and $|\phi_1 - \phi_2| > 7\pi/8$.

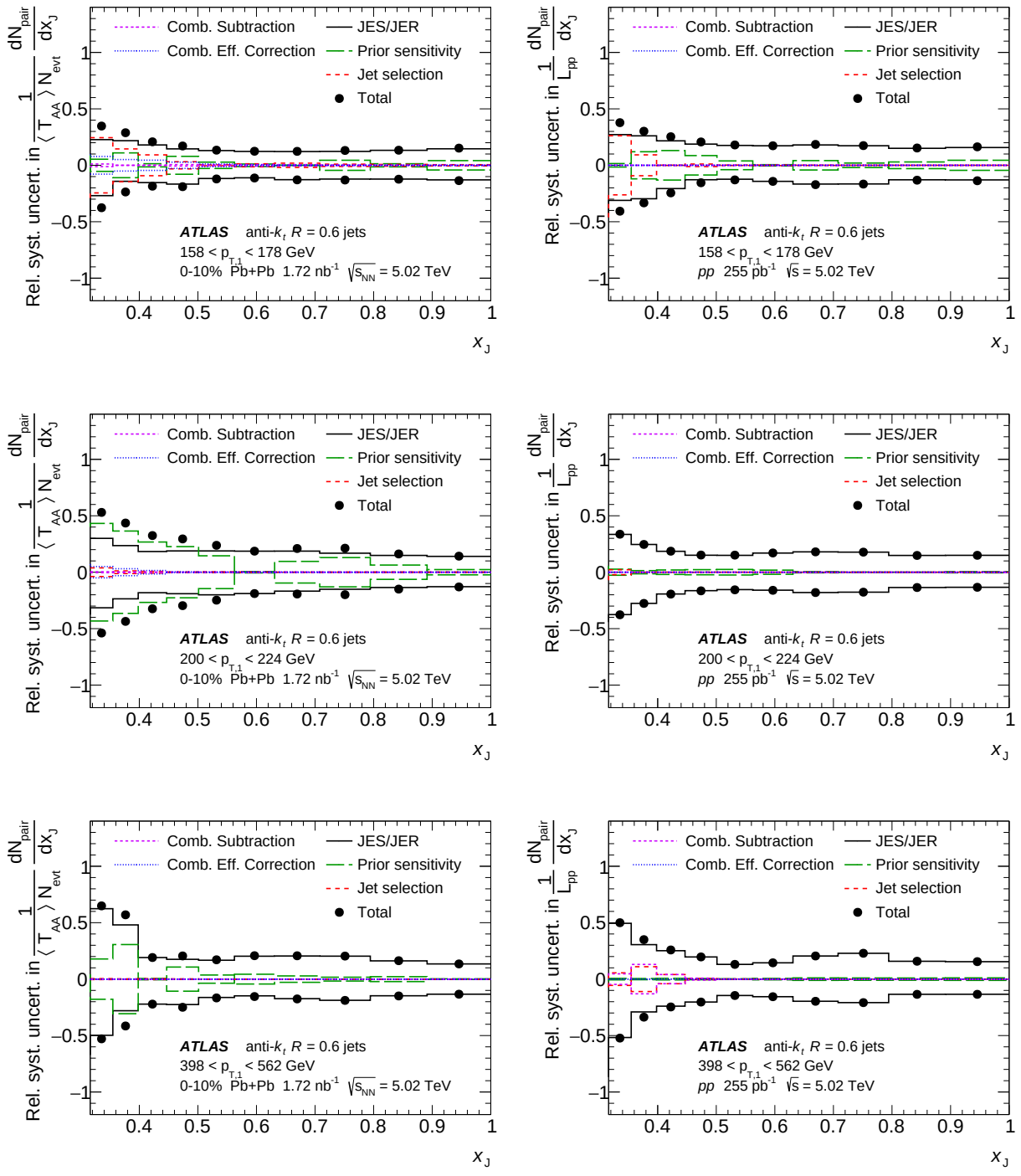

Figure 4.40: Systematic uncertainties of the absolutely normalized x_J distributions in 0–10% central Pb+Pb collisions (left) and pp collisions (right) for $R = 0.6$ jets. Leading jets with $158 < p_{T,1} < 178$ GeV (top), $200 < p_{T,1} < 224$ GeV (middle), $398 < p_{T,1} < 562$ GeV (bottom) are shown. Jets are selected with $|y| < 2.1$ and $|\phi_1 - \phi_2| > 7\pi/8$.

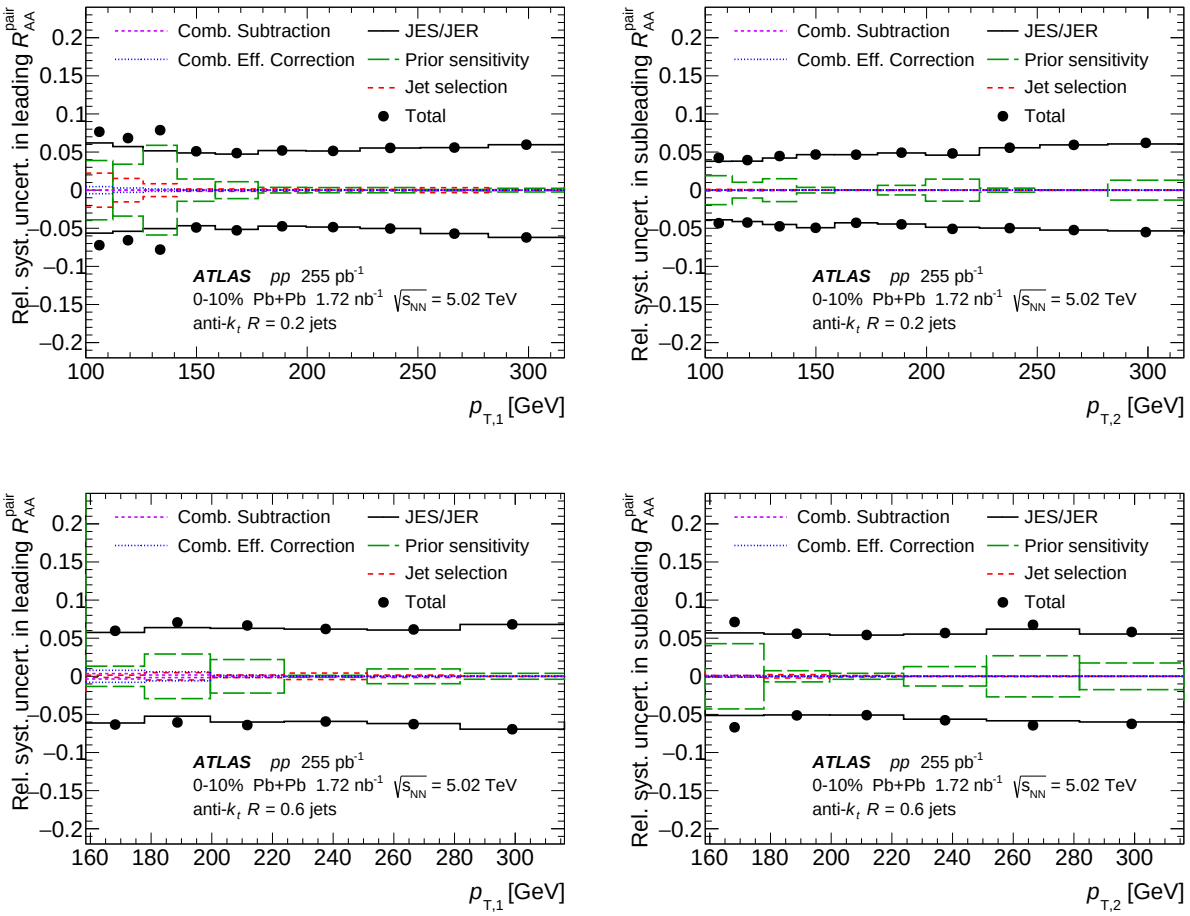

Figure 4.41: Systematic uncertainties of the $R_{\mathrm{AA}}^{\mathrm{pair}}$ for leading (left) and subleading (right) $R = 0.2$ (top) and $R = 0.6$ (bottom) jets. The uncertainties on the T_{AA} and pp luminosity values are not shown. Jets are selected with $|y| < 2.1$ and $|\phi_1 - \phi_2| > 7\pi/8$.

4.4 Results

4.4.1 $R_{\mathrm{AA}}^{\mathrm{pair}}$ distributions

The leading and subleading dijet yields in 0–10% central Pb+Pb collisions and the dijet cross sections in pp collisions are shown in Figure 4.42 for the various jet radii. Notice that these distributions correspond to the numerators and denominators in Eqs. (1.14) and (1.15). Additional distributions for other centrality selections are shown in the Appendix.

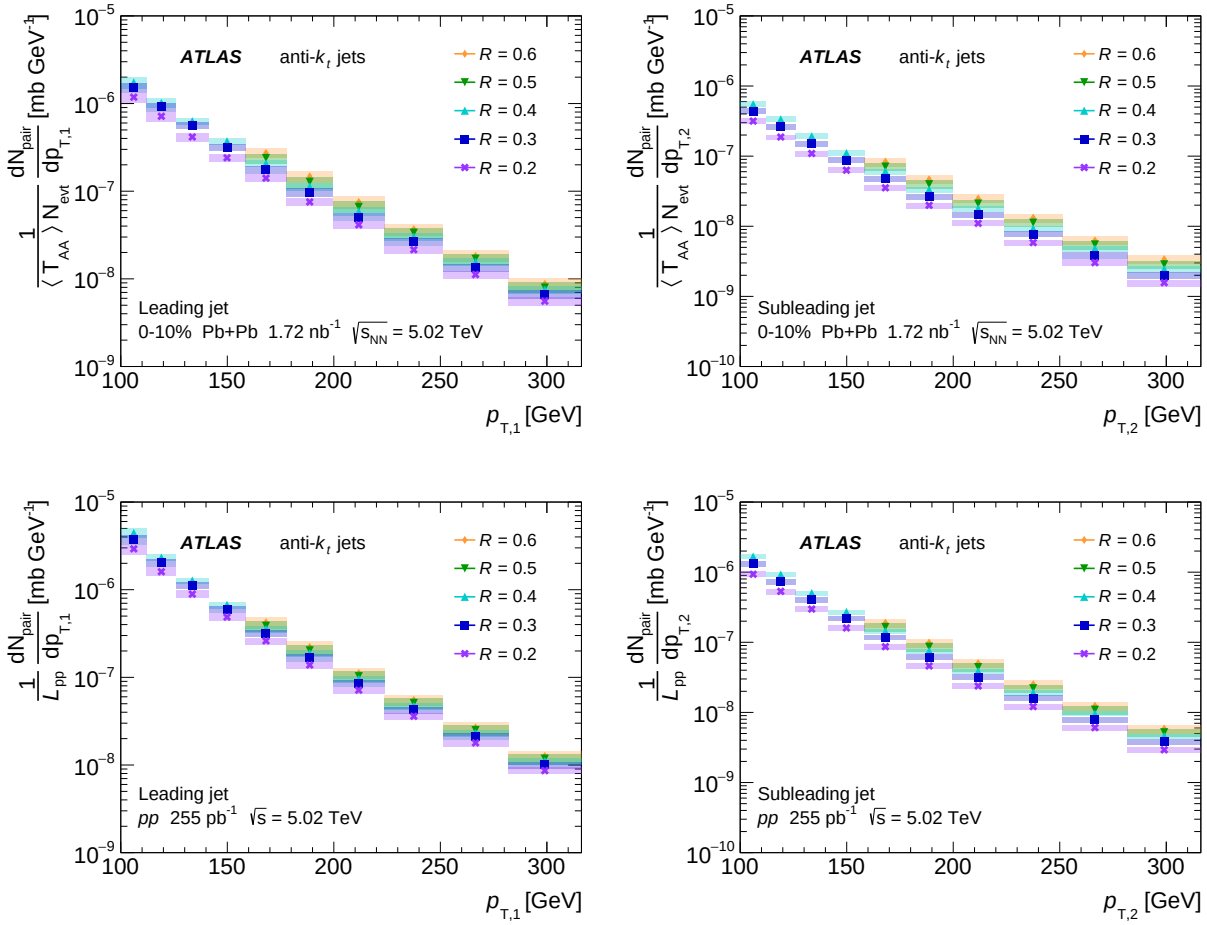

Figure 4.42: Leading (left) and subleading (right) dijet yields in 0–10% central Pb+Pb collisions (top) and dijet cross sections in pp collisions (bottom) as a function of p_{T} for the various jet radii. Jets are selected with $|y| < 2.1$ and $|\phi_1 - \phi_2| > 7\pi/8$. The normalization uncertainties (not shown) are $\delta\langle T_{\mathrm{AA}}\rangle/\langle T_{\mathrm{AA}}\rangle = 0.9\%$ in 0–10% Pb+Pb collisions and $\delta L_{pp}/L_{pp} = 1\%$ in pp collisions. The boxes correspond to systematic uncertainties and the bars to statistical uncertainties.

Figure 4.43 shows the ratios of $R = 0.3, 0.4, 0.5, 0.6$ with respect to $R = 0.2$ of the dijet yields in central Pb+Pb collisions and the dijet cross sections in pp collisions. The dijet yields increase with increasing jet

radius for both the leading and subleading jets in both collision systems. Additionally, the ratios of jet radius R to $R = 0.2$ of the dijet cross sections in pp data are compared with PYTHIA 8 and HERWIG7 simulations in Figure 4.43. Generally the PYTHIA 8 results are closer to the data than the HERWIG7 results. HERWIG7 consistently underpredicts the cross-section ratios. Additional distributions for other centrality selections are shown in the Appendix.

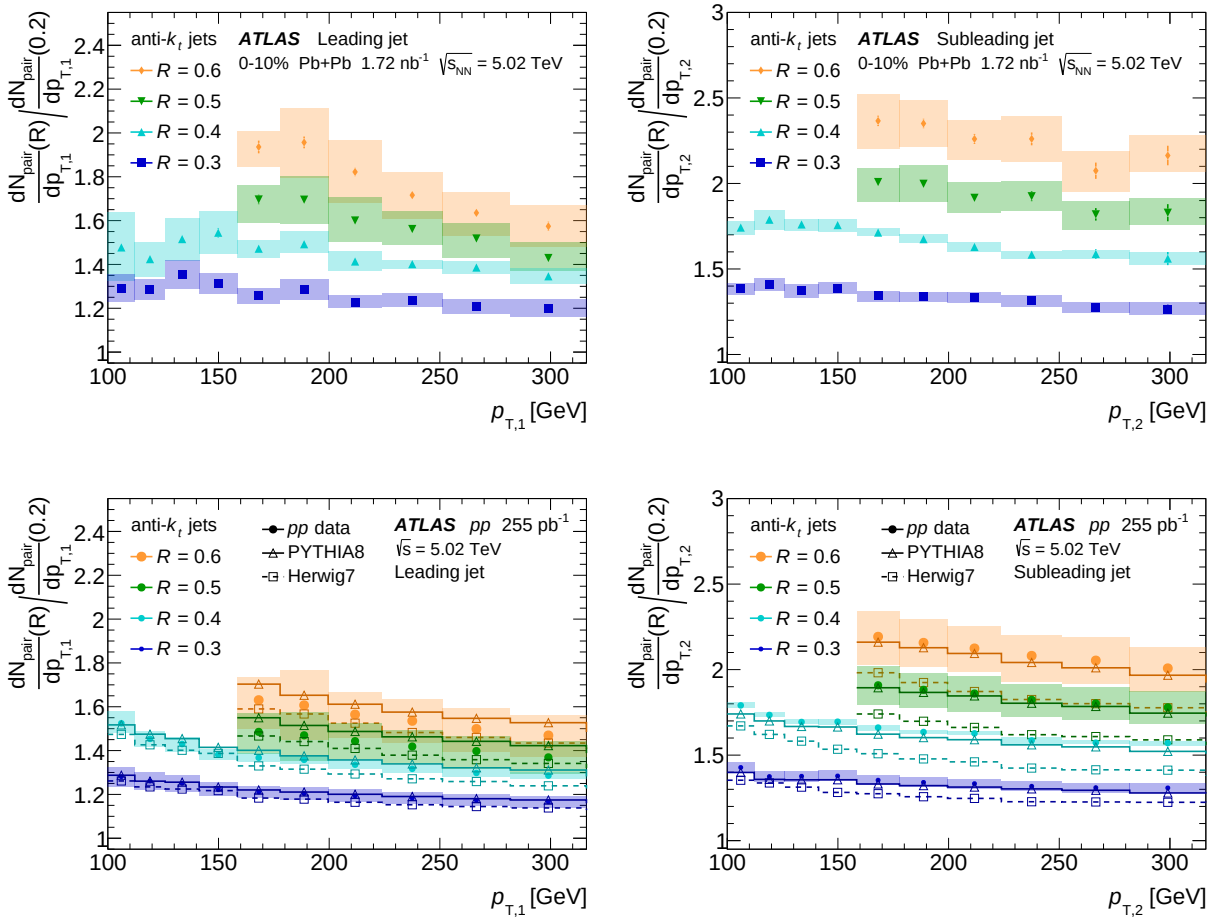

Figure 4.43: Leading (left) and subleading (right) dijet cross-section ratios of jet radius R with respect to $R = 0.2$ as a function of p_{T} for the various jet radii in 0–10% central Pb+Pb (top) and pp (bottom) collisions. The pp data is compared with PYTHIA 8 and HERWIG7 simulations. Jets are selected with $|y| < 2.1$ and $|\phi_1 - \phi_2| > 7\pi/8$. The boxes correspond to systematic uncertainties and the bars to statistical uncertainties.

The $R_{\mathrm{AA}}^{\mathrm{pair}}$ distributions are shown in Figure 4.44 for $R = 0.2$ and $R = 0.6$ jets. For both jet radii, the leading jet $R_{\mathrm{AA}}^{\mathrm{pair}}(p_{\mathrm{T},1})$ is larger than the subleading jet $R_{\mathrm{AA}}^{\mathrm{pair}}(p_{\mathrm{T},2})$ for all p_{T} considered here. It is also observed that $R_{\mathrm{AA}}^{\mathrm{pair}}(p_{\mathrm{T},1})$ and $R_{\mathrm{AA}}^{\mathrm{pair}}(p_{\mathrm{T},2})$ generally increase with increasing p_{T}, except for the leading $R_{\mathrm{AA}}^{\mathrm{pair}}(p_{\mathrm{T},1})$ of the $R = 0.6$ jets, which is flatter as a function of p_{T}. This behavior had also been previously observed with $R = 0.4$ jets in Ref. [39]. Additional distributions for other jet radii and centrality selections are shown in

the Appendix.

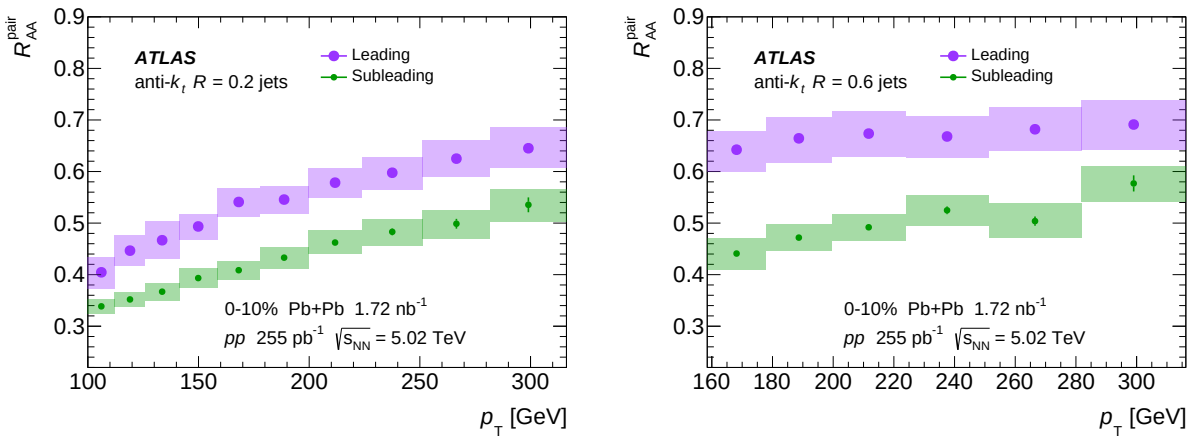

Figure 4.44: Leading and subleading jet $R_{\mathrm{AA}}^{\mathrm{pair}}$ distributions in dijets as a function of p_{T} for $R = 0.2$ (left) and $R = 0.6$ (right) jets in 0–10% Pb+Pb collisions. Jets are selected with $|y| < 2.1$ and $|\phi_1 - \phi_2| > 7\pi/8$. The normalization uncertainties (not shown) are $\delta\langle T_{\mathrm{AA}}\rangle/\langle T_{\mathrm{AA}}\rangle = 0.9\%$ in 0–10% Pb+Pb collisions and $\delta L_{pp}/L_{pp} = 1\%$ in pp collisions. The boxes correspond to systematic uncertainties and the bars to statistical uncertainties.

To understand the differences between the $R_{\mathrm{AA}}^{\mathrm{pair}}$ of leading and subleading jets, the $R_{\mathrm{AA}}^{\mathrm{pair}}(p_{\mathrm{T},2})/R_{\mathrm{AA}}^{\mathrm{pair}}(p_{\mathrm{T},1})$ ratio is considered. Figure 4.45 shows $R_{\mathrm{AA}}^{\mathrm{pair}}(p_{\mathrm{T},2})/R_{\mathrm{AA}}^{\mathrm{pair}}(p_{\mathrm{T},1})$ as a function of centrality, jet radius, and p_{T} for jets with $158 < p_{\mathrm{T}} < 316$ GeV. The overall trend as a function of centrality is as expected; for all jet radii, the most central collisions show the most suppression of the subleading jet relative to the leading jet in the dijet, and the most peripheral collisions show the least. The R dependence of this ratio is isolated for both the most central and most peripheral Pb+Pb collisions; no significant R dependence is observed for either. For central Pb+Pb collisions the value of this ratio is approximately 0.7–0.8, whereas for peripheral collisions the value is higher, approximately 0.9–1.1. Additionally, the $R_{\mathrm{AA}}^{\mathrm{pair}}(p_{\mathrm{T},2})/R_{\mathrm{AA}}^{\mathrm{pair}}(p_{\mathrm{T},1})$ ratio shows no significant dependence on p_{T}, for both central and peripheral collisions. This can be explained in terms of a path length dependent jet energy loss, which causes the subleading jets to experience an additional amount of quenching by traversing a longer distance within the QGP medium compared to the leading jets.

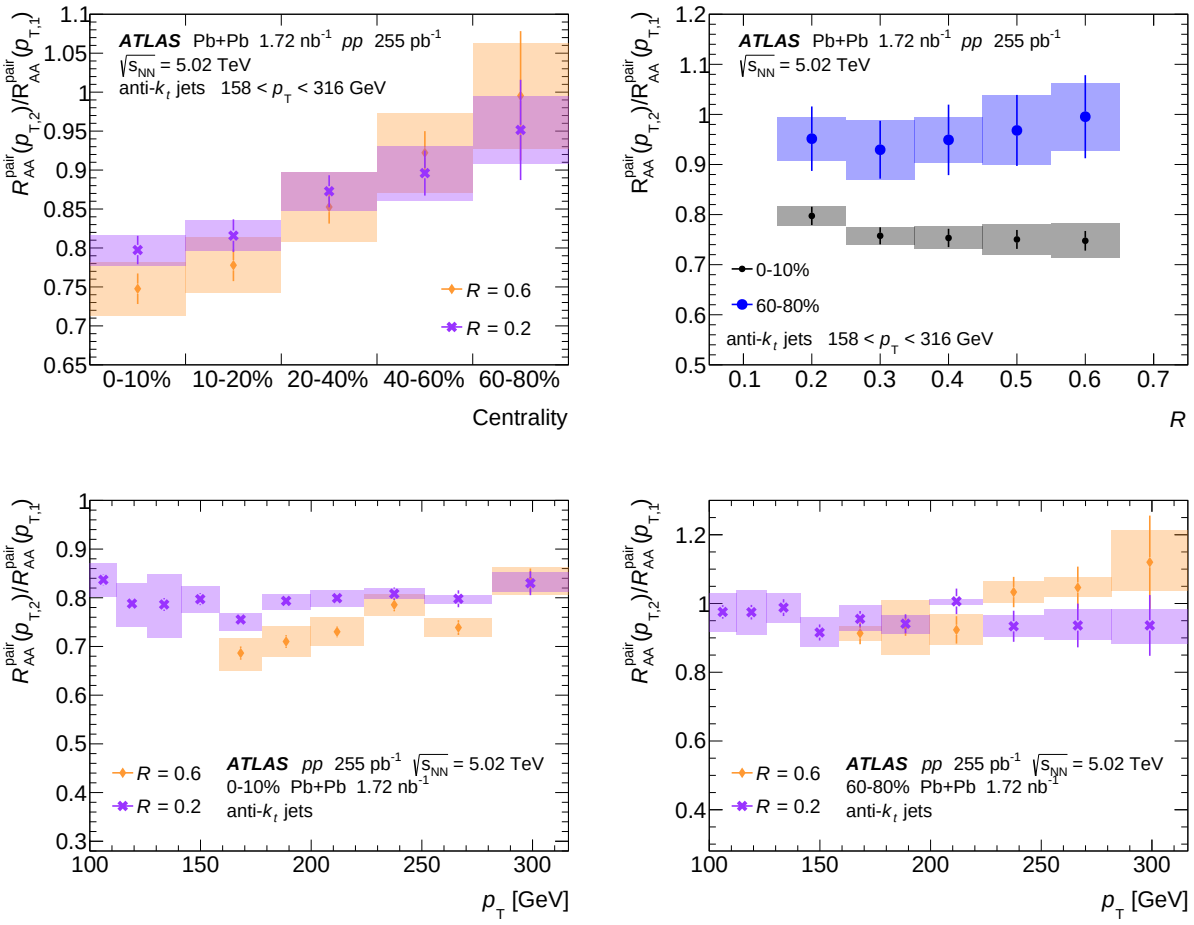

Figure 4.45: Double ratio $R_{\mathrm{AA}}^{\mathrm{pair}}(p_{\mathrm{T},2})/R_{\mathrm{AA}}^{\mathrm{pair}}(p_{\mathrm{T},1})$ of the subleading to leading jet $R_{\mathrm{AA}}^{\mathrm{pair}}$ distributions in dijets as a function of centrality (top left), jet radius (top right), and p_{T} for 0–10% (bottom left) and 60–80% (bottom right) central Pb+Pb collisions, for $158 < p_{\mathrm{T}} < 316$ GeV. Jets are selected with $|y| < 2.1$ and $|\phi_1 - \phi_2| > 7\pi/8$. The boxes correspond to systematic uncertainties and the bars to statistical uncertainties.

Discussion of $R_{\mathrm{AA}}^{\mathrm{pair}}$ distributions

To evaluate the R dependence of the $R_{\mathrm{AA}}^{\mathrm{pair}}$ distributions, the leading and subleading jet R_{AA}, along with the corresponding $R_{\mathrm{AA}}^{\mathrm{pair}}(R)/R_{\mathrm{AA}}^{\mathrm{pair}}(0.2)$ ratios, are shown in Figure 4.46 for the various jet radii for the 0–10% centrality selection. Some R dependence is observed for the leading jets, with the $R_{\mathrm{AA}}^{\mathrm{pair}}(p_{\mathrm{T},1})$ increasing with the jet radius. In the most central collisions at p_{T} approximately 200 GeV, the $R_{\mathrm{AA}}^{\mathrm{pair}}(p_{\mathrm{T},1})$ of $R = 0.2$ jets is approximately 0.55, whereas for $R = 0.6$ it is closer to 0.65. This R dependence is consistent with larger R jets being less suppressed than smaller R jets. A similar R dependence was observed in Ref. [60]. An R dependence is also observed for subleading jets, but the $R_{\mathrm{AA}}^{\mathrm{pair}}(p_{\mathrm{T},2})$ values and the deviations from unity in the $R_{\mathrm{AA}}^{\mathrm{pair}}(R)/R_{\mathrm{AA}}^{\mathrm{pair}}(0.2)$ ratio is smaller than for the leading jets. Since the $R_{\mathrm{AA}}^{\mathrm{pair}}(p_{\mathrm{T},2})/R_{\mathrm{AA}}^{\mathrm{pair}}(p_{\mathrm{T},1})$ ratio shows no significant dependence on R or p_{T} (as seen in Figure 4.45), the $R_{\mathrm{AA}}^{\mathrm{pair}}(p_{\mathrm{T},2})$ of subleading jets can

be seen, approximately, as a scaled down version of the $R_{\mathrm{AA}}^{\mathrm{pair}}(p_{\mathrm{T},1})$ of leading jets, by a factor dependent on centrality only.

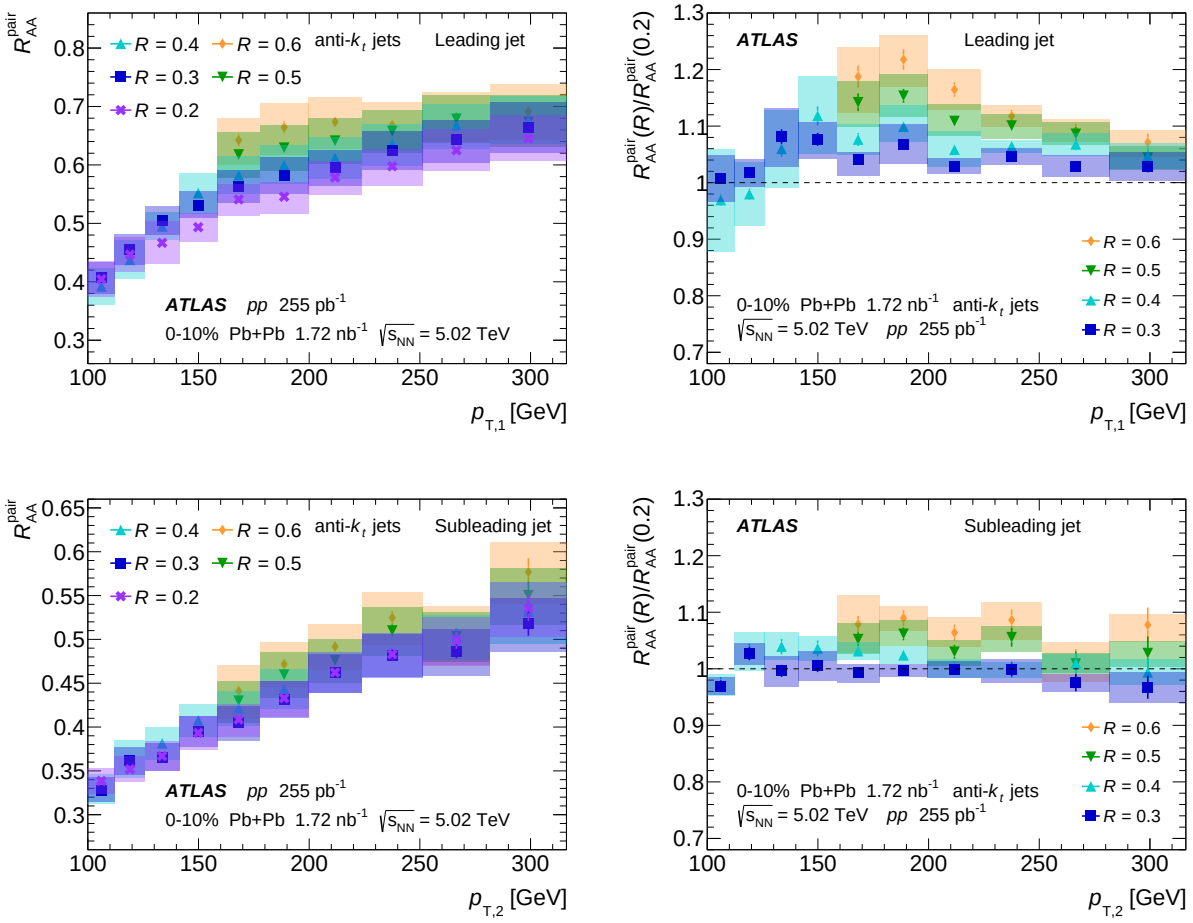

Figure 4.46: Leading (top) and subleading (bottom) jet $R_{\mathrm{AA}}^{\mathrm{pair}}$ distributions (left) in dijets and the corresponding $R_{\mathrm{AA}}^{\mathrm{pair}}(R)/R_{\mathrm{AA}}^{\mathrm{pair}}(0.2)$ ratios (right) as a function of jet p_{T} in 0–10% central Pb+Pb collisions. Jets are selected with $|y| < 2.1$ and $|\phi_1 - \phi_2| > 7\pi/8$. The normalization uncertainties (not shown) are $\delta\langle T_{\mathrm{AA}}\rangle/\langle T_{\mathrm{AA}}\rangle = 0.9\%$ in 0–10% Pb+Pb collisions and $\delta L_{pp}/L_{pp} = 1\%$ in pp collisions. The boxes correspond to systematic uncertainties and the bars to statistical uncertainties.

Additionally, the $R_{\mathrm{AA}}^{\mathrm{pair}}$ as a function of jet radius is shown in Figure 4.47 for two p_{T} selections in 0–10% central collisions, $158 < p_{\mathrm{T}} < 178$ GeV and $282 < p_{\mathrm{T}} < 316$ GeV. Some R dependence of the $R_{\mathrm{AA}}^{\mathrm{pair}}$ is observed, with $R_{\mathrm{AA}}^{\mathrm{pair}}$ increasing with the jet radius, which is stronger at lower p_{T}.

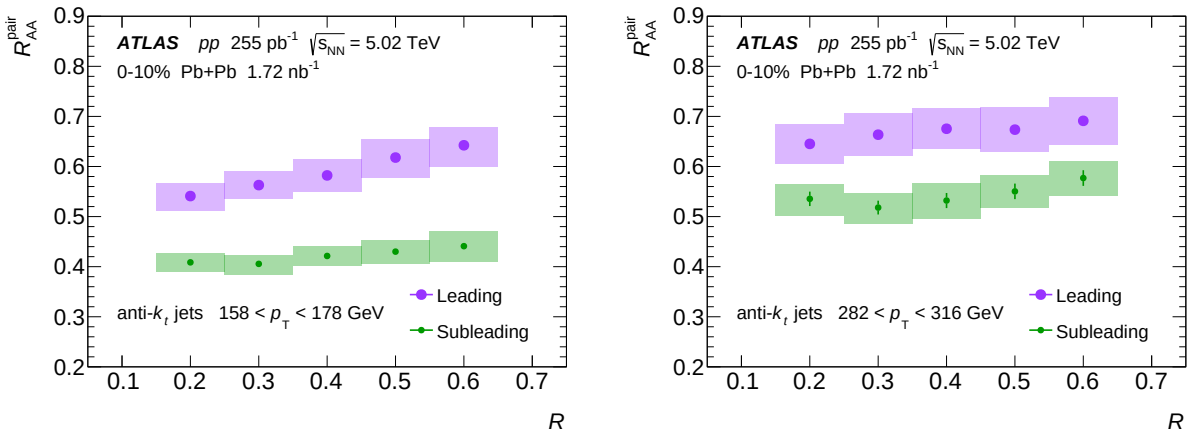

Figure 4.47: Leading and subleading jet $R_{\mathrm{AA}}^{\mathrm{pair}}$ distributions in dijets as a function of jet radius in 0–10% central Pb+Pb collisions, for $158 < p_{\mathrm{T}} < 178$ GeV (left) and $282 < p_{\mathrm{T}} < 316$ GeV (right). Jets are selected with $|y| < 2.1$ and $|\phi_1 - \phi_2| > 7\pi/8$. The normalization uncertainties (not shown) are $\delta\langle T_{\mathrm{AA}}\rangle/\langle T_{\mathrm{AA}}\rangle = 0.9\%$ in 0–10% Pb+Pb collisions and $\delta L_{pp}/L_{pp} = 1\%$ in pp collisions. The boxes correspond to systematic uncertainties and the bars to statistical uncertainties.

4.4.2 x_{J} distributions

The absolutely normalized x_{J} distributions in pp collisions, as defined in Eq. (1.9), are shown in Figure 4.48, for leading jets with $158 < p_{\mathrm{T},1} < 178$ GeV and $398 < p_{\mathrm{T},1} < 562$ GeV, for all jet radii considered here. The shapes of the distributions are similar for the two $p_{\mathrm{T},1}$ selections shown. In both cases, the distributions are peaked toward balanced dijets as expected. The distributions are more sharply peaked at $x_{\mathrm{J}} \approx 1$ for larger radius jets. This is expected if the larger radius jets cluster together radiation that could be reconstructed as separate jets for the smaller radii. For higher $p_{\mathrm{T},1}$, the distributions for the various jet radii are closer together than for lower $p_{\mathrm{T},1}$, presumably because higher p_{T} jets are more collimated. Additional distributions for other $p_{\mathrm{T},1}$ selections are shown in the Appendix.

A comparison of the pp data to Pythia 8 and Herwig7 simulations is shown in Figure 4.49. Here the self normalized x_{J} distributions are plotted for $R = 0.2$ and $R = 0.6$ jets with $158 < p_{\mathrm{T},1} < 178$ GeV and $398 < p_{\mathrm{T},1} < 562$ GeV. The self normalized x_{J} distributions are considered in order to take out any overall cross-section difference between the models and data. The pp data is well described by the simulations for the various jet radii. Additional distributions for other jet radii and $p_{\mathrm{T},1}$ selections are shown in the Appendix.

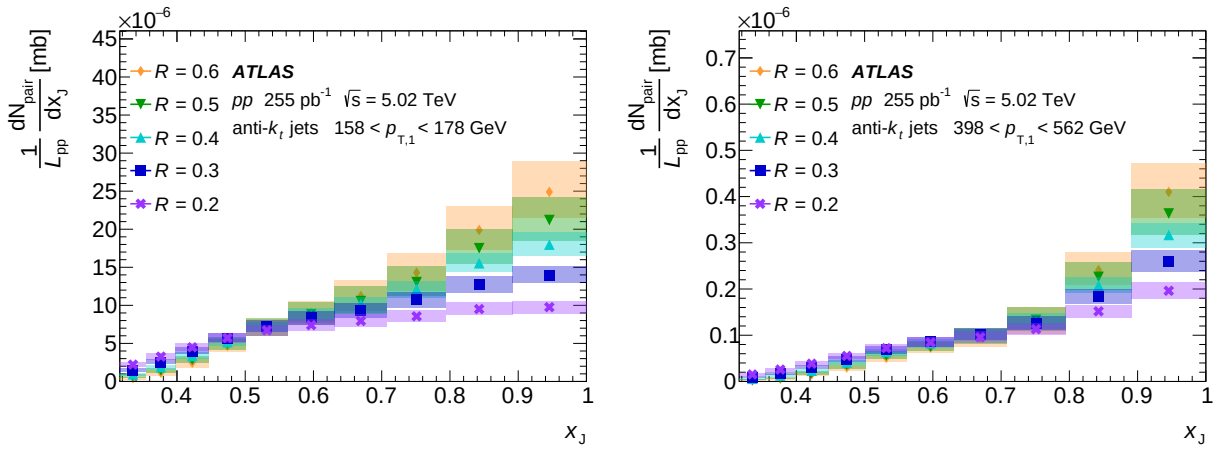

Figure 4.48: The absolutely normalized x_{J} distributions in pp collisions for leading jets with $158 < p_{\mathrm{T},1} < 178$ GeV (left) and $398 < p_{\mathrm{T},1} < 562$ GeV (right). Jets are selected with $|y| < 2.1$ and $|\phi_1 - \phi_2| > 7\pi/8$. The normalization uncertainty (not shown) is $\delta L_{pp}/L_{pp} = 1\%$. The boxes correspond to systematic uncertainties and the bars to statistical uncertainties.

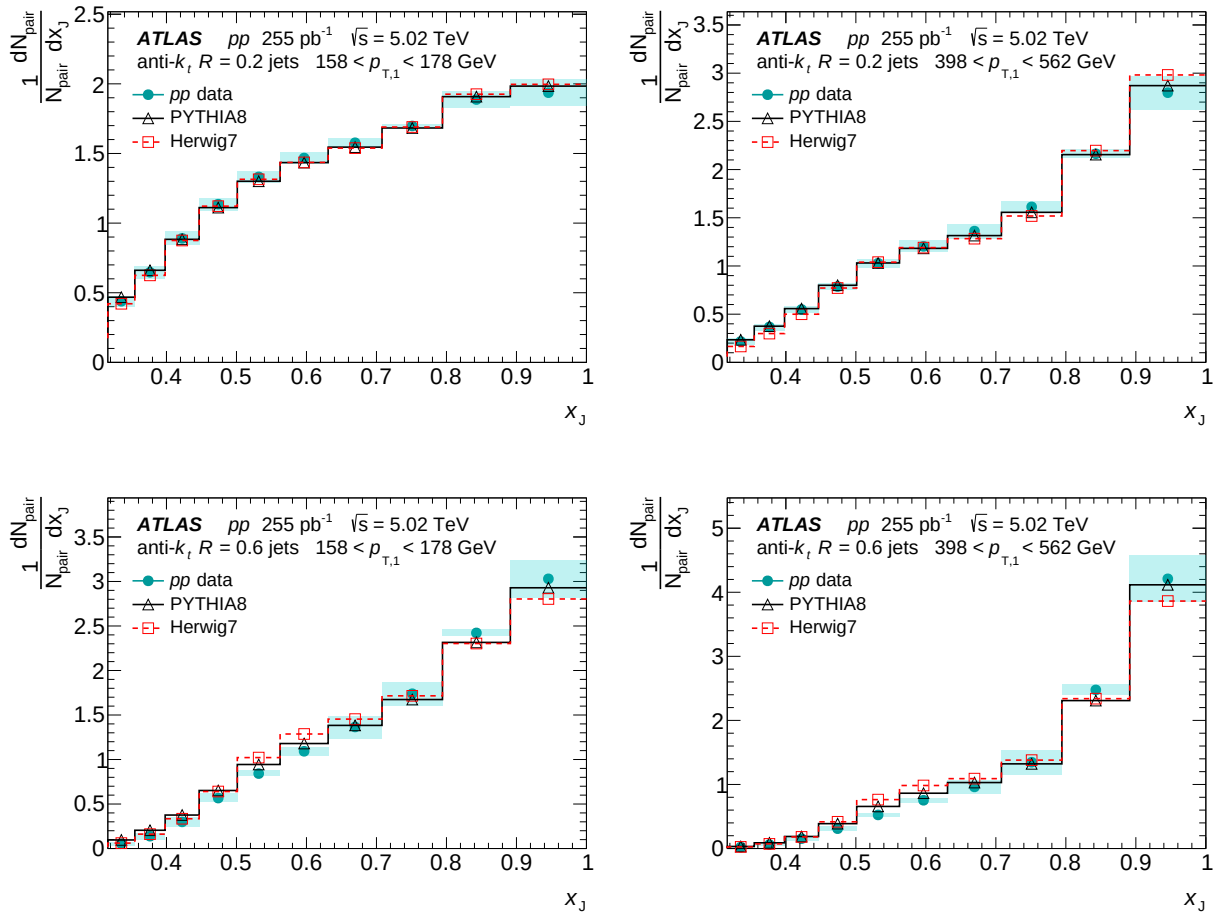

Figure 4.49: The dijet-yield-normalized x_{J} distributions in pp collisions, and PYTHIA 8 and HERWIG7 simulations, for leading $R = 0.2$ (top) and $R = 0.6$ (bottom) jets with $158 < p_{\mathrm{T},1} < 178$ GeV (left) and $398 < p_{\mathrm{T},1} < 562$ GeV (right). Jets are selected with $|y| < 2.1$ and $|\phi_1 - \phi_2| > 7\pi/8$. The boxes correspond to systematic uncertainties and the bars to statistical uncertainties.

Discussion of x_{J} distributions

Figure 4.50 shows the R dependence of the absolutely normalized x_{J} distributions in Pb+Pb collisions, as defined in Eq. (1.8), for centrality selections 0–10% and 20–40%, and the same $p_{\mathrm{T},1}$ selections as shown for pp collisions. The x_{J} distributions in Pb+Pb collisions are broadened compared to those in pp collisions in Figure 4.48. The magnitude of the modification is larger for lower $p_{\mathrm{T},1}$ values and for more central collisions. For the $158 < p_{\mathrm{T},1} < 178$ GeV selection in mid-central collisions, the peak at balanced dijets remains compared to pp collisions, but becomes weaker as the jet radius decreases. For this $p_{\mathrm{T},1}$ selection in 0–10% central collisions, the distributions are nearly flat for $x_{\mathrm{J}} > 0.5$. For the $398 < p_{\mathrm{T},1} < 562$ GeV selection, the x_{J} distributions in both central and mid-central Pb+Pb collisions remain peaked at $x_{\mathrm{J}} \approx 1$ for the jet radii considered here. Additional distributions for other centrality selections and $p_{\mathrm{T},1}$ selections are shown in the Appendix.

To look more closely at the centrality dependent modification from the distributions in pp collisions, Figure 4.51 shows the overlaid x_{J} distributions for 0–10%, 20–40%, and 40–60% central Pb+Pb collisions. Two $p_{\mathrm{T},1}$ selections, $158 < p_{\mathrm{T},1} < 178$ GeV and $398 < p_{\mathrm{T},1} < 562$ GeV, for $R = 0.2$ and $R = 0.6$ jets are shown. As expected, x_{J} distributions in the most central Pb+Pb collisions are the most modified compared to those in pp collisions, with the rate of balanced dijets being strongly suppressed.

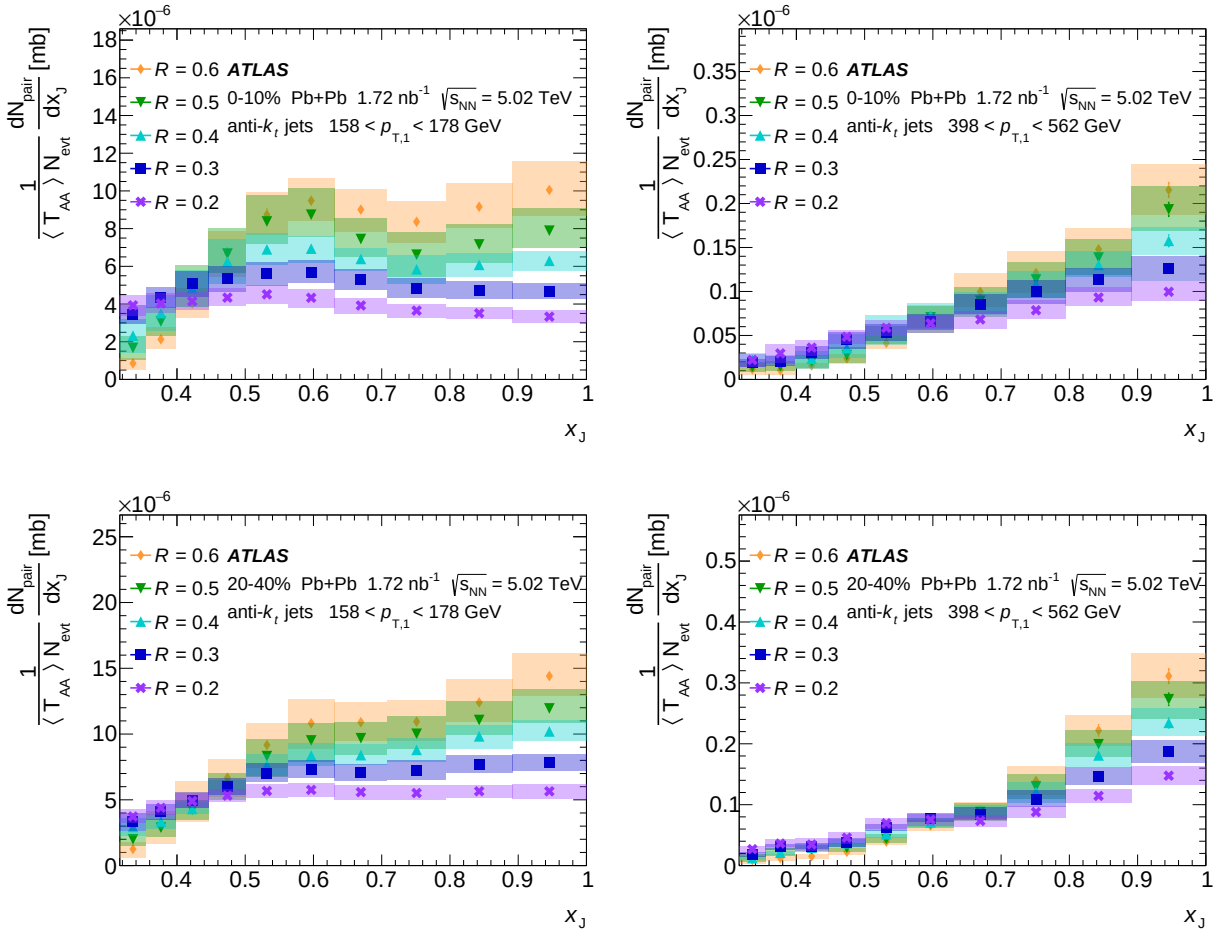

Figure 4.50: The absolutely normalized x_{J} distributions in 0–10% central Pb+Pb collisions (top), 20–40% central Pb+Pb collisions (bottom) for leading jets with $158 < p_{\mathrm{T},1} < 178$ GeV (left) and $398 < p_{\mathrm{T},1} < 562$ GeV (right). Jets are selected with $|y| < 2.1$ and $|\phi_1 - \phi_2| > 7\pi/8$. The normalization uncertainties (not shown) are $\delta\langle T_{\mathrm{AA}}\rangle/\langle T_{\mathrm{AA}}\rangle = 0.9\%$ and 2% for Pb+Pb centrality selections 0–10% and 20–40%, respectively. The boxes correspond to systematic uncertainties and the bars to statistical uncertainties.

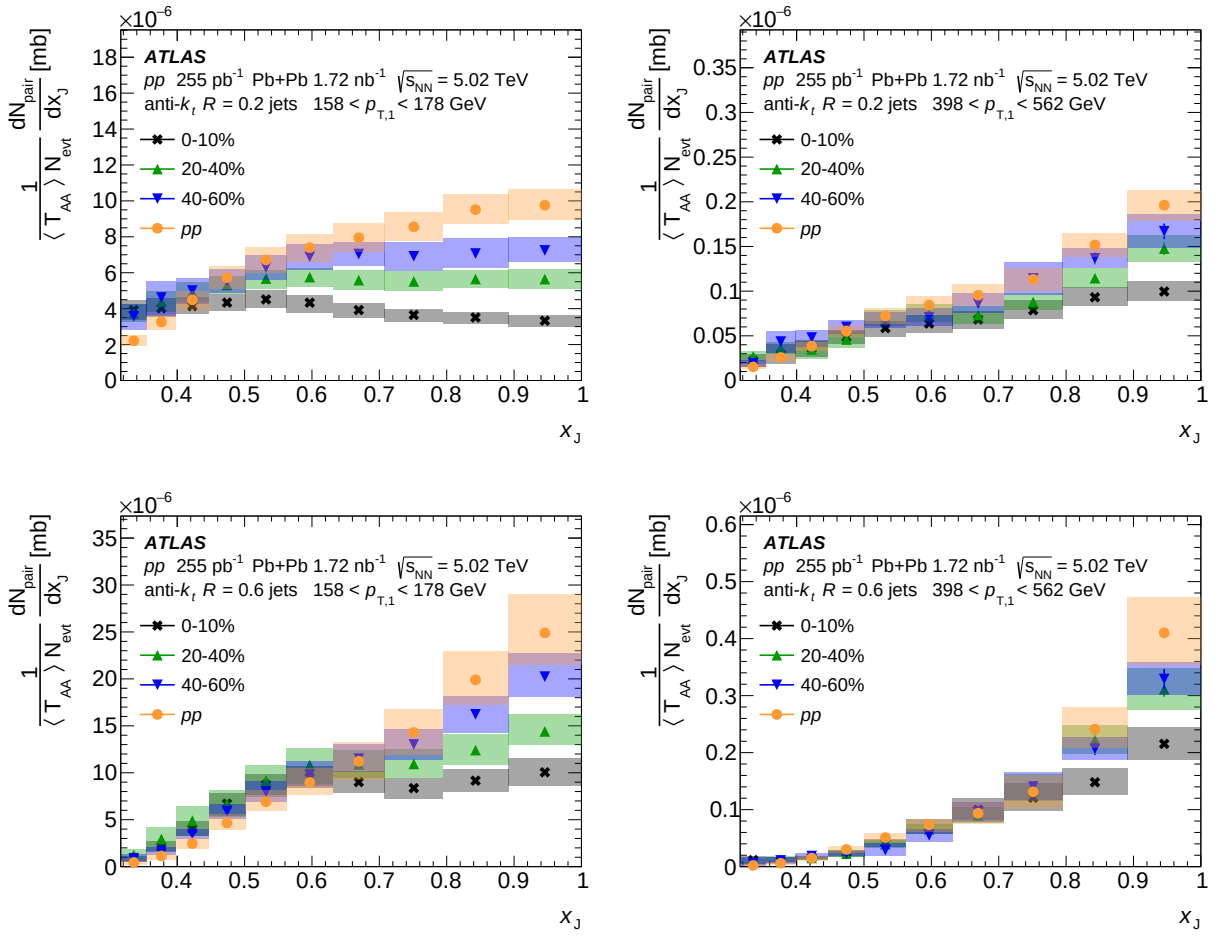

Figure 4.51: The absolutely normalized x_{J} distributions for $R = 0.2$ (top) and $R = 0.6$ (bottom) jets for three centrality selections in Pb+Pb collisions and pp collisions. Leading jets with $158 < p_{\mathrm{T},1} < 178$ GeV (left) and $398 < p_{\mathrm{T},1} < 562$ GeV (right) are shown. Jets are selected with $|y| < 2.1$ and $|\phi_1 - \phi_2| > 7\pi/8$. The normalization uncertainties (not shown) are $\delta\langle T_{\mathrm{AA}}\rangle/\langle T_{\mathrm{AA}}\rangle = 0.9\%$, 2%, and 5% in 0–10%, 20–40%, and 40–60% Pb+Pb collisions, respectively, and $\delta L_{pp}/L_{pp} = 1\%$ in pp collisions. The boxes correspond to systematic uncertainties and the bars to statistical uncertainties.

4.4.3 J_{AA} distributions

The J_{AA} is defined in Eq. (1.11) as the ratio of the dijet yields in Pb+Pb collisions to pp collisions. The J_{AA} distributions for 0–10%, 20–40%, and 40–60%, and $200 < p_{\mathrm{T},1} < 224$ GeV, are shown in Figure 4.52 for $R = 0.2$, $R = 0.4$, and $R = 0.6$ jets. For the various centralities, there is a suppression of the number of balanced (high x_{J}) dijets and an enhancement of imbalanced (low x_{J}) dijets, with the modifications being larger towards more central collisions. While the enhancement at low x_{J} can be large in terms of the J_{AA}, it is worth recalling that the corresponding absolute dijet yields are small at low x_{J}, especially for the larger R jets, as was previously seen in Figure 4.50. The larger uncertainties on the J_{AA} of the $R = 0.6$ jets in the most central collisions are driven by the sensitivity to the unfolding prior weights as well as the JES and JER, which affect the bins at low x_{J}.

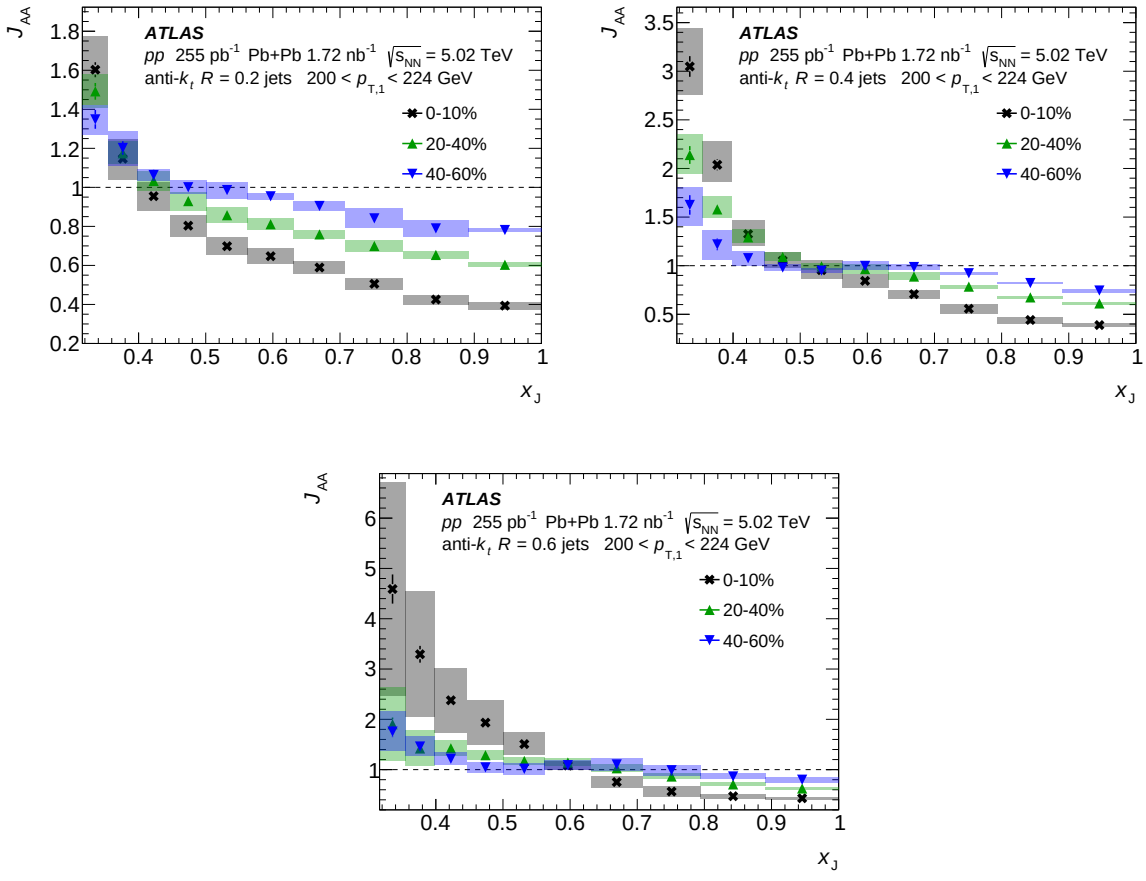

Figure 4.52: J_{AA} distributions for $R = 0.2$ (top left), $R = 0.4$ (top right), and $R = 0.6$ (bottom) jets for three centrality selections in Pb+Pb collisions and pp collisions. Leading jets with $200 < p_{\mathrm{T},1} < 224$ GeV are shown. Jets are selected with $|y| < 2.1$ and $|\phi_1 - \phi_2| > 7\pi/8$. The normalization uncertainties (not shown) are $\delta\langle T_{\mathrm{AA}}\rangle/\langle T_{\mathrm{AA}}\rangle = 0.9\%$, 2%, and 5% in 0–10%, 20–40%, and 40–60% Pb+Pb collisions, respectively, and $\delta L_{pp}/L_{pp} = 1\%$ in pp collisions. The boxes correspond to systematic uncertainties and the bars to statistical uncertainties.

Discussion of J_{AA} distributions

The J_{AA} distributions are overlaid for the various jet radii in Figure 4.53, along with their corresponding $J_{\mathrm{AA}}(R)/J_{\mathrm{AA}}(0.2)$ ratios. In the most central collisions, 0–10%, a larger J_{AA} is observed for larger jet radius, more noticeable towards lower x_{J}. In 20–40% central collisions, the same quantitative trend is observed but the magnitude of the deviation from unity is smaller. Similarly, in terms of the $J_{\mathrm{AA}}(R)/J_{\mathrm{AA}}(0.2)$ ratios, at low x_{J} there is a spread of the central values of J_{AA} for the various jet radii and the uncertainties are larger. At high-x_{J}, the J_{AA} values show an R dependence of smaller magnitude. Additional distributions for other centrality selections and $p_{\mathrm{T},1}$ selections are shown in the Appendix.

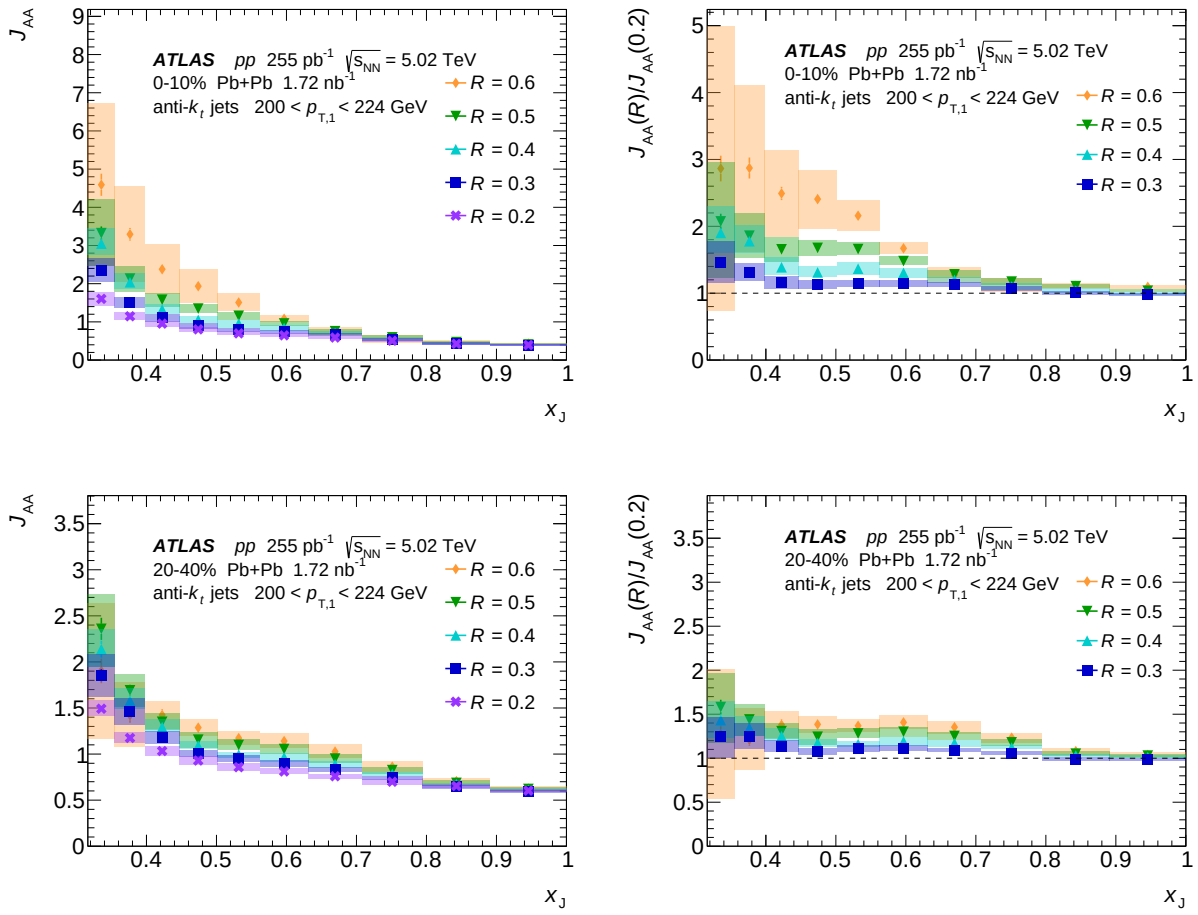

Figure 4.53: J_{AA} distributions (left) and its corresponding $J_{\mathrm{AA}}(R)/J_{\mathrm{AA}}(0.2)$ ratios (right) in 0–10% (top) and 20–40% (bottom) central Pb+Pb collisions, for $200 < p_{\mathrm{T},1} < 224$ GeV. Jets are selected with $|y| < 2.1$ and $|\phi_1 - \phi_2| > 7\pi/8$. The normalization uncertainties in J_{AA} (not shown) are $\delta\langle T_{\mathrm{AA}}\rangle/\langle T_{\mathrm{AA}}\rangle = 0.9\%$ and 2% in 0–10% and 20–40% Pb+Pb collisions, respectively, and $\delta L_{pp}/L_{pp} = 1\%$ in pp collisions. The boxes correspond to systematic uncertainties and the bars to statistical uncertainties.

To evaluate the R dependence of these distributions, the J_{AA} is plotted as a function of the jet radius

in Figure 4.54, for several $p_{\mathrm{T},1}$ selections at x_{J} values of $0.89 < x_{\mathrm{J}} < 1.0$ and $0.50 < x_{\mathrm{J}} < 0.56$ in the most central collisions. The corresponding $J_{\mathrm{AA}}(R)/J_{\mathrm{AA}}(0.2)$ ratios are shown in Figure 4.55. For nearly balanced dijets ($0.89 < x_{\mathrm{J}} < 1.0$), a small R dependence to J_{AA} is observed, with the J_{AA} increasing with the jet radius. As the dijets become more imbalanced ($0.50 < x_{\mathrm{J}} < 0.56$), this R dependence becomes stronger. For both balanced and imbalanced dijets, the R dependence is observed to be larger for lower $p_{\mathrm{T},1}$ values. This R-dependent behavior can be explained by considering that the subleading jets, which have lost energy and thus caused the dijets to become imbalanced, recover some of the lost energy as the jet radius increases. Another contribution comes from the medium response, which can add energy to the jets.

To assess the p_{T} dependence of the $J_{\mathrm{AA}}(R)/J_{\mathrm{AA}}(0.2)$ ratios, Figure 4.56 shows the $J_{\mathrm{AA}}(R)/J_{\mathrm{AA}}(0.2)$ ratios as a function of $p_{\mathrm{T},1}$, for $R = 0.4$ and $R = 0.6$ jets, and two x_{J} selections, $0.50 < x_{\mathrm{J}} < 0.56$ and $0.89 < x_{\mathrm{J}} < 1.0$. The $J_{\mathrm{AA}}(R)/J_{\mathrm{AA}}(0.2)$ ratios come closer to unity with increasing $p_{\mathrm{T},1}$, with the modification being larger for larger R jets. The deviations from unity are much smaller for balanced dijets than for imbalanced dijets.

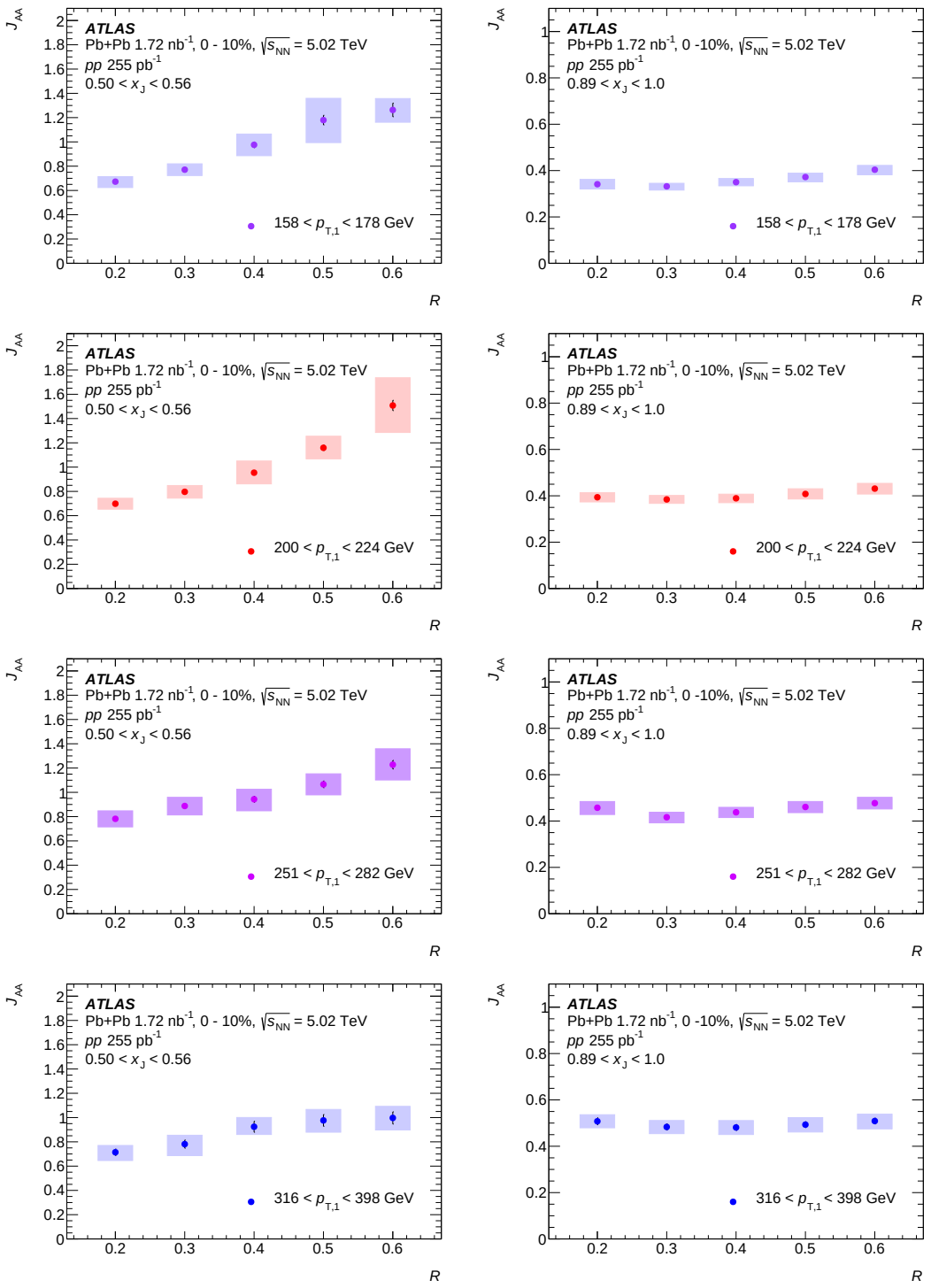

Figure 4.54: The J_{AA} values as a function of R for jets with (from the top row) $158 < p_{\mathrm{T},1} < 178$ GeV, $200 < p_{\mathrm{T},1} < 224$ GeV, $251 < p_{\mathrm{T},1} < 282$ GeV, and $316 < p_{\mathrm{T},1} < 398$ GeV in 0–10% central Pb+Pb collisions, for $0.50 < x_{\mathrm{J}} < 0.56$ (left) and $0.89 < x_{\mathrm{J}} < 1.0$ (right). Jets are selected with $|y| < 2.1$ and $|\phi_1 - \phi_2| > 7\pi/8$. The normalization uncertainties (not shown) are $\delta\langle T_{\mathrm{AA}}\rangle/\langle T_{\mathrm{AA}}\rangle = 0.9\%$ and 2% in 0–10% and 20–40% Pb+Pb collisions, respectively, and $\delta L_{pp}/L_{pp} = 1\%$ in pp collisions. The boxes correspond to systematic uncertainties and the bars to statistical uncertainties.

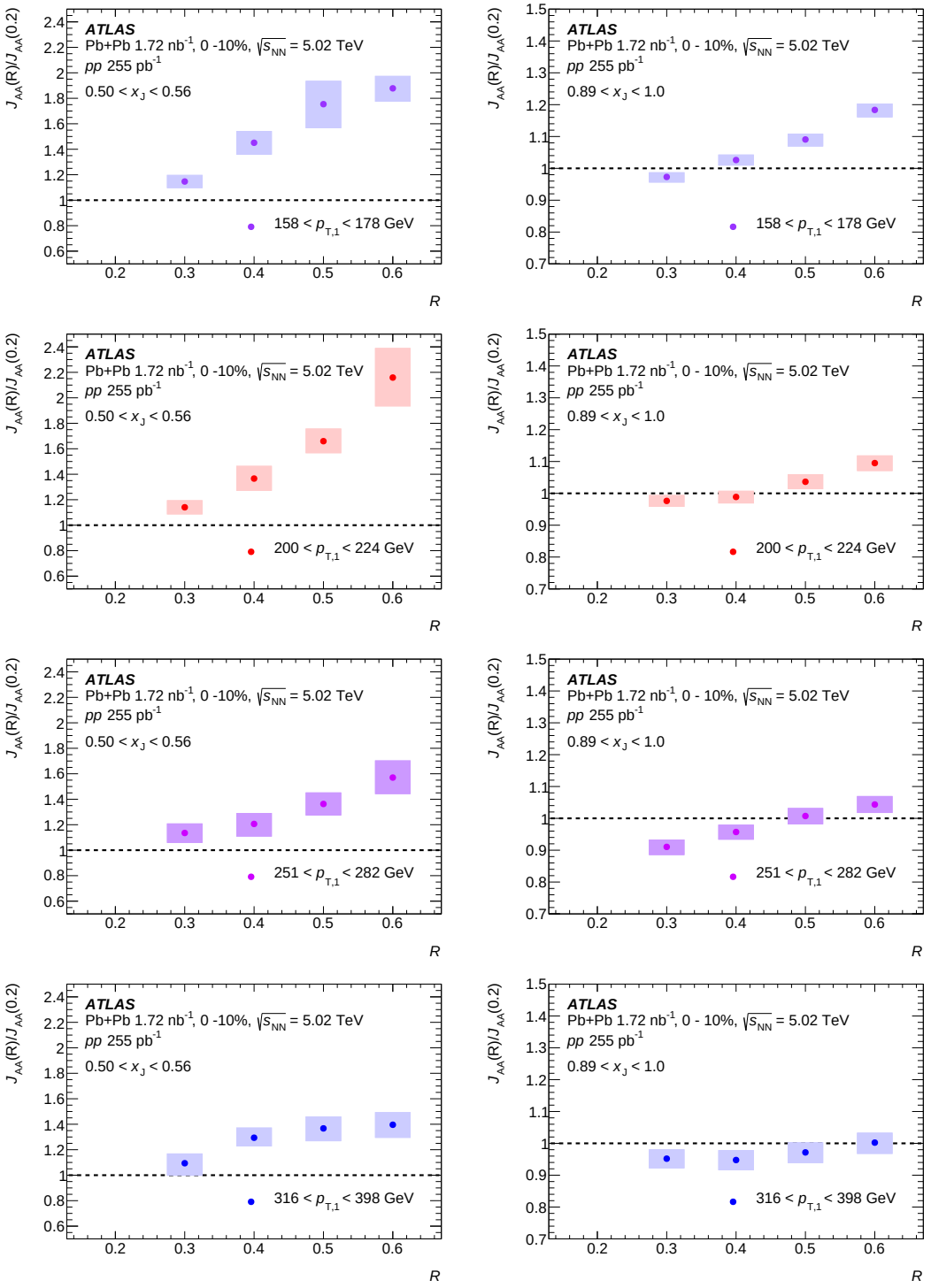

Figure 4.55: The $J_{\mathrm{AA}}(R)/J_{\mathrm{AA}}(0.2)$ ratios as a function of R for jets with (from the top row) $158 < p_{\mathrm{T},1} < 178$ GeV, $200 < p_{\mathrm{T},1} < 224$ GeV, $251 < p_{\mathrm{T},1} < 282$ GeV, $316 < p_{\mathrm{T},1} < 398$ GeV in 0–10% central Pb+Pb collisions, for $0.50 < x_{\mathrm{J}} < 0.56$ (left) and $0.89 < x_{\mathrm{J}} < 1.0$ (right). Jets are selected with $|y| < 2.1$ and $|\phi_1 - \phi_2| > 7\pi/8$. The boxes correspond to systematic uncertainties and the bars to statistical uncertainties.

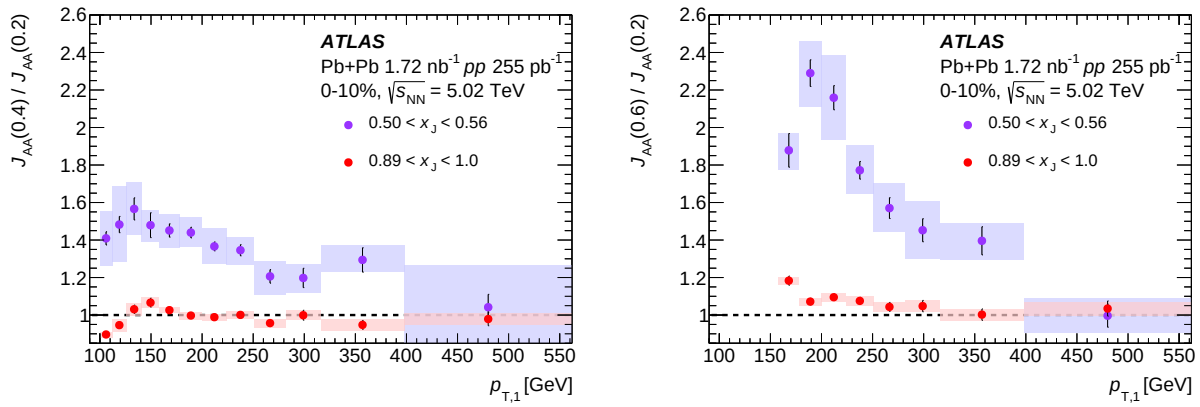

Figure 4.56: $J_{\mathrm{AA}}(R)/J_{\mathrm{AA}}(0.2)$ ratios as a function of $p_{\mathrm{T},1}$ for $R = 0.4$ (left) and $R = 0.6$ (right) jets in 0–10% central Pb+Pb collisions, for $0.50 < x_{\mathrm{J}} < 0.56$ and $0.89 < x_{\mathrm{J}} < 1.0$. Jets are selected with $|y| < 2.1$ and $|\phi_1 - \phi_2| > 7\pi/8$. The boxes correspond to systematic uncertainties and the bars to statistical uncertainties.

4.4.4 Comparison to Theory

Results were compared with the Linear Boltzmann Transport (LBT) [115] and JETSCAPE [116] models. Both of these models use PYTHIA 8 as the base for the hard processes, but a different evolution of the parton showers. The LBT model uses Boltzmann transport equations to describe the propagation of jet and medium partons as they traverse a QGP, including elastic and inelastic perturbative QCD processes. The JETSCAPE model combines [117], in tune v3.5 AA22, the LBT model at low parton virtuality with a MATTER [118] medium-modified parton shower at high parton virtuality.

Figure 4.57 shows the absolutely normalized x_{J} distributions in data compared with the JETSCAPE model for the various jet radii in 0–10% central Pb+Pb and in pp collisions. At high x_{J} values ($x_{\mathrm{J}} > 0.65$), the model describes the pp data well, while at lower x_{J} values it overestimates the data. In the case of the Pb+Pb data, the model describes the data at high x_{J} values. For $0.45 < x_{\mathrm{J}} < 0.65$, the model underestimates the Pb+Pb data. For lower x_{J} values, the model overestimates the Pb+Pb data. Additional distributions for other $p_{\mathrm{T},1}$ selections are shown in the Appendix.

Figure 4.58 shows the $R_{\mathrm{AA}}^{\mathrm{pair}}$ distributions of leading and subleading jets compared with the LBT and JETSCAPE models, for $R = 0.2$ and $R = 0.6$ jets in 0–10% central collisions. For both the large and small jets, the models predict that the subleading jets are more suppressed than the leading jets in dijets in terms of the $R_{\mathrm{AA}}^{\mathrm{pair}}$. However, they have varying degrees of success in describing the measured $R_{\mathrm{AA}}^{\mathrm{pair}}$ values. For $R = 0.2$ jets, the LBT model underestimates the data for both the leading and subleading jets; the JETSCAPE model describes the leading jet $R_{\mathrm{AA}}^{\mathrm{pair}}$ distribution well, but overestimates the subleading jet distribution. For $R = 0.6$ jets, the LBT model fully describes the leading jet $R_{\mathrm{AA}}^{\mathrm{pair}}$ distribution, but overestimates the subleading jet distribution; the JETSCAPE model describes the subleading jet $R_{\mathrm{AA}}^{\mathrm{pair}}$ distribution, but underestimates the

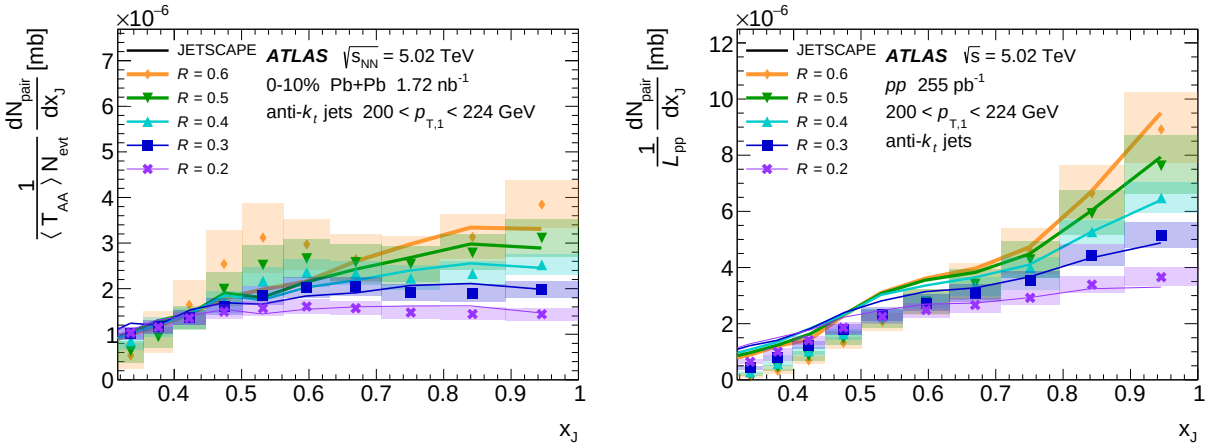

Figure 4.57: x_{J} distributions in data compared with the JETSCAPE (LBT+MATTER) model, for $R = 0.2, 0.3, 0.4, 0.5$ and 0.6 jets in 0–10% central Pb+Pb collisions (left) and pp collisions (right), for $200 < p_{\mathrm{T},1} < 224$ GeV. Jets are selected with $|y| < 2.1$ and $|\phi_1 - \phi_2| > 7\pi/8$. The normalization uncertainties in the data (not shown) are $\delta\langle T_{\mathrm{AA}}\rangle/\langle T_{\mathrm{AA}}\rangle = 0.9\%$ in 0–10% Pb+Pb collisions and $\delta L_{pp}/L_{pp} = 1\%$ in pp collisions. The boxes correspond to systematic uncertainties and the bars to statistical uncertainties.

leading jet distribution.

The $R_{\mathrm{AA}}^{\mathrm{pair}}(R = 0.6)/R_{\mathrm{AA}}^{\mathrm{pair}}(R = 0.2)$ ratio of $R = 0.6$ jets with respect to $R = 0.2$ jets is shown in Figure 4.59 for both the leading and subleading jets in 0–10% central collisions. For both the leading and subleading jet $R_{\mathrm{AA}}^{\mathrm{pair}}$, the data lies between the models for the full p_{T} range, with the LBT model above the data and the JETSCAPE model below the data. Additionally, the data shows larger values of the $R_{\mathrm{AA}}^{\mathrm{pair}}(R = 0.6)/R_{\mathrm{AA}}^{\mathrm{pair}}(R = 0.2)$ ratio for the leading jets than for the subleading jets. The JETSCAPE model predicts this order while the LBT model predicts the opposite order.

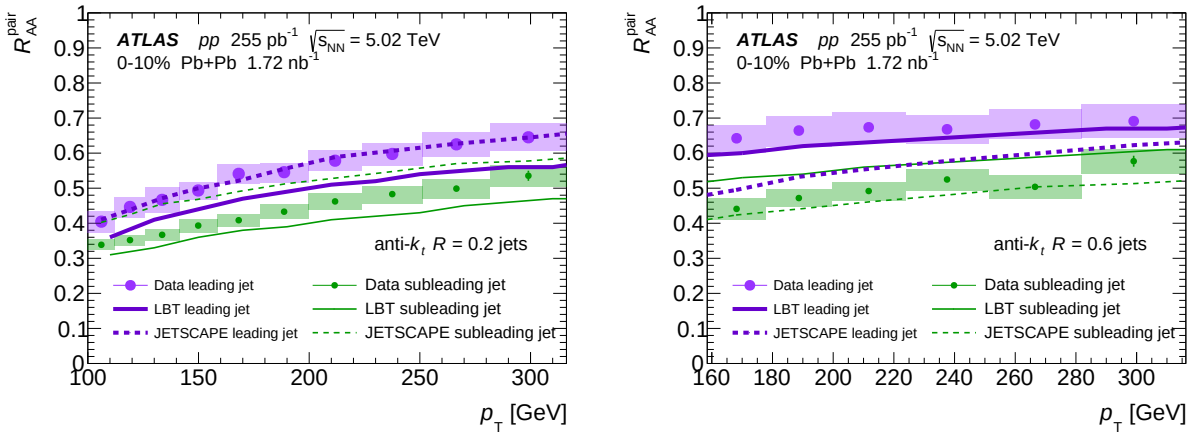

Figure 4.58: Leading and subleading jet $R_{\mathrm{AA}}^{\mathrm{pair}}$ distributions in dijets in data, compared with the LBT and JETSCAPE (LBT+MATTER) models. $R = 0.2$ (left) and $R = 0.6$ (right) jets are shown for 0–10% central collisions. Jets are selected with $|y| < 2.1$ and $|\phi_1 - \phi_2| > 7\pi/8$. The normalization uncertainties in the data (not shown) are $\delta\langle T_{\mathrm{AA}}\rangle/\langle T_{\mathrm{AA}}\rangle = 0.9\%$ in 0–10% Pb+Pb collisions and $\delta L_{pp}/L_{pp} = 1\%$ in pp collisions. The boxes correspond to systematic uncertainties and the bars to statistical uncertainties.

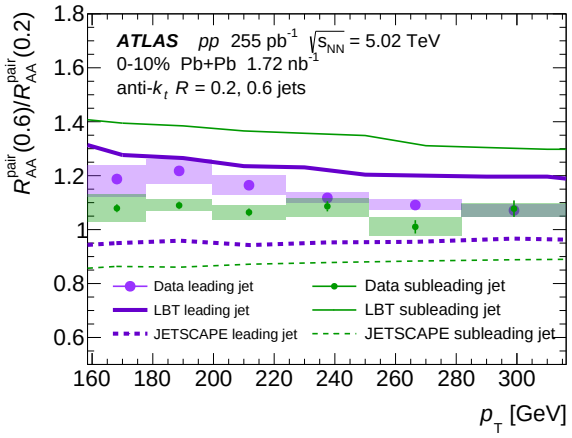

Figure 4.59: Leading and subleading jet $R_{\mathrm{AA}}^{\mathrm{pair}}(R = 0.6)/R_{\mathrm{AA}}^{\mathrm{pair}}(R = 0.2)$ in dijets in data, compared with the LBT and JETSCAPE (LBT+MATTER) models, for 0–10% central collisions. Jets are selected with $|y| < 2.1$ and $|\phi_1 - \phi_2| > 7\pi/8$. The boxes correspond to systematic uncertainties and the bars to statistical uncertainties.

Chapter 5

Summary and conclusions

The quark gluon plasma (QGP) is an ultra hot, ultra dense state of matter in which partons are deconfined. The QGP can be created in ultrarelativistic heavy ion collisions in which nuclei of heavy elements are collided at almost the speed of light. Partons are hard scattered in these collisions, interact with the QGP as they traverse it, and come out as pairs of back-to-back jets called dijets. Dijet measurements provide a powerful tool for studying the QGP.

This thesis presents a measurement of the jet radius dependence of the dijet momentum balance between leading back-to-back jets in Pb+Pb and pp collisions at a per-nucleon-pair center of mass energy $\sqrt{s_{\mathrm{NN}}} = 5.02$ TeV, measured by the ATLAS detector at the LHC. The data corresponds to a total integrated luminosity of 1.72 nb^{-1} of Pb+Pb collisions collected in 2018 and 255 pb^{-1} of pp collisions collected in 2017.

Dijets were studied for jet radii $R = 0.2, 0.3, 0.4, 0.5$ and 0.6 by measuring the absolutely normalized x_{J} distributions, the J_{AA} distributions, and the $R_{\mathrm{AA}}^{\mathrm{pair}}$ distributions. The measurements cover a broad jet transverse momentum range, with leading jet p_{T} ranging from 100 to 562 GeV for $R = 0.2, 0.3$ and 0.4 jets, and from 158 to 562 GeV for $R = 0.5$ and 0.6 jets.

The analysis focused on measuring the two-dimensional yield of dijets as a function of leading and subleading jet transverse momentum. These dijet yields were corrected for the combinatoric dijet background and unfolded using an iterative Bayesian method. The unfolded dijet yields were normalized and projected to construct x_{J}, $R_{\mathrm{AA}}^{\mathrm{pair}}$, and J_{AA} distributions. Systematic uncertainties were considered in order to account for the effects of the jet energy scale and resolution, the unfolding, and the combinatoric dijet background.

The results show that larger jet radii give x_{J} distributions peaked at higher x_{J} values, whereas smaller jet radii give flatter distributions, as seen in Figures 4.48 and 4.50. This is true in both the Pb+Pb and pp collisions, but the Pb+Pb collisions show broader and more modified distributions compared to pp, with the modifications being larger for more central collisions, as seen in Figure 4.51.

The J_{AA} results for more imbalanced dijets, primarily at low leading jet transverse momentum, show that jet suppression decreases (J_{AA} increases) with increasing jet radius, as seen in Figures 4.54 and 4.55. For more balanced dijets, the suppression is also present and dependent on jet radius, but smaller in magnitude

than for imbalanced dijets. The modifications are stronger for more central collisions, as seen in Figure 4.52.

The $R_{\mathrm{AA}}^{\mathrm{pair}}$ results show that subleading jets in dijets are more suppressed than leading jets, for the various jet radii considered, as seen in Figure 4.44. Significant jet radius dependence of the $R_{\mathrm{AA}}^{\mathrm{pair}}$ is observed, with jet suppression decreasing ($R_{\mathrm{AA}}^{\mathrm{pair}}$ increasing) with increasing jet radius, as seen in Figure 4.46. This jet radius dependence is observed in both the leading jet $R_{\mathrm{AA}}^{\mathrm{pair}}(p_{\mathrm{T},1})$ and subleading jet $R_{\mathrm{AA}}^{\mathrm{pair}}(p_{\mathrm{T},2})$, though not in the $R_{\mathrm{AA}}^{\mathrm{pair}}(p_{\mathrm{T},2})/R_{\mathrm{AA}}^{\mathrm{pair}}(p_{\mathrm{T},1})$ ratio, which is dependent on centrality only, as seen in Figure 4.45.

These results present a comprehensive look at the modification of dijet rates in Pb+Pb collisions compared to *pp* collisions. These results are complementary to existing measurements of the jet radius dependence of jet suppression, and will provide important new constraints to theoretical models of jet energy loss.

Bibliography

[1] M. Thomson, *Modern particle physics*, New York: Cambridge University Press, 2013, ISBN: 978-1-107-03426-6 (cit. on pp. 1, 3, 12).

[2] P. D. Group et al., *Review of Particle Physics*, Progress of Theoretical and Experimental Physics **2022** (2022) 083C01, ISSN: 2050-3911, eprint: https://academic.oup.com/ptep/article-pdf/2022/8/083C01/49175539/ptac097.pdf, URL: https://doi.org/10.1093/ptep/ptac097 (cit. on pp. 1–3).

[3] Wikimedia Commons, *File:Standard Model of Elementary Particles.svg*, URL: https://en.wikipedia.org/wiki/File:Standard_Model_of_Elementary_Particles.svg (cit. on p. 1).

[4] B. V. Jacak and B. Müller, *The Exploration of Hot Nuclear Matter*, Science **337** (2012) 310, ISSN: 0036-8075, URL: http://science.sciencemag.org/content/337/6092/310 (cit. on pp. 3, 4).

[5] M. Connors, C. Nattrass, R. Reed, and S. Salur, *Jet measurements in heavy ion physics*, Rev. Mod. Phys. **90** (2 2018) 025005, URL: https://link.aps.org/doi/10.1103/RevModPhys.90.025005 (cit. on pp. 3, 7, 8).

[6] S. Sarkar, H. Satz, and B. Sinha, eds., *The physics of the quark-gluon plasma*, vol. 785, 2010 (cit. on p. 4).

[7] W. Busza, K. Rajagopal, and W. van der Schee, *Heavy Ion Collisions: The Big Picture and the Big Questions*, Annual Review of Nuclear and Particle Science **68** (2018) 339, ISSN: 1545-4134, URL: http://dx.doi.org/10.1146/annurev-nucl-101917-020852 (cit. on pp. 4, 8).

[8] M. L. Miller, K. Reygers, S. J. Sanders, and P. Steinberg, *Glauber Modeling in High-Energy Nuclear Collisions*, Annual Review of Nuclear and Particle Science **57** (2007) 205, ISSN: 1545-4134, URL: http://dx.doi.org/10.1146/annurev.nucl.57.090506.123020 (cit. on pp. 5, 6, 19, 21).

[9] *Observation of a Centrality-Dependent Dijet Asymmetry in Lead-Lead Collisions at $\sqrt{s_{NN}}$=2.76 TeV with the ATLAS Detector at the LHC*, Physical Review Letters **105** (2010), ISSN: 1079-7114, URL: http://dx.doi.org/10.1103/PhysRevLett.105.252303 (cit. on pp. 7, 14).

[10] A. K. Chaudhuri, *Viscous Hydrodynamic Model for Relativistic Heavy Ion Collisions*, Advances in High Energy Physics **2013** (2013), URL: https://doi.org/10.1155/2013/693180 (cit. on p. 7).

[11] *Measurement of the pseudorapidity and transverse momentum dependence of the elliptic flow of charged particles in lead-lead collisions at $\sqrt{s_{NN}}$ = 2.76 TeV with the ATLAS detector.*, Phys. Lett. B **707** (2011) 330, URL: https://cds.cern.ch/record/1379860 (cit. on p. 7).

[12] A. M. Poskanzer and S. A. Voloshin, *Methods for analyzing anisotropic flow in relativistic nuclear collisions*, Physical Review C **58** (1998) 1671, ISSN: 1089-490X, URL: http://dx.doi.org/10.1103/PhysRevC.58.1671 (cit. on pp. 7, 23).

[13] K. H. Ackermann et al., *Elliptic flow in Au + Au collisions at (S(NN))**(1/2) = 130 GeV*, Phys. Rev. Lett. **86** (2001) 402, arXiv: nucl-ex/0009011 (cit. on pp. 7, 9).

[14] K. Aamodt et al., *Higher harmonic anisotropic flow measurements of charged particles in Pb-Pb collisions at $\sqrt{s_{NN}}$=2.76 TeV*, Phys. Rev. Lett. **107** (2011) 032301, arXiv: 1105.3865 [nucl-ex] (cit. on pp. 7, 10).

[15] J. Adam et al., *Anisotropic flow of charged particles in Pb-Pb collisions at $\sqrt{s_{\mathrm{NN}}}$ = 5.02 TeV*, Phys. Rev. Lett. **116** (2016) 132302, arXiv: 1602.01119 [nucl-ex] (cit. on pp. 7, 9).

[16] *Creation of quark–gluon plasma droplets with three distinct geometries*, Nature Physics **15** (2018) 214, ISSN: 1745-2481, URL: http://dx.doi.org/10.1038/s41567-018-0360-0 (cit. on pp. 8, 10).

[17] M. Habich, J. L. Nagle, and P. Romatschke, *Particle spectra and HBT radii for simulated central nuclear collisions of C+C, Al+Al, Cu+Cu, Au+Au, and Pb+Pb from $\sqrt{s}$=62.4 – 2760 GeV*, The European Physical Journal C **75** (2015), ISSN: 1434-6052, URL: http://dx.doi.org/10.1140/epjc/s10052-014-3206-7 (cit. on p. 8).

[18] B. Alver and G. Roland, *Collision geometry fluctuations and triangular flow in heavy-ion collisions*, Phys. Rev. C **81** (2010) 054905, [Erratum: Phys.Rev.C 82, 039903 (2010)], arXiv: 1003.0194 [nucl-th] (cit. on p. 8).

[19] S. Voloshin and Y. Zhang,
Flow study in relativistic nuclear collisions by Fourier expansion of azimuthal particle distributions,
Zeitschrift fur Physik C Particles and Fields **70** (1996) 665, ISSN: 1431-5858,
URL: http://dx.doi.org/10.1007/s002880050141 (cit. on p. 8).

[20] J. E. Bernhard, J. S. Moreland, and S. A. Bass,
Bayesian estimation of the specific shear and bulk viscosity of quark–gluon plasma,
Nature Phys. **15** (2019) 1113 (cit. on p. 8).

[21] P. K. Kovtun, D. T. Son, and A. O. Starinets,
Viscosity in Strongly Interacting Quantum Field Theories from Black Hole Physics,
Physical Review Letters **94** (2005), ISSN: 1079-7114,
URL: http://dx.doi.org/10.1103/PhysRevLett.94.111601 (cit. on p. 9).

[22] M. Cacciari, G. P. Salam, and G. Soyez, *The anti-k_t jet clustering algorithm*, JHEP **04** (2008) 063,
arXiv: 0802.1189 [hep-ph] (cit. on pp. 12, 16, 39).

[23] *Measurement of the inclusive jet cross-section in proton-proton collisions at $\sqrt{s} = 7$ TeV using 4.5 $fb^{-}1$ of data with the ATLAS detector*, Journal of High Energy Physics **2015** (2015), ISSN: 1029-8479,
URL: http://dx.doi.org/10.1007/JHEP02(2015)153 (cit. on pp. 12, 13).

[24] *Measurement of the inclusive jet cross-sections in proton-proton collisions at $\sqrt{s} = 8$ TeV with the ATLAS detector*, Journal of High Energy Physics **2017** (2017), ISSN: 1029-8479,
URL: http://dx.doi.org/10.1007/JHEP09(2017)020 (cit. on pp. 12, 13).

[25] *Measurement of inclusive jet and dijet cross-sections in proton-proton collisions at $\sqrt{s} = 13$ TeV with the ATLAS detector*, Journal of High Energy Physics **2018** (2018), ISSN: 1029-8479,
URL: http://dx.doi.org/10.1007/JHEP05(2018)195 (cit. on pp. 12, 13).

[26] *Measurement of the double-differential inclusive jet cross section in proton–proton collisions at $\sqrt{s} = 13$ TeV*, The European Physical Journal C **76** (2016), ISSN: 1434-6052,
URL: http://dx.doi.org/10.1140/epjc/s10052-016-4286-3 (cit. on pp. 12, 13).

[27] *Measurement and QCD analysis of double-differential inclusive jet cross sections in pp collisions at $\sqrt{s} = 8$ TeV and cross section ratios to 2.76 and 7 TeV*, Journal of High Energy Physics **2017** (2017),
ISSN: 1029-8479, URL: http://dx.doi.org/10.1007/JHEP03(2017)156 (cit. on pp. 12, 13).

[28] G.-Y. Qin and X.-N. Wang, *Jet quenching in high-energy heavy-ion collisions*,
Int. J. Mod. Phys. E **24** (2015) 1530014, ed. by X.-N. Wang, arXiv: 1511.00790 [hep-ph]
(cit. on pp. 12, 14).

[29] G.-Y. Qin and B. Müller,
Explanation of Dijet Asymmetry in Pb+Pb Collisions at the Large Hadron Collider,
Phys. Rev. Lett. **106** (2011) 162302, arXiv: 1012.5280 [hep-ph] (cit. on pp. 14, 15),
Erratum: Phys. Rev. Lett. **106** (2011) 162302.

[30] *Observation and studies of jet quenching in PbPb collisions at* $\sqrt{s_{NN}} = 2.76TeV$,
Physical Review C **84** (2011), ISSN: 1089-490X,
URL: http://dx.doi.org/10.1103/PhysRevC.84.024906 (cit. on p. 14).

[31] ATLAS Collaboration, *Measurement of the dijet momentum balance in Pb+Pb and pp collisions at* $\sqrt{s_{NN}} = 5.02$ *TeV with the ATLAS detector*, ATLAS-CONF-2020-017, 2020,
URL: https://cds.cern.ch/record/2720247 (cit. on p. 14).

[32] *Measurement of jet pT correlations in Pb+Pb and pp collisions at* $\sqrt{s_{NN}}$*=2.76 TeV with the ATLAS detector*, Physics Letters B **774** (2017) 379, ISSN: 0370-2693,
URL: http://www.sciencedirect.com/science/article/pii/S0370269317307906 (cit. on p. 14).

[33] L. Cunqueiro and A. M. Sickles, *Studying the QGP with Jets at the LHC and RHIC*,
Prog. Part. Nucl. Phys. **124** (2022) 103940, arXiv: 2110.14490 [nucl-ex] (cit. on p. 14).

[34] I. Vitev, S. Wicks, and B.-W. Zhang,
A Theory of jet shapes and cross sections: From hadrons to nuclei, JHEP **11** (2008) 093,
arXiv: 0810.2807 [hep-ph] (cit. on p. 15).

[35] M. L. Miller, K. Reygers, S. J. Sanders, and P. Steinberg,
Glauber modeling in high energy nuclear collisions, Ann. Rev. Nucl. Part. Sci. **57** (2007) 205,
arXiv: nucl-ex/0701025 (cit. on pp. 15, 46).

[36] ATLAS Collaboration, *Measurements of azimuthal anisotropies of jet production in Pb+Pb collisions at* $\sqrt{s_{NN}} = 5.02$ *TeV with the ATLAS detector*, Phys. Rev. C **105** (2021) 064903,
arXiv: 2111.06606 [nucl-ex] (cit. on pp. 15, 39).

[37] J. G. Milhano and K. C. Zapp, *Origins of the di-jet asymmetry in heavy ion collisions*,
Eur. Phys. J. C **76** (2016) 288, arXiv: 1512.08107 [hep-ph] (cit. on p. 15).

[38] ATLAS Collaboration, *Measurement of jet* p_{T} *correlations in Pb+Pb and pp collisions at* $\sqrt{s_{\mathrm{NN}}} =$ *2.76 TeV with the ATLAS detector*, Phys. Lett. B **774** (2017) 379, arXiv: 1706.09363 [hep-ex] (cit. on pp. 16, 17, 69).

[39] ATLAS Collaboration,
Measurements of the suppression and correlations of dijets in Pb+Pb collisions at $\sqrt{s_{NN}} = 5.02$ *TeV*, (2022), arXiv: 2205.00682 [nucl-ex] (cit. on pp. 16, 17, 21, 22, 29, 30, 69, 71, 84),
Erratum: Phys. Rev. C **109** (2 2024) 029901.

[40] ATLAS Collaboration, *Observation of a Centrality-Dependent Dijet Asymmetry in Lead-Lead Collisions at* $\sqrt{s_{NN}} = 2.77$ *TeV with the ATLAS Detector at the LHC*,
Phys. Rev. Lett. **105** (2010) 252303, arXiv: 1011.6182 [hep-ex] (cit. on pp. 16, 17).

[41] CMS Collaboration, *Observation and studies of jet quenching in PbPb collisions at nucleon-nucleon center-of-mass energy = 2.76 TeV*, Phys. Rev. C **84** (2011) 024906, arXiv: 1102.1957 [nucl-ex] (cit. on pp. 16, 17).

[42] ATLAS Collaboration, *Measurement of the nuclear modification factor for inclusive jets in Pb+Pb collisions at* $\sqrt{s_{\mathrm{NN}}} = 5.02$ *TeV with the ATLAS detector*, Phys. Lett. B **790** (2019) 108, arXiv: 1805.05635 [nucl-ex] (cit. on pp. 16, 39).

[43] A. Collaboration, *Jet radius dependence of dijet momentum balance and suppression in Pb+Pb collisions at 5.02 TeV with the ATLAS detector*, 2024, arXiv: 2407.18796 [nucl-ex], URL: https://arxiv.org/abs/2407.18796 (cit. on p. 16).

[44] ATLAS Collaboration, *The ATLAS Experiment at the CERN Large Hadron Collider*, JINST **3** (2008) S08003 (cit. on p. 16).

[45] *Measurement of the nuclear modification factor for inclusive jets in Pb+Pb collisions at* $\sqrt{s_{NN}}$*=5.02 TeV with the ATLAS detector*, Physics Letters B **790** (2019) 108, ISSN: 0370-2693, URL: http://www.sciencedirect.com/science/article/pii/S037026931830995X (cit. on pp. 19, 20).

[46] *Measurements of the Nuclear Modification Factor for Jets in Pb+Pb Collisions at* $\sqrt{s_{\mathrm{NN}}} = 2.76$ TeV *with the ATLAS Detector*, Phys. Rev. Lett. **114** (7 2015) 072302, URL: https://link.aps.org/doi/10.1103/PhysRevLett.114.072302 (cit. on p. 19).

[47] *Measurement of inclusive jet cross sections in pp and PbPb collisions at* $\sqrt{s_{NN}} = 2.76$ *TeV*, Phys. Rev. C **96** (2017) 015202, arXiv: 1609.05383 [nucl-ex] (cit. on pp. 19, 20).

[48] S. Chatrchyan et al., *Evidence of b-Jet Quenching in PbPb Collisions at* $\sqrt{s_{NN}} = 2.76$ TeV, Phys. Rev. Lett. **113** (13 2014) 132301, URL: https://link.aps.org/doi/10.1103/PhysRevLett.113.132301 (cit. on p. 21),
Erratum: S. Chatrchyan and Anonymous, *Erratum: Evidence of b-Jet Quenching in PbPb Collisions*

at $\sqrt{s_{NN}} = 2.76$ TeV *[Phys. Rev. Lett. 113, 132301 (2014)]*, Phys. Rev. Lett. **115** (2 2015) 029903, URL: https://link.aps.org/doi/10.1103/PhysRevLett.115.029903.

[49] ATLAS Collaboration, *Measurement of the nuclear modification factor of b-jets in* 5.02 *TeV Pb+Pb collisions with the ATLAS detector*, (2022), arXiv: 2204.13530 [nucl-ex] (cit. on p. 21).

[50] CMS Collaboration,
Measurement of isolated photon production in pp and PbPb collisions at $\sqrt{s_{NN}} = 2.76$ *TeV*,
Phys. Lett. B **710** (2012) 256, arXiv: 1201.3093 [hep-ex] (cit. on pp. 21, 22).

[51] G. Aad et al.,
Z boson production in Pb+Pb collisions at $\sqrt{s_{NN}} = 5.02$ *TeV measured by the ATLAS experiment*,
Physics Letters B **802** (2020) 135262, ISSN: 0370-2693,
URL: http://dx.doi.org/10.1016/j.physletb.2020.135262 (cit. on pp. 21, 22).

[52] A. Collaboration, *Measurements of azimuthal anisotropies of jet production in Pb+Pb collisions at* $\sqrt{s_{NN}} = 5.02$ *TeV with the ATLAS detector*, Physical Review C **105** (2022), ISSN: 2469-9993,
URL: http://dx.doi.org/10.1103/PhysRevC.105.064903 (cit. on pp. 23, 24).

[53] *Measurement of jet fragmentation in Pb+Pb and pp collisions at* $\sqrt{s_{NN}} = 5.02$ *TeV with the ATLAS detector*, Phys. Rev. C **98** (2 2018) 024908,
URL: https://link.aps.org/doi/10.1103/PhysRevC.98.024908 (cit. on pp. 25–27).

[54] M. Spousta and B. Cole, *Interpreting single jet measurements in Pb+Pb collisions at the LHC*,
The European Physical Journal C **76** (2016), ISSN: 1434-6052,
URL: http://dx.doi.org/10.1140/epjc/s10052-016-3896-0 (cit. on p. 25).

[55] A. Puri, *Measurement of angular and momentum distributions of charged particles within and around jets in Pb+Pb and pp collisions at sqrt*(s_{NN}) *=5.02 TeV with ATLAS at the LHC*,
(2019), PhD thesis at the University of Illinois at Urbana-Champaign,
URL: http://hdl.handle.net/2142/106141 (cit. on p. 28).

[56] *Measurement of angular and momentum distributions of charged particles within and around jets in Pb+Pb and pp collisions at* $\sqrt{s_{NN}}$*=5.02 TeV with the ATLAS detector*,
Physical Review C **100** (2019), ISSN: 2469-9993,
URL: http://dx.doi.org/10.1103/PhysRevC.100.064901 (cit. on pp. 27, 28).

[57] D. Pablos, *Jet Suppression From a Small to Intermediate to Large Radius*,
Phys. Rev. Lett. **124** (2020) 052301, arXiv: 1907.12301 [hep-ph] (cit. on p. 30).

[58] Y. Mehtar-Tani, D. Pablos, and K. Tywoniuk,
Jet Suppression and Azimuthal Anisotropy from RHIC to LHC, 2024, arXiv: 2402.07869 [hep-ph] (cit. on p. 30).

[59] ATLAS Collaboration, *Measurement of the jet radius and transverse momentum dependence of inclusive jet suppression in lead-lead collisions at $\sqrt{s_{NN}}$= 2.76 TeV with the ATLAS detector*, Phys. Lett. B **719** (2013) 220, arXiv: 1208.1967 [hep-ex] (cit. on p. 30).

[60] ATLAS Collaboration, *Measurement of the jet radius and transverse momentum dependence of inclusive jet suppression in lead–lead collisions at $\sqrt{s_{NN}}$ = 2.76 TeV with the ATLAS detector*, Phys. Lett. B **719** (2013) 220, arXiv: 1208.1967 [hep-ex] (cit. on pp. 31, 86).

[61] ALICE Collaboration, *Measurement of the radius dependence of charged-particle jet suppression in Pb-Pb collisions at $\sqrt{s_{NN}}$ = 5.02 TeV*, (2023), arXiv: 2303.00592 [nucl-ex] (cit. on pp. 30, 32).

[62] CMS Collaboration,
First measurement of large area jet transverse momentum spectra in heavy-ion collisions, JHEP **05** (2021) 284, arXiv: 2102.13080 [hep-ex] (cit. on pp. 30, 32).

[63] L. Evans and P. Bryant, *LHC Machine*, Journal of Instrumentation **3** (2008) S08001, URL: https://dx.doi.org/10.1088/1748-0221/3/08/S08001 (cit. on p. 33).

[64] O. S. Brüning et al., *LHC Design Report*, CERN Yellow Reports: Monographs, Geneva: CERN, 2004, URL: https://cds.cern.ch/record/782076 (cit. on p. 33).

[65] "LHC Guide", 2017, URL: https://cds.cern.ch/record/2255762 (cit. on p. 33).

[66] CERN, *The CERN accelerator complex, layout in 2022*,
https://cds.cern.ch/images/CERN-GRAPHICS-2022-001-1,
URL: https://cds.cern.ch/images/CERN-GRAPHICS-2022-001-1 (cit. on p. 34).

[67] *The ATLAS Experiment at the CERN Large Hadron Collider*,
JINST **3** (2008) S08003. 437 p, Also published by CERN Geneva in 2010,
URL: https://cds.cern.ch/record/1129811 (cit. on pp. 33, 34).

[68] J. Wenninger, *Operation and Configuration of the LHC in Run 2*, (2019),
URL: https://cds.cern.ch/record/2668326 (cit. on p. 33).

[69] R. M. Bianchi and A. Collaboration, "ATLAS experiment schematic or layout illustration", General Photo, 2022, URL: https://cds.cern.ch/record/2837191 (cit. on pp. 34, 35).

[70] ATLAS Collaboration, *ATLAS Inner Detector: Technical Design Report, Volume 1*, ATLAS-TDR-4; CERN-LHCC-97-016, 1997, URL: https://cds.cern.ch/record/331063 (cit. on p. 35).

[71] ATLAS Collaboration, *ATLAS Inner Detector: Technical Design Report, Volume 2*, ATLAS-TDR-5, CERN-LHCC-97-017, 1997, URL: https://cds.cern.ch/record/331064 (cit. on p. 35).

[72] K. Potamianos, *The upgraded Pixel detector and the commissioning of the Inner Detector tracking of the ATLAS experiment for Run-2 at the Large Hadron Collider*, 2016, arXiv: 1608.07850 [physics.ins-det] (cit. on p. 35).

[73] CERN, *Experiment Briefing: Keeping the ATLAS Inner Detector in perfect alignment*, https://cds.cern.ch/images/ATLAS-PHOTO-2020-018-1, URL: https://cds.cern.ch/images/ATLAS-PHOTO-2020-018-1 (cit. on p. 36).

[74] ATLAS Collaboration, *ATLAS Insertable B-Layer Technical Design Report*, ATLAS-TDR-19; CERN-LHCC-2010-013, 2010, URL: https://cds.cern.ch/record/1291633 (cit. on p. 36), Addendum: ATLAS-TDR-19-ADD-1; CERN-LHCC-2012-009, 2012, URL: https://cds.cern.ch/record/1451888.

[75] B. Abbott et al., *Production and integration of the ATLAS Insertable B-Layer*, JINST **13** (2018) T05008, arXiv: 1803.00844 [physics.ins-det] (cit. on p. 36).

[76] ATLAS Collaboration, *ATLAS Calorimeter Performance: Technical Design Report*, ATLAS-TDR-1; CERN-LHCC-96-040, 1996, URL: https://cds.cern.ch/record/331059 (cit. on p. 37).

[77] CERN, *Computer Generated image of the ATLAS calorimeter*, https://cds.cern.ch/images/CERN-GE-0803015-01, URL: https://cds.cern.ch/images/CERN-GE-0803015-01 (cit. on p. 37).

[78] ATLAS Collaboration, *ATLAS Liquid Argon Calorimeter: Technical Design Report*, ATLAS-TDR-2; CERN-LHCC-96-041, 1996, URL: https://cds.cern.ch/record/331061 (cit. on p. 37).

[79] ATLAS Collaboration, *ATLAS Tile Calorimeter: Technical Design Report*, ATLAS-TDR-3; CERN-LHCC-96-042, 1996, URL: https://cds.cern.ch/record/331062 (cit. on p. 38).

[80] ATLAS Collaboration, *ATLAS Muon Spectrometer: Technical Design Report*, ATLAS-TDR-10; CERN-LHCC-97-022, CERN, 1997, URL: https://cds.cern.ch/record/331068 (cit. on p. 38).

[81] ATLAS Collaboration, *ATLAS Muon Spectrometer Phase-II Upgrade: Technical Design Report*, ATLAS-TDR-026; CERN-LHCC-2017-017, 2017, URL: https://cds.cern.ch/record/2285580 (cit. on p. 38).

[82] *ATLAS muon spectrometer: Technical Design Report*, Technical design report. ATLAS, Geneva: CERN, 1997, URL: https://cds.cern.ch/record/331068 (cit. on p. 38).

[83] T. Kawamoto et al., *New Small Wheel Technical Design Report*, (2013) (cit. on p. 38).

[84] ATLAS Collaboration, *Performance of the ATLAS trigger system in 2015*, Eur. Phys. J. C **77** (2017) 317, arXiv: 1611.09661 [hep-ex] (cit. on pp. 39, 47).

[85] ATLAS Collaboration, *The ATLAS Collaboration Software and Firmware*, ATL-SOFT-PUB-2021-001, 2021, URL: https://cds.cern.ch/record/2767187 (cit. on p. 39).

[86] ATLAS Collaboration, *Trigger menu in 2018*, tech. rep., All figures including auxiliary figures are available at https://atlas.web.cern.ch/Atlas/GROUPS/PHYSICS/PUBNOTES/ATL-DAQ-PUB-2019-001: CERN, 2019, URL: https://cds.cern.ch/record/2693402 (cit. on pp. 39, 47).

[87] M. Cacciari, G. P. Salam, and G. Soyez, *FastJet User Manual*, Eur. Phys. J. C **72** (2012) 1896, arXiv: 1111.6097 [hep-ph] (cit. on p. 39).

[88] *Performance plots from 2018 Pb+Pb collisions at $\sqrt{s_{NN}}$ = 5.02 TeV for Council Week*, tech. rep., CERN, 2018, URL: https://atlas.web.cern.ch/Atlas/GROUPS/PHYSICS/PLOTS/HION-2018-001/ (cit. on p. 40).

[89] ATLAS Collaboration, *Jet energy scale and its uncertainty for jets reconstructed using the ATLAS heavy ion jet algorithm*, ATLAS-CONF-2015-016, 2015, URL: https://cds.cern.ch/record/2008677 (cit. on p. 40).

[90] ATLAS Collaboration, *Measurement of the azimuthal anisotropy of charged particles produced in $\sqrt{s_{NN}} = 5.02$ TeV Pb+Pb collisions with the ATLAS detector*, Eur. Phys. J. C **78** (2018) 997, arXiv: 1808.03951 [hep-ex] (cit. on p. 40).

[91] ATLAS Collaboration, *Jet energy measurement and its systematic uncertainty in proton-proton collisions at $\sqrt{s} = 7$ TeV with the ATLAS detector*, Eur. Phys. J. C **75** (2015) 17, arXiv: 1406.0076 [hep-ex] (cit. on p. 40).

[92] ATLAS Collaboration,
Jet energy scale and its uncertainty for jets reconstructed using the ATLAS heavy ion jet algorithm,
ATLAS-CONF-2015-016, 2015, URL: https://cds.cern.ch/record/2008677
(cit. on pp. 40, 41, 71, 75).

[93] ATLAS Collaboration, *Measurement of photon-jet transverse momentum correlations in* 5.02 *TeV Pb+Pb and pp collisions with ATLAS*, Phys. Lett. B **789** (2019) 167, arXiv: 1809.07280 [hep-ex]
(cit. on p. 40).

[94] T. Sjöstrand et al., *An introduction to PYTHIA 8.2*, Comput. Phys. Commun. **191** (2015) 159,
arXiv: 1410.3012 [hep-ph] (cit. on pp. 44, 48).

[95] S. Agostinelli et al., *GEANT4–a simulation toolkit*, Nucl. Instrum. Meth. A **506** (2003) 250
(cit. on pp. 44, 48, 49).

[96] ATLAS Collaboration, *The ATLAS Simulation Infrastructure*, Eur. Phys. J. C **70** (2010) 823,
arXiv: 1005.4568 [physics.ins-det] (cit. on pp. 44, 48, 49).

[97] ATLAS Collaboration, *Measurement of longitudinal flow decorrelations in Pb+Pb collisions at* $\sqrt{s_{NN}} = 2.76$ *and 5.02 TeV with the ATLAS detector*, Eur. Phys. J. C **78** (2018) 142,
arXiv: 1709.02301 [nucl-ex] (cit. on p. 46).

[98] C. Loizides, J. Kamin, and D. d'Enterria,
Improved Monte Carlo Glauber predictions at present and future nuclear colliders,
Phys. Rev. C **97** (2018) 054910, arXiv: 1710.07098 [nucl-ex] (cit. on p. 46),
Erratum: Phys. Rev. C **99** (2018) 019901.

[99] ATLAS Collaboration, *Measurement of* $W^{\pm}$ *boson production in Pb+Pb collisions at* $\sqrt{s_{\mathrm{NN}}} = 5.02$ *TeV with the ATLAS detector*, Eur. Phys. J. C **79** (2019) 935,
arXiv: 1907.10414 [nucl-ex] (cit. on p. 46).

[100] ATLAS Collaboration, *Operation of the ATLAS trigger system in Run 2*, JINST **15** (2020) P10004,
arXiv: 2007.12539 [physics.ins-det] (cit. on p. 47).

[101] ATLAS Collaboration, *ATLAS Pythia 8 tunes to* 7 *TeV data*, ATL-PHYS-PUB-2014-021, 2014,
URL: https://cds.cern.ch/record/1966419 (cit. on p. 48).

[102] R. D. Ball et al., *Parton distributions with LHC data*, Nucl. Phys. B **867** (2013) 244,
arXiv: 1207.1303 [hep-ph] (cit. on p. 48).

[103] M. Bähr et al., *Herwig++ physics and manual*, Eur. Phys. J. C **58** (2008) 639,
arXiv: 0803.0883 [hep-ph] (cit. on p. 49).

[104] J. Bellm et al., *Herwig 7.0/Herwig++ 3.0 release note*, Eur. Phys. J. C **76** (2016) 196, arXiv: 1512.01178 [hep-ph] (cit. on p. 49).

[105] S. Gieseke, C. Röhr, and A. Siódmok, *Colour reconnections in Herwig++*, Eur. Phys. J. C **72** (2012) 2225, arXiv: 1206.0041 [hep-ph] (cit. on p. 49).

[106] J. Pumplin et al., *New generation of Parton Distributions with Uncertainties from Global QCD Analysis*, JHEP **07** (2002) 012, arXiv: hep-ph/0201195 (cit. on p. 49).

[107] G. D'Agostini, *A Multidimensional unfolding method based on Bayes' theorem*, Nucl. Instrum. Meth. A **362** (1995) 487 (cit. on p. 60).

[108] T. Adye, "Unfolding algorithms and tests using RooUnfold", *Proceedings of the PHYSTAT 2011 Workshop*, CERN Yellow Reports: Conference Proceedings, Geneva: CERN, 2011 313, arXiv: 1105.1160 [physics.data-an], URL: http://dx.doi.org/10.5170/CERN-2011-006 (cit. on p. 60).

[109] *Evaluating statistical uncertainties and correlations using the bootstrap method*, (2021), All figures including auxiliary figures are available at https://atlas.web.cern.ch/Atlas/GROUPS/PHYSICS/PUBNOTES/ATL-PHYS-PUB-2021-011, URL: https://cds.cern.ch/record/2759945 (cit. on p. 60).

[110] ATLAS Collaboration, *Measurements of the suppression and correlations of dijets in Xe+Xe collisions at* $\sqrt{s_{NN}} = 5.44$ *TeV*, (2023), arXiv: 2302.03967 [nucl-ex] (cit. on p. 69).

[111] ATLAS Collaboration, *Jet energy scale measurements and their systematic uncertainties in proton-proton collisions at* $\sqrt{s} = 13$ *TeV with the ATLAS detector*, Phys. Rev. D **96** (2017) 072002, arXiv: 1703.09665 [hep-ex] (cit. on p. 70).

[112] ATLAS Collaboration, *Measurement of jet fragmentation in Pb+Pb and pp collisions at* $\sqrt{s_{NN}} = 5.02$ *TeV with the ATLAS detector*, Phys. Rev. C **98** (2018) 024908, arXiv: 1805.05424 [nucl-ex] (cit. on p. 75).

[113] ATLAS Collaboration, *Jet energy scale and resolution measured in proton–proton collisions at* $\sqrt{s} = 13$ *TeV with the ATLAS detector*, Eur. Phys. J. C **81** (2021) 689, arXiv: 2007.02645 [hep-ex] (cit. on p. 75).

[114] *Luminosity determination for low-pileup datasets at $\sqrt{s} = 5$ and 13 TeV using the ATLAS detector at the LHC*, tech. rep., All figures including auxiliary figures are available at https://atlas.web.cern.ch/Atlas/GROUPS/PHYSICS/CONFNOTES/ATLAS-CONF-2020-023: CERN, 2020, URL: https://cds.cern.ch/record/2725195 (cit. on p. 78).

[115] Y. He et al., *Interplaying mechanisms behind single inclusive jet suppression in heavy-ion collisions*, Phys. Rev. C **99** (5 2019) 054911, URL: https://link.aps.org/doi/10.1103/PhysRevC.99.054911 (cit. on p. 99).

[116] J. H. Putschke et al., *The JETSCAPE framework*, 2019, arXiv: 1903.07706 [nucl-th] (cit. on p. 99).

[117] S. Cao et al., *Multistage Monte-Carlo simulation of jet modification in a static medium*, Phys. Rev. C **96** (2017) 024909, arXiv: 1705.00050 [nucl-th] (cit. on p. 99).

[118] S. Cao and A. Majumder, *Nuclear modification of leading hadrons and jets within a virtuality ordered parton shower*, Physical Review C **101** (2020), ISSN: 2469-9993, URL: http://dx.doi.org/10.1103/PhysRevC.101.024903 (cit. on p. 99).

Appendix A: Additional distributions

The full set of results for the various jet radii, centrality selections, and jet transverse momentum selections are shown in this appendix.

- The leading jet yields for various Pb+Pb collisions centralities and the *pp* cross section are shown in Figure A.1, for the various jet radii. The corresponding $R/0.2$ ratios are shown in Figure A.2.
- The subleading jet yields for various Pb+Pb collisions centralities and the *pp* cross section are shown in Figure A.3, for the various jet radii. The corresponding $R/0.2$ ratios are shown in Figure A.4.
- The leading jet $R_{\mathrm{AA}}^{\mathrm{pair}}(p_{\mathrm{T},1})$ distributions for the various jet radii and various collision centralities are shown in Figure A.5. The corresponding $R/0.2$ ratios are shown in Figure A.6.
- The subleading jet $R_{\mathrm{AA}}^{\mathrm{pair}}(p_{\mathrm{T},2})$ distributions for the various jet radii and various collision centralities are shown in Figure A.7. The corresponding $R/0.2$ ratios are shown in Figure A.8.
- The absolutely normalized x_{J} distributions for the various jet radii and various $p_{\mathrm{T},1}$ bins are shown for Pb+Pb collisions in Figure A.9 for 0–10% central, in Figure A.10 for 10–20% central, in Figure A.11 for 20–40% central, in Figure A.12 for 40–60% central, in Figure A.13 for 60–80% central, and in Figure A.14 for *pp* collisions.
- The dijet-yield-normalized x_{J} distributions for the *pp* collisions, Pythia 8 and Herwig++7 simulations, and various $p_{\mathrm{T},1}$ bins are shown in Figure A.15 for $R = 0.2$ jets, in Figure A.16 for $R = 0.3$ jets, in Figure A.17 for $R = 0.4$ jets, in Figure A.18 for $R = 0.5$ jets, and in Figure A.19 for $R = 0.6$ jets.
- The J_{AA} distributions for the various jet radii and various $p_{\mathrm{T},1}$ bins are shown in Figure A.20 for 0–10% central, in Figure A.21 for 10–20% central, in Figure A.22 for 20–40% central, in Figure A.23 for 40–60% central, and in Figure A.24 for 60–80% central Pb+Pb collisions.
- The $J_{\mathrm{AA}}(R)/J_{\mathrm{AA}}(0.2)$ ratios for the various jet radii and various $p_{\mathrm{T},1}$ bins are shown in Figure A.25 for 0–10% central, in Figure A.26 for 10–20% central, in Figure A.27 for 20–40% central, in Figure A.28 for 40–60% central, and in Figure A.29 for 60–80% central Pb+Pb collisions.

- The absolutely normalized x_{J} distributions compared with the JETSCAPE model for the various jet radii and various $p_{\mathrm{T},1}$ bins are shown in Figure A.30 for 0–10% central Pb+Pb collisions and in Figure A.31 for pp collisions.

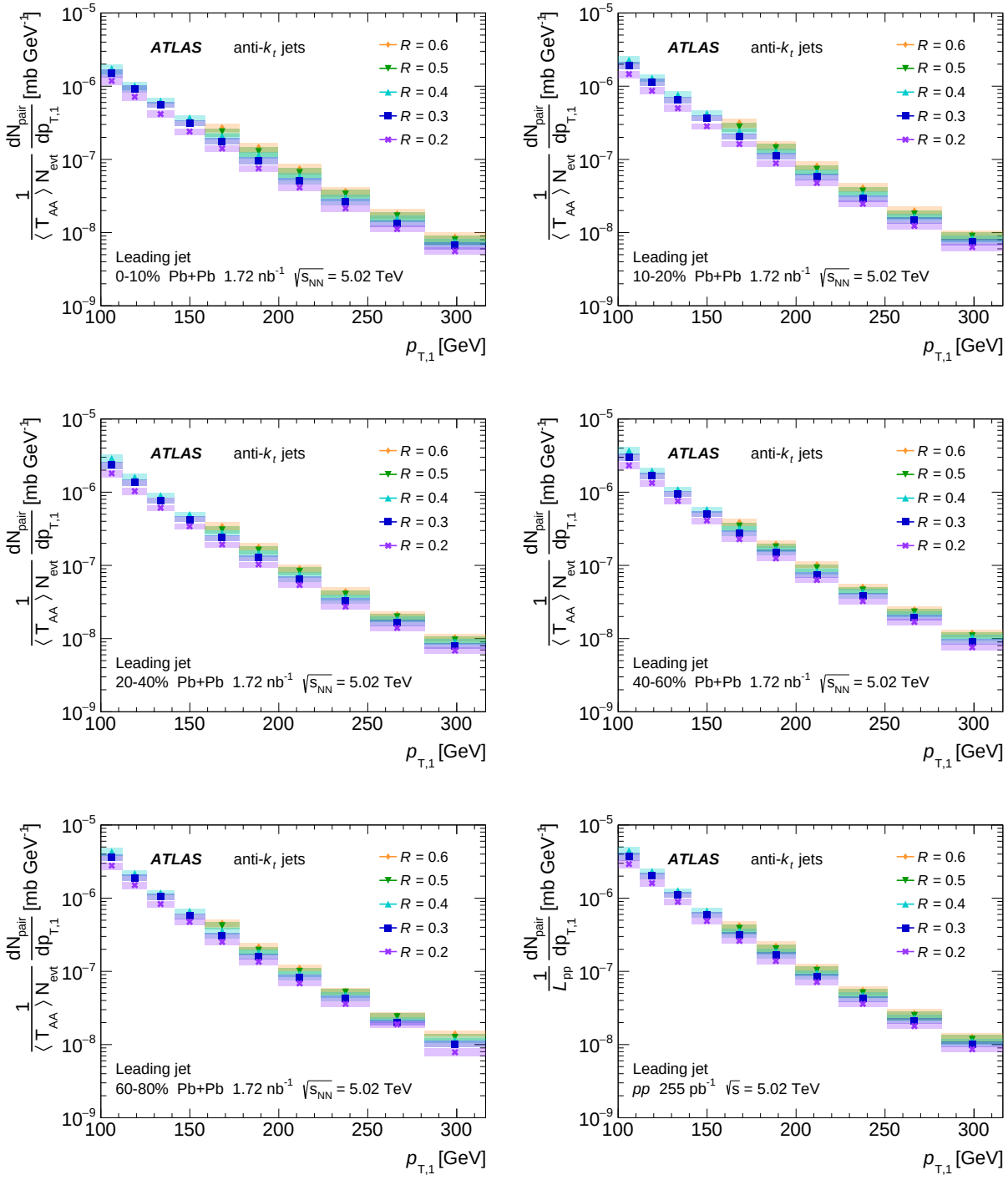

Figure A.1: Leading jet yields in Pb+Pb collisions of various centralities and cross section in pp collisions, as a function of jet p_{T}, for $R = 0.2, 0.3, 0.4, 0.5$ and 0.6 jets.

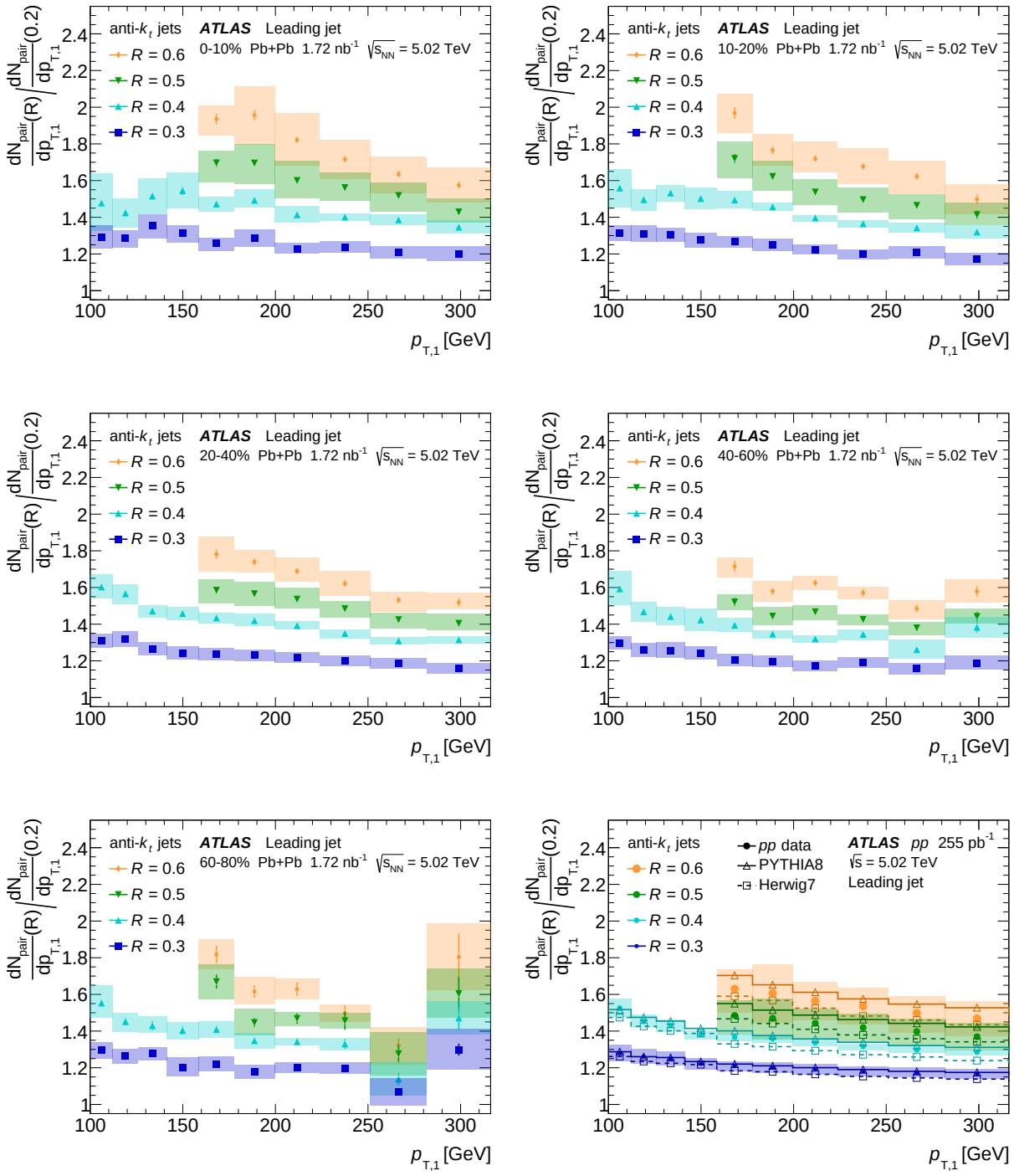

Figure A.2: Leading jet yields $R/0.2$ ratios in Pb+Pb collisions of various centralities and cross section $R/0.2$ ratios in pp collisions, as a function of jet p_{T}, for $R = 0.2, 0.3, 0.4, 0.5$ and 0.6 jets.

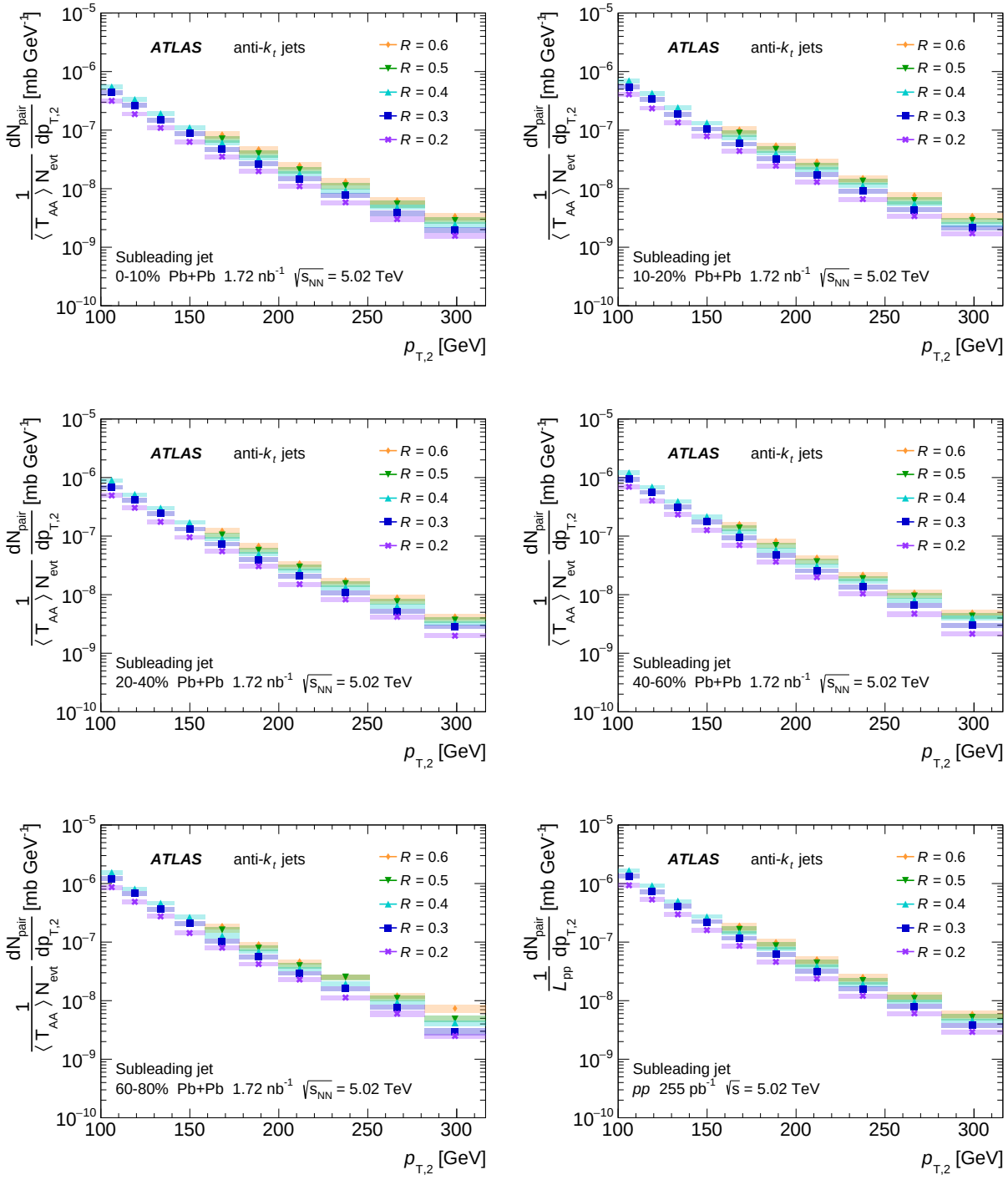

Figure A.3: Subleading jet yields in Pb+Pb collisions of various centralities and cross section in pp collisions, as a function of jet p_{T}, for $R = 0.2, 0.3, 0.4, 0.5$ and 0.6 jets.

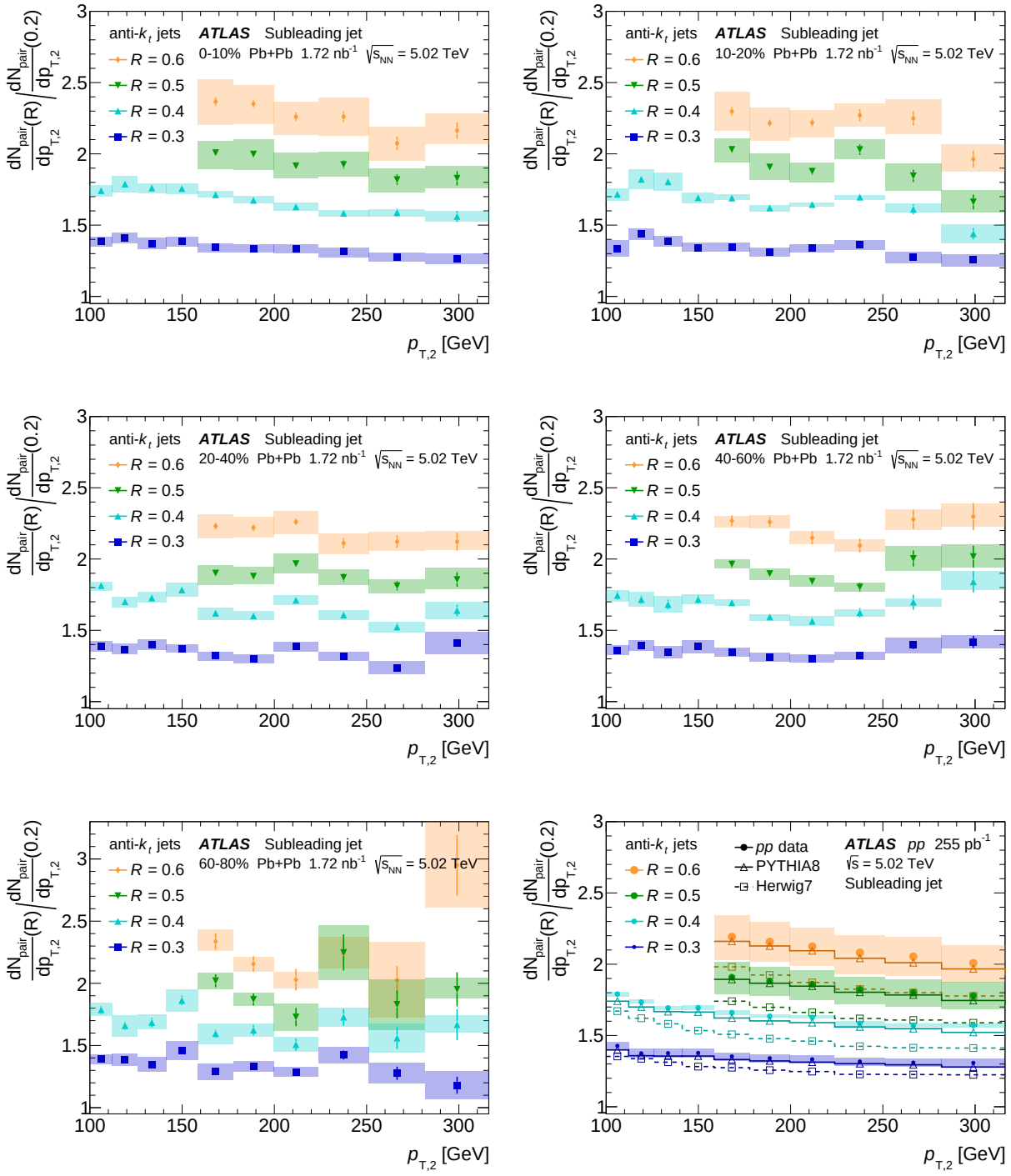

Figure A.4: Subleading jet yields $R/0.2$ ratios in Pb+Pb collisions of various centralities and cross section $R/0.2$ ratios in pp collisions, as a function of jet p_{T}, for $R = 0.2, 0.3, 0.4, 0.5$ and 0.6 jets.

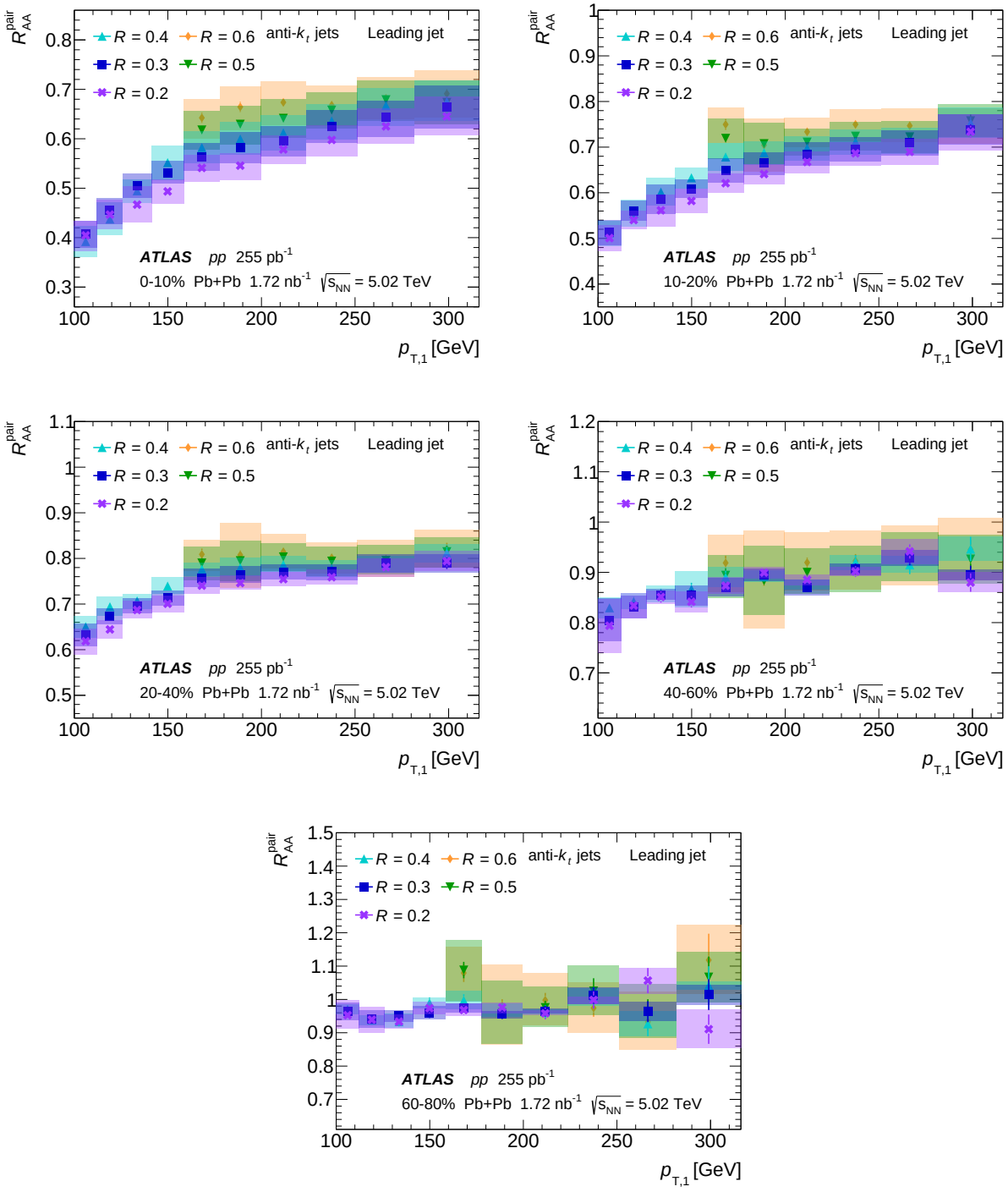

Figure A.5: Leading jet $R_{\mathrm{AA}}^{\mathrm{pair}}(p_{\mathrm{T},1})$ distributions as a function of jet p_{T} in Pb+Pb collisions of various centralities, for $R = 0.2, 0.3, 0.4, 0.5$ and 0.6 jets.

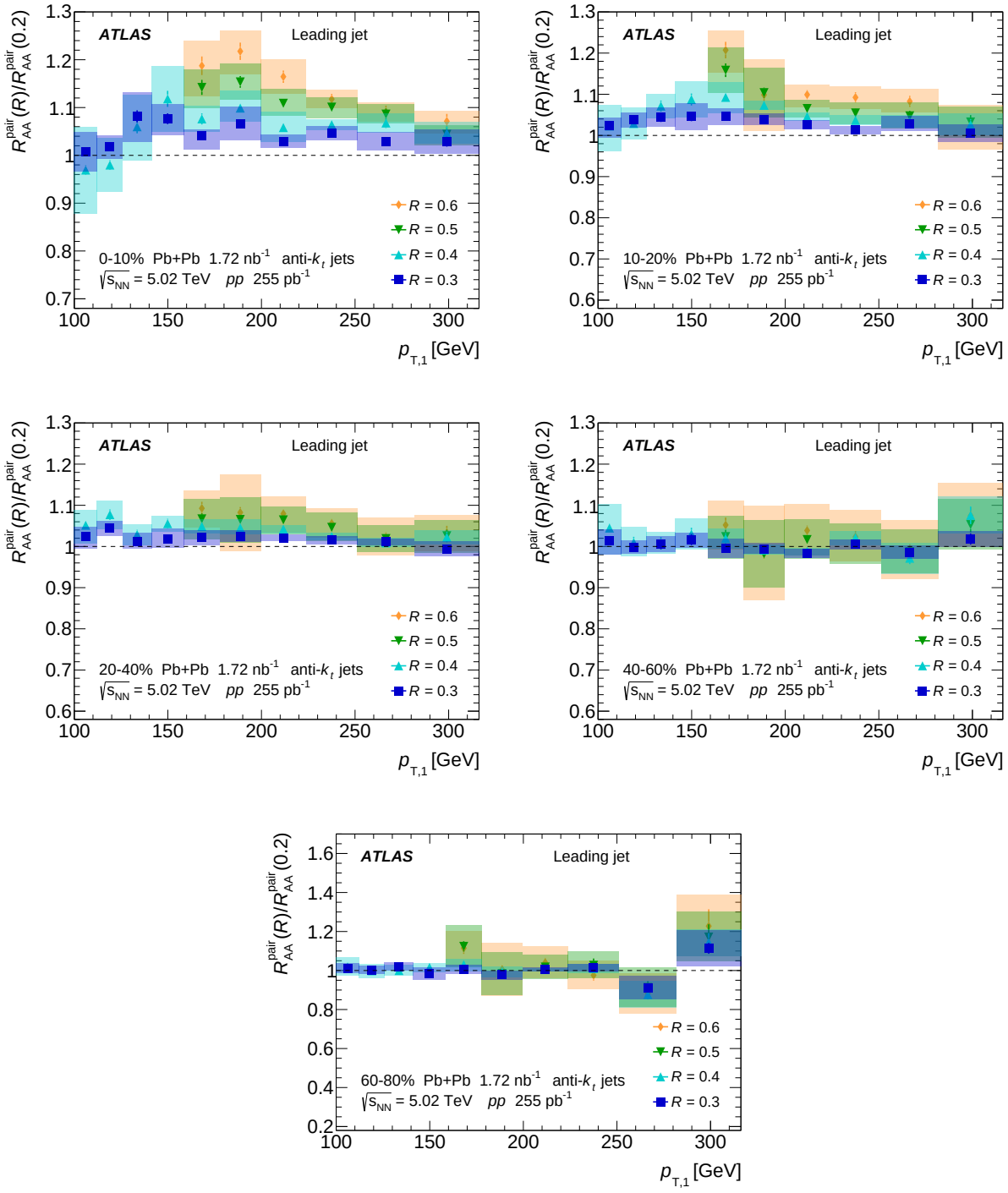

Figure A.6: Leading jet $R_{\mathrm{AA}}^{\mathrm{pair}}(R)/R_{\mathrm{AA}}^{\mathrm{pair}}(0.2)$ ratios as a function of jet p_{T} in Pb+Pb collisions of various centralities.

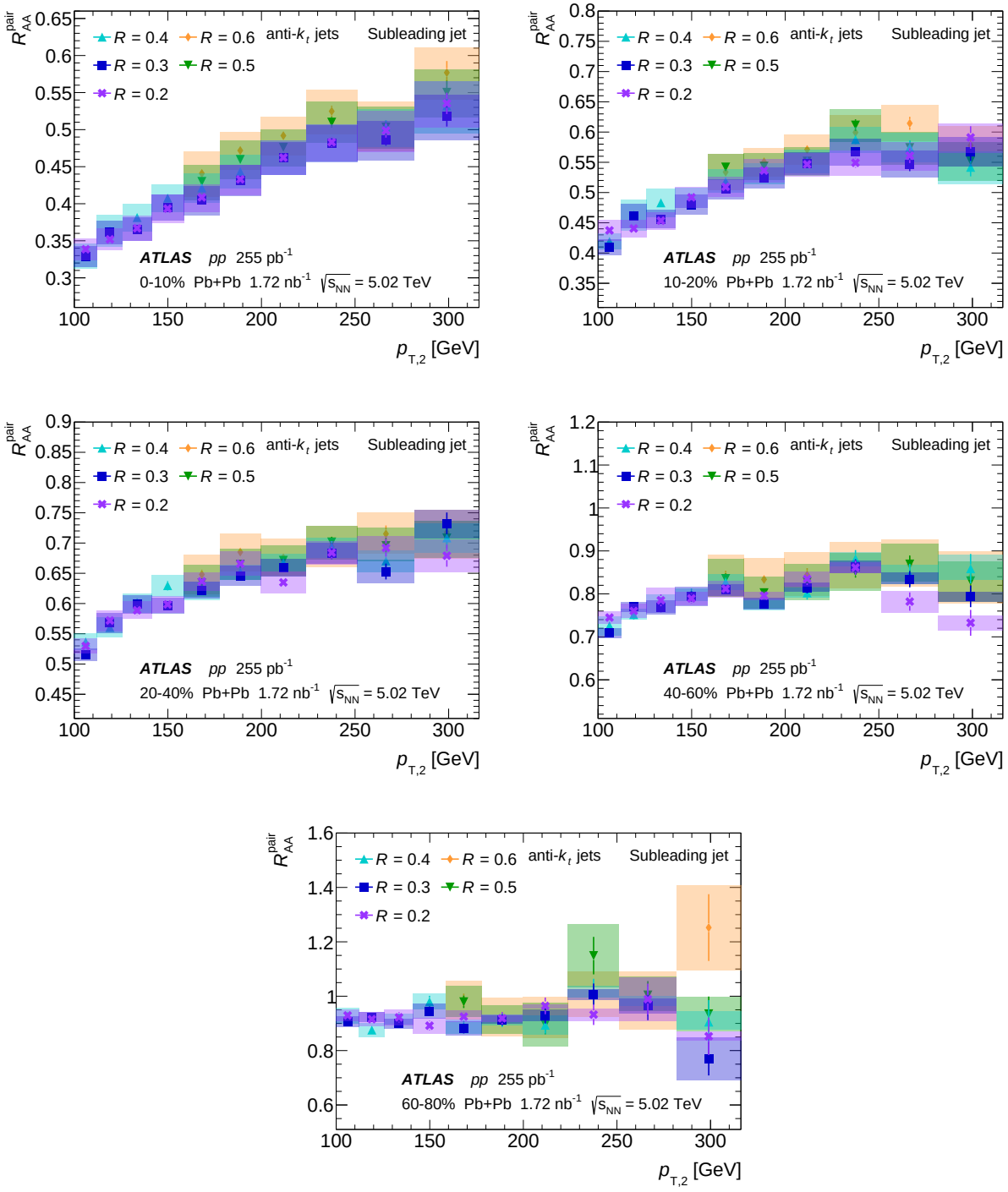

Figure A.7: Subleading jet $R^{\text{pair}}_{\text{AA}}(p_{\text{T},2})$ distributions as a function of jet p_{T} in Pb+Pb collisions of various centralities, for $R = 0.2, 0.3, 0.4, 0.5$ and 0.6 jets.

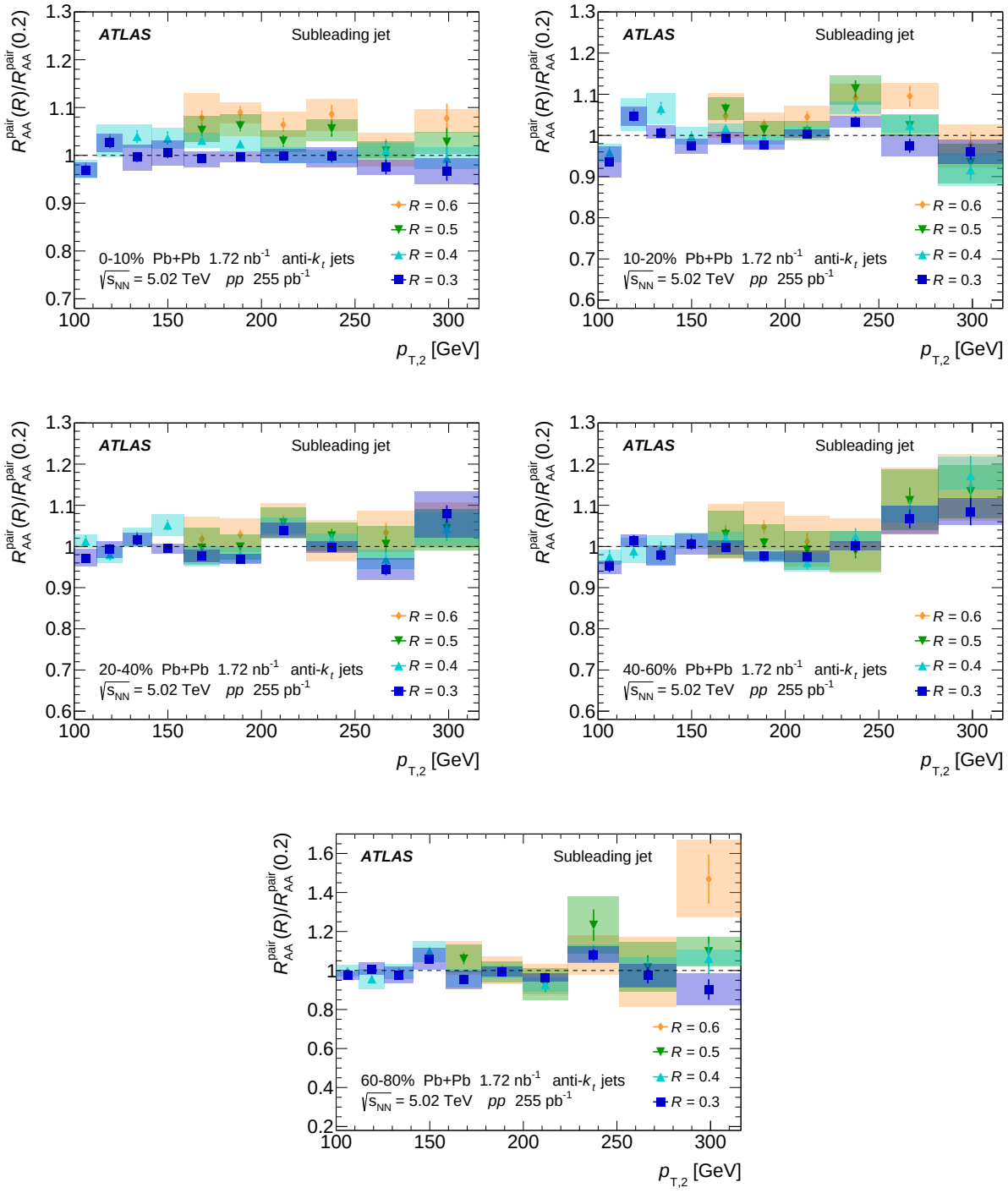

Figure A.8: Subleading jet $R_{\mathrm{AA}}^{\mathrm{pair}}(R)/R_{\mathrm{AA}}^{\mathrm{pair}}(0.2)$ ratios as a function of jet p_{T} in Pb+Pb collisions of various centralities.

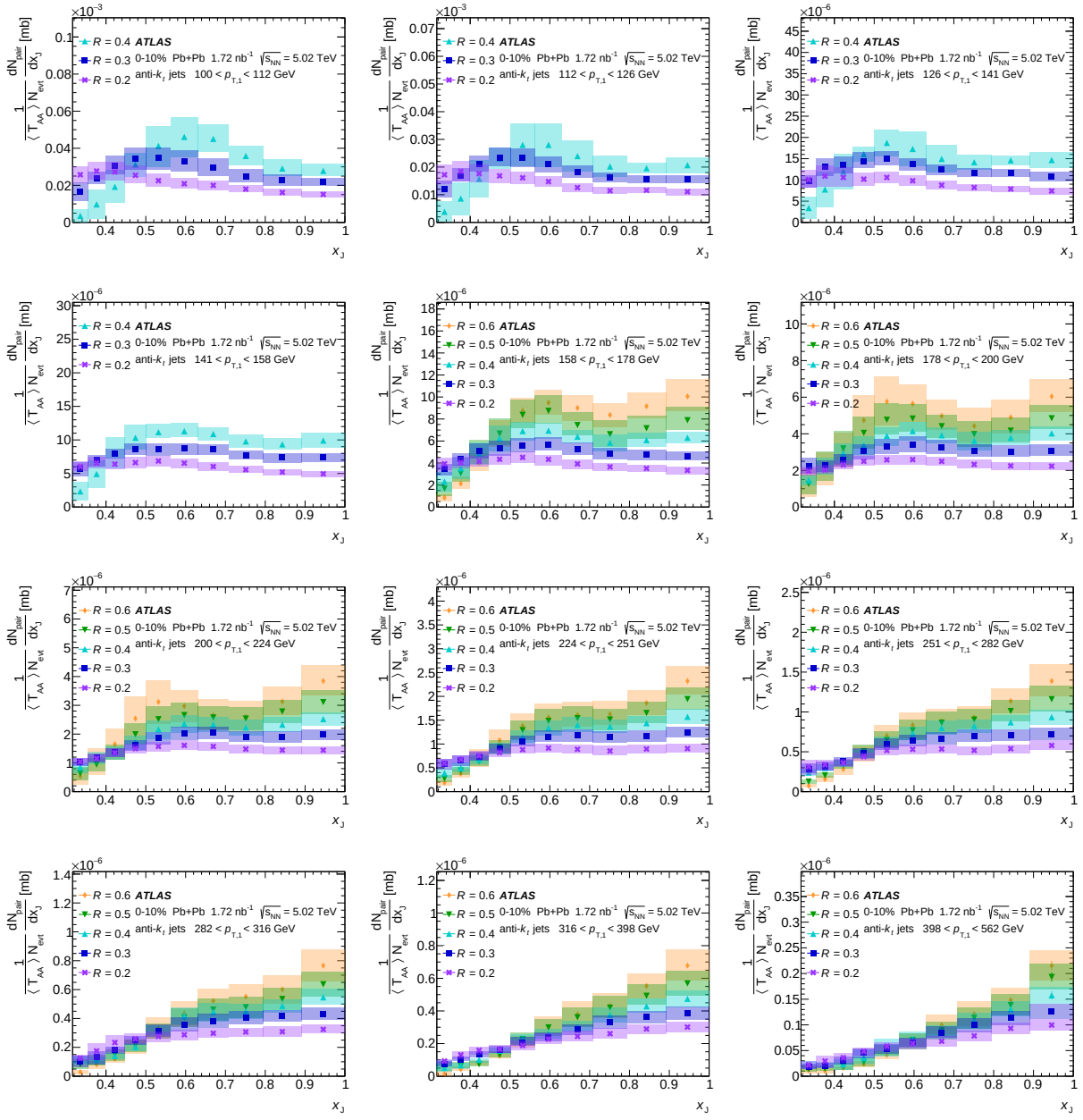

Figure A.9: The absolutely normalized x_J distributions in 0–10% central Pb+Pb collisions, for $R = 0.2, 0.3, 0.4, 0.5$ and 0.6 jets and various $p_{T,1}$ bins.

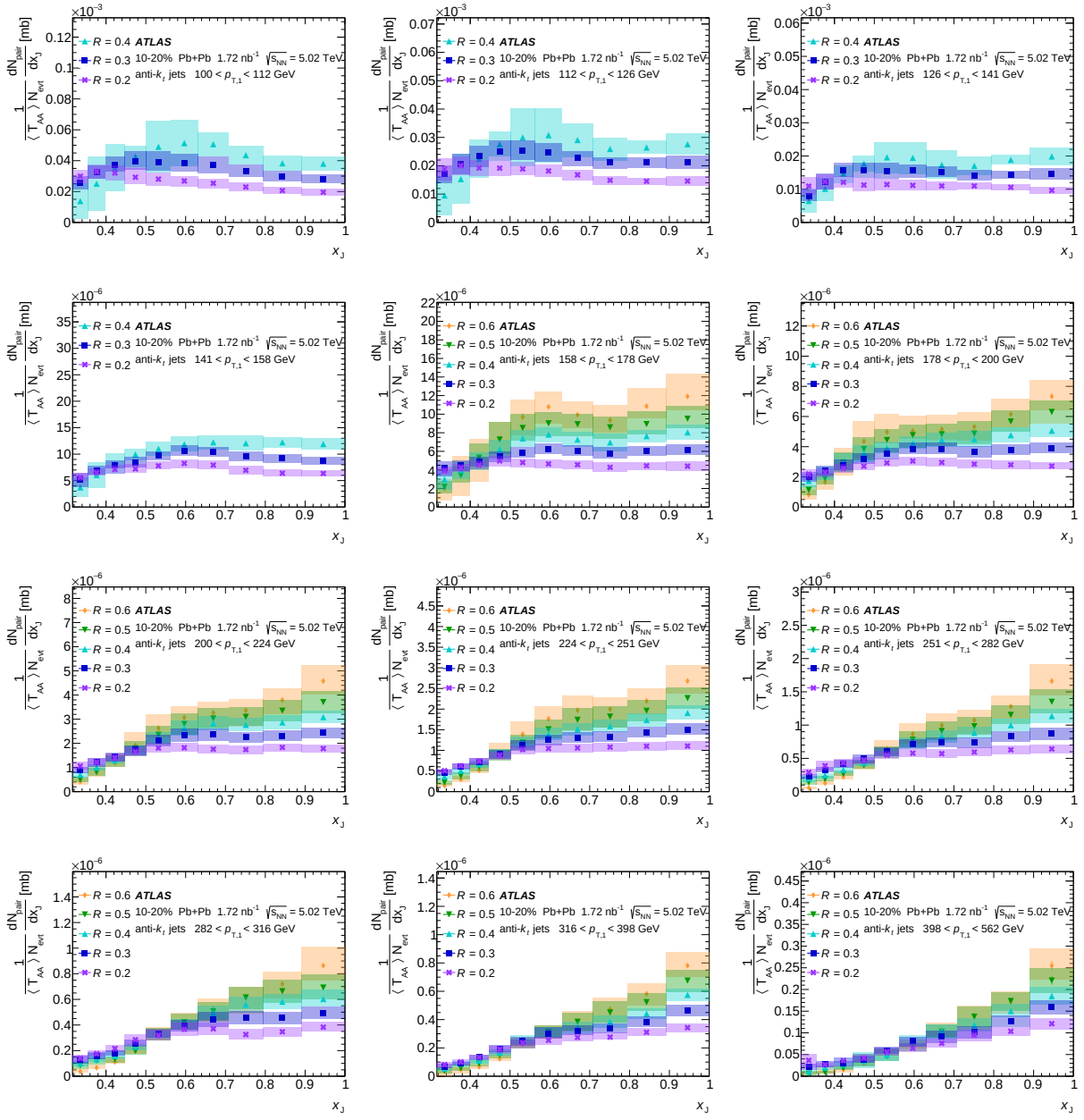

Figure A.10: The absolutely normalized x_J distributions in 10–20% central Pb+Pb collisions, for $R = 0.2, 0.3, 0.4, 0.5$ and 0.6 jets and various $p_{T,1}$ bins.

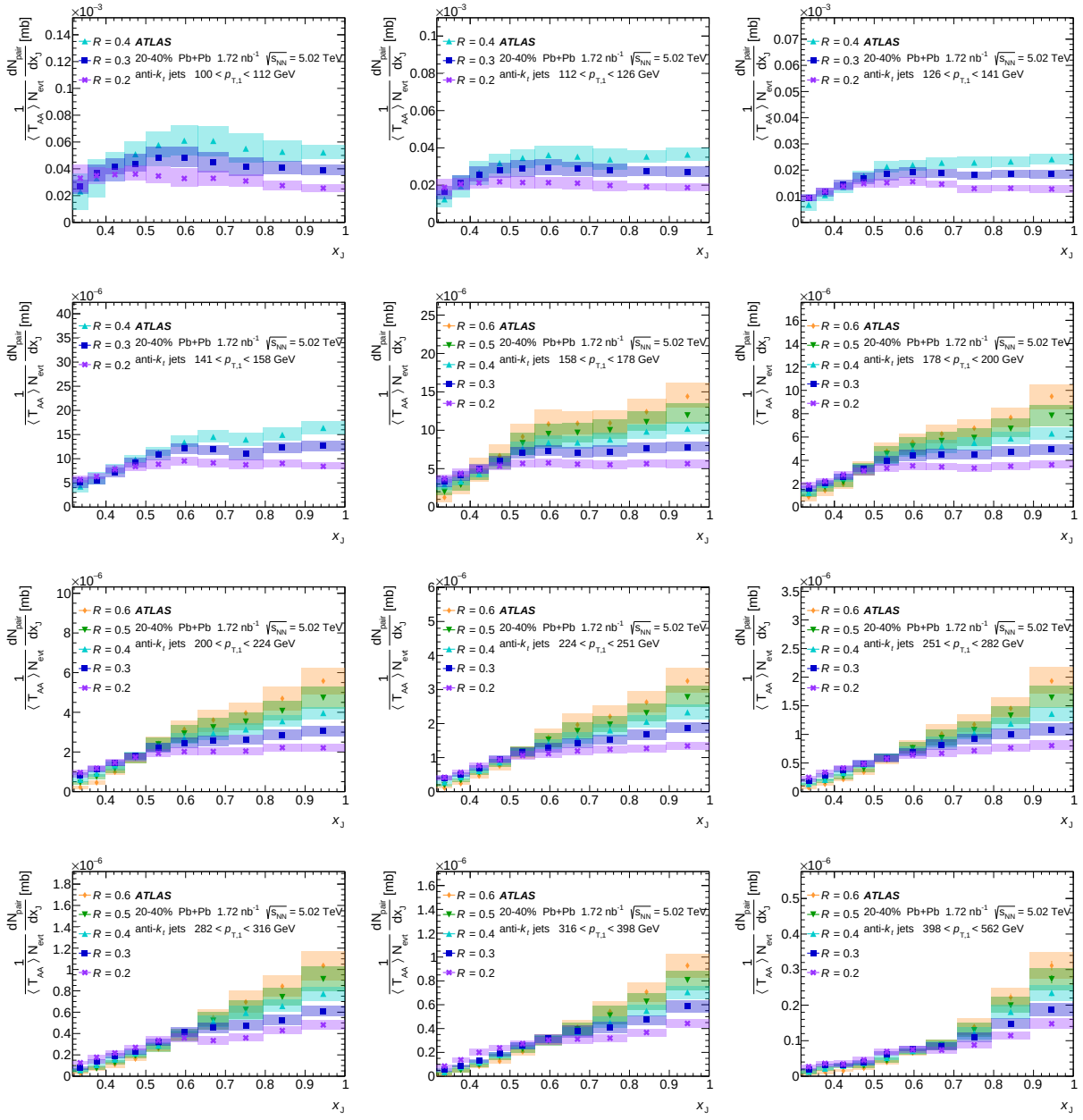

Figure A.11: The absolutely normalized x_{J} distributions in 20–40% central Pb+Pb collisions, for $R = 0.2, 0.3, 0.4, 0.5$ and 0.6 jets and various $p_{\mathrm{T},1}$ bins.

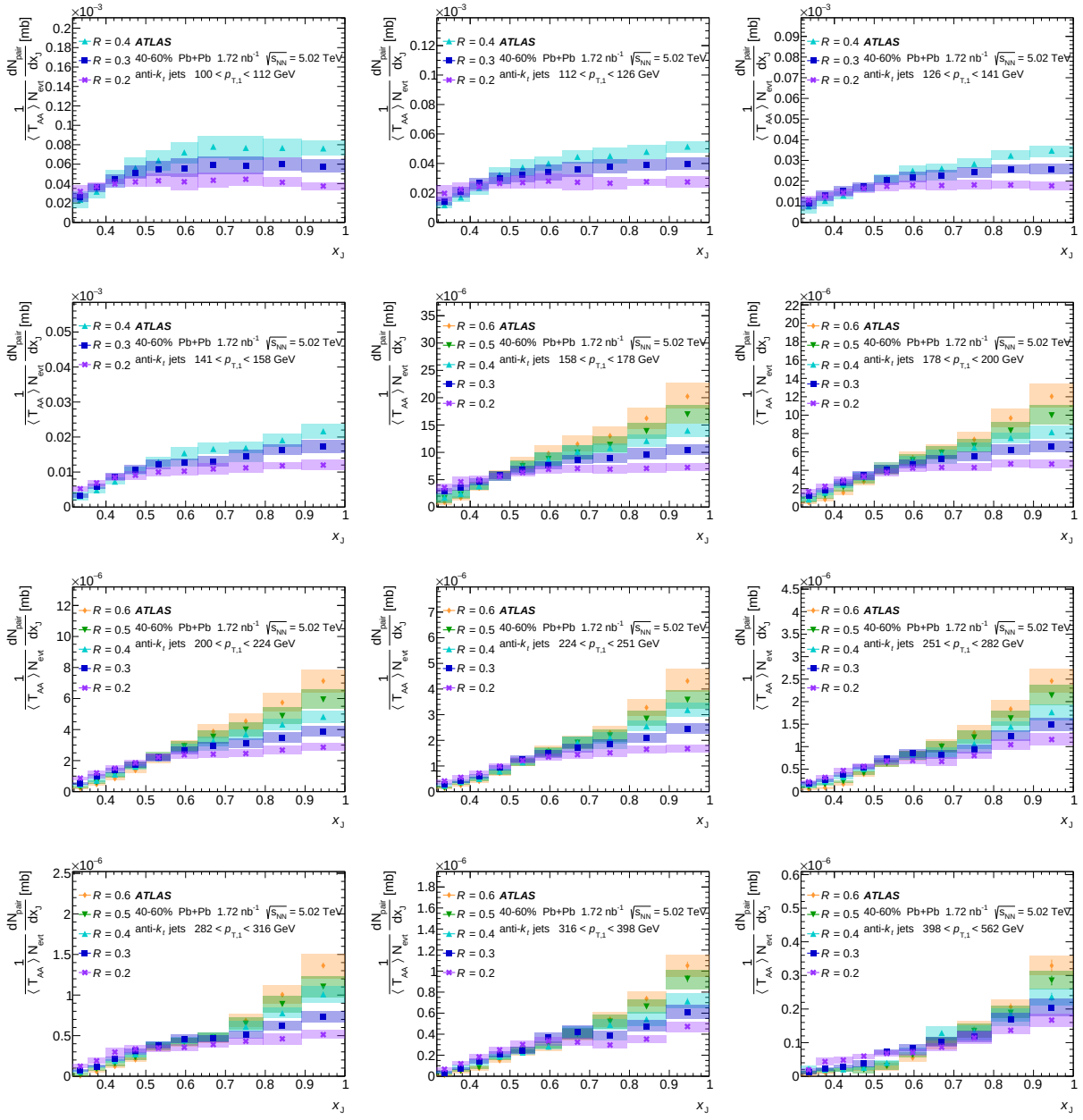

Figure A.12: The absolutely normalized x_{J} distributions in 40–60% central Pb+Pb collisions, for $R = 0.2, 0.3, 0.4, 0.5$ and 0.6 jets and various $p_{\mathrm{T},1}$ bins.

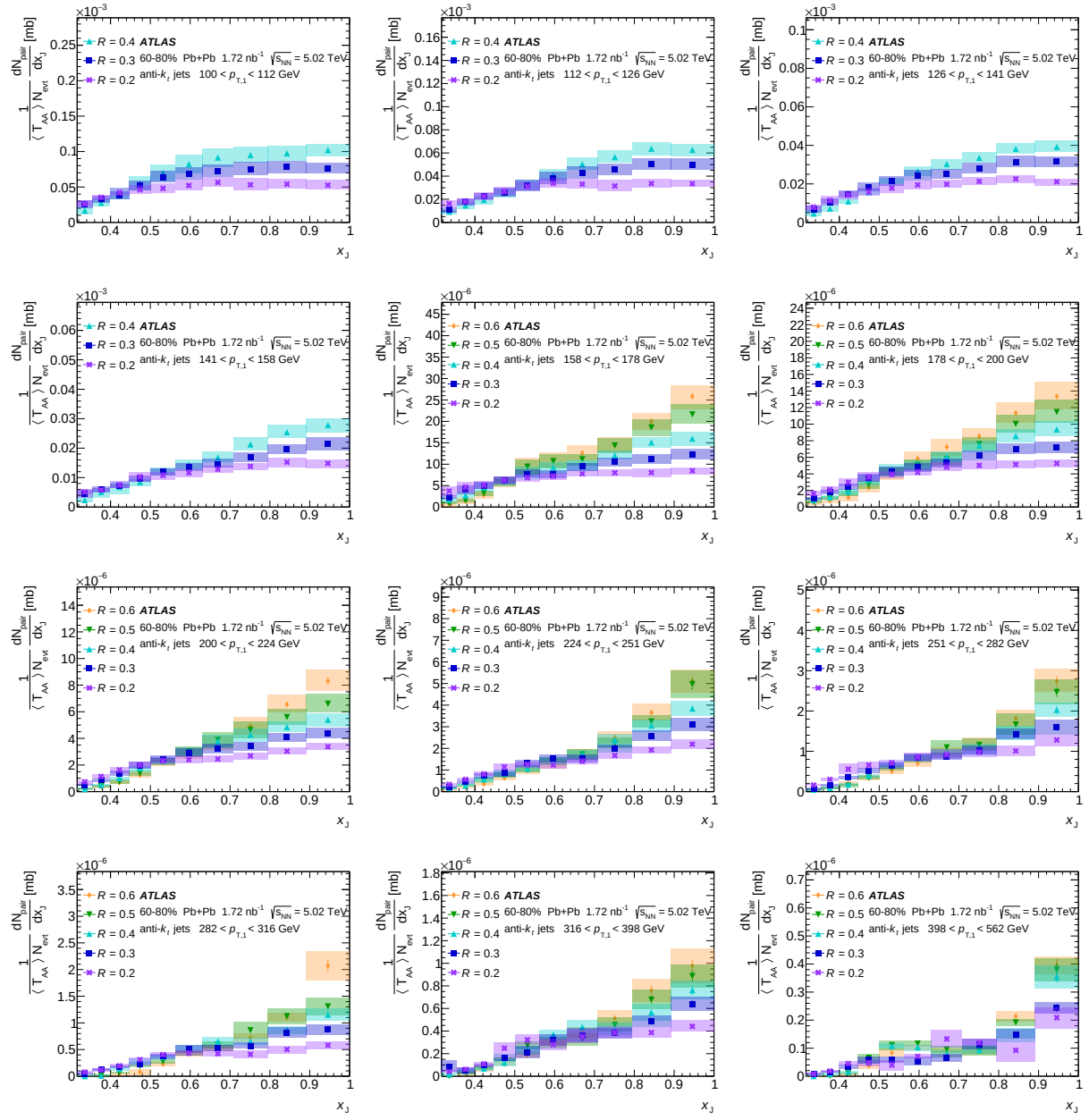

Figure A.13: The absolutely normalized x_J distributions in 60–80% central Pb+Pb collisions, for $R = 0.2, 0.3, 0.4, 0.5$ and 0.6 jets and various $p_{T,1}$ bins.

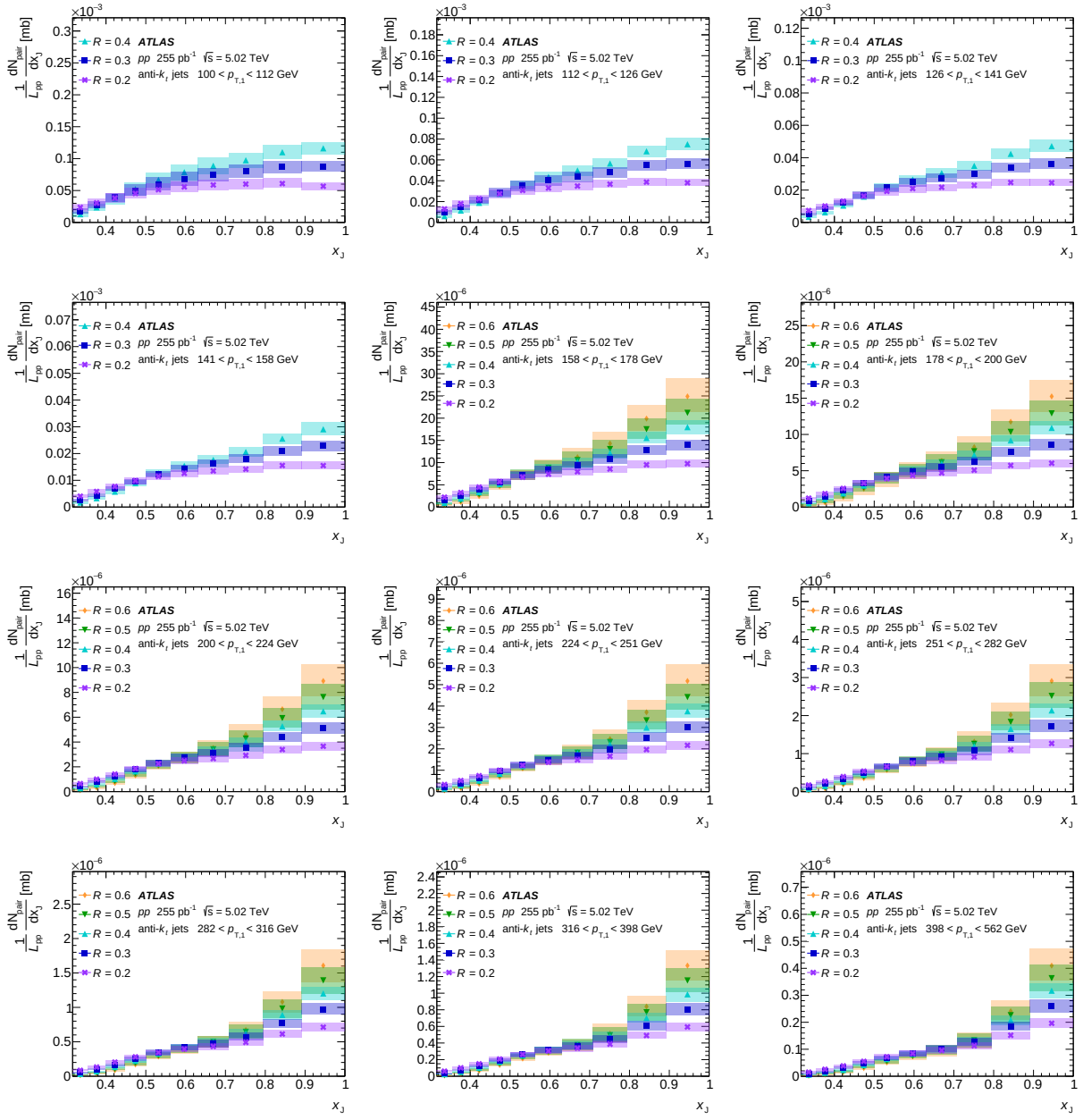

Figure A.14: The absolutely normalized x_{J} distributions in pp collisions, for $R = 0.2, 0.3, 0.4, 0.5$ and 0.6 jets and various $p_{\mathrm{T},1}$ bins.

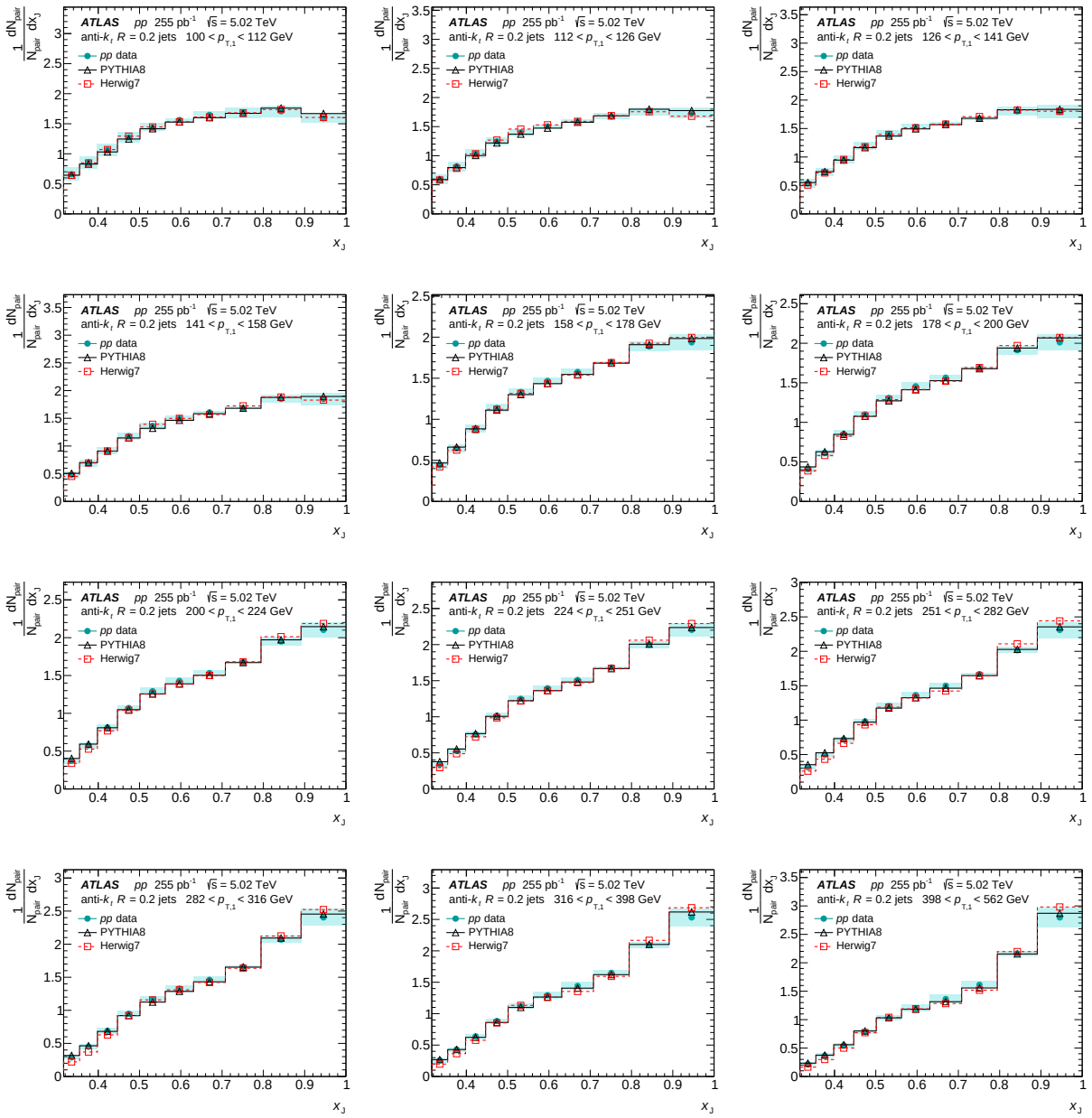

Figure A.15: The self normalized x_{J} distributions in pp collisions, and PYTHIA 8 and Herwig++7 simulations, for $R = 0.2$ jets of various $p_{\mathrm{T},1}$.

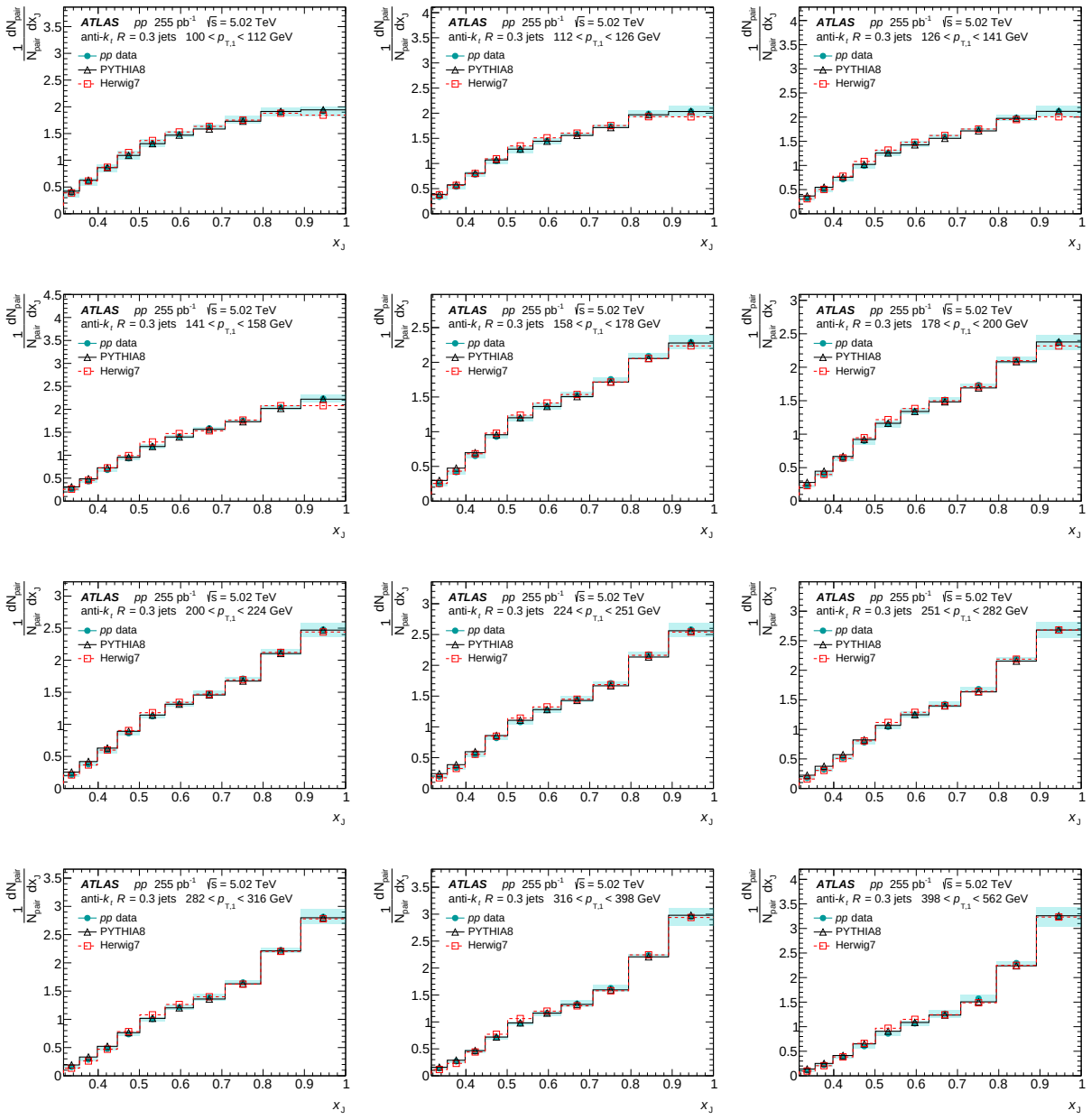

Figure A.16: The self normalized x_{J} distributions in pp collisions, and PYTHIA 8 and Herwig++7 simulations, for $R = 0.3$ jets of various $p_{\mathrm{T},1}$.

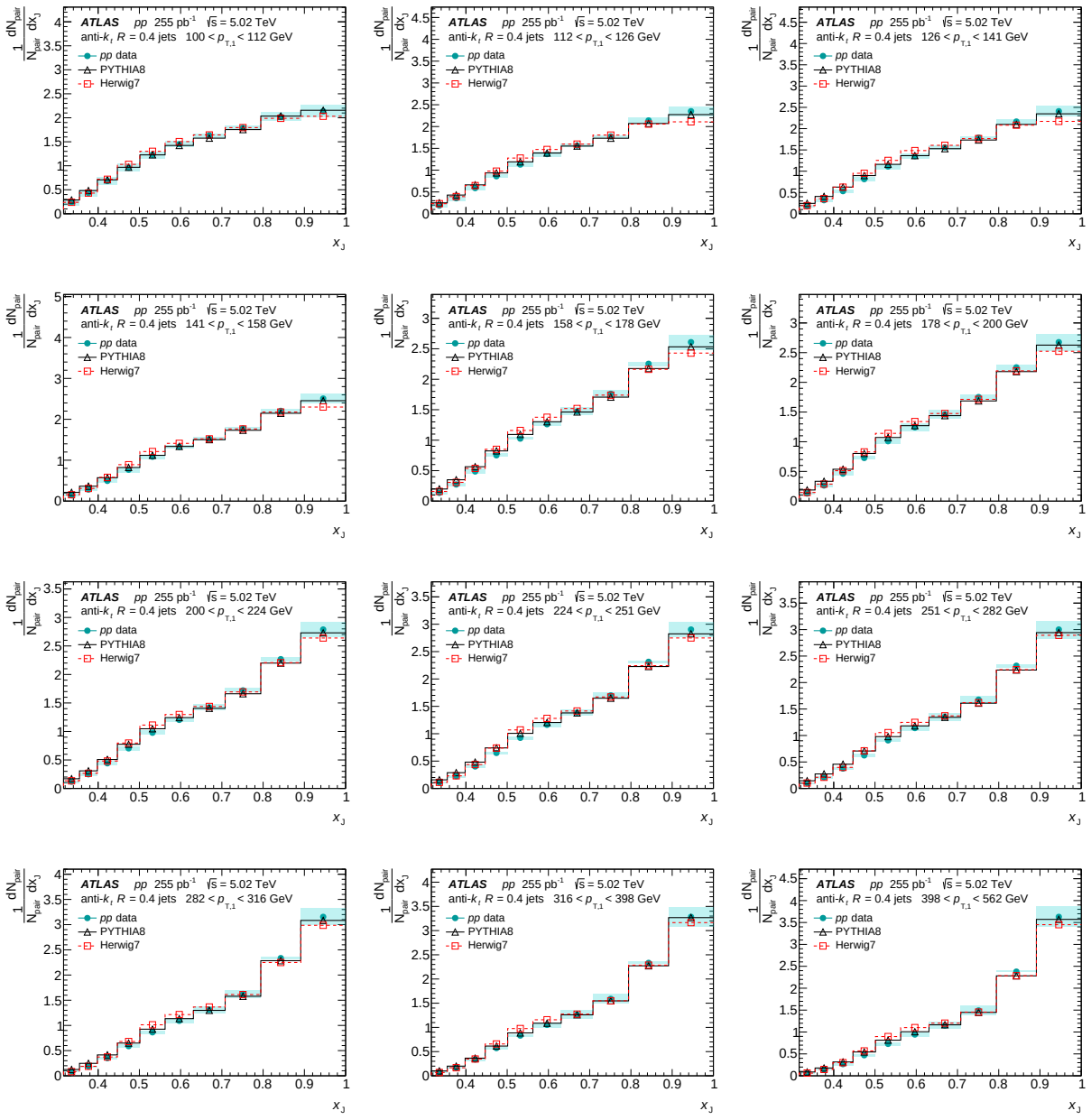

Figure A.17: The self normalized x_{J} distributions in pp collisions, and PYTHIA 8 and Herwig++7 simulations, for $R = 0.4$ jets of various $p_{\mathrm{T},1}$.

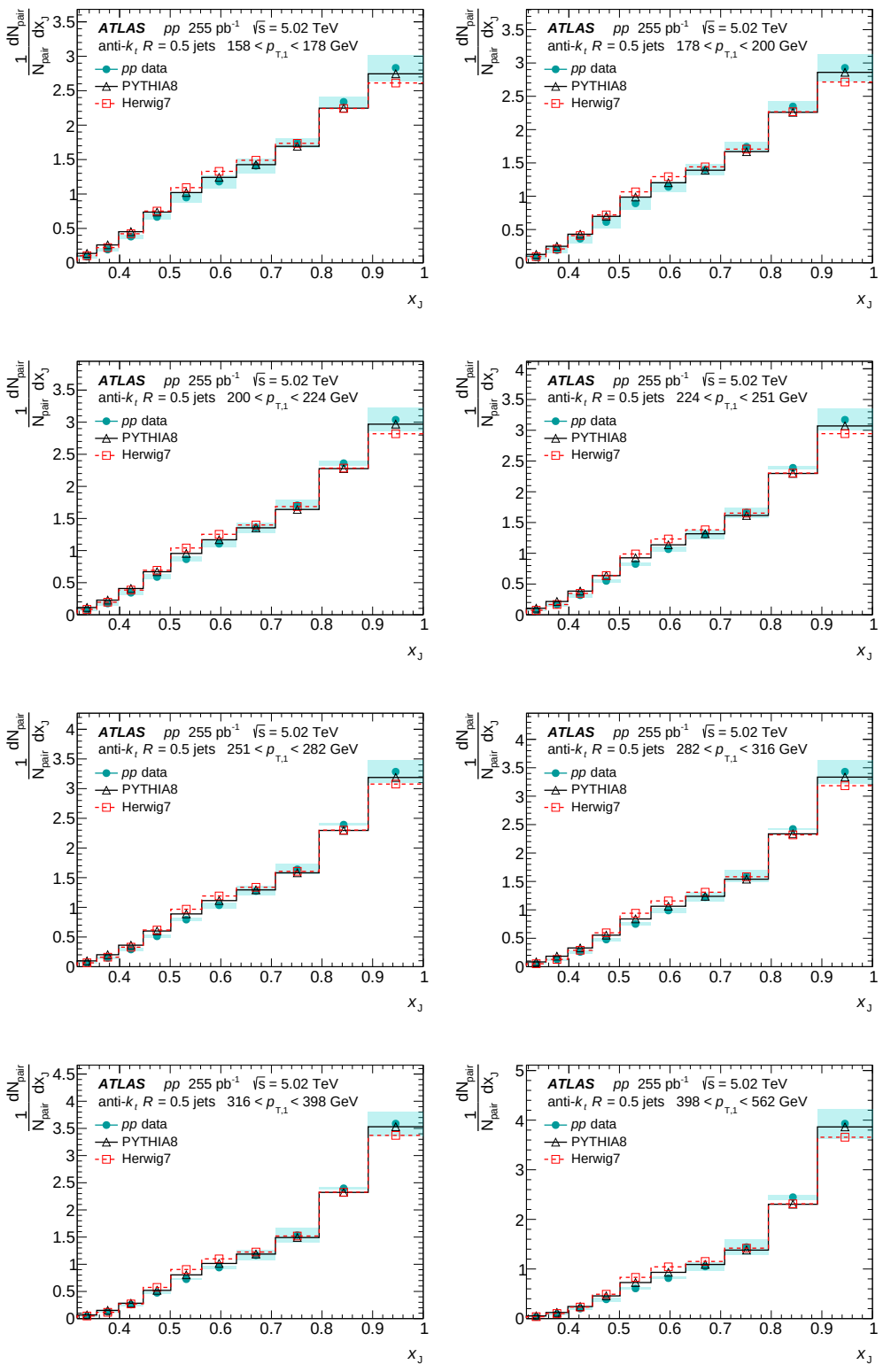

Figure A.18: The self normalized x_{J} distributions in pp collisions, and PYTHIA 8 and Herwig++7 simulations, for $R = 0.5$ jets of various $p_{\mathrm{T},1}$.

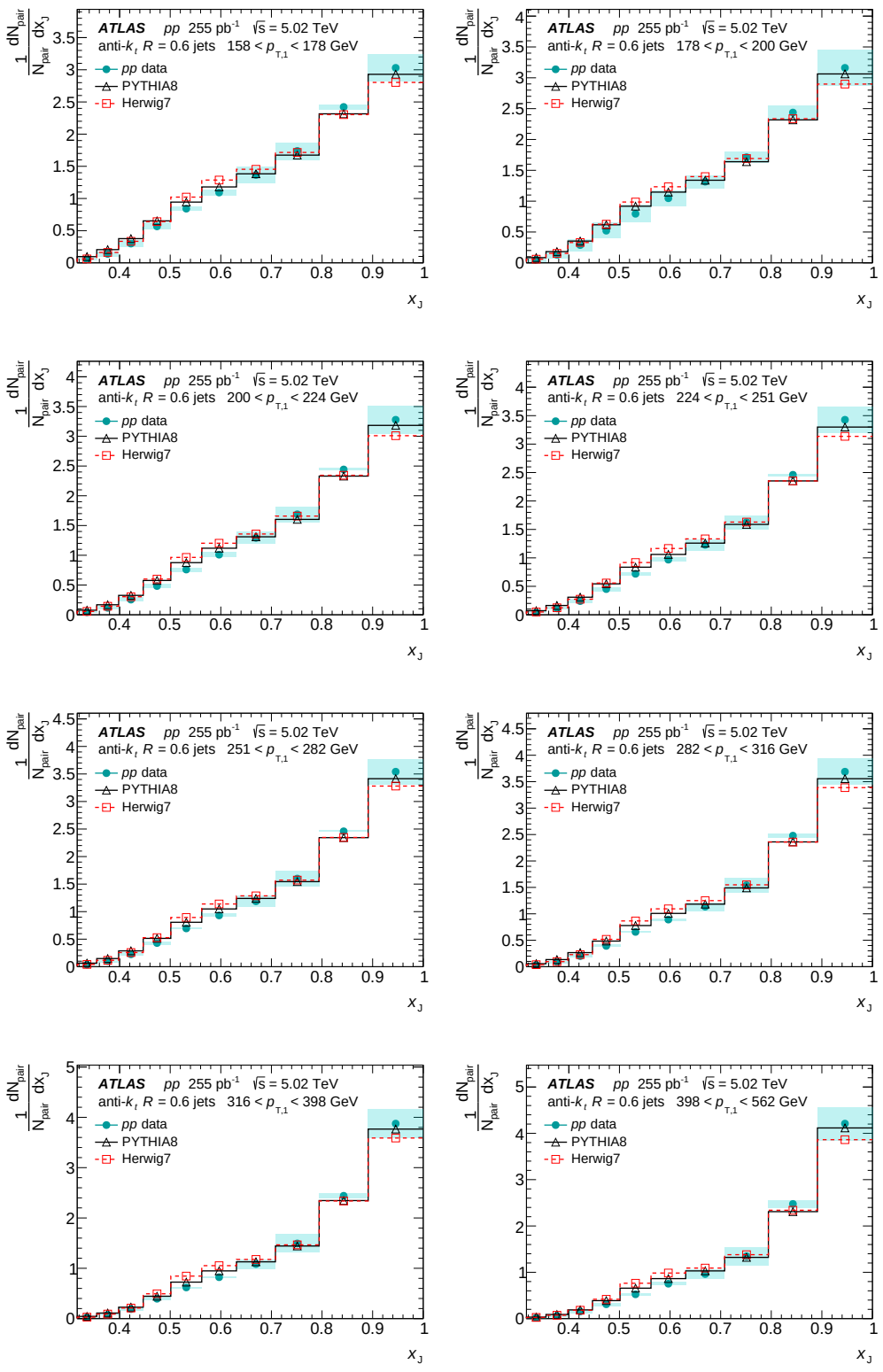

Figure A.19: The self normalized x_{J} distributions in pp collisions, and PYTHIA 8 and Herwig++7 simulations, for $R = 0.6$ jets of various $p_{\mathrm{T},1}$.

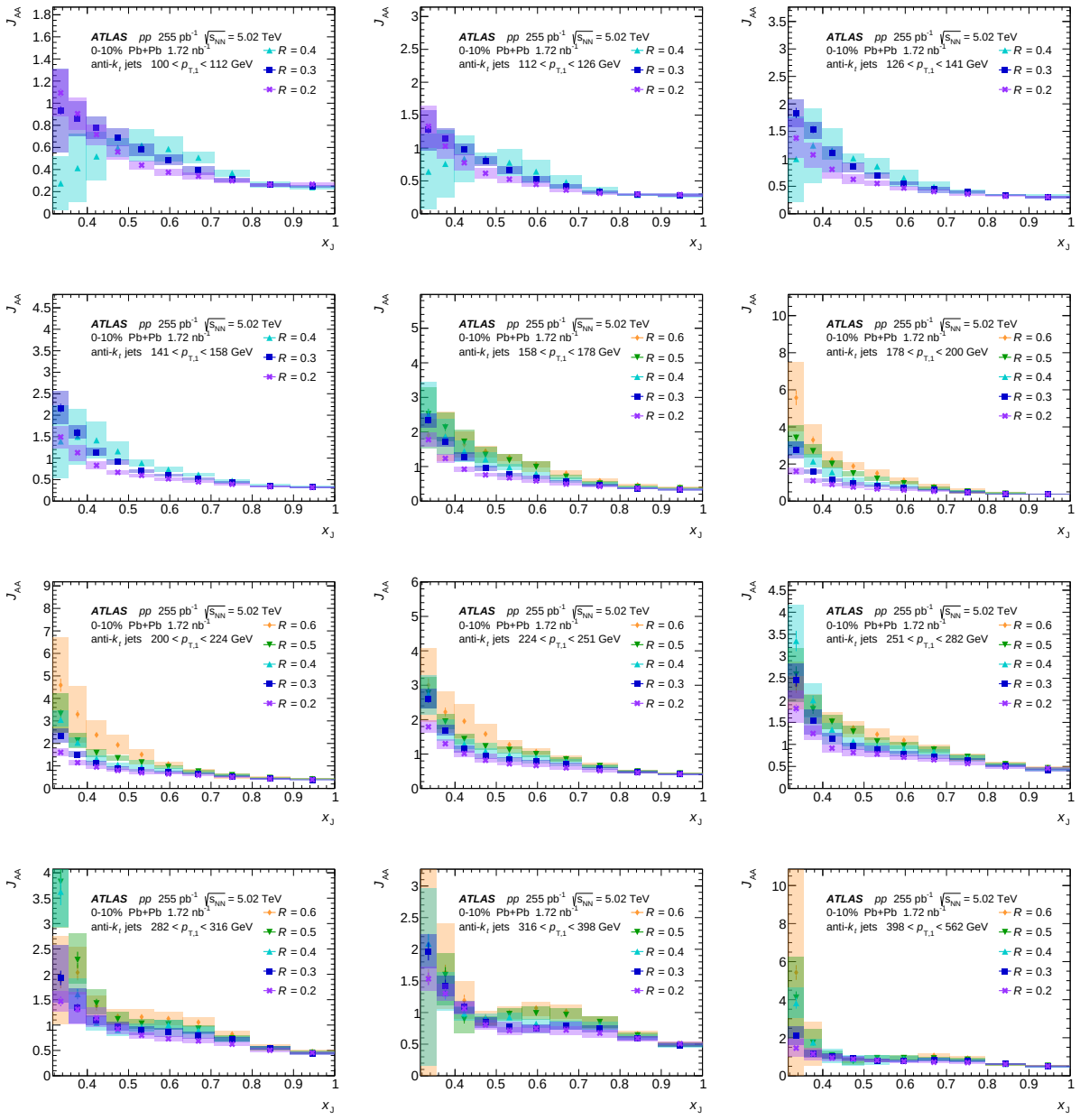

Figure A.20: The J_{AA} distributions in 0–10% central Pb+Pb collisions, for $R = 0.2, 0.3, 0.4, 0.5$ and 0.6 jets and various $p_{\mathrm{T},1}$ bins.

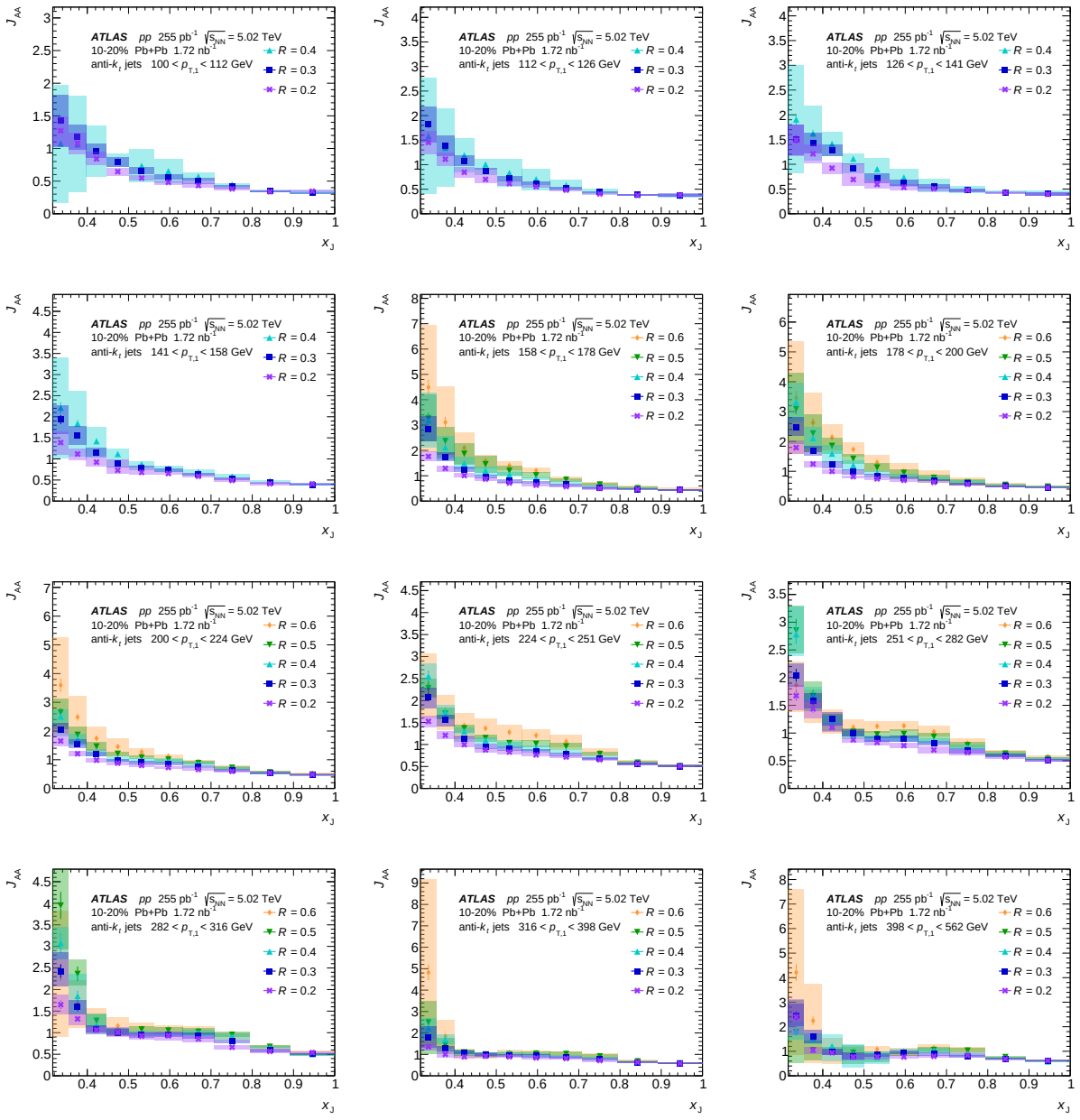

Figure A.21: The J_{AA} distributions in 10–20% central Pb+Pb collisions, for $R = 0.2, 0.3, 0.4, 0.5$ and 0.6 jets and various $p_{\mathrm{T},1}$ bins.

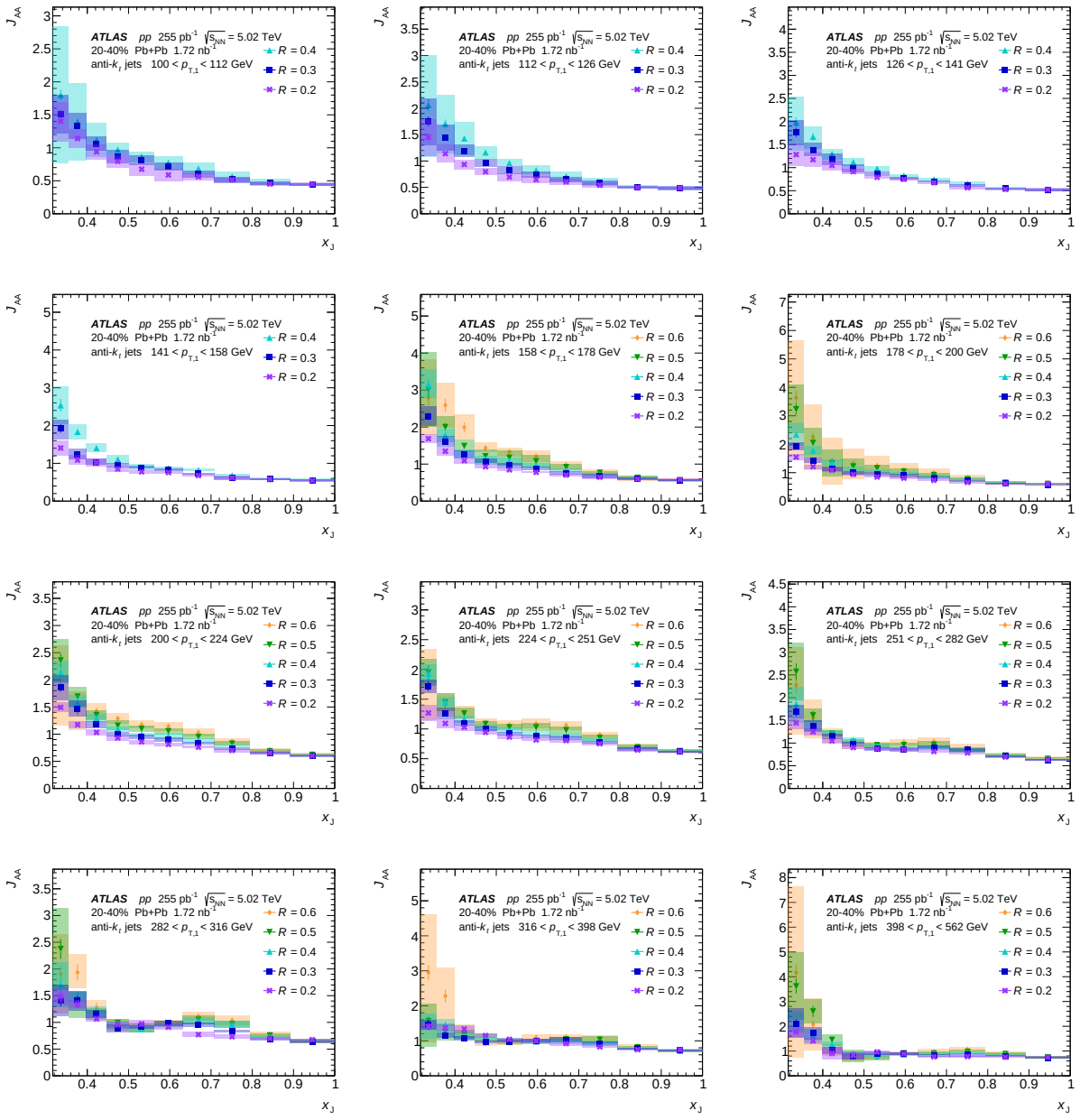

Figure A.22: The J_{AA} distributions in 20–40% central Pb+Pb collisions, for $R = 0.2, 0.3, 0.4, 0.5$ and 0.6 jets and various $p_{\mathrm{T},1}$ bins.

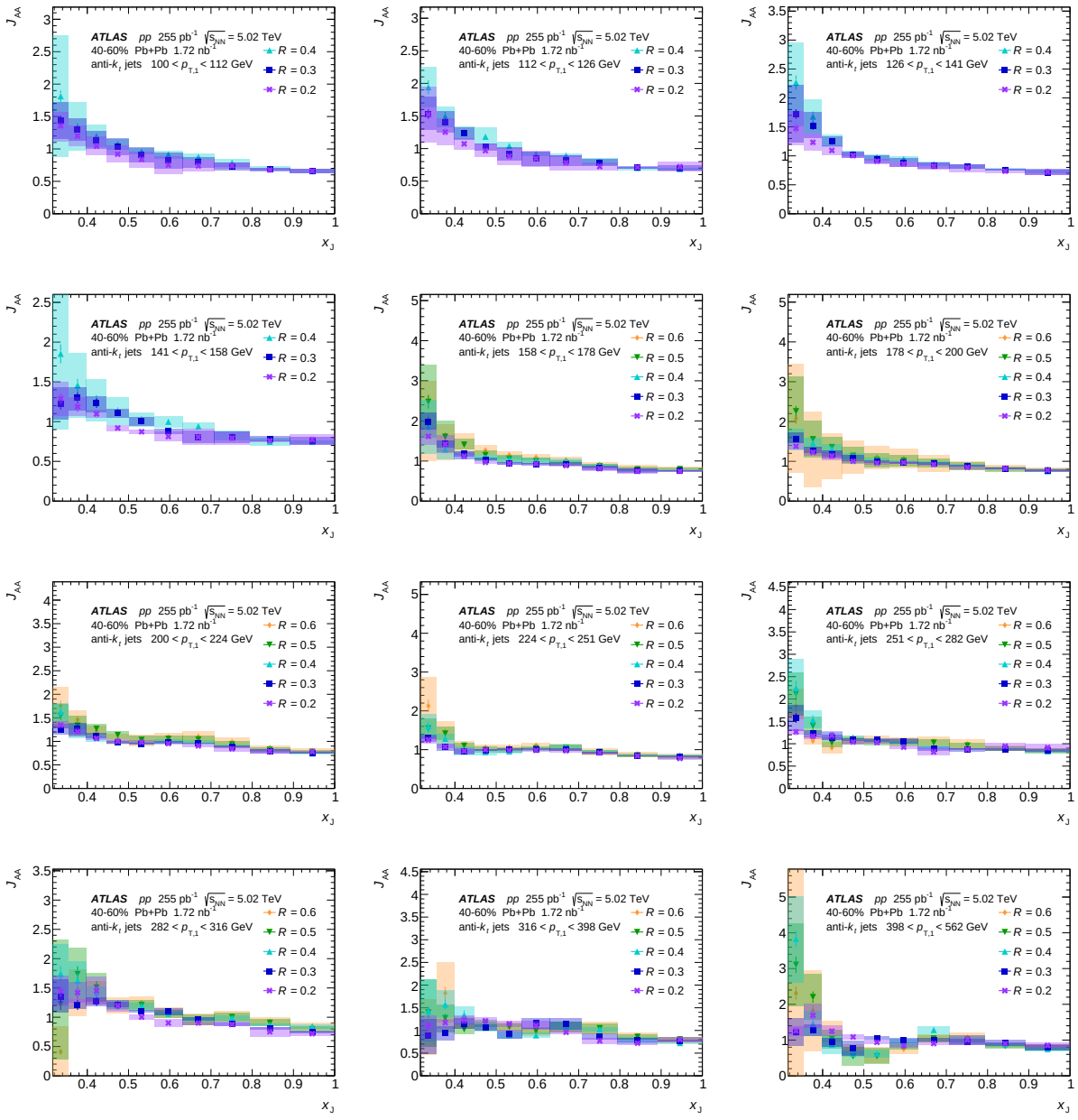

Figure A.23: The J_{AA} distributions in 40–60% central Pb+Pb collisions, for $R = 0.2, 0.3, 0.4, 0.5$ and 0.6 jets and various $p_{\mathrm{T},1}$ bins.

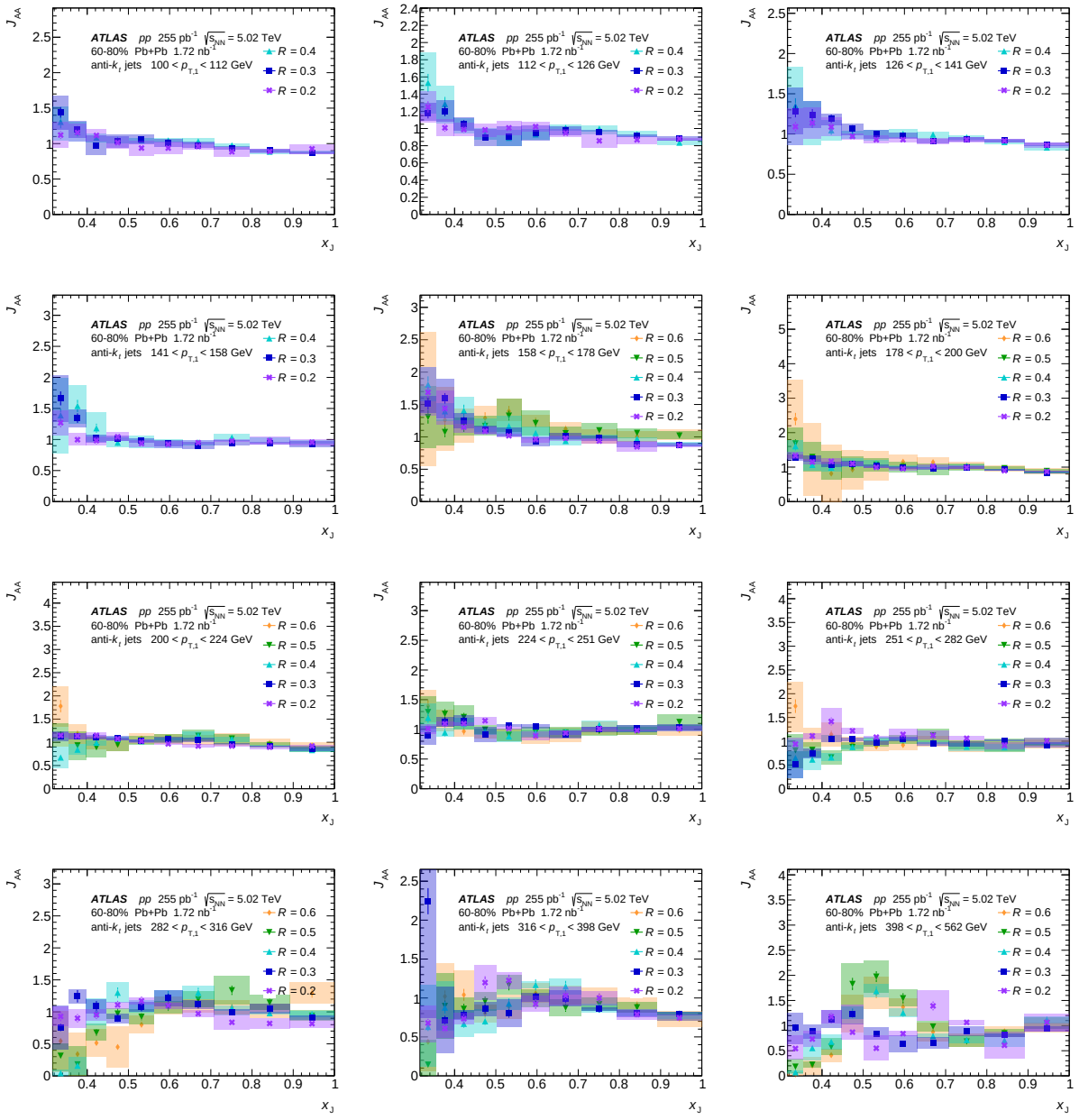

Figure A.24: The J_{AA} distributions in 60–80% central Pb+Pb collisions, for $R = 0.2, 0.3, 0.4, 0.5$ and 0.6 jets and various $p_{\mathrm{T},1}$ bins.

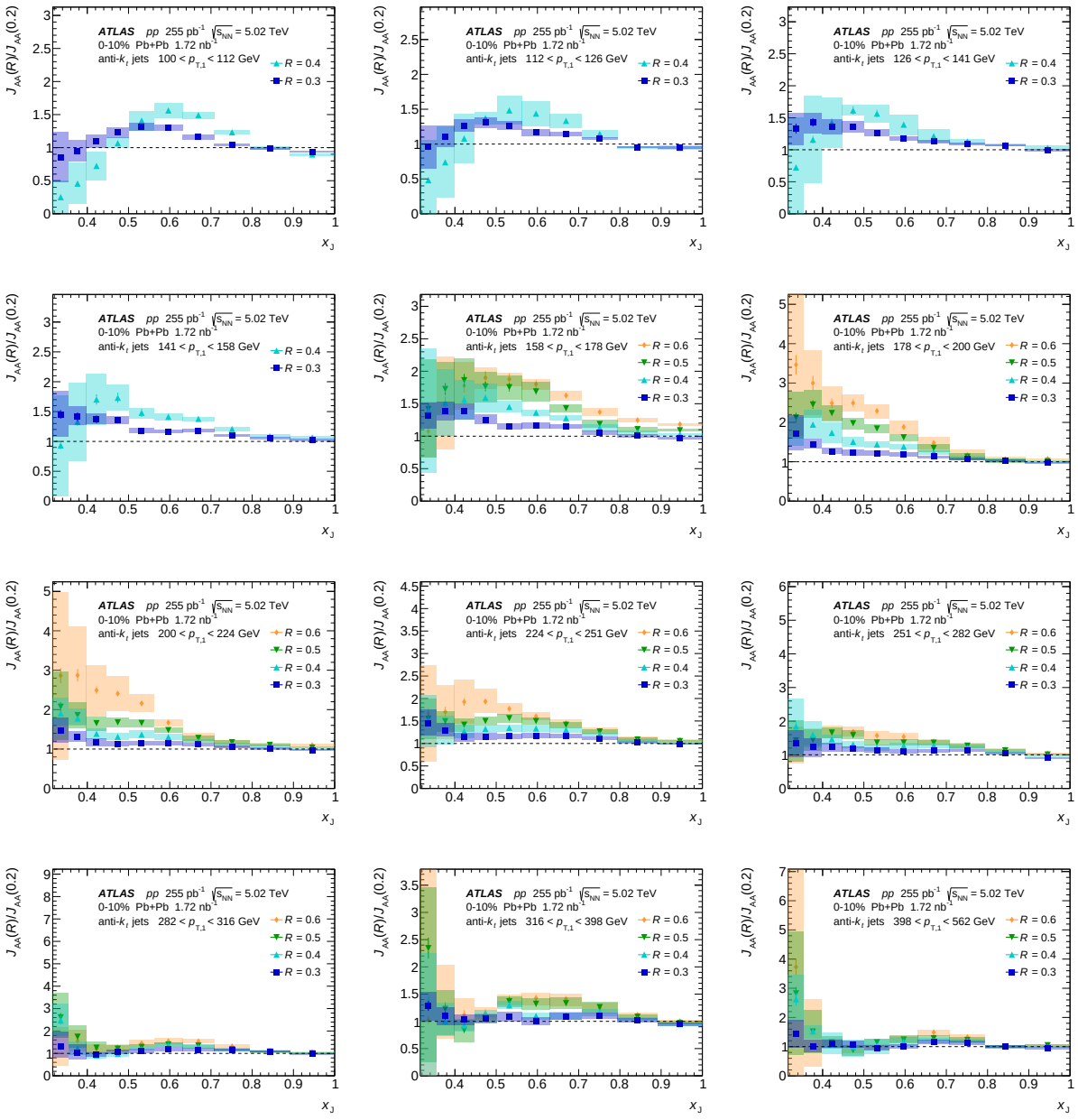

Figure A.25: The $J_{\mathrm{AA}}(R)/J_{\mathrm{AA}}(0.2)$ ratios in 0–10% central Pb+Pb collisions, for $R = 0.2, 0.3, 0.4, 0.5$ and 0.6 jets and various $p_{\mathrm{T},1}$ bins.

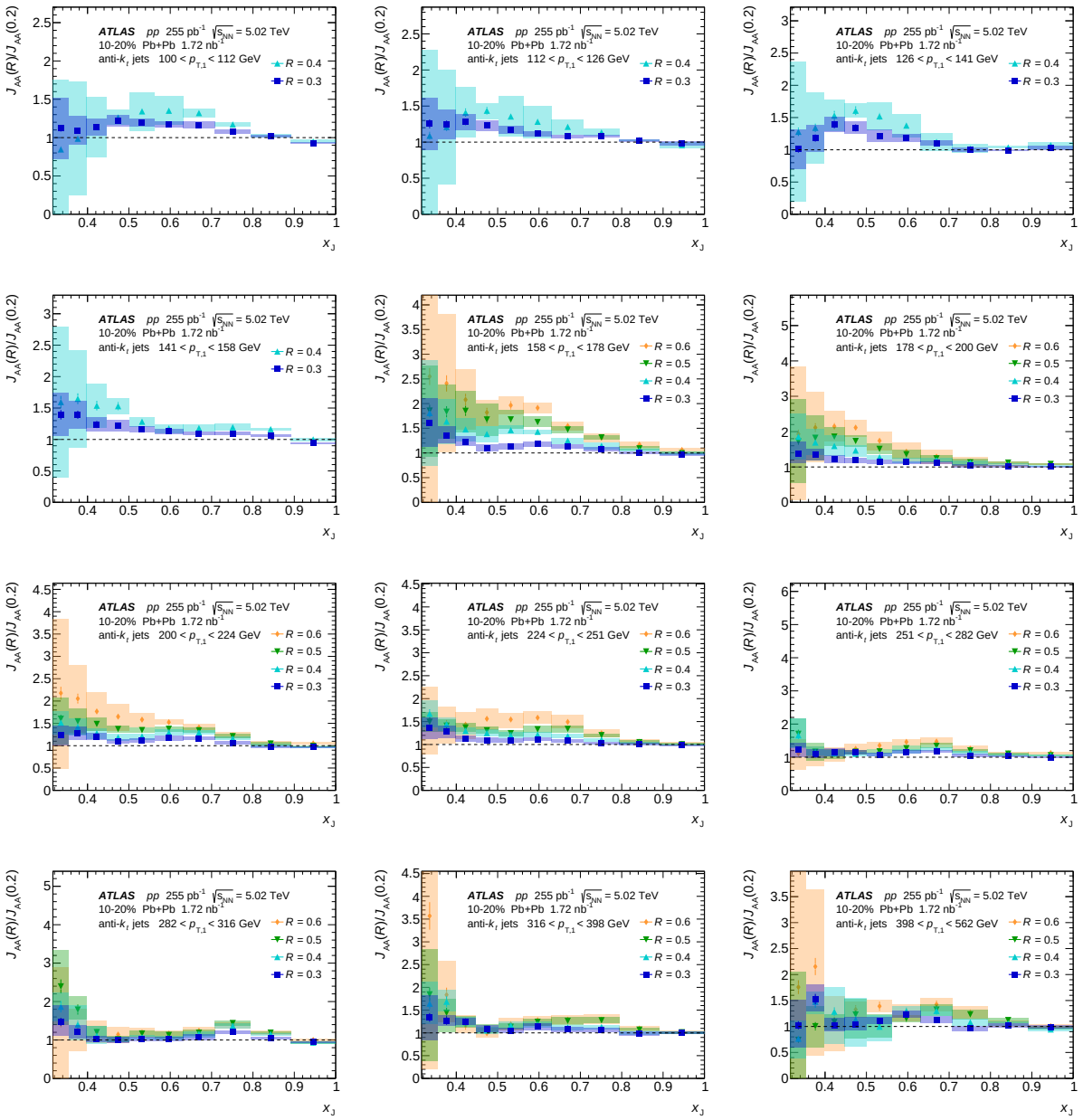

Figure A.26: The $J_{\mathrm{AA}}(R)/J_{\mathrm{AA}}(0.2)$ ratios in 10–20% central Pb+Pb collisions, for $R = 0.2, 0.3, 0.4, 0.5$ and 0.6 jets and various $p_{\mathrm{T},1}$ bins.

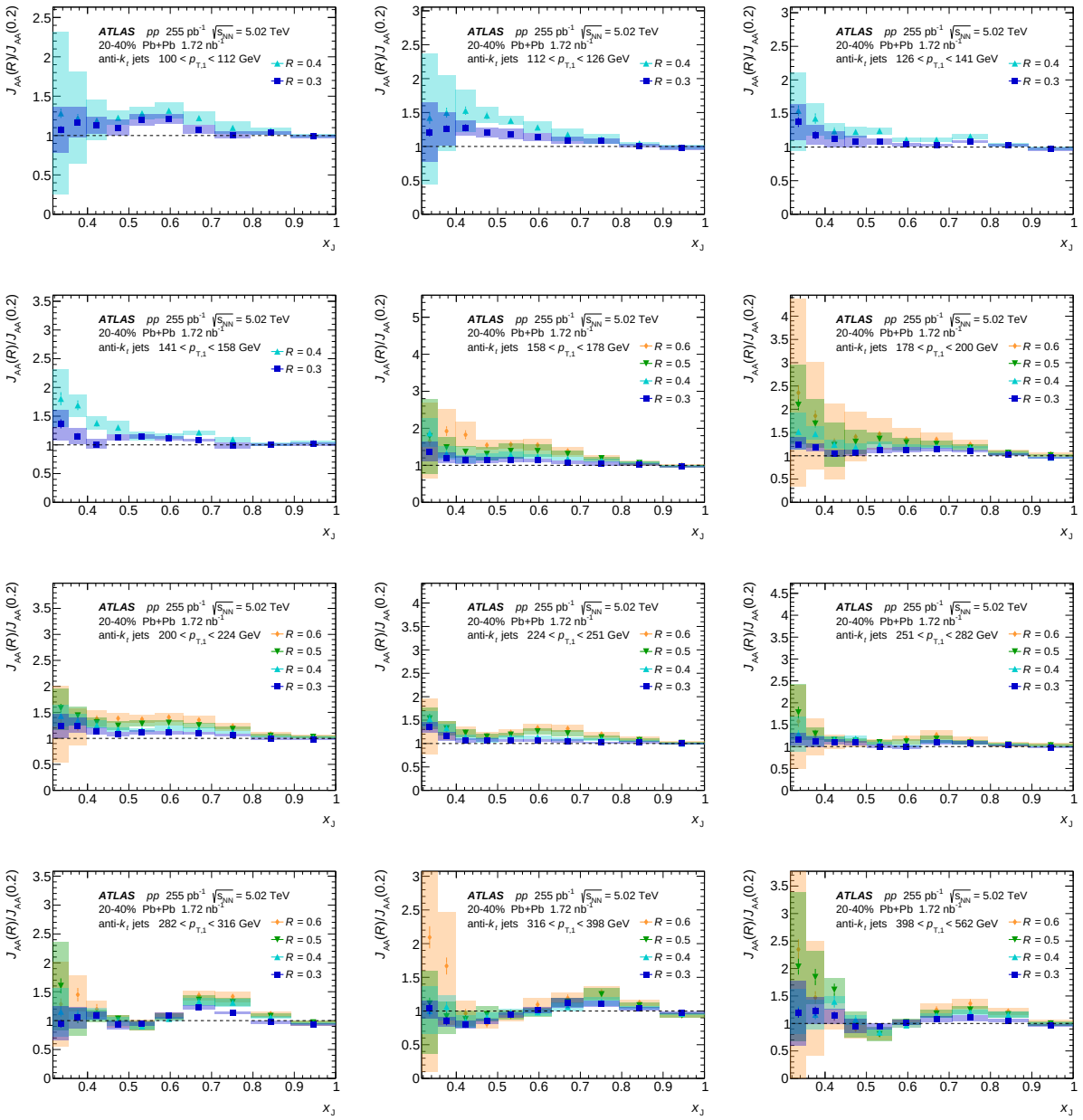

Figure A.27: The $J_{\mathrm{AA}}(R)/J_{\mathrm{AA}}(0.2)$ ratios in 20–40% central Pb+Pb collisions, for $R = 0.2, 0.3, 0.4, 0.5$ and 0.6 jets and various $p_{\mathrm{T},1}$ bins.

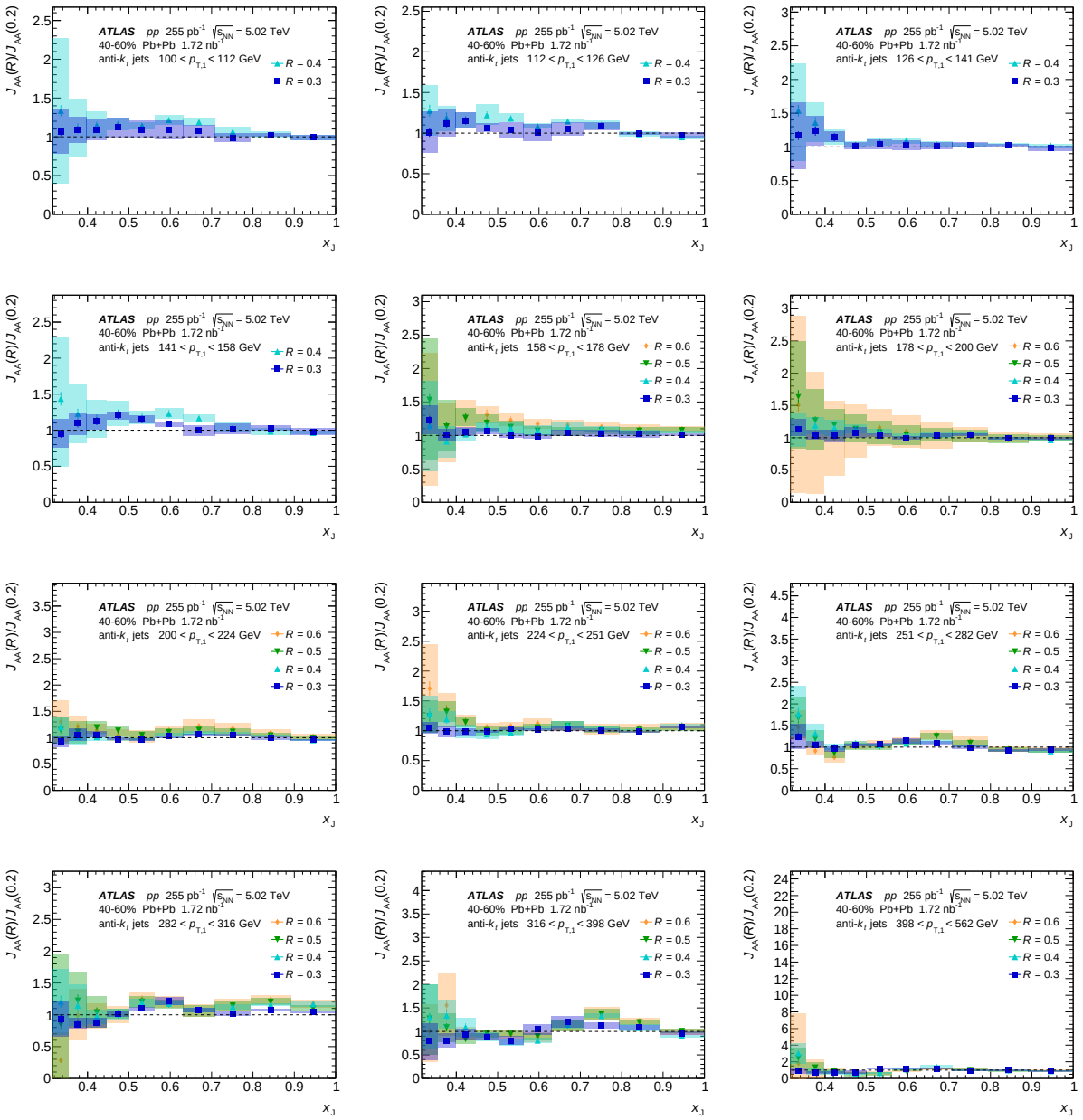

Figure A.28: The $J_{\mathrm{AA}}(R)/J_{\mathrm{AA}}(0.2)$ ratios in 40–60% central Pb+Pb collisions, for $R = 0.2, 0.3, 0.4, 0.5$ and 0.6 jets and various $p_{\mathrm{T},1}$ bins.

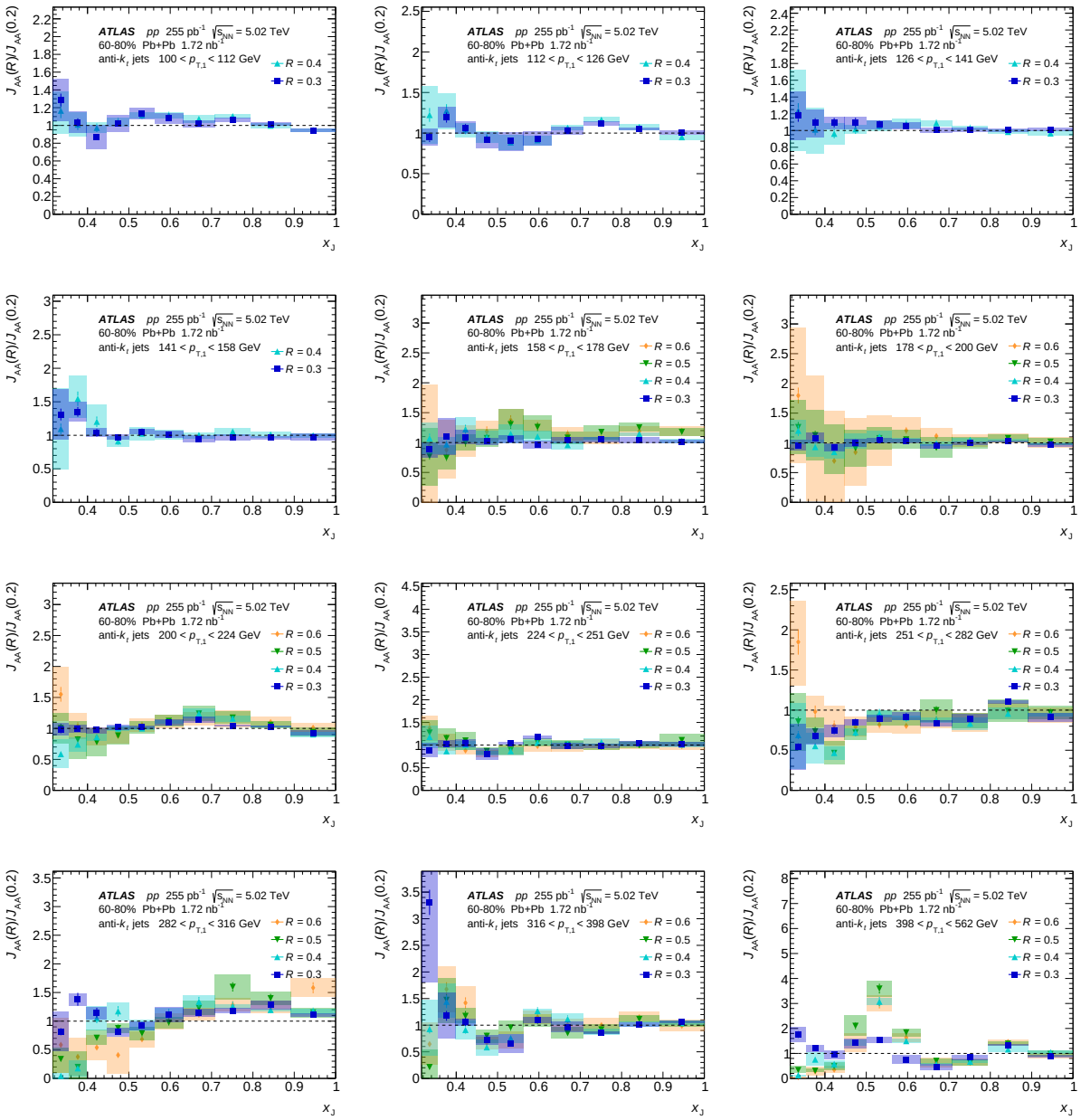

Figure A.29: The $J_{\mathrm{AA}}(R)/J_{\mathrm{AA}}(0.2)$ ratios in 60–80% central Pb+Pb collisions, for $R = 0.2, 0.3, 0.4, 0.5$ and 0.6 jets and various $p_{\mathrm{T},1}$ bins.

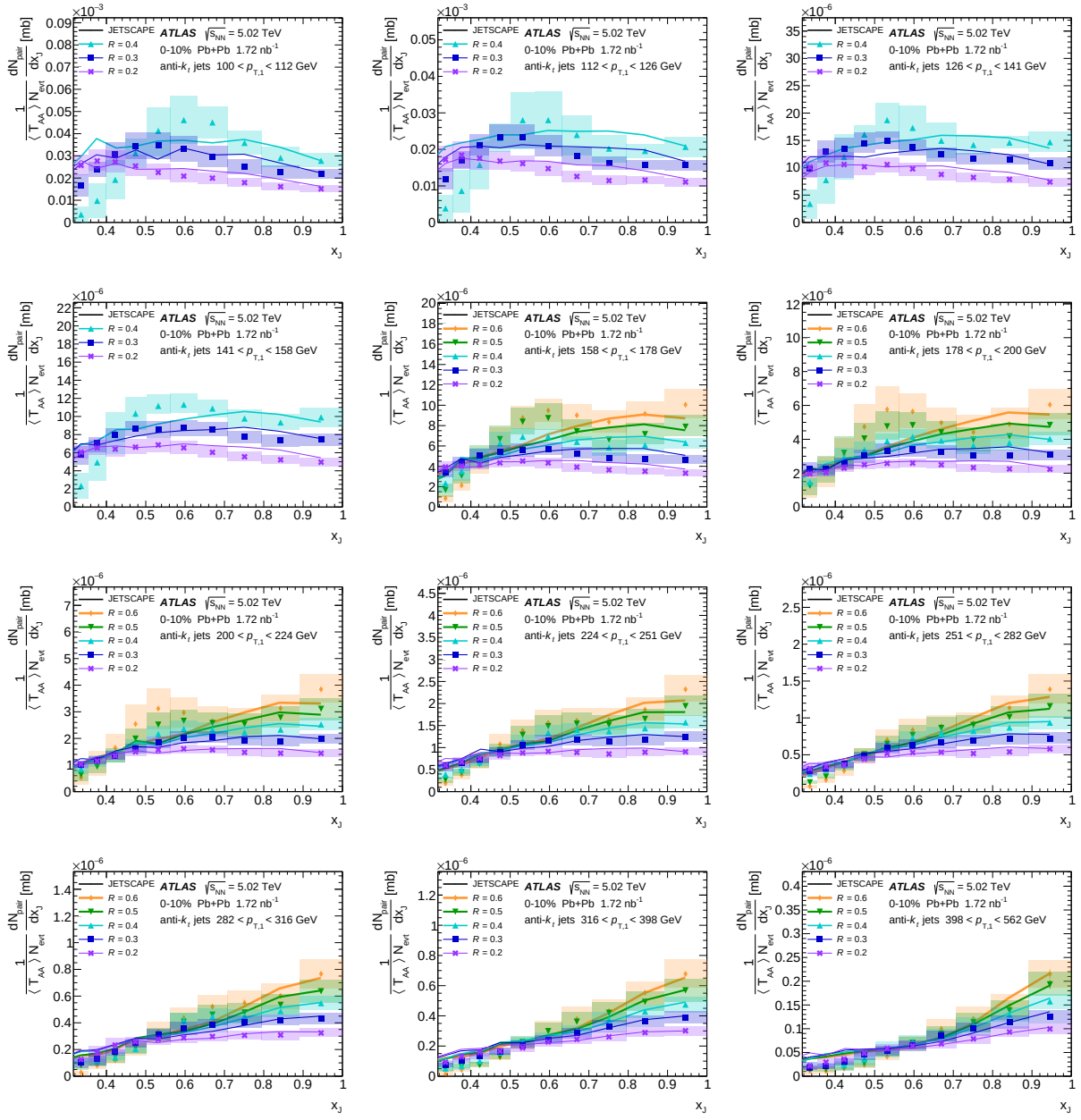

Figure A.30: x_J distributions in data compared with the JETSCAPE model, for $R = 0.2, 0.3, 0.4, 0.5$ and 0.6 jets in 0–10% central Pb+Pb collisions and various $p_{T,1}$ bins.

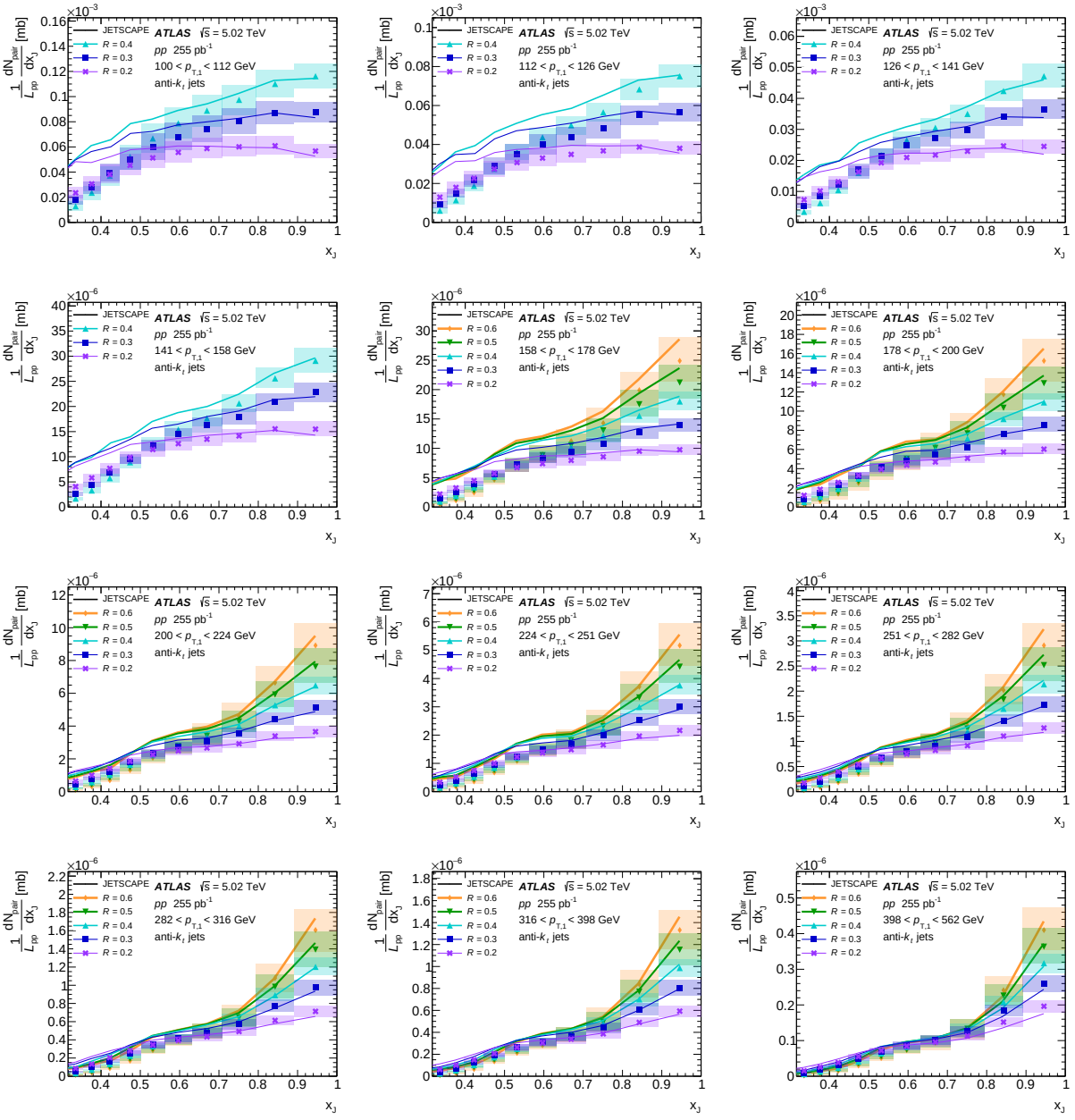

Figure A.31: x_{J} distributions in data compared with the JETSCAPE model, for $R = 0.2, 0.3, 0.4, 0.5$ and 0.6 jets in pp collisions and various $p_{\mathrm{T},1}$ bins.